Multiscale Mechanics of Failure in Extreme Environments

by

Justin W. Wilkerson

A dissertation submitted to The Johns Hopkins University in conformity with the requirements for the degree of Doctor of Philosophy.

Baltimore, Maryland

November, 2014

Abstract

Over the past five decades there has been an intense effort to understand and control the thermomechanical response of materials in extreme environments. A number of technologies and applications critical to our safety and well-being stand to benefit from such understanding, including inertial confinement fusion, nuclear stockpile reliability, defense systems, spacecraft and hypersonic aircraft shielding, as well as vehicular crashworthiness. Materials in such extreme environments often exhibit complex, somewhat non-intuitive behavior that is difficult to predict with empirical or phenomenological models. As such, there has been an increasing effort to understand the microscale processes that govern the macroscale response.

Here we provide a contribution to this effort through the development of a number of multiscale mechanism-based models that explore the fundamental nature of various microscale processes governing the macroscale thermomechanical response of materials in extreme environments.

The extreme environments of interest here may include pressures on the order of the bulk modulus, shear stresses near the ideal strength, temperatures approaching

ABSTRACT

melting, and timescales ranging from nanoseconds to the age of our Solar System ($\sim$ 5 billion years). We focus on materials in two particular extreme environments in this thesis. First and foremost, we explore the behavior of metals subject to very high rate deformation. Second, we study the behavior of planetary materials subject to the extreme thermomechanical environments in our Solar System.

One of the main themes presented in the thesis is that the time-dependent failure of materials is governed, in part, by the kinetics of a hierarchy of microscopic material defects. Furthermore, the kinetics of one particular defect are often governed by lower length-scale defects. Examples of this are provided for twin boundary propagation at high loading rates, dynamic void growth in ductile materials, and fatigue crack growth in quasi-brittle asteroidal materials.

A second theme is that simple mechanism-based models are powerful and instructive, particularly when it comes to building an intuition for dynamic failure processes. We make use of such simple scaling laws to help establish a deeper understanding of dynamic ductile failure of metals. We particularly focus on understanding how the rate-sensitivity of spall strength depends on a competition between the pre-existing material microstructure (e.g. second-phase particles and grain boundaries) and the shock-induced microstructure.

Thesis Advisor and Primary Reader: KT Ramesh

Secondary Readers: Lori Graham-Brady and Jaafar El-Awady

Acknowledgments

Crystals are like people: it's their defects that make them interesting.

– Sir Charles Frank

Most people will view this dissertation as a sole personal achievement representing the culmination of a two and a half decade pursuit of academic excellence. However, this dissertation would not have come to fruition without the many teachers, mentors, advisors, professors, friends, and loved ones who have pushed me to this point in my life, for which I am extremely appreciative.

I came to Johns Hopkins in the fall of 2010, and I vividly remember my first meeting with Dr. KT Ramesh, who had graciously agreed to be my Ph.D. advisor on rather short notice. We instantly connected while sketching out a half dozen potential research directions. I left the meeting full of enthusiasm, and I remember trying to explain to my wife, to no avail, the concept of the *KT high* I was experiencing. Over the next four years, there were many such meetings, which served as continuous sources of inspiration. KT has played a profound role in shaping and molding me

into the scholar I have become today. I hope to continue to learn and evolve from his many lessons and pass them on to the next generation of scholars.

A special thank you goes out to Drs. Daniel Davis and Dimitris Lagoudas, who I had the great pleasure of working with at Texas A&M. Dr. Davis nurtured and cultivated my enthusiasm for basic research and taught me to see the broader impact of our work. Thank you to Dr. Lagoudas who patiently mentored and guided me through my evolution into a more disciplined and focused researcher. The strong research foundation instilled in me at Texas A&M was vital to my success at Hopkins.

Today, the most exciting and groundbreaking research is taking place at the interface of traditional disciplines. To Dr. Marco Delbo, it has been an absolute pleasure to work with you at the interface of solid mechanics and planetary science. Your enthusiasm and passion for the subject is incredibly infectious, and working with you has been a blast. To Dr. Guangli Hu, I wish there had been a greater overlap between our times at Hopkins so that a concrete contribution could have come out of our many interactions on brittle fracture modeling. To Drs. Nitin Daphalaparkur and Tim Wright, it was a joy to work with you on pushing continuum mechanics down to atomistic length-scales. To Dr. Leslie Lamberson, I've had great fun working with you on the micromechanics of failure in piezoelectric materials. To Drs. Kavan Hazeli, Jamie Hogan, and Cyril Williams, thank you for helping me to provide some real-world validation of my seemingly half-baked theories. I look forward to many more collaborations with each of you.

ACKNOWLEDGMENTS

Drs. Lori Graham-Brady and Jaafar El-Awady rounded out my thesis committee. Thank you for being so flexible with me, and I very much appreciate the constructive feedback. I would also like to acknowledge the words of encouragement from Drs. Dave McDowell, Alan Needleman, Amine Benzerga, and John Foster whose support refueled my motivation. And to the HEMI staff, in particular, Matt Shaeffer, Katie Vaught, Bess Bieluczyk, and Melissa Rosenberger, thank you for making everything run so smoothly.

This thesis would have undoubtedly been a far greater struggle without the many excellent teachers who imparted their knowledge to me over the years. In particular, thank you to Dr. Dimitris Lagoudas who showed me the beauty of Eshelby micromechanics, Dr. KT Ramesh who taught me continuum mechanics in the spirit of Truesdell, and Dr. Kevin Hemker who introduced me to the wonders of dislocations. I would also like to thank Drs. Johnny Hurtado and Adonios Karpetis whose courses on introductory mechanics and thermodynamics first sparked my interests in pursuing graduate studies, and to Dr. Robert (Bob) Cammarata, thank you for finally teaching me what the heck entropy was all about. To Drs. Gary Seidel and Rashid Abu Al-Rub, thank you for walking me through the practical details of micromechanics and continuum damage mechanics modeling.

I would also like to acknowledge the many graduate students, post-docs, and visiting scholars in KT's group who exposed me to a wide variety of topics. To Dr. Jessica Muelbrook thank you for walking me through the details of your ductile

fragmentation code as well as the codes on dynamic void growth and shear banding. Thank you Dr. Swapnil Patel for helping me with the theoretical as well as practical details of your nonlocal crystal plasticity simulations. To Dr. Cyril Williams, our many discussions and debates on spall failure were very fruitful, and I rather enjoyed how you would sprinkle in seemingly unrelated stories to liven things up.

A number of graduate students and post-docs also helped me to gain a better understanding of some of the fields that interface with traditional solid mechanics. Thank you to Drs. Jamie Kimberley and Angela Stickle for helping me transition into planetary science. To Dr. Andy Tonge, I enjoyed our numerous discussions and debates on the many computational methods that keep popping up. Thank you to Drs. K. Eswar Prasad and Lukasz Farbaniec for being my resident material scientists and schooling me on Hall-Petch strengthening, twin boundaries, and second-phase particles.

Along with KT, a few of you helped me to become a better communicator of science to the broad audience. Thank you Dr. Emily Huskins for showing me how to give great conference talks. I stole your presentation template and still use it today. To Dr. Leslie Lamberson, thank you for converting me to LaTeX early on, and saving me much headache. To Drs. Cindy Byer and Rika Wright, thank you for convincing me to get involved with science advocacy at the congressional level. Seeing the making of the sausage will be invaluable to my future endeavors.

To the younger graduate students in KT's group, I was constantly re-invigorated

by your passion and eagerness for learning. At times you all have asked probing questions that have made me rethink a basic assumption or reformulate an argument. To Vignesh Kannan, Meng Zhao, Charles El-Mir, Fatma Madouh, Amy Dagro, Debjoy Mallick, Kimmie Leonard, and Andrew Robinson I wish you all the best at Hopkins and look forward to hearing of your many successes.

Making it through the dissertation writing process with one's sanity intact demands a support network of friends and family who deserve acknowledgement. A special thank you goes out to Amy and Debjoy who kindly opened their home to me so I could finish the last two months of writing in Baltimore. They nourished me with delicious home-cooked meals and went out of their way to make sure that I didn't have to worry about anything but thesis writing. From what I hear, thesis writing is supposed to be a tortuous experience in one's life, but the great friends I had at Hopkins turned it into something that I will long reminisce over. Thank you, in particular, to Andrew "Mullet Man" Robinson, Debjoy "Little Debbie" Mallick, Amy "Little Ebola" Dagro, Katie "Crazy Cat" Vaught, Dr. Jamie "Dontcha know" Hogan, Dr. Adam "Papa AJ" Fournier, and soon-to-be Dr. Neha "Leafy Bug" Dixit for keeping my spirits up with an endless supply of shenanigans.

To Magda, Dimitris, and Georgia Lagoudas, thank you for your continued personal and professional guidance. You all have been with me for every milestone, for which I am very grateful. I also thank you all for pushing me to take on the twelve Herculean challenges, which was great preparation for writing this dissertation. Whenever times

get tough you all taught me to think of Agamemnon who was rumored to have said "Πάθει μαθός" and the wise words of Alexander the Great, "Ουδέν τοις θαρρούσιν ανάλωτον."

Thank you to my mother and father who raised me. They made incredible sacrifices for my academic success, for which I am very thankful. To my late father, thank you for nurturing my scientific curiosity, allowing me to keep my many insect collections in the house and forgiving me when experiments on my little brothers, Kevin and Dillon, went awry. To my mother thank you for being deeply invested in my academic success: attending all school functions, field trips, and award ceremonies as well as taking it upon yourself to change my dorm assignment, unbeknownst to me, to Lechner Hall, the freshman honors dorm at Texas A&M, which turned out to be a transformative environment.

Last on the list, but first in my heart, is my wonderful wife Natasha. You supported me through every step of my graduate studies. This accomplishment is as much yours as mine. I am so very thankful to share life's journey with you.

To my loving & supportive family

Contents

List of Tables

List of Figures

Chapter 1

Introduction and motivation

In 2008, the U.S. National Academy of Engineering (NAE) released a list of 14 grand challenges for engineering in the 21st century [1]. Cracking even a fraction of these has the potential to greatly improve the human condition across the globe and continue the advancement of our civilization. Of these 14 challenges, at least four intimately depend on our ability to predict and control the behavior of materials in extreme environments [2], i.e.

- ✦ Combat climate change by engineering carbon sequestration methods
- ✦ Greatly improve the efficiency and economics of solar energy
- ✦ Make nuclear fusion an affordable, environmentally benign source of energy
- ✦ Engineer the tools to prevent nuclear terror and maintain global security.

In addition to these incredibly important engineering challenges, extreme environments are also ubiquitous in Earth, planetary, and space sciences, e.g.

- ✦ Early formation of our Solar System
- ✦ Composition and structure of planet cores
- ✦ Prediction of subsonic and supersonic earthquakes
- ✦ Impact cratering and surface evolution of asteroids, moons, and planets
- ✦ Spacecraft shielding from orbital debris and micrometeroid impact
- ✦ Defending Earth from the threat of asteroid and comet impact

With these engineering challenges and scientific opportunities in mind, the primary aim of this dissertation is to advance the fundamental understanding of material failure in extreme thermomechanical environments. Such extreme environments may include pressures on the order of the bulk modulus, shear stresses near the ideal strength, temperatures approaching melting, and timescales ranging from nanoseconds to the age of our Solar System ($\sim$ 5 billion years).

Two particular extreme environments are considered in this thesis. First and fore most, we explore the behavior of metals subject to very high rate deformation ($10^4 - 10^{10}$ s^{-1}). Additionally, we study the behavior of celestial materials subject to the extreme thermomechanical environments experienced in our Solar System.

1.1 Complex physics and material behavior unique to extreme dynamic environments

The central tenet that fundamentally differentiates the *dynamic* behavior of materials from their simpler *quasi-static* response is the fact that

Every mechanism or process evolves over finite timescales.

A loading state is considered to be quasi-static if the system remains in an equilibrium condition throughout the loading. On the other hand, we consider loading states to be *dynamic* if the timescale over which energy enters the system is comparable to

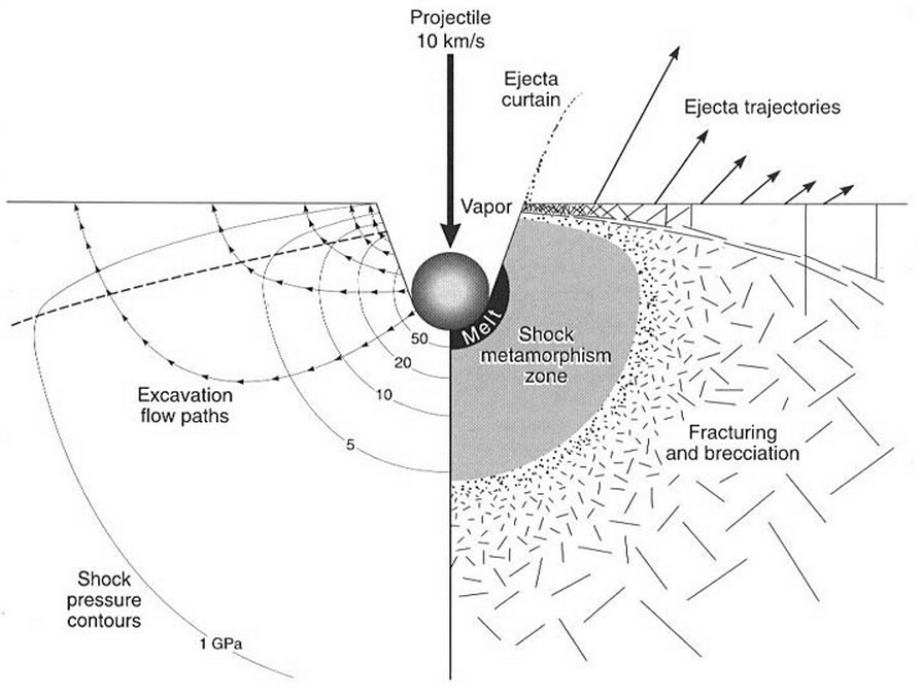

Fig. 1.1: Mechanism map associated with hypervelocity impact on a celestial body [3].

or faster than the timescales associated with the dynamic response of the relevant mechanisms and processes. In solid materials and structures these mechanisms and processes may include:

- ✦ stress propagation at finite wave speeds, $\mathcal{O}(\text{km/s})$
- ✦ thermal transport over finite timescales, $\mathcal{O}(\text{cm}^2/\text{s})$
- ✦ propagation or growth of defects, $\mathcal{O}(\text{nm/s} - \text{km/s})$
- ✦ nucleation of defects, $\mathcal{O}(\text{ps} - \text{ns})$
- ✦ elastic deformations, $\mathcal{O}(\text{ps})$
- ✦ phase transformations, $\mathcal{O}(\text{ns} - \mu\text{s})$,

where the approximate process timescales are representative of metals and ceramics. Purely mechanical loading of materials may be considered *dynamic* if the applied strain rates are $\gtrsim 10^1\ \text{s}^{-1}$, while problems governed by nonequilibrium thermal transport may be considered *dynamic*, e.g. *thermal shock*, for much slower loading conditions, i.e. $\gtrsim 2$ K/min. This dissertation focuses heavily on the first four time-dependent processes of the above list, and their consequences on the unique behavior of solids subject to dynamic loading conditions.

The most prevalent source of dynamic loading results from a high-speed impact, which may induce a variety of complex physics [5], e.g.

- ✦ Shock waves
- ✦ Rarefaction waves
- ✦ Nonequilibrium thermal transport
- ✦ Nonequilibrium thermodynamics
- ✦ Melting *&* vaporization
- ✦ Ionization *&* plasma formation
- ✦ Dynamic recovery
- ✦ Dynamic recrystallization
- ✦ Dynamic crack propagation
- ✦ Dynamic crack branching
- ✦ Impact ejecta
- ✦ Crater formation
- ✦ Spall failure
- ✦ Fragmentation
- ✦ Shear banding
- ✦ Shear plugging

Many of these mechanisms and processes occur in planetary impact events, as shown in Fig. 1.1. These impact mechanisms play an important role in, for example,

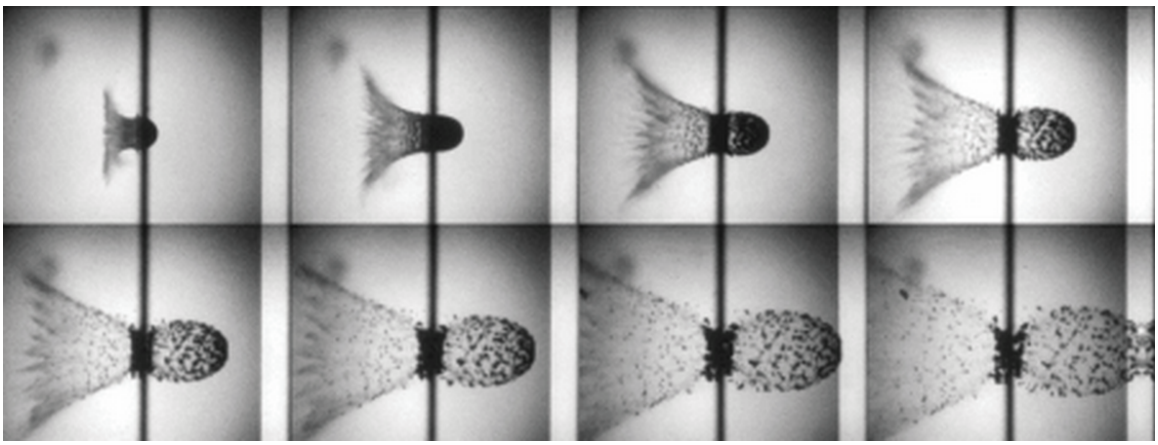

Fig. 1.2: Sequence of *in-situ* images showing the progression of fragmentation, ejecta, and debris cloud formation resulting from the impact of a spherical aluminum projectile traveling at ∼8 km/s on a thin aluminum plate [4].

the early formation of our Solar System and the surface evolution of planetary bodies.

Much of our current fundamental understanding regarding these impact processes has come from laboratory investigations that provide *in-situ imaging of the dynamic processes over the appropriate timescales.* For example, consider the sequence of *in-situ* images reproduced in Fig. 1.2 from [4] that clearly demonstrate the progression of fragmentation, ejecta, and debris cloud formation processes resulting from a hypervelocity impact. Understanding these dynamic processes is particularly important to missile defense applications and spacecraft shielding, in addition to the planetary impact applications discussed earlier.

Another common occurrence in high-speed impact problems (and extreme environments more generally) is nonintuitive behavior. One excellent example of this is the process of spall failure. Consider again the hypervelocity impact shown in Fig. 1.2. In this case, the plate is far too thin to prevent the penetration of the projectile. Obviously, the projectile can be defeated by sufficiently increasing the thickness of the

(a)  (b) 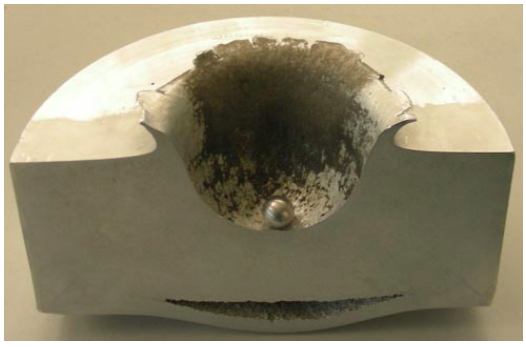

Fig. 1.3: *Post-mortem* images of thick aluminum plate impacted by a spherical aluminum projectile traveling at ∼6.8 km/s [6]. An impact crater is formed on the front face (top here) of the plate, and a spall failure develops on the back face (bottom) of the plate.

plate. Figure 1.3 shows the aftermath of a hypervelocity impact with similar materials and conditions utilized in Fig. 1.2, but a much thicker plate. The projectile is vaporized by the hypervelocity impact with none of its components penetrating the thick plate. However, a spall failure develops on the back face of the plate, opposite from the impact face. This spall failure develops as a result of the complex interaction of stress waves with free-surfaces and interfaces. Although not the case in Fig. 1.3, typically the spall fracture results in the generation of a high velocity cloud of fragments that is a primary cause of armor vehicle kills during combat [7]. In addition to these geometric concerns, designing impact-resistant structures is further complicated by the nonintuitive observation that weak high-purity single crystals often exhibit a greater resistance to spall failure than their corresponding stronger polycrystalline alloys.

(a) 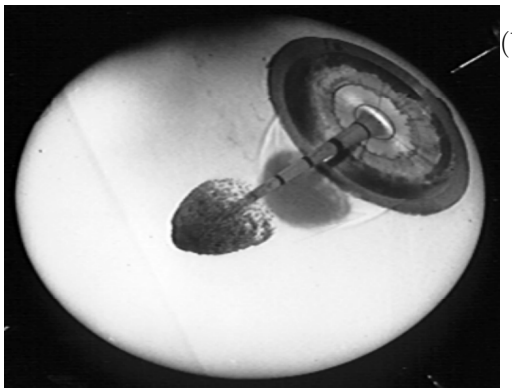 (b) 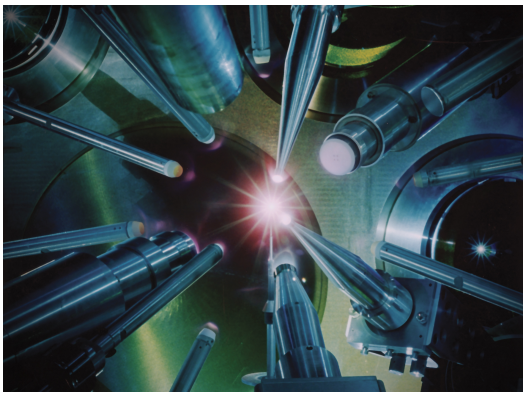

Fig. 1.4: (a) *In-situ* images of the initial formation of a shaped charge jet resulting from the explosively driven collapse of a thin conical copper liner [8]. (b) Image representing the laser-driven dynamic compression of a deuterium-tritium capsule to achieve inertial confinement fusion (courtesy of U.S. Department of Energy).

Clearly, understanding and controlling the behavior of materials in extreme dynamic environments is anything but simple. However, once a sufficient level of understanding has been achieved, the unique properties of materials and structures in these environments can be harnessed to achieve some remarkable behavior. Two excellent examples of this are shown in Fig. 1.4: (a) the Munroe Effect utilized in the formation of shaped charge hypersonic jets used in armor penetration as well as oil and gas perforation applications and (b) inertial confinement fusion achieved through the dynamic compression of cryogenic deuterium-tritium capsules driven by high-intensity lasers. Being able to predict and delay the onset of material instabilities in these extreme dynamic environments is one of the primary challenges to the advancement of such technologies.

1.2 Multi-scale mechanism-based modeling and materials in extreme environments: A symbiotic relationship

Over the past few decades, an intense effort has been underway to develop the capabilities and tools to predict macroscopic material behavior from the underlying material structure. Prediction of inelastic thermomechanical properties has proven particularly challenging, as these properties are highly sensitive to defects in the

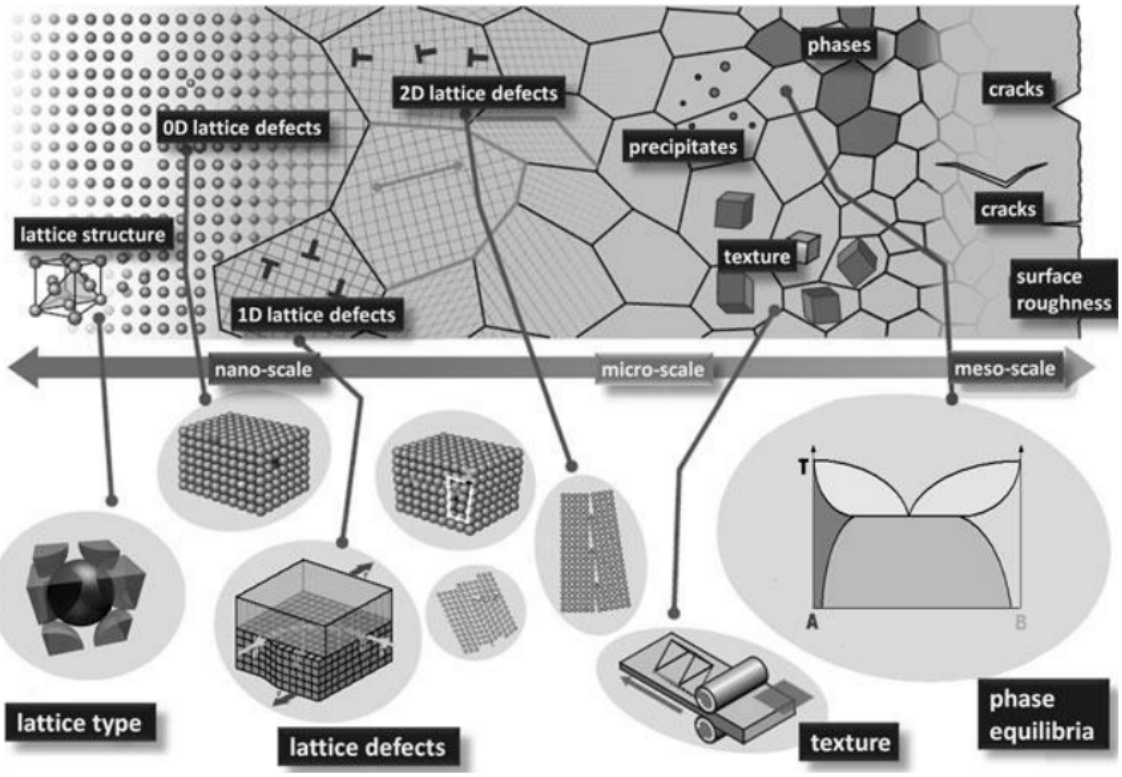

Fig. 1.5: The cascading hierarchy of material structure and defects across the relevant length scales [9].

atomic structure. These defects span the gamut of length scales (see Fig. 1.5), from angstroms to millimeters, and are strongly coupled, thus posing a formidable challenge for computational multi-scale modeling. Since the thermomechanical limits of materials are often the principal bottleneck to the advancement of most technologies, meeting this challenge has the possibility to drastically improve the human condition.

Multi-scale mechanism-based modeling of inelastic thermomechanical behavior may have its earliest and perhaps greatest successes in predicting the behavior of materials subject to extreme dynamic environments. Consider the task of The National Nuclear Security Administration (NNSA) to ensure the reliability of the U.S.

stockpile under the current ban on full-scale testing. Here, by pure necessity, multi-scale mechanism-based modeling must play a critical role.

Understanding the behavior of materials in extreme dynamic environments is also vital to the broader field of multiscale modeling across all disciplines of engineering, physics, chemistry, and biology. *Ab initio*, atomistic, molecular, and discrete defect simulations are ubiquitous throughout engineering and science research, see for example Fig. 1.6 for an application of multiscale modeling to the improvement of vehicular crashworthiness. These methods are attractive because they resolve a great amount of physical detail, for example the fine-scale motion of individual atoms and molecules

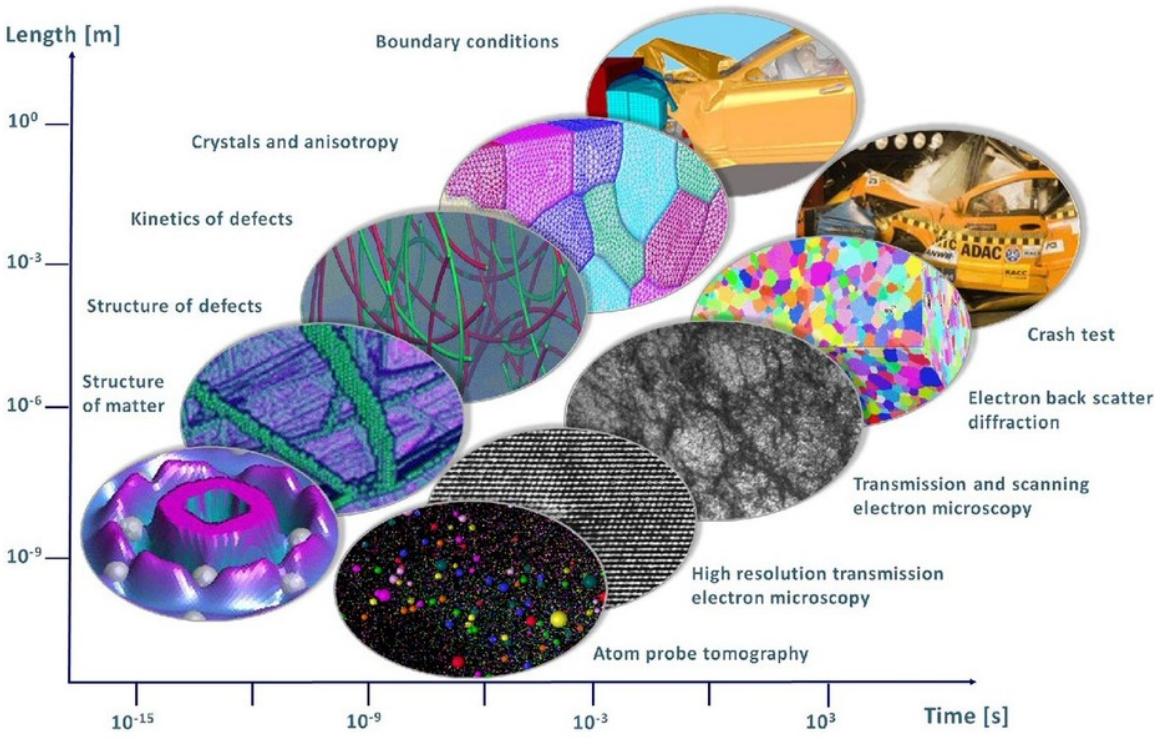

Fig. 1.6: The length and timescales currently associated with various computational and experimental capabilities for probing the multi-scale structure and behavior of materials [9].

are explicitly resolved in molecular dynamics simulations. One of the inherent problems with these methods, however, is that current computational capabilities limit these simulations to extremely short timescales, as can be seen in Fig. 1.6. Often the scientific or technological interest involves understanding a process that occurs on human timescales. Nevertheless, these methods are pervasive. It should be understood that these simulations are interrogating the physical processes under conditions associated with extreme dynamic environments.

By focusing on first developing a fundamental understanding of the behavior of materials on extremely short timescales and how it differs from more *quasi-static* ambient conditions, we may find greater success in applying the predictions of atomistic and discrete defect simulations to processes that operate under fairly ambient conditions. Through this symbiotic relationship it is clear how the study of materials in extreme environments (a seemingly esoteric subject) may play a critical role in the advancement of the broader science as well as the vast number of somewhat ambient technologies that permeate today's society.

1.3 Organization and common themes

The thesis covers a range of topics related to the failure of materials subject to extreme dynamic environments. The focus of the thesis is on the development of multi-scale mechanism-based failure models that are predictive while also shedding

light on the most important governing mechanisms. Throughout the thesis the reader will find three central recurring themes:

- ✦ Kinetics of defects across multiple length scales govern time-dependent failure
- ✦ Kinetics of a particular defect are often governed by lower length-scale defects
- ✦ Simple mechanism-based failure models are powerful and instructive.

Each chapter of the thesis hits upon at least two of these central themes. In chapter 2 we utilize molecular dynamics simulations and theory to build on the fundamental understanding of lattice defect kinetics. We first show that the kinetics of full dislocations (atomistic line defects) are very similar to those of twinning partial dislocations. Additionally, we provide a simple mechanism-based model demonstrating that the kinetics of these twins (atomistic planar defects) are governed by a combination of the discrete kinetics of these twinning dislocations as well as their population density. The relationship between the kinetics of dislocations and twins has a number of implications for the high-rate deformation of materials that twin.

In chapter 3, we continue with the theme that kinetics of one defect are governed by lower length-scale defects; here, exploring the relationship between dislocation kinetics and void dynamics (volumetric defects). Implementing a dislocation-based viscoplasticity model (proposed by Austin and McDowell [10]) in our simple mechanism-based void growth framework, we are able to define the regimes in which a combination of mobile dislocation densities and dislocation kinetics directly govern the kinetics

of void growth. The consequence of this fundamental relationship has a number of experimentally-observable implications that are discussed.

One significant prediction of the mechanism-based model developed in chapter 3 is the eventual shutdown of void growth due to an exhaustion of the supply of mobile dislocations. Chapter 4 provides a discussion of one particular mechanism for replenishing the supply of mobile dislocations in the vicinity of the void: dislocation emission. This emission-driven replenishment allows voids to continue growing past the shutdown point discussed in chapter 3. Additionally, chapter 4 provides an argument for how the activation of dislocation emission enables extremely small nanovoids to grow and contribute to the dynamic failure of ductile metals, the consequences of which are studied in chapter 5. However, prior to proceeding to these implications it was necessary to provide a number of extensions to the state-of-the-art mechanism-based model for dislocation emission, e.g. Lubarda [11]. In addition, chapter 4 proposes a methodology for independently calibrating model parameters and provides extensive model validation against molecular dynamics simulations.

Chapter 5 effectively incorporates the key findings of chapter 3 and chapter 4 into a simple multi-scale mechanism-based framework for predicting the spall strength of ductile metals. With this framework in hand, we are able to effectively demonstrate the role of defect kinetics on dynamic ductile failure. Under the most extreme loading conditions ($\gtrsim 10^7$ s^{-1}), the dynamic failure response is governed by a hierarchy of mobile defects on cascading length scales. Under somewhat less extreme loading

conditions ($\lesssim 10^6$ s^{-1}), the material microstructure, e.g. second-phase particles, grain boundaries, triple junctions, etc., plays a more important role in the dynamic failure response. Through this mechanism-based model we are also able to shed some light on a number of traditionally perplexing observations in the literature and make some predictions that may have technological significance.

Chapter 5 makes a number of assumptions that lead to a simplified analysis that is very instructional and helps in the development of a general intuition about these problems. Although these assumptions seem reasonable for the prediction of one-dimensional spall failure, they may not be valid under more general loading conditions. In chapter 6, we provide an extension of the mechanism-based framework to account for arbitrary three-dimensional loading paths, anisotropic materials or crystals that experience significant hardening, and a more rigorous treatment of the nonequilibrium thermodynamics and inelastic dissipations.

In chapter 7, we turn our attention to a second extreme environment: our Solar System. In particular, we examine the competition between impact processes and thermal processes on the surface evolution of near-Earth asteroids and similar celestial bodies. The problem serves as an excellent example of the power of our simple multi-scale mechanism-based approach. We provide a computationally-efficient framework that is capable of resolving the short timescales associated with nonequilibrium thermal transport, $\mathcal{O}$(seconds), as well as the extremely long timescales associated with breakup and fragmentation by gradual fatigue crack growth, $\mathcal{O}(10^4 - 10^9$ years).

Additionally, we account for the effect of material heterogeneities on the kinetics of thermal fatigue crack growth. This particular application touches upon all three of the common themes discussed earlier. Lastly, chapter 8 provides a summary of the key findings and discusses some opportunities for future work.

Chapter 2

Kinetics of twin boundaries governed by dislocation kinetics[†]

A complete description of high-rate, dynamic deformation of metals demands the fundamental understanding and characterization of defect kinetics. Our understanding of the kinetics of linear defects is extensive, see Hirth and Lothe [13] and references therein. However, a similar level of understanding is lacking for the kinetics of planar defects, e.g. twin boundaries, phase boundaries, grain boundaries, etc., as well as the kinetics of volumetric defects, i.e. voids. Fortunately, the kinetics of planar and volumetric defects may often be fundamentally related to the kinetics of linear defects. In the present chapter we explore this relationship between linear and planar defect

[†]The present chapter is largely based on a publication by Daphalapurkar et al. [12]. The contribution of J.W. was significant, particularly to the theoretical analysis and writing.

kinetics by examining the kinetics of twin boundaries and their relationship to the kinetics of twinning dislocations. In chapter 3 we demonstrate a similar relationship between the kinetics of dislocations and dynamically growing voids.

Here we utilize molecular dynamics (MD) to characterize the twin boundary (TB) kinetics in nickel, which serves as a model material for understanding TB kinetics in face-centered cubic metals. The kinetics of twinning dislocations (TD) fundamentally govern the TB kinetics, which share many common features with full dislocation kinetics, including non-linear kinetics, stable propagation regimes and *forbidden* velocities. However, we find that a TD experiences an additional drag (as compared to a full dislocation) due to damping interactions with the TB; these characteristics are reflected in the TB kinetics. We show that in nickel, TB velocities are limited to ~ 650 m/s, well below the shear wave speed. The insights gained from the MD simulations inform our proposed kinetic relations for TD and TB, and we show how these kinetic relations may be utilized in both macroscopic and crystal plasticity formulations.

2.1 Introduction and background

Twinning is an important deformation mechanism in a number of structural metals, such as nanocrystalline face-centered cubic metals (e.g. Al, Cu, Ni) [14–16], hexagonal close packed metals (e.g. Mg, Ti) [17, 18], body-centered cubic metals (e.g. Ta) under high loading rates [19] and advanced materials such as nanotwinned

Cu [20] and ferromagnetic shape memory alloys [21]. A twin is a variant of its host lattice and is bounded between twin boundaries and grain boundaries. For example, in face-centered cubic (FCC) metals a twin can be bounded by a pair of $\Sigma 3 \langle 111 \rangle$ coherent twin boundaries, and on some other sides it can be bounded by a number of dislocations (called twinning dislocations) to form a $\Sigma 3 \langle 211 \rangle$ incoherent twin boundary, schematically shown in Fig. 2.1(b). A twin can accommodate a considerable amount of plastic deformation as it grows in size, which is accomplished by motion of the twin boundaries [22]. Fig. 2.1(a) shows the development of twins in shock compressed Ni [23].

A particular mechanism for twin boundary (TB) motion in FCC metals involves the glide of twinning dislocations (TDs) along the TB [24], schematically shown in Fig. 2.1(b). Wang et al. [24] demonstrate this mechanism through *in situ* transmission electron microscopy experiments on Cu with pre-existing nanoscale twins. They observed numerous TDs emitting in a sequential fashion from the intersection of a TB with a grain-boundary [24]. This was also suggested by molecular dynamics (MD) simulations [20].

In the case of dislocation motion, the kinetics at high velocities are commonly described by $Bv = \tau|\boldsymbol{b}|$, where v is the dislocation velocity and B is the drag coefficient (typically due to the interaction of dislocations with lattice phonons and electrons), $|\boldsymbol{b}|$ is the magnitude of the Burgers vector and τ is the resolved shear stress along $\boldsymbol{b}$. This equation assumes that the barriers to motion are negligible compared to the

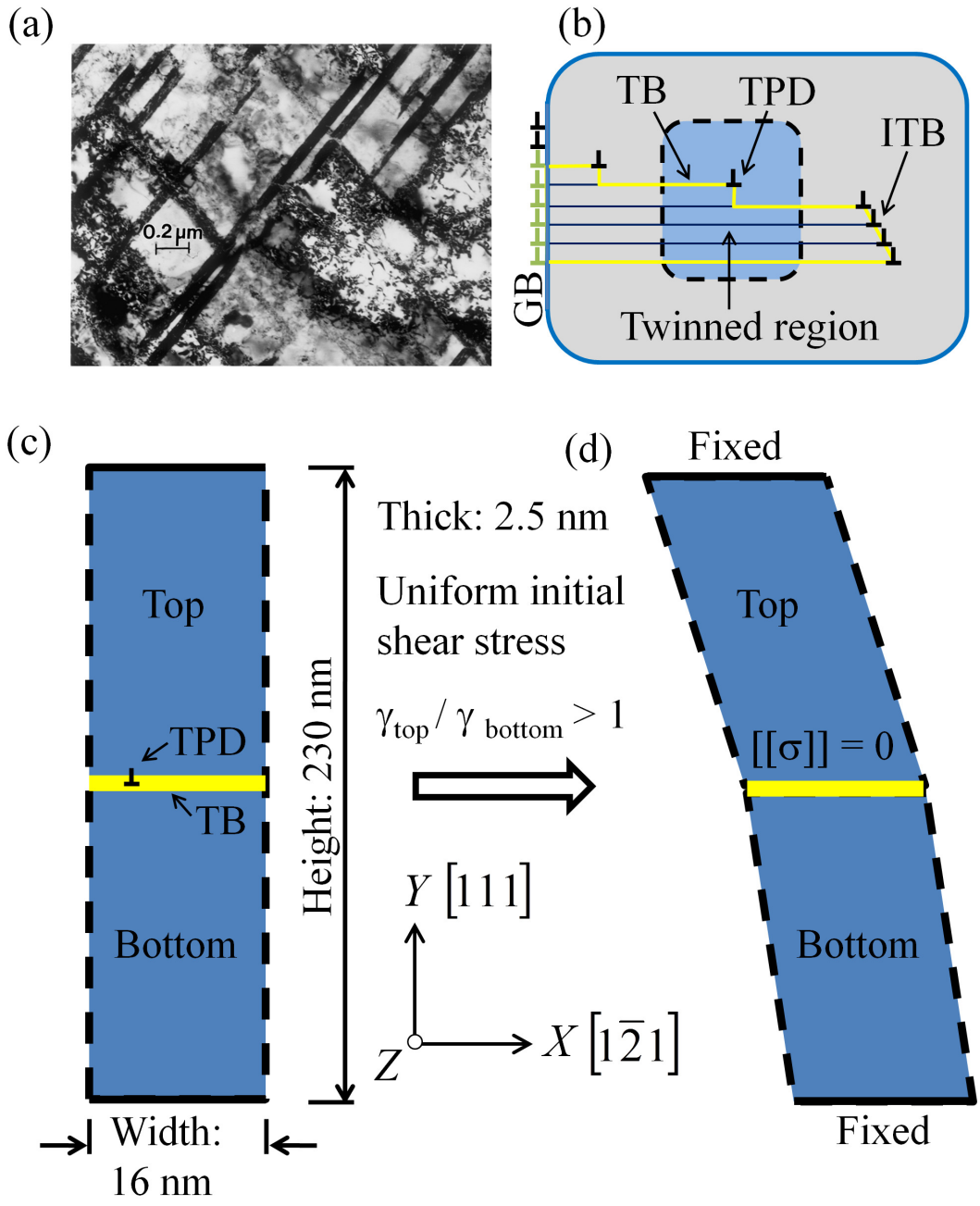

Fig. 2.1: (a) Twins in shock-compressed Ni [23]. (b) Schematic for the development of a twin, accomplished by nucleation and propagation of TDs. (c) TB model in this work for MD simulations. (d) Specimen with a uniform shear stress, $\sigma_{xy} := \tau \neq 0$, while all other components were zero in the initial condition.

applied shear stress. Results from MD simulations on Al using potentials based on the embedded atom method have shown consistency with the range of experimental values for the drag coefficient of a fast moving full dislocation [25]. The rate of plastic deformation in metals that deform by dislocations is governed, in part, by the kinetics of dislocations [25, 26]. Similarly, the rate of plastic deformation in metals that deform by twinning is governed, in part, by the kinetics of twin boundaries. Characterizing the TB kinetics (i.e. the stress-velocity relations for a TB) is an important step towards understanding and controlling the dynamic response of metals. In this chapter, we approach this objective using MD simulations.

The present knowledge of the kinetics of a TB in various metals is still in its infancy. However, there have been a few notable investigations. Ghoniem and coworkers [27] utilized MD to study TB motion and observed a *stick-slip* character in the position history. However, this observation may not be fundamental to the nature of TB motion, and is instead likely a manifestation of complicated stress wave interactions that occur in their simulations. The *stick* seems to correspond with the time required for stress waves to travel from the TB to the sample boundaries and back again. Ghoniem et al. [27] extracted the TB kinetics from averaging numerous such *stick-slip* events. Our study addresses the complications associated with stress wave interactions through the utilization of a sample geometry with high aspect ratio that does not permit interaction of reflected stress waves with the twin boundary, further discussed in section 2.2.

Abeyaratne and co-workers [28] proposed a mechanism-based model for TB kinetics. Their model was shown to sufficiently capture the TB kinetics of shape memory alloys observed in experiments [29] and MD simulations [30]. It is currently unclear whether their model is only applicable to shape memory alloys or has broader utility. This investigation confirms the applicability of Abeyaratne's model for an FCC metal within a particular regime.

The focus of the present work is to establish kinetic relations for a TB and TDs, and to show how they are fundamentally related to one another. The velocity of a TB is governed, in part, by the velocity at which the TDs propagate along the TB [17]. Although no systematic studies of TD kinetics have been previously reported, a substantial literature exists on the kinetics of full dislocations, e.g. Ni [25] and Cu [26].

We exploit periodic boundary conditions to simulate an array of TDs gliding along a single TB, further discussed in section 2.2. This array of TDs glides along the TB generating a transient temperature field that is analyzed in subsubsection 7.3.2.1. The TDs quickly achieve a nearly constant velocity, which non-linearly depends on shear stress and linearly depends on temperature as discussed in section 2.4. Above a particular critical shear stress, new TDs nucleate along the TB, allowing even faster TB propagation, presented in section 2.5. In section 2.6, we discuss the implications of our proposed kinetics relations for constitutive modeling, for both macroscopic and crystal-level plasticity. Finally, section 2.7 summarizes the major findings.

2.2 Molecular dynamics simulations

Here we utilize the LAMMPS ([31] lammps.sandia.gov) package for the present MD simulations. An embedded-atom method potential [32] was used for FCC Ni, which captures the elastic constants and the twin boundary energy from experiments, and the generalized planar fault energy surface from density-functional theory calculations [33].

We model the motion of a TB by simulating a part of the twinned region indicated by dashed lines in Fig. 2.1(b). Fig. 2.1(c) shows a schematic of the specimen geometry with a TB at the interface between the top and the bottom parts of the specimen. The MD simulations use specimens with two different widths (16 and 32 nm); the height of the specimen is 230 nm. The FCC crystal structure of Ni was generated using a lattice constant of $a_0 = 3.518$Å. The crystal was oriented such that the maximum resolved shear stress due to the applied shear was developed on the (111) glide plane. Periodic boundary conditions were used all around the specimen, with the exception of the Y-faces for which a fixed boundary condition was applied (since the crystal orientations across the TB have a mismatch). Adopting the method of Serra and Bacon [34], we create a TB and insert a TD on the TB-plane. The TD constructed using this procedure can successively glide over multiple glide planes, effectively modeling a specimen with an infinite width. The specimen was relaxed to a pressure of ≈ 0.1 MPa. Simulations were conducted using a constant volume and energy ensemble (adiabatic conditions) at ≈ 0 and ≈ 300 K temperatures.

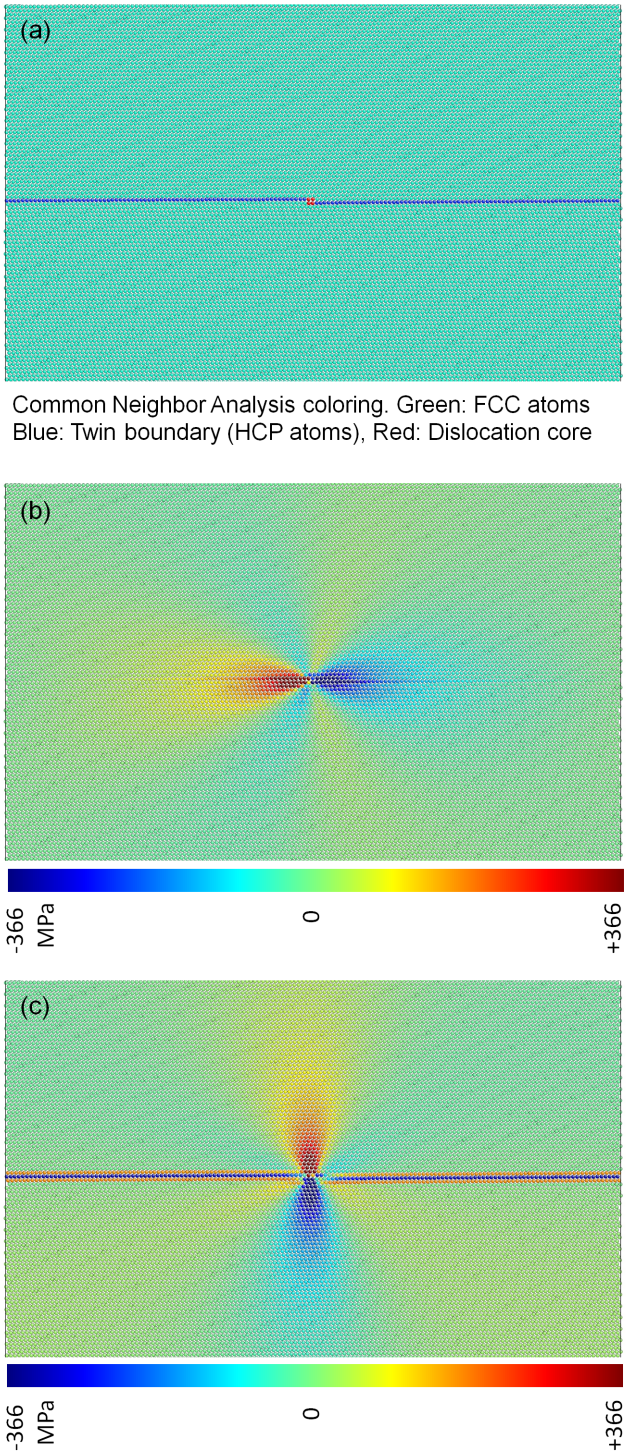

Fig. 2.2: Atomistic snapshots of a pre-existing twin boundary with a twinning dislocation in Ni. (a) Spatial arrangement of atoms belonging to the TB and the core of the twinning dislocation. (b) Shear stress ($\sigma_{xy} := \tau$) field and (c) Normal stress (σ_{yy}) field around a twinning dislocation.

A common neighbor analysis [35] coloring scheme was adopted for atoms based on the local crystal structure which helped distinguish atoms belonging to the TB and the core of the twinning dislocation (TD). The X-position of the TD core was tracked, and the velocity history of the TD was then calculated by applying a (two-point) moving average and then taking a time-derivative of the X-position history. The position history of the TB was calculated by averaging the Y-position of all the atoms that belong to the TB. The TB velocity was calculated from the slope of a straight-line fit to the linear portion of the position history.

The tensorial stress $\boldsymbol{\sigma}$ was calculated at a spatial point using the Virial theorem [36, 37] and was averaged temporally over 1 ps. Shear stress σ_{xy} and normal stress σ_{yy} intensities around a TD are shown in Figs. 2.2(b) and (c). The local shear stress σ_{xy} across the TB was calculated by averaging $\boldsymbol{\sigma}$ over a 3 nm height window (extended over the entire width and thickness of the specimen) in the vicinity of the moving TB. For convenience, we will use the symbol τ to represent the applied shear stress σ_{xy} in the remainder of this chapter.

Due to crystal anisotropy, the portions of the specimen on either side of the TB respond to the shear ($-\gamma_{xy}$) differently [38]. The bottom and the top portions of the specimen experience this shear in the $[\bar{1}2\bar{1}]$ anti-twinning and $[1\bar{2}1]$ twinning directions, respectively. Shearing a nickel specimen (without any TB) to large strains gives different responses along the two directions, as shown by stress-strain curves in Fig. 2.3. In the anti-twinning direction, the crystal has a stiffer stress-strain response

and can sustain a higher value of shear stress (12 GPa, dislocations are nucleated above this value) compared to the twinning direction, which is relatively compliant and can sustain a shear stress of only 7 GPa. When both variants are incorporated in a specimen with a TB (Fig. 2.1(c)), TDs were nucleated at the TB at a critical value of shear stress (we refer to this as $\tau_{nuc} = 6.4$ GPa). These TDs assist in moving the TB towards the relatively compliant side of the crystal.

The TB was subjected to shear by applying a uniform shear stress to the entire

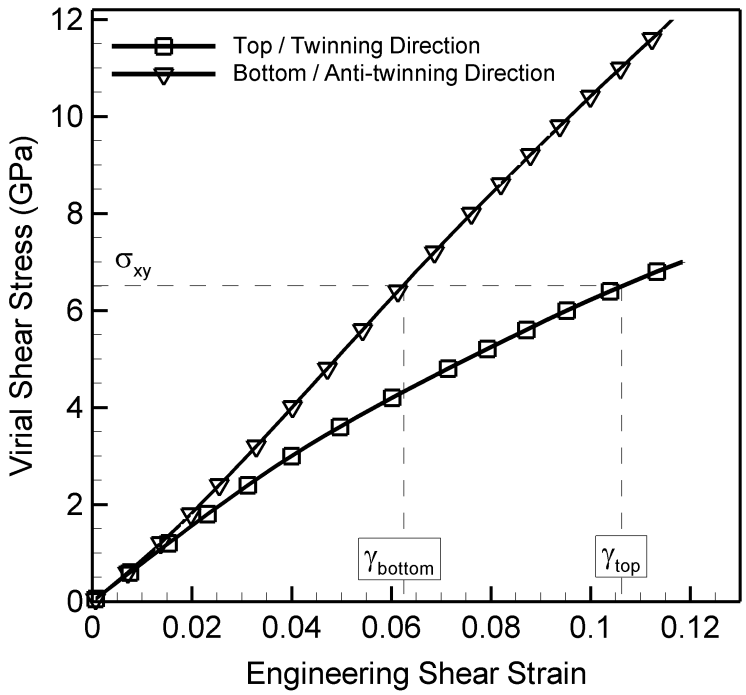

Fig. 2.3: Stress-strain curves for Ni in simple shear along $[1\bar{2}1]$ twinning and $[\bar{1}2\bar{1}]$ anti-twinning directions indicating orientation dependence of response in shear at large strains. A uniform shear stress, σ_{xy}, is applied to the specimen in the initial condition by subjecting the top and the bottom portions of the specimen (the variants of the crystal) to shear strains γ_{top} and γ_{bottom}, respectively, schematically shown in Fig. 2.1(d)

specimen in the initial condition. To accomplish this, the invariants were independently subjected to uniform shear strains using Fig. 2.3 as reference, such that $\tau \neq 0$ and all other components of the stress tensor were relaxed to zero, as in Fig. 2.1(d). The shear stress in the top portion of the specimen was not allowed to exceed τ_{nuc}. A number of MD simulations were performed at various initial values of the applied shear stress, ranging from $\tau = 10$ MPa to 12 GPa. These stress values and the corresponding values of TD and TB velocities were used to construct kinetic plots.

The local shear stress drives the TB and the stress field in the specimen partially

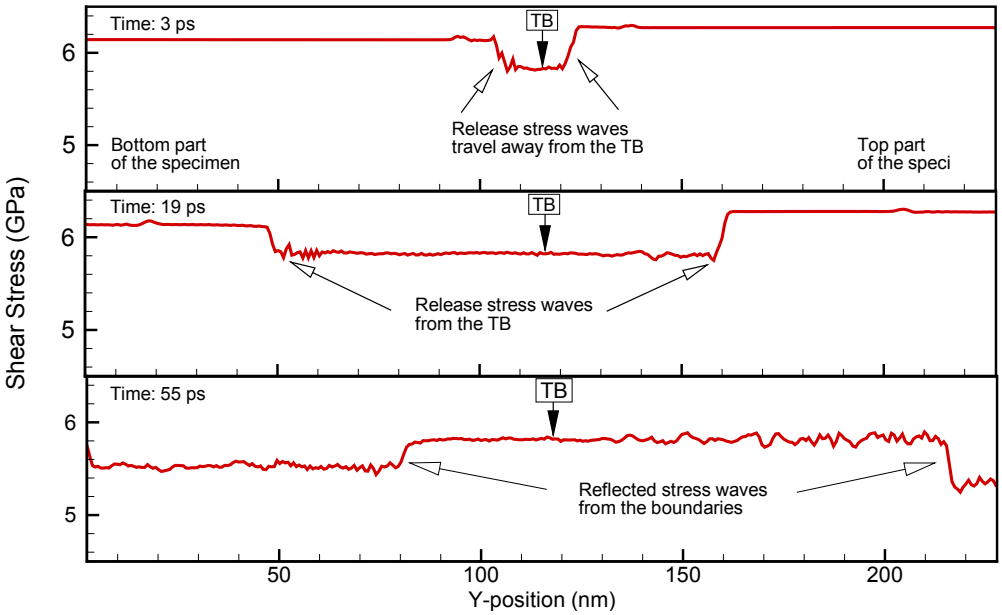

Fig. 2.4: Shear stress profile as a function of Y-position (specimen height), averaged over the specimen width and thickness, presented at three different times for the representative simulation (specimen width 32 nm). These snapshots show the stress release wavefront emitted by the moving TB; these waves reflect from the specimen boundaries (on the top and the bottom) and eventually interact with the TB. The average value of local shear stress at the TB is initially (at t=0) 6.2 GPa and the steady state value is 5.8 GPa

relaxes as the TB begins to move [39]. The process of TB motion is highly dynamic, with the moving TB emitting stress-release waves, as shown in Fig. 2.4. These stress waves will eventually interact with the TB after reflection from the top and bottom sides of the specimen (see Fig. 2.1).

The TB moves one atomic plane each time a TD traverses the sample width, schematically shown in Fig. 2.1(c). The periodic boundary conditions in our simulations can be considered as the surrogates for the grain boundary (shown by dashed lines in Figs. 2.1(b) and (c). The TD moves on to the next glide plane when it crosses the periodic boundary conditions. These apparent TDs that exit and re-enter into the specimen are eqivalent to having a continuous source of TDs of frequency v_{TD}/w, where v_{TD} is the TD velocity and w is the specimen width.

Under steady state conditions and when no new TDs nucleate, the shear stress across the TB and the velocity of the TD reach a steady value. Nucleation of new TDs creates a locally non-uniform stress field, in which case, extracting a local shear stress across the TB is not trivial. For this reason we choose to represent our kinetics plot using the initial applied shear stress.

By using a sufficiently large specimen height, we were able to ensure that the moving TB was able to sustain the steady state motion over a sufficient time duration before it interacted with the reflected waves (the wave interaction time was 65 ps, see Fig. 2.4). Velocities of the TD and TB were extracted from the MD simulations for different values of initial applied shear stress, discussed in the next section.

2.3 Transient temperature field around a gliding dislocation

As discussed in the previous section, special care must be given to the interpretation of molecular dynamics simulations that are inherently nonequilibrium in nature. In addition to the nonequilibrium stress waves generated in the MD simulations (see Fig. 2.4), one must also consider the nonequilibrium temperature field generated around the gliding dislocations.

The MD simulations provide some measure of the temperature rise averaged over the simulation domain. However, it is theoretically possible for a highly localized transient temperature field to develop around the gliding dislocations in the MD simulations since they involve such extremely short timescales. This local temperature field in the vicinity of the dislocation could potentially be much higher than the temperature averaged over the entire MD simulation domiain, and this could significantly complicate the interpretation of the temperature-dependent dislocation kinetics observed in MD simulations. For this reason, we provide here a simple continuum analysis intended to demonstrate that this effect is negligible unless the shear stresses (and dislocation velocities) are exceedingly high.

The isotropic continuum heat equation is expressed as

$$\rho c_p \partial_t \vartheta(\boldsymbol{x}, t) + q(\boldsymbol{x}, t) = k \nabla^2 \vartheta(\boldsymbol{x}, t), \tag{2.1}$$

where ϑ is the local absolute temperature, $q(\boldsymbol{x}, t)$ is the strength of a heat source, ρc_p is the heat capacity per unit volume, and the thermal conductivity is denoted as k. The problem is approximated as two-dimensional with the TD taken to be parallel to z-axis. The gliding TD produces a line heat source located at $x = x_p$ and $y = 0$ moving at a constant velocity v_d in the x-direction. The rate of elastic strain energy dissipated per unit dislocation length may be approximated as

$$q(\boldsymbol{x}, t) = \tau |\boldsymbol{b}| v_d \delta(x - x_p)\delta(y), \tag{2.2}$$

where τ is the xy-shear stress, $|\boldsymbol{b}|$ is the magnitude of the Burgers, and $\delta(\cdot)$ is the Dirac delta function. Since the MD simulations are initiated from absolute zero the initial condition is simply $\vartheta(\boldsymbol{x}, t = 0) = 0$ K. The MD simulations make use of the microcanonical (NVE) ensemble; therefore, the corresponding continuum adiabatic boundary conditions are taken as $\partial_t \vartheta(x = \pm L_x, y, t) = 0$ and $\partial_t \vartheta(x, y = \pm L_y, t) = 0$, where $2L_x$ and $2L_y$ are the width and height of the simulation domain. The solution of Eq. (2.1) may be expressed as a double Fourier cosine series expansion, i.e.

$$\vartheta(\boldsymbol{x}, t) = \sum_{m=0}^{\infty} \sum_{n=0}^{\infty} A_{mn}(t) \cos \lambda_m x \cos \lambda_n y, \tag{2.3}$$

where $\lambda_m \equiv m\pi L_x^{-1}$, $\lambda_n \equiv n\pi L_y^{-1}$, and $A_{mn}(t)$ is obtained as

$$A_{mn}(t) = \frac{\tau |\boldsymbol{b}| v_d}{\rho c_p L_x L_y} \frac{\lambda_{mn}^2 \cos \lambda_m x_p + \lambda_m v_d \kappa^{-1} \sin \lambda_m x_p - \lambda_{mn}^2 \exp -\lambda_{mn}^2 \kappa t}{\kappa w_{mn} \left(\lambda_{mn}^4 + \lambda_m^2 v_d^2 \kappa^{-2}\right)}, \tag{2.4}$$

with $\kappa \equiv k\rho^{-1} c_p^{-1}$ being the thermal diffusivity, $\lambda_{mn}^2 \equiv \lambda_m^2 + \lambda_n^2$, and w_{mn} is expressed

as

$$w_{mn} = \begin{cases} 4 & \text{for} \quad m = n = 0 \\ 2 & \text{for} \quad m \neq n = 0 \quad \text{or} \quad n \neq m = 0 \\ 1 & \text{for} \quad m \neq n \neq 0. \end{cases} \tag{2.5}$$

Fig. 2.5 provides numerical calculations of Eq. (2.3) giving the change in temperature field for a twinning dislocation gliding at a velocity $v_d = 2260$ m/s corresponding to an applied shear stress of $\tau = 1$ GPa at four successive spatial locations. Notice

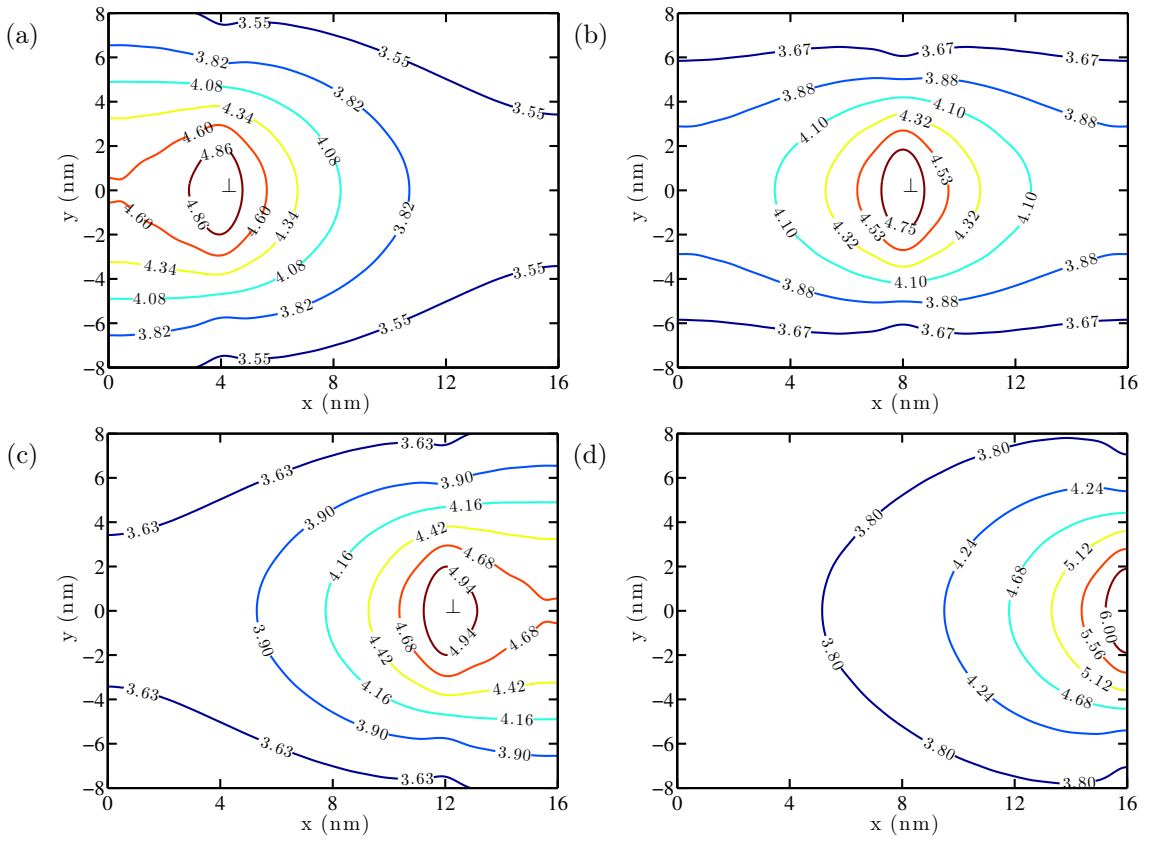

Fig. 2.5: Contours of the change in the transient temperature, i.e. $\vartheta(\boldsymbol{x}, t) - \vartheta(\boldsymbol{x}, t = 0)$, field generated around a gliding dislocation at various time increments corresponding to dislocation positions at (a) $x_p = 4$nm, (b) $x_p = 8$nm, (c) $x_p = 12$nm, and (d) $x_p = 16$nm. Model parameters: $\tau = 1$ GPa; $v_d = 2260$ m/s; $|\boldsymbol{b}| = 0.144$ Å; $\rho c_p = 3.92 \times 10^6$ J m^{-3}K^{-1}; $\kappa = 2.32 \times 10^{-5}$ m^{2}s^{-1}; $L_x = 16$ nm; $L_y = 115$ nm.

that the magnitude of the temperature is highest in the vicinity of the gliding dislocation. However, on the timescales of interest to our MD simulations ($\lesssim$ 70 ps) the highest temperature rises achieved in the immediate vicinity of the dislocation are negligible for shear stress at or below about 1 GPa (corresponding to a dislocation velocity at or below about 2260 m/s in nickel).

For the purposes of theoretical analysis it proves useful to compute a spatially averaged local temperature, $\bar{\vartheta}(t)$, around a moving dislocation. We take the spatially averaged local temperature to be defined as

$$\bar{\vartheta}(t) = \frac{1}{4\ \ell_x \ell_y} \int_{-\ell_y}^{\ell_y} \int_{-\ell_x}^{\ell_x} \vartheta(x - x_p, y, t)\ dx\ dy, \tag{2.6}$$

where $2\ell_x$ and $2\ell_y$ are the width and height of a moving *averaging window* centered around the TD located at $(x_p, 0)$. The spatially averaged local temperature $\bar{\vartheta}(t)$ defined in Eq. (2.6) may now be computed from Eq. (2.3) as

$$\bar{\vartheta}(t) = \sum_{m=0}^{\infty} \sum_{n=0}^{\infty} \frac{A_{mn}(t)}{2\ell_x \ell_y \lambda_m \lambda_n} \{\sin \lambda_m(\ell_x + x_p) + \sin \lambda_m(\ell_x - x_p)\} \cos \lambda_n \ell_y. \tag{2.7}$$

Since some measure of $\bar{\vartheta}$ is required for determining the magnitude of phonon damping (see Eq. (2.9)), the size of the *averaging window* associated with phonon damping should be on the order of the phonon wavelengths, and is thus chosen as $\ell_x = \ell_y = 1$ nm for these type of calculations. Alternatively, by setting $\ell_x = L_x$ and $\ell_y = L_y$, Eq. (2.9) may also be utilized to compute the transient temperature averaged over the entire simulation domain. Fig. 2.6 demonstrates the evolution of this average temperature in the simulation domain. The agreement with the temperature

evolution observed in molecular dynamics simulations is noteworthy. The local average temperature in the immediate vicinity of the gliding dislocation is also obtained from Eq. (2.7) only with $\ell_x = \ell_y = 1$ nm. At about 200 ps this local temperature rise

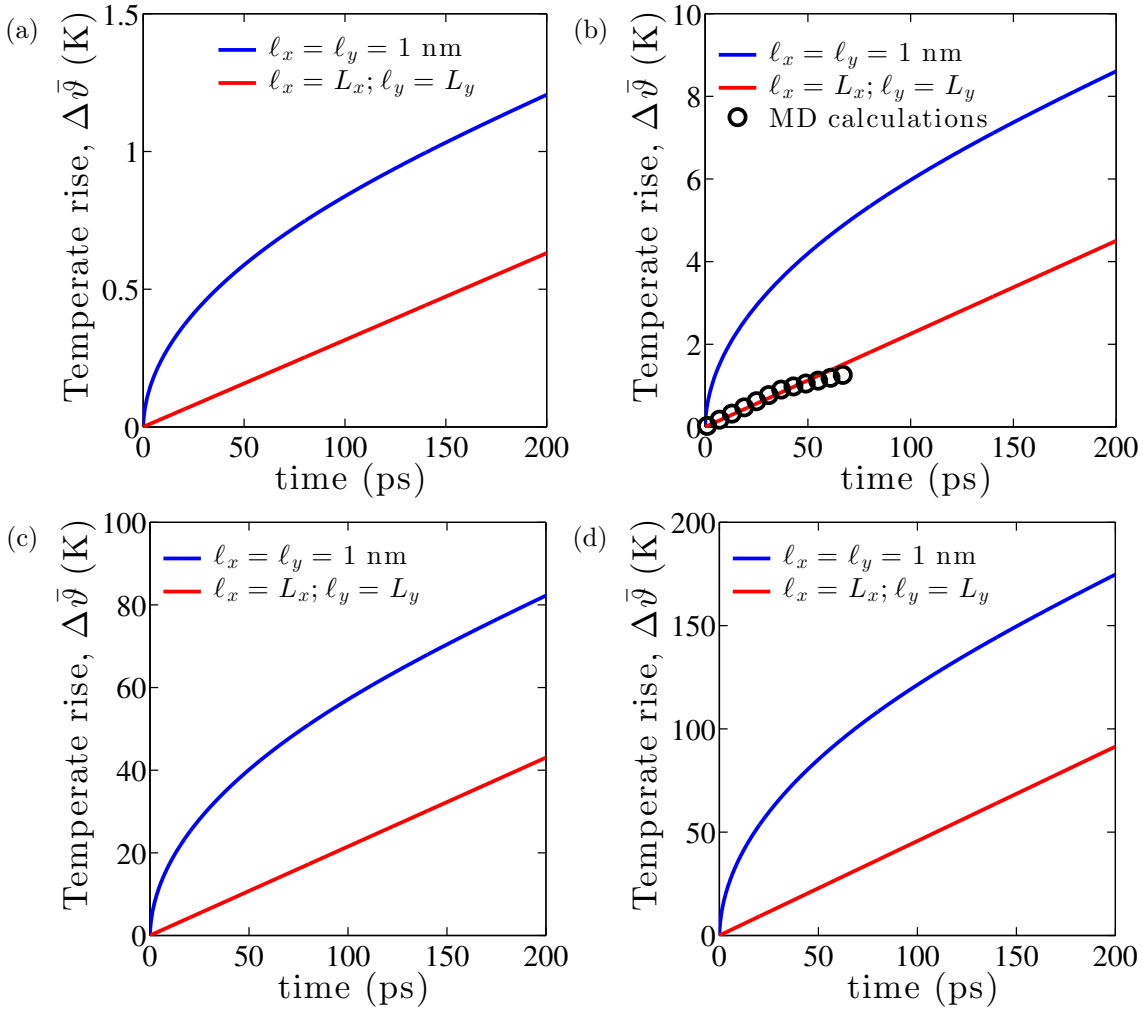

Fig. 2.6: Evolution of average temperature field in simulation domain, i.e. Eq. (2.7) with $\ell_x = L_x = 16$ nm and $\ell_y = L_y = 115$ nm, and local average temperature in the immediate vicinity of a gliding dislocation, i.e. $\ell_x = \ell_y = 1$ nm. Dislocation velocities are considered corresponding to the various kinetic regimes (a) linear subsonic ($\tau = 0.2$ GPa), (b) nonlinear subsonic ($\tau = 1.0$ GPa), (c) intersonic ($\tau = 4.0$ GPa), and (d) supersonic ($\tau = 6.2$ GPa). Model parameters: $|\boldsymbol{b}| = 0.144$ Å; $\rho c_p = 3.92 \times 10^6$ J m^{-3}K^{-1}; $\kappa = 2.32 \times 10^{-5}$ m^{2}s^{-1}.

is found to be about twice the temperature rise averaged over the simulation domain. Although this effect is negligible for dislocations gliding in the subsonic regime, it may be very important in the analysis of dislocation kinetics in the intersonic and supersonic regimes.

The TD velocities reported in section 2.4 are obtained from MD calculations by averaging the TD velocity over a time period of $20-70$ ps, for which the TD velocity is nearly constant. Over this time period, calculations of $\bar{\vartheta}(t)$ from Eq. (2.7) predict local temperature rises of $\Delta\bar{\vartheta} \lesssim 1$ K within the linear subsonic regime of TD kinetics, and $\Delta\bar{\vartheta} \lesssim 15$ K within the non-linear subsonic regime (see Fig. 2.6). Therefore, at least within the linear regime, phonon damping should be negligible in our MD calculations that are initiated from 0 K.

2.4 Kinetics of twinning dislocations

A representative result from MD for an applied shear stress of $\tau = 6.2$ GPa is shown in Fig. 2.7. The TD attains a steady state within a short time (a few picoseconds). From a purely geometric stand point, the TB velocity is governed by the spacing and the velocity of the TD through the relation

$$v_{TB} = \sqrt{2}\frac{|\boldsymbol{b}_p|}{\ell_p} v_{TD}, \tag{2.8}$$

where $|\boldsymbol{b}_p|$ is the magnitude of the TD Burgers vector and is related to the lattice constant a_0 (for FCC, $|\boldsymbol{b}_p| = a_0/\sqrt{3}$), ℓ_p is the mean spacing between TDs along the

TB ($\ell_p = w$ in our MD model), v_{TD} is the TD velocity, and the spacing between the glide planes is $|\boldsymbol{b}_p|\sqrt{2}$ for FCC metals.

The observed TD velocities are shown in Fig. 2.8 for a range of shear stress values. To our knowledge, this is the first measure of the dynamics of a twinning dislocation over such a wide range of stress values. TD kinetics share many of the same characteristics with full dislocations, as will be discussed further in subsequent sections. The critical value of shear stress required for nucleation of a TD partitions the kinet-

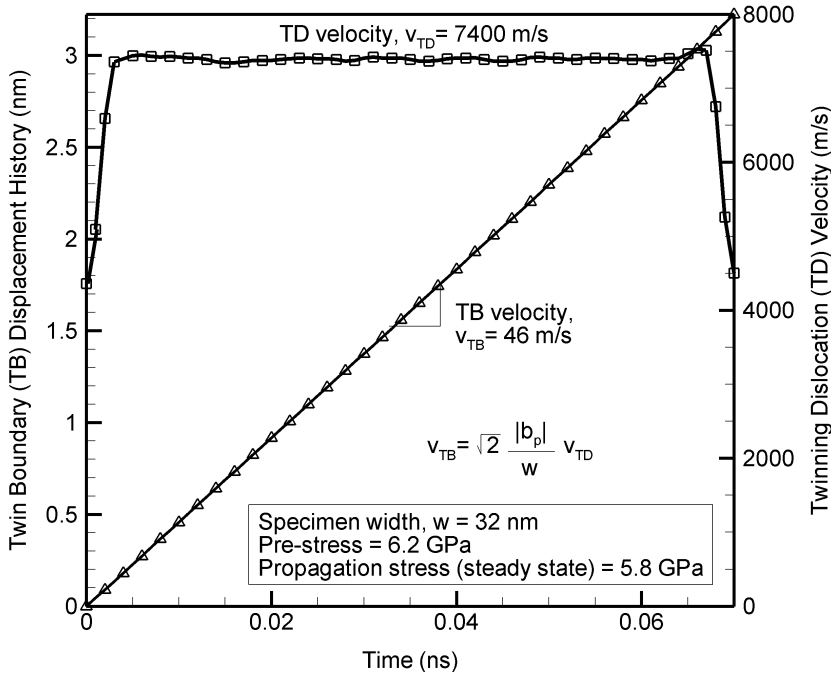

Fig. 2.7: Results from a representative simulation for twin boundary motion under an initial applied shear stress of 6.2 GPa. The TD accelerates and reaches a steady velocity in $\approx$ 0.005 ns, after which the velocity of TD and the slope of the TB displacement history are nearly constant over a time duration of $\approx$ 0.06 ns. The stress waves reflected from the specimen boundaries interfere with the moving TD beyond time $>$ 0.065 ns.

ics plot for a TB (Fig. 2.11) into two regimes: the propagation regime for $\tau < \tau_{nuc}$, and the nucleation dominated regime for $\tau \geq \tau_{nuc}$ (where τ_{nuc} is the shear stress for nucleating a TD). TB motion in the propagation regime occurs due to the motion of a single pre-existing TD; in the nucleation regime new TDs nucleate and contribute to the TB motion. In the propagation regime (i.e. no new TDs nucleate), the mean spacing between TDs is trivially given by $\ell_p = w$. The velocities of the TD and the TB are consistent with Eq. (2.8). Within the nucleation dominated regime, it should

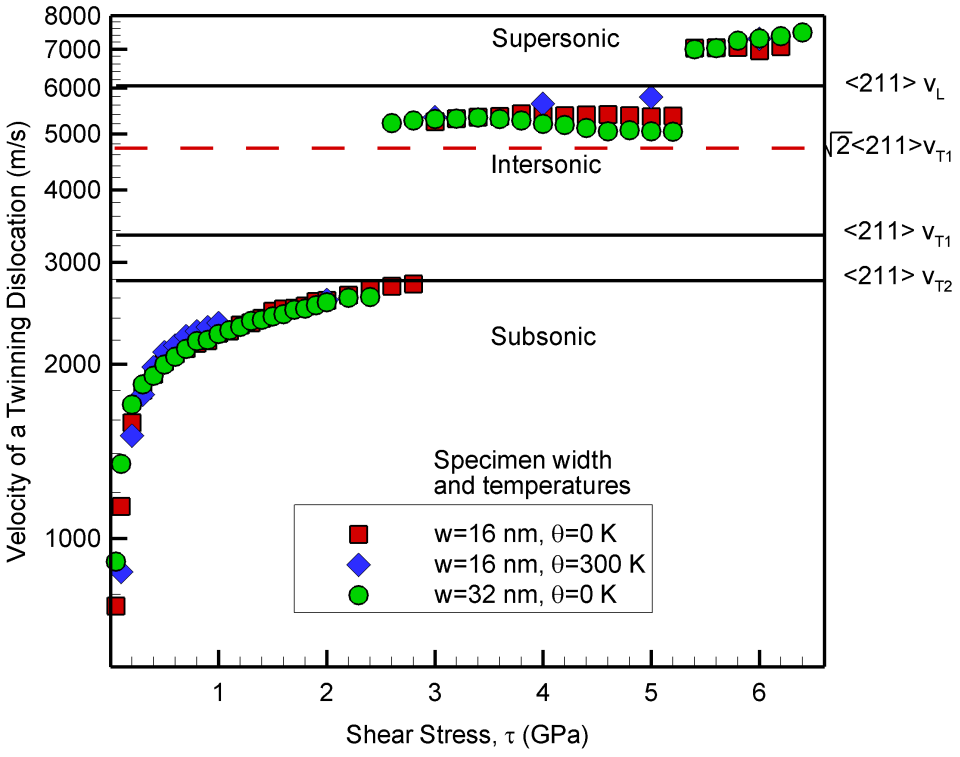

Fig. 2.8: Kinetics of a twinning dislocation in Nickel for different specimen widths, at 0 K and 300 K temperatures. Horizontal lines in black are the wave speeds and the dashed line is the Eshelby speed, all based on the linear elastic constants for Ni.

be noted that Eq. (2.8) is still applicable; however, determination of ℓ_p and v_{TD} is no longer trivial. Indeed, the conservative movement of a TB (no atomic diffusion) occurs solely by the glide of TDs, and therefore TB velocity depends on both, the nucleation and the velocity of TDs. In the subsections that follow, we present observations on the velocities of a TD, their comparisons with those of a full dislocation, and analytical models to describe the kinetics of a TD and a TB.

In Fig. 2.8, the TD is moving along the $[1\bar{2}1]$ direction, and we expect the $\langle 211 \rangle$ material wave speeds to influence TD velocities. The maximum shear stress in this plot was restricted to τ_{nuc}, because above this value additional TDs nucleate and their interacting stress fields complicate the analysis. The longitudinal and transverse wave speeds for Ni [40] based on the linear elastic constants are shown using solid lines. The procedure used for calculation of the wave speeds is included in the appendix of [12]. The terminologies subsonic, intersonic and supersonic in this chapter refer to regimes of dislocation velocities below the lower of the two transverse wave speeds $\langle 211 \rangle v_{T2}$, in between the higher of the two transverse wave speeds $\langle 211 \rangle v_{T1}$ and the longitudinal wave speed $\langle 211 \rangle v_L$, and above the longitudinal wave speed, respectively.

The TD velocity increases linearly with shear stress, for $v_{TD} < 1700$ m/s. The velocity is nearly independent of the specimen width. Below 0.01 GPa, the TD is unable to overcome the Peierl's barrier. At stresses above 1.5 GPa, the TD velocity increases and has a tendency to saturate below the transverse wave speed, $\langle 211 \rangle v_{T2}$. This behavior is similar to that of a full dislocation (Ni [25] and Cu [26]), for which

the radiation and/or relativistic effects dominate. The saturation velocity in the subsonic regime was ($> 0.93 \times v_{T2}$), somewhat higher than reported values for the full dislocation ($\sim 0.9 \times v_{T2}$, [25]).

With a further increase in the shear stress above 2.4 GPa, the TD can achieve steady state velocities above the transverse wave speed. Like full dislocations, a TD can move with velocities in the intersonic regime and the supersonic regime. The transition into these regimes does not occur in a smooth fashion because (from energy considerations) the material wave speeds act as *forbidden* velocities at which steady-state propagation is not permitted (see discussion in [25] and references therein). A TD achieves the transition between the regimes by undertaking discrete jumps [41] across the transverse wave speeds and the longitudinal wave speed. This behavior of a TD (which in our work has a pure edge character) is similar to that of a full dislocation of an edge character [25].

In the intersonic regime, the TD velocity experiences a plateau (independent of the shear stress), and the velocities vary slightly within a narrow range for the values of shear stress from 2.6 through 5.2 GPa. The TD velocity experiences a single plateau compared to two such plateaus observed for a full dislocation [25]. Increasing the shear stress beyond 5.2 GPa the TD velocity encounters a second discrete jump to 7000 m/s in the supersonic regime, and thereafter a moderate increase in the velocity with stress was observed.

In the intersonic regime, theoretical analysis by Weertman [42] suggests stable

dislocation velocities in the regime that is typically bounded between the Eshelby velocity (defined as $\sqrt{2}\times$ shear wave speed for an isotropic material) and the longitudinal wave speed. The analysis further suggests that the velocity regime between the transverse wave speed and the Eshelby velocity is inherently unstable. Indeed, the intersonic velocities of the TD were found to be bounded between the Eshelby velocity $\sqrt{2}\,\langle 211\rangle\, v_{T1}$ and the longitudinal wave speed $\langle 211\rangle\, v_L$ (Fig. 2.8). Our MD results are in agreement with Weertman's analysis. No TD velocities were observed between $\sqrt{2}\,\langle 211\rangle\, v_{T1}$ and $\langle 211\rangle\, v_{T2}$. Note that, under such high stresses there exists a mismatch of elastic constants across the TB (see section 2.2); the TB itself is a bimaterial interface. Weertman's solution for a steadily moving dislocation on a bimaterial interface [43] should ideally be modified to account for the non-linear elastic constants and the anisotropy of the crystals. However, this is beyond the scope of this chapter.

Much literature [25] exists on modeling full dislocation kinetics below the shear wave speed in an isotropic material. However, the same understanding does not yet exist for a TD in a anisotropic material. Building on the kinetics relationship for full dislocations established by [25], we propose a similar relationship for the kinetics of a TD in the propagation regime, i.e. $0 \leq v_{TD} < v_{T2}$:

$$|\tau| - \tau_y = \left(\beta_{\mathrm{TB}} + \beta_{\mathrm{FD}}\bar{\vartheta}\right)|\boldsymbol{b}_p|^{-1}\langle v_{TD} - v_{min}\rangle + \beta_{\mathrm{Rad}}|\boldsymbol{b}_p|^{-1}\langle v_{TD} - v_0\rangle^{3/2}, \tag{2.9}$$

where $\langle\cdot\rangle$ is the Macaulay bracket, $\bar{\vartheta}$ is the mean temperature in the vicinity of the TD, τ_y is the critical resolved shear stress for the slip system of interest, v_{T2} is the

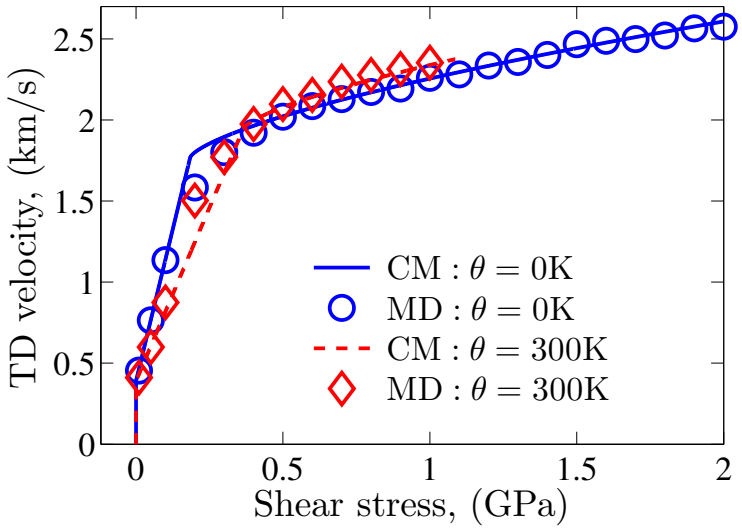

Fig. 2.9: Agreement of MD prediction and our model Eq. (2.9) for twinning dislocation (TD) kinetics.

lowest transverse wave speed ($\langle 211 \rangle$ v_{T2}, in this work), and β_{TB}, β_{FD}, β_{Rad}, v_{min} and v_0 are fitting parameters. The temperature dependent phonon damping coefficient [10], typically denoted as B_0, is equivalent to $\beta_{\text{FD}}\bar{\vartheta}$ in our nomenclature. As noted in [25], the final term in Eq. (2.9) accounts for the non-linear regime that is assumed to be governed by radiation damping. Results from MD indicate the TD must experience relatively higher amount of damping compared to a full dislocation (Fig. 2.10). We propose an additional damping term, i.e. β_{TB}, related to damping interactions with the twin boundary. It should be noted that Eq. (2.9) ignores the contribution of electronic drag [44], which is not captured by classical atomistic potentials, but should be accounted for in the analysis of TD in real metals at low temperatures.

Leibfried [45] modeled the phonon damping coefficient as $B_0 = 3k_b\bar{\vartheta}z/20v_T|\boldsymbol{b}_d|^2$, where k_b is the Boltzmann constant, $z = 4$ (for FCC) is the number of atoms per unit

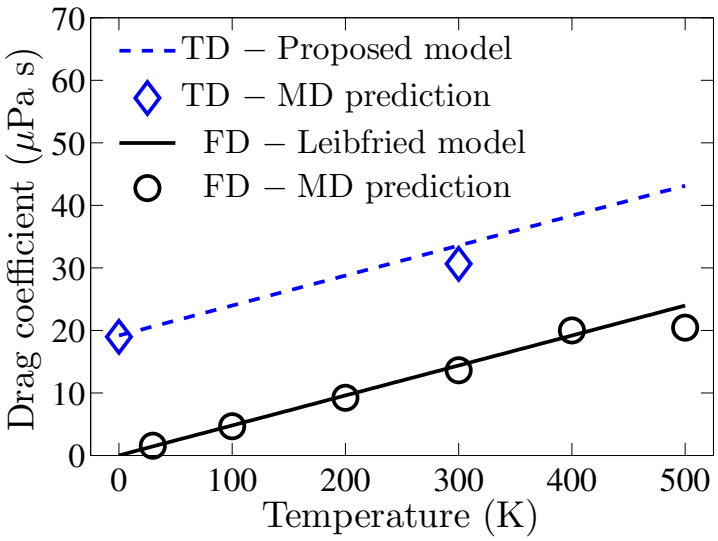

Fig. 2.10: Comparison of the drag coefficients (in the linear regime) for a full dislocation (FD) and a twinning dislocation (TD), and comparison of their temperature dependence. The Leibfried model for the drag coefficient [45] is expressed as $B_0 = \beta_d \bar{\vartheta} = 3k_b \bar{\vartheta} z / 20 v_T |\boldsymbol{b}_d|^2$, while our proposed model (see linear part of Eq. (2.9)) is expressed as $\beta_{\text{TB}} + 3k_b \bar{\vartheta} z / 20 v_T |\boldsymbol{b}_d|^2$. The MD simulations for full edge dislocations (open circles) are reported in [46].

cell, and v_T is the shear wave speed. Leibfried's model is utilized here in determining β_{Ph}, and seems to be applicable to TD in addition to full dislocations. For cubic Ni, we used the lower of the two transverse wave speeds $v_T = \langle 211 \rangle v_{T2} = 2790$ m/s. Fitting our MD results to Eq. (2.9), we find $\beta_{\text{TB}} = 19.2$ μPa-s, which is comparable to B_0 at ~400 K (see Fig. 2.10). We also found $v_{min} = 390$ m/s for a TD; note that v_{min} for a full dislocation is typically zero. Here the MD simulations are initiated from 0 K and 300 K; therefore, damping associated with the TB mostly governs the TD kinetics in the linear regime. Fitting Eq. (2.9) in the non-linear regime we obtain $\beta_{\text{Rad}} = 10.1$ μPa-s$^{3/2}$m$^{-1/2}$; $v_0 = 1770$ m/s for 0 K and $v_0 = 1950$ m/s for 300 K, which are both similar to the values for full dislocations in Ni, although, v_0 was found

to be temperature independent for full dislocations [25].

Fig. 2.9 demonstrates the agreement between Eq. (2.9) and the MD simulations. The TD velocity decreases with temperature in the linear (drag-dominated) portion of the TD kinetics due to phonon damping. A crossover was observed for the TD kinetics at 0 and 300 K; this happens as the velocities transition from drag-dominated to the radiation-dominated regime. This crossover is not observed in case of a full dislocation [25], but the observed crossover could be an artifact of the atomic potential and may not necessarily be physical. TDs thus share many of the qualitative and even some quantitative features of full dislocations. The additional dislocation damping associated with the TB is unique to TD and must be accounted for appropriately.

2.5 Kinetics of twin boundaries

Fig. 2.11 shows the kinetics for the TB obtained from MD simulations. In the propagation regime ($\tau < \tau_{nuc} = 6.4$ GPa), the TB velocity is governed by the velocity of the TD and the spacing between the TDs (ℓ_p). The values of TB velocities in Fig. 2.11 and the TD velocities in Fig. 2.8 are consistent with Eq. (2.8). Eq. (2.8) shows that the kinetics of a TB should include the kinetics of a TD (given by Eq. (2.9)).

In the nucleation-dominated regime ($\tau \geq \tau_{nuc} = 6.4$ GPa), multiple TDs nucleate and assist in moving the TB. The TB kinetics is independent of the specimen width, w, in the nucleation-dominated regime. The velocities of TB are limited to below

≈650 m/s in Ni. Our value of τ_{nuc} is in fair agreement with experimental observations of Murr [23], who observed numerous twins after shock compressing Ni to pressures of $\sim 30 - 35$ GPa (which correspond to a shear stress in the range $8.2 - 9.6$ GPa). Additionally, dislocation loop analysis predicts the transition from slip to twinning dominated deformation for Ni occurs at ≈ 7.4 GPa (estimated from reported pressure of 27 GPa) [23].

Following the model proposed by Abeyaratne and Vedantam [28] for TB kinetics in SMAs, the kinetics of TB in FCC metals in the nucleation-dominated regime may

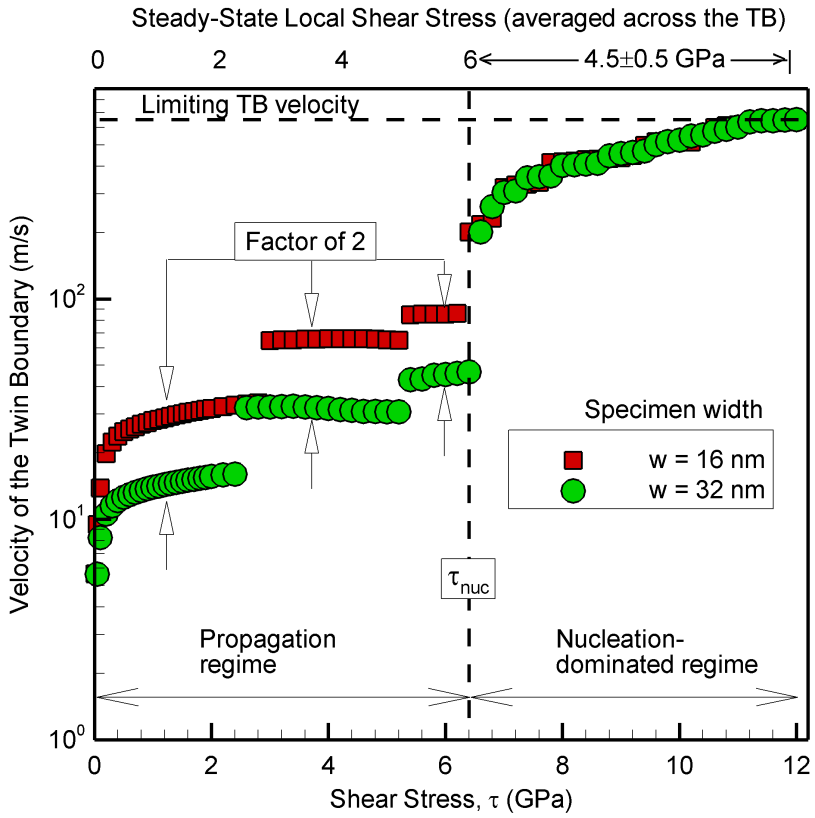

Fig. 2.11: Kinetics of a moving twin boundary in Nickel.

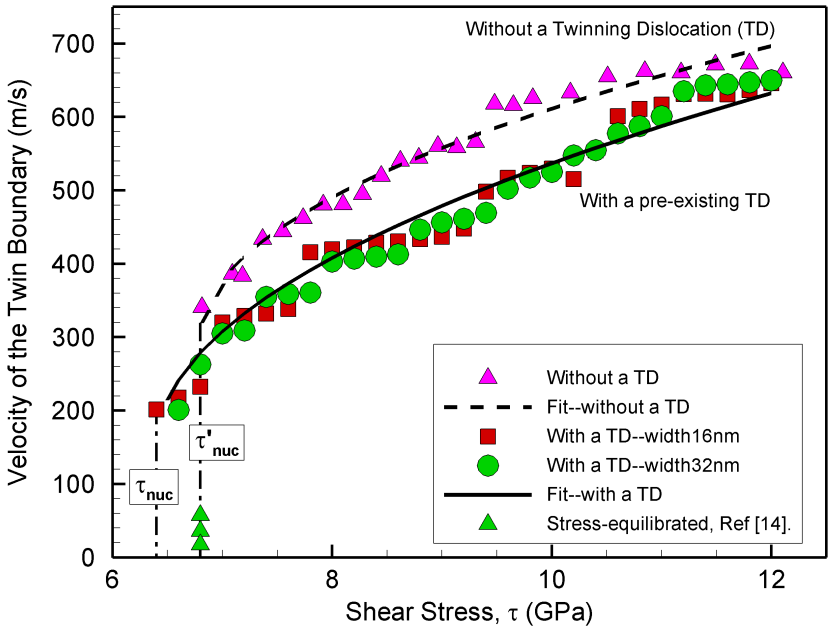

Fig. 2.12: Kinetics of a twin boundary with and without a pre-existing twinning dislocation (TD). Abyeratne and Vedantam [28] fit to the data from MD yields following constants: $v_{TB0} = 105$ m/s, $\xi = 204$ m/s and $\tau_{nuc} = 6.4$ GPa for TB with a pre-existing TD; $v_{TB0} = 300$ m/s, $\xi = 174$ m/s and $\tau_{nuc} = 6.8$ GPa for TB without a pre-existing TD. The root mean square errors are 21.5 m/s and 16.45 m/s for the fits to the data with and without a TD.

be modeled as

$$v_{TB} = v_{TB0} + \xi\sqrt{|\tau| - \tau_{nuc}} \qquad \text{for } \tau_{nuc} \le |\tau| \le \tau_{hom}, \tag{2.10}$$

where $\xi = 180$ m/s GPa$^{-1/2}$, $\tau_{hom} = 12$ GPa, and $v_{TB0} = 200$ m/s is the velocity of the TB corresponding to $|\tau| = \tau_{nuc} = 6.4$ GPa. The agreement with MD predictions may be seen in Fig. 2.12. Above a critical shear stress of about $|\tau| = 12$ GPa, additional dislocations homogeneously nucleate in other parts of the specimen leading to multiple TBs. This critical shear stress is in fair agreement with the expected stress for homogenous nucleation of dislocation, i.e. $|\tau| = \tau_{hom} \sim \mu/10 \approx 12$ GPa.

2.6 Implications for crystal plasticity

The typical plastic deformation mechanism in metals is either slip, twinning, or a combination of both. Provided a material has sufficient TDs, the results of the propagation regime seem to indicate that twinning is always competitive with slip, as the stress required to overcome barriers to TD motion is not much different than that required of a full dislocation (at least in FCC metals) . However, experiments show that conventional FCC metals only twin under the most extreme of dynamic loading conditions, i.e. over-driven shock compression. Clearly, this is due to the fact that FCC metals do not typically contain pre-existing TBs and TDs, and nucleating them requires very large shear stresses. Using MD, we additionally characterized the kinetics of a TB without a pre-existing TD (Fig. 2.12). Our observed TB kinetics of Ni are in qualitative agreement with those of shape memory alloys experimentally observed by Faran and Shilo [21]. Both demonstrate the presence of a threshold nucleation stress for TDs (τ'_{nuc}, without a pre-existing TD), although this threshold stress is an order of magnitude smaller in shape memory alloys as compared to Ni.

Provided a metal is able to generate TDs and TBs, the kinetics of TB motion will partially govern the response of metals subjected to high strain rates. Generalizing the tensorial Orowan's relation [22] to account for both slip and twinning, we propose

a relationship for the norm of the plastic rate of deformation tensor as

$$\left|\left|\dot{\boldsymbol{F}}^{p}\boldsymbol{F}^{p^{-1}}\right|\right| = \begin{cases} \rho_d|\boldsymbol{b}_d|\bar{v}_d + \frac{|\boldsymbol{b}_p|}{\ell_t\ell_p}\bar{v}_{TD} & \text{for} \quad \tau_y \leq |\tau| < \tau_{nuc} \\ \rho_d|\boldsymbol{b}_d|\bar{v}_d + \frac{|\boldsymbol{b}_p|}{\ell_t\ell_p}\bar{v}_{TD}\Big|_{|\tau|=\tau_{nuc}} + \frac{\gamma_t\xi}{\ell_t}\sqrt{|\tau| - \tau_{nuc}} & \text{for } \tau_{nuc} \leq |\tau| \leq \tau_{hom}, \end{cases} \tag{2.11}$$

where ℓ_t is the mean spacing between TBs, γ_t is the twinning shear ($1/\sqrt{2}$ in FCC), and ρ_d, $|\boldsymbol{b}_d|$, and $\bar{v}_d$ are the dislocation density, Burgers vector magnitude, and mean velocity of the full dislocations, respectively. Eq. (2.11) provides a description for the evolution of plastic strain due to a density of twins propagating in a self-similar manner and a density of full dislocations (mobile). The equation assumes an additive decomposition of total plastic strain, and the strains due to propagating TBs and full dislocations independently contribute to the total strain without influencing one another. Note that Eq. (2.11) assumes that the TB traverses the entire crystal; if this is not the case then Eq. (2.11) must be generalized to also account for the twin boundary tip velocity. Similar to Clifton [47], the mean TD velocity is defined such that $\bar{v}_{TD} = \bar{\ell}_O(t_w + t_g)^{-1}$, where $t_g = \bar{\ell}_O/v_{TD}$ is the time TD spends gliding between obstacles of spacing $\bar{\ell}_O$, and t_w is the time TD spends waiting at obstacles (a thermally-activated process typically modeled by an Arrhenius relation). The gliding velocity of TDs between obstacles is governed by Eq. (2.9) up to the lowest *forbidden* velocity (v_{T2}).

Our proposed kinetics relations are also useful in slip-twinning crystal plasticity formulations [48]. These formulations require constitutive relations for the rate of

change of volume fraction $\dot{f}_j$ of each twin variant j. This constitutive relationship is essential as it partially governs the rate-sensitivity of the material and thus localization phenomena; however, $\dot{f}_j$ is typically phenomenological in nature and thus has limited predictive capability. We propose a more fundamental, mechanism-based relationship for the evolution of the volume fraction of twin variants based on the kinetics of twinning dislocations, expressed as

$$\dot{f}_j = \begin{cases} \frac{a_g^j}{\ell_t^j \ell_p^j} \bar{v}_{TD}^j & \text{for} \quad \tau_y^j \leq |\tau^j| < \tau_{nuc}^j \\ \frac{a_g^j}{\ell_t^j \ell_p^j} \bar{v}_{TD}^j \Big|_{|\tau^j|=\tau_{nuc}^j} + \frac{\gamma_t^j \xi^j}{\ell_t^j} \sqrt{|\tau^j| - \tau_{nuc}^j} & \text{for } \tau_{nuc}^j \leq |\tau^j| \leq \tau_{hom}^j, \end{cases} \tag{2.12}$$

where a_g is the spacing between glide planes. A kinetics relation similar in form to Eq. (2.9) governs v_{TD}^j, the velocity of TDs gliding between obstacles, which is utilized to compute the mean TD velocity of a particular variant, i.e. $\bar{v}_{TD}^j = (t_w^j/\bar{\ell}_O^j + 1/v_{TD}^j)^{-1}$.

Completeness of the constitutive formulation (either macroscopic plasticity Eq. (2.11) or crystal plasticity Eq. (2.12)) requires evolution equations, i.e. $\dot{\ell}_t$ and $\dot{\ell}_p$, similarly to those proposed for $\dot{\rho}_d$ in [10]. These evolution equations are beyond the scope of the current chapter; however, examination of some limiting cases is useful. If $\rho_d \ell_t \ell_p \sim 1$, in the drag regime twinning will contribute slightly less to the rate of plastic deformation as compared to slip, since $v_{TD} < v_d$ due to the additional damping experienced by TDs (see Fig. 2.10), i.e. $\beta_{\text{TB}} \neq 0$. On the other hand, if $\rho_d \ell_t \ell_p >> 1$ then slip dominates the plastic deformation, which is the case for conventional FCC metals under all but the most extreme loading conditions, e.g. over-driven shock compression. However, this is clearly not the case for metals that are susceptible to twinning at quasi-static

loading rates, e.g. some shape memory alloys, some hexagonal close packed metals (Mg, Ti), and some nanocrystalline FCC metals (Cu). In the nucleation-dominated regime ($\tau_{nuc} \leq |\tau| \leq \tau_{hom}$), it is likely that twinning dominates the plastic deformation since many twinning dislocations are nucleated along the TB. For example, in Ni we found the TB velocity to be $300 - 650$ m/s in the nucleation-dominated regime, which results in twinning plastic strain rates of $2 - 5 \times 10^9$ s^{-1} for $\ell_t = 100$ nm, or $2 - 5 \times 10^{10}$ s^{-1} for $\ell_t = 10$ nm (see Eq. (2.11)). These extreme twinning plastic strain rates are $1 - 2$ orders of magnitude higher than what may be realistically achieved through slip alone without homogeneous dislocation nucleation ($|\tau| < \tau_{hom}$) [10, 49]. Thus one may anticipate FCC metals to transition from slip-dominated deformation to twinning-dominated deformation at some critical strain-rate.

2.7 Summary of key findings

Molecular dynamics simulations were utilized to understand the kinetics of a fast moving twin boundary (TB). The current work demonstrates how the twinning dislocation (TD) kinetics and the mean spacing between TDs fundamentally govern the kinetics of a TB, see Eq. (2.8). The kinetics of a moving TD shares many common features with the kinetics of a full dislocation: a linear (drag-dominated) regime of velocity against shear stress with a linear dependence of the phonon drag coefficient on the temperature, followed by a non-linear (radiation-dominated) regime with a

tendency to saturate below the lowest transverse wave speed (the relativistic effect), and an inability to sustain steady-state propagation velocities at the transverse wave speeds (so called *forbidden* velocities). Similar to a full edge dislocation, an edge TD can sustain to velocities above the transverse wave speed into the intersonic regime and the supersonic regime (calculated using the linear elastic constants), and it does so by undergoing discrete jumps across the lowest transverse wave speed and the longitudinal wave speed, respectively.

The kinetics show some features that are specific to only TD. The saturation velocity in the subsonic regime was ($> 0.93 \times v_{T2}$) higher than that for the full dislocation (average $0.9 v_{T2}$, [25]). At high stresses, considering the crystal anisotropic is crucial to analyzing the TD kinetics. In the intersonic regime, the twinning dislocation velocity experiences a single plateau independent of the stress, compared to two such plateaus observed for a full dislocation [25]. TD velocities in the intersonic regime fall between $\sqrt{2}\,\langle 211\rangle\, v_{T1}$ and $\langle 211\rangle\, v_L$, in agreement with the stable propagation regime predicted by Weertman [42]. Of the two transverse wave speeds, the lower ($\langle 211\rangle\, v_{T2}$) acts as a saturation velocity for TD velocities in the subsonic regime and the higher ($\langle 211\rangle\, v_{T1}$) bounds the stable velocity plateau in the intersonic regime.

Under steady state conditions, the TB motion is smooth without any tendencies to move in a *stick-slip* fashion, which was possible due to the tall specimen height that precluded interactions with the reflected stress waves. In Ni, TB velocities are limited to ~ 650 m/s, well below the lowest transverse wave speed. Features from the

kinetics of a TD are reflected within the kinetics of a TB. MD suggests an additional damping due to the TB and influences the kinetics of the TD. In the nucleation-dominated regime, the mechanism-based model of Abeyaratne and Vedantam, i.e. Eq. (2.10), sufficiently captures the TB kinetics. A new kinetic relation is proposed for a combination of a TB and a TD, i.e. Eqs. (2.11) and (2.12). The proposed model for TB consists of TD kinetics, which is crucial to accurately model the response of metals under dynamic and extreme loading conditions involving shock. The integrated mechanism-based kinetics relation developed in this work may be applicable to inform continuum-level constitutive models and mesoscale discrete-dislocation/twin simulations.

Chapter 3

Void dynamics governed by dislocation kinetics[†]

In chapter 2 we explored the role that dislocation kinetics play in governing the kinetics of planar defects, e.g. twin boundaries. In the present chapter we examine the role that dislocation kinetics and substructure evolution play in governing the dynamic growth of volumetric defects, i.e. voids, under very high strain rates. In particular, we account for the combined effects of relativistic dislocation drag and an evolving mobile dislocation density on the dynamics of void growth. We compare these effects to the constraints imposed by micro-inertia and discuss the conditions under which each mechanism governs the rate of void growth. The consequences of these constraints may be seen in a number of experimental observations associated

[†]The present chapter is largely based on a publication by Wilkerson and Ramesh [50].

with dynamic tensile failure, including the extreme rate-sensitivity of spall strength observed in laser shock experiments, an apparent anomalous temperate dependence of spall strength, and some particular features of void size distributions on spall surfaces. In addition, we provide a methodology for accounting for these effects in a computationally efficient manner, which is then utilized in chapter 5.

3.1 Introduction and background

For the past five decades there has been an intense effort to describe and understand the mechanical response of metals subjected to high strain rates, i.e. $10^3 - 10^8$ s^{-1}. More recently, there has been an increasing effort to understand the fundamental microscale processes governing the macroscale mechanical response of metals subjected to very high strain rates, and to capture these processes in multiscale predictive models, e.g. Barton et al. [51]. A number of applications stand to benefit from such understanding, e.g. personal and vehicular protection, nuclear stockpile reliability, spacecraft shielding, vehicular crashworthiness, and advanced manufacturing. Our aim here is to understand the role of dislocation kinetics in dynamic void growth, the essential microscale process governing the dynamic tensile strength of ductile metals.

Ductile failure of metals is known to be governed by the microscopic processes of void nucleation, growth, and finally coalescence leading to fracture [52–56]. The ear-

liest investigations regarded void nucleation as a cavitation instability in an otherwise homogenous elastic-perfectly plastic [57, 58], non-linear elastic [59], or a power-law hardening medium [60]. In his thesis Wu [61] extended these early instability analyses to account for thermal softening, heat conduction, and strain gradient effects. Void nucleation by cavitation instability has also been addressed in a number of molecular dynamics studies, e.g. Belak [62], Rudd and Belak [63], Bringa et al. [64]. Recent work [64–70] suggests that under extremely high tensile stresses, voids may also nucleate from vacancy clusters. Nevertheless, the most widely accepted void nucleation mechanism is associated with second-phase particles [71, 72]. Hard inclusions, e.g. carbide and oxide particles, may either internally crack or debond from the ductile metal matrix, see [73–75]. Voids have also been seen to nucleate within soft inclusions, e.g. sulfides [76]. For the purpose of the present work, it is sufficient to understand that freshly nucleated voids are likely to have a broad distribution of initial sizes, ranging from tens of nanometers (carbides and vacancy clusters) to hundreds of micrometers.

Subsequent growth of voids has been extensively studied and numerous micromechanical models have been proposed over the last five decades, with the most widely used being the Gurson model [77] as well as the modified version that has come to be known as the GTN model [78]. The early work analyzed the deformation of a single void in an otherwise homogenous rate-independent, perfectly plastic medium [52, 53]. Viscoplasticity was later incorporated by a number of authors, e.g. [79–81], demonstrating its stabilizing effect on the quasi-static void growth. Intense development of

this class of viscoplastic porous models is currently underway at numerous research centers.

Far less effort has been dedicated to understanding the dynamic growth of voids under extreme loading conditions. Knowles and Jakub [82] were the first to incorporate inertia into a non-linear elastic spherical-shell analysis. Later, Carroll and Holt [83] extended the analysis to a rate-independent, elastic-perfectly plastic material. Johnson [84] incorporated material viscosity into the analysis and concluded that the stabilizing effects of viscosity were greater than those of inertia for the cases considered. Cortés [85, 86] along with Wang [87] and Zheng et al. [88] performed similar analyses for thermoviscoplastic materials and confirmed the relative importance of rate-dependence. A comprehensive re-examination of the spherical-shell analysis was provided by Wu in a series of papers [89–91] demonstrating in detail the relative importance of inertia, rate-sensitivity, deformation hardening, thermal softening, and strain-gradient effects. This work clearly demonstrated that viscoplasticity governed the early stages of void growth; however, inertia quickly becomes the dominant stabilizing force as the voids become large. Similar conclusions were drawn by Ortiz and Molinari [92] on basis of energetics and later by Tong and Ravichandran [93, 94]. To the best of the authors' knowledge, all previous spherical-shell analyses have utilized simple power-law type rate-sensitivity models that are perhaps only applicable in the thermally activated glide regime. Under extreme loading conditions, the rate-sensitivity may be governed by dislocation drag and relativistic effects [10]. The aim

of the current chapter is to address dynamic void growth in this regime.

The present chapter is organized as follows. In section 3.2, we provide motivation for the need to incorporate dislocation drag and relativistic effects into the state-of-the art of dynamic void growth models. A few key experimental observations as well as micromechanical analysis indicates that dislocation drag and relativistic effects are important factors in the dynamic tensile strength of metals at extreme strain rates, i.e. $\gtrsim 5 \times 10^6$ s^{-1}. Section 3.3 provides a brief review of the dislocation-based viscoplasticity model of Austin and McDowell [10], which is used in this chapter to describe the constitutive behavior of the solid material surrounding a dynamically growing void. Finally, section 3.4 ties everything together in a micromechanical dynamic void growth framework governed by both dislocation kinetics and micro-inertia. Section 3.5 provides a discussion of the key results and addresses the implications of the model as they pertain to experimental observations. This section also explores the effects of various physical parameters on the rate of void growth, particularly those that affect either dislocation mobility or substructure evolution. Attention is also given to establishing regimes in which the physics permits particular assumptions that reduce the complexity of the model. Lastly, a brief summary and key conclusions are provided in section 3.6.

3.2 High strain rate tensile failure and dislocation drag mechanisms

There is strong experimental evidence that the dynamic tensile failure of metals (e.g. through spallation) is strongly dependent on the rate of deformation at high strain rates. For example, Fig. 3.1 shows the dependence of the spall strength on tensile strain rate for the case of commercially pure aluminum. Although the results in this figure are derived from two very different experimental techniques (plate impact and laser shock) and there are some subtleties associated with the analysis of each experimental type, it is apparent that the spall strength of commercially pure aluminum increases rapidly with increasing rate of deformation at volumetric strain rates $\dot{\varepsilon}_v$ larger than 10^7 s^{-1}. Note that a similar, although less drastic, rapid increase in dynamic flow stress has been measured in the pressure-shear response of commercially pure aluminum [95]. Defining the rate-sensitivity of spall strength as $m^* \triangleq \partial \ln \sigma^* / \partial \ln \dot{\varepsilon}_v$, where σ^* is the spall strength, Kanel et al. [96] observed that the spall strength rate-sensitivity for commercially pure aluminum is approximately equal to $m^* \approx 0.06$ over the strain rate range of 10^4 s$^{-1} \leq \dot{\varepsilon}_v \leq 10^6$ s^{-1}, see Fig. 3.1(a). A similar rate-sensitivity was observed by Fortov et al. [97] for aluminum foil over the same strain rate range. The laser shock experiments of Cuq-Lelandais et al. [98] examined higher strain rates and suggests slightly higher rate sensitivity of the spall strength. The highest strain rates were achieved by Moshe et al. [99], who used laser

shock experiments with ultrashort pulses of $20 - 100$ picoseconds to experimentally measure spall strength at the extreme strain rates of $\dot{\varepsilon}_v \gtrsim 10^8$ s^{-1}. Over this range, the measurements of Moshe et al. [99] show a spall strength rate-sensitivity of about $m^* \sim 1$ for aluminum foil, see Fig. 3.1(a). Such a dramatic change in the spall strength rate-sensitivity is suggestive of a transition in the underlying dominant mechanism. Shear strain rates greater than 10^7 s^{-1} are often assumed to be affected by dislocation drag and relativistic effects [5], and since void growth requires plastic flow at the void surface, the experimental results in Fig. 3.1(a) suggest that dislocation drag and relativistic effects may be important mechanisms in the spall strength of metals above some critical volumetric strain rate of approximately $\dot{\varepsilon}_v \gtrsim 10^7$ s^{-1}. However, since spall is related to void growth, it is unclear from these experimental observations alone whether this transition in mechanism is a) from thermally activated glide to relativistic glide or b) from thermally activated glide to a micro-inertia dominated regime.

The model of Wright and Ramesh [101] based on micro-inertia mediated void growth, as well as the subsequent model [102] accounting for both thermally activated glide and micro-inertia, demonstrated success in modeling spall strength of pure copper over a smaller range of strain rates 10^3 s$^{-1} \leq \dot{\varepsilon}_v \leq 3 \times 10^5$ s^{-1}. However, that approach underestimates the experimentally observed spall strength of copper subject to extreme strain rates $\dot{\varepsilon}_v \geq 10^7$ s^{-1} generated in laser-induced shock loading experiments. Thus the existing models suggest that a transition to relativistic

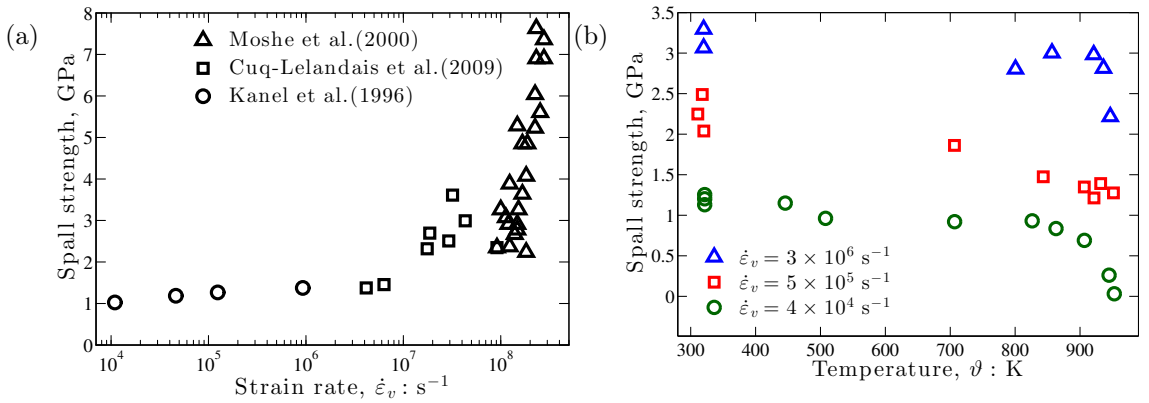

Fig. 3.1: Experimental observations supporting the importance of dislocation drag and relativistic effects on dynamic void growth and spall failure. (a) Dramatic change in rate-sensitivity of spall strength in aluminum at extreme loading rates, and (b) apparent change in the temperature dependence of spall strength in aluminum [100].

dislocation glide plays a role in the laser shock experiments presented in Fig. 3.1(a).

Another key experimental observation is the peculiar temperature dependence of spall strength, shown in Fig. 3.1(b). Kanel et al. [100] showed that for 10^4 s$^{-1} \leq \dot{\varepsilon}_v \leq 10^6$ s^{-1} the spall strength softens with increasing pre-heat temperature, presumably due to increased thermal activation. However, their experimental results demonstrate that for $\dot{\varepsilon}_v \gtrsim 3 \times 10^6$ s^{-1} the spall strength changes very little with increasing temperature (provided the material remains entirely solid, i.e. $\vartheta/\vartheta_m \lesssim 0.95$, where ϑ is the temperature and ϑ_m is the melting temperature). A similar temperature dependence was observed by Clifton [47], who showed that the dynamic shear strength of materials increased with increasing temperature for shear strain rates $\gtrsim 5 \times 10^6$ s^{-1}. This anomalous temperature dependence is attributed to increased dislocation drag due to increased phonon damping at higher temperatures [103, 104]. Thus the temperature-dependent results also suggest that relativistic dislocation drag may limit the rate

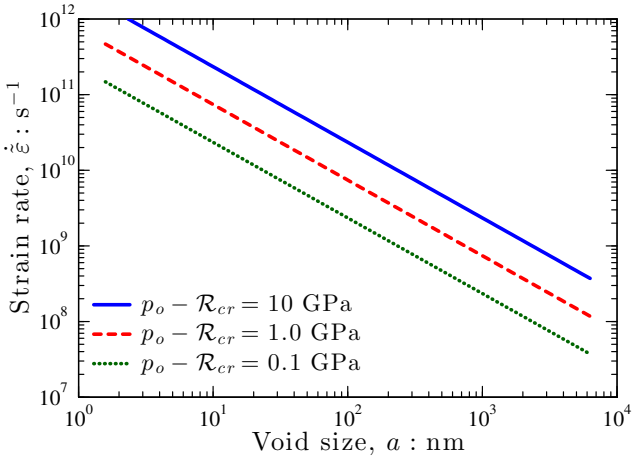

Fig. 3.2: Strain rates on the surface of a dynamically growing void constrained by micro-inertia alone.

at which voids grow (and thus the resulting spall strength) at very high volumetric strain rates.

The micromechanical analysis of Molinari and Wright [105] also supports the need to account for dislocation kinetics in dynamic void growth models. Molinari and Wright [105] were able to derive an analytic relationship for the void surface velocity ($\dot{a}$, where a is the void radius) experienced by a dynamically growing void in an elastic-perfectly plastic infinite medium, i.e.

$$\dot{a} = \sqrt{\frac{6}{11}\frac{\langle p_o - \mathcal{R}_{cr}\rangle}{\rho}}, \tag{3.1}$$

where p_o is the local macroscopic pressure, $\mathcal{R}_{cr}$ is the critical bifurcation pressure, and ρ is the mass density of the material. The critical bifurcation stress was calculated by Huang et al. [60] and Wu et al. [90] as $\mathcal{R}_{cr} = \frac{2}{3}\sigma_y\left(1 + \ln \varepsilon'_y\right) \sim 4\sigma_y$. The corresponding logarithmic Hencky equivalent strain rate on the void surface may be expressed as $\dot{\bar{\varepsilon}} = 3\dot{a}/a$ (see section 3.4 for derivation). Substitution of Eq. (3.1) into

this expression provides the associated surface strain rate as a function of the void size and the current over-pressure, $p_o - \mathcal{R}_{cr}$. The corresponding strain rate is plotted in Fig. 3.2 as a function of void size for various over-pressures, and clearly demonstrates the extreme surface strain rates experienced by the material at the surface of a dynamically growing void constrained only by micro-inertia. At these extreme strain rates dislocation kinetics are most certainly important, and micromechanical models based on micro-inertia alone are insufficient. With these motivations in hand, we develop a dynamic void growth model that incorporates the physics of dislocation drag and relativistic effects.

3.3 Dislocation-based viscoplasticity

The growth of voids in ductile metals is accommodated by the plastic deformation of the surrounding matrix. Therefore, any effort undertaken to improve upon micromechanics-based models for void growth must begin with the selection of an appropriate plasticity model. For quasi-static void growth, this essentially comes down to how accurately the hardening is captured, e.g. [106]. However, for dynamic void growth the most essential element of the plasticity model is the rate-sensitivity [102]. Although several micromechanics-based models have demonstrated the effects of rate-sensitivity on dynamic void growth [85, 86, 90], none have utilized a dislocation-based viscoplasticity model explicitly developed for very high strain rates, i.e. $10^4 - 10^8$ s^{-1}.

Later sections of this chapter will demonstrate that the utilization of such a viscoplasticity model gives rise to novel, somewhat non-intuitive, macroscopic response. In the current section, the essential elements of the dislocation-based viscoplasticity model of Austin and McDowell [10] are summarized and, where necessary, augmented.

Assuming J_2 flow theory with isotropic hardening, the tensorial form of Orowan's equation may be written as

$$\mathbf{d}^p = bN_m v_\perp \frac{\mathbf{s}}{3\tau} \tag{3.2}$$

where $\mathbf{d}^p$ is the rate of plastic deformation, b is the magnitude of the Burgers vector, N_m is the mobile dislocation density, $v_\perp$ is the mean dislocation velocity at the corresponding microscale material point, $\mathbf{s}$ is the deviatoric part of the Cauchy stress tensor, $\tau \triangleq \sigma_{vm}/2$ is an effective shear stress, and $\sigma_{vm} \triangleq \sqrt{3/2\ \mathbf{s} : \mathbf{s}}$ is the von Mises effective stress. The mean dislocation velocity is a function of the over-stress, $\tau - \tau_\mu$, where τ_μ is the athermal threshold shear stress required for dislocations to overcome long-range glide resistance. For relatively pure FCC metals, the athermal threshold shear stress may be modeled by the Taylor hardening relation,

$$\tau_\mu = \alpha_0 \mu b \sqrt{N_{im} + N_m}, \tag{3.3}$$

where α_0 is a dislocation-interaction parameter typically of order $1/2$, μ is the temperature-dependent shear modulus, and N_{im} is the density of immobile dislocations. For high dislocation velocities, the over-stress line forces are balanced by the dislocation drag force, i.e.

$$Bv_\perp = (\tau - \tau_\mu)\, b, \tag{3.4}$$

where B is the dislocation drag coefficient. In order to account for relativistic effects [107], the drag coefficient is commonly expressed as

$$B = \frac{B_0}{1 - (v_\perp / c_s)^2} \tag{3.5}$$

where $c_s \triangleq \sqrt{\mu/\rho}$ is the shear wave speed and B_0 is the temperature-dependent nominal drag coefficient that governs the kinetics in the linear regime, see Austin and McDowell [10]. For $\vartheta \gtrsim 100$K, B_0 is assumed to be governed by phonon damping [103, 108], for which Leibfried [104] developed the expression $B_0 = 3k_b\vartheta z/20c_s b^2$, where z is the number of atoms per unit cell and k_b is the Boltzmann constant.

In addition to the time dislocations spend gliding, they also spend a finite amount of time waiting at obstacles. However, at sufficiently high stresses the dislocations overcome these obstacles without any assistance from thermal energy, and in this case the waiting time may be ignored in comparison to the gliding time. Our present interests are in this high shear stress regime, i.e. drag regime.

Following Austin and McDowell [49] evolution equations for the dislocation densities may be constructed as

$$\dot{N}_m = \dot{N}_{nuc} + \dot{N}_{mult} - \dot{N}_{ann} - \dot{N}_{trap} \tag{3.6}$$

$$\dot{N}_{im} = \dot{N}_{trap} - \dot{N}_{rec}, \tag{3.7}$$

where the subscripts *nuc*, *mult*, *ann*, *trap*, and *rec* refer to dislocation nucleation, multiplication, annihilation, trapping, and recovery, respectively. Several groups are current working to develop experimental and dislocation dynamics simulation capa-

bilities to study the time-resolved evolution of the dislocation density components. However, what follows is a physically-based framework that is assumed to sufficiently capture the correct physics [10]:

$$\dot{N}_{mult} = \delta_{mult} N_m v_\perp \tag{3.8}$$

$$\dot{N}_{ann} = \alpha_{ann} b N_m^2 v_\perp \tag{3.9}$$

$$\dot{N}_{trap} = \frac{N_m v_\perp}{\Lambda}, \tag{3.10}$$

where δ_{mult} and α_{ann} are model parameters and Λ is the effective mean free path of dislocations and decreases with increasing dislocation density, i.e. $\Lambda^{-1} = \alpha_{dis}\sqrt{N_{im} + N_m}$, see [10]. Appropriate material properties and model parameters are given in Table 3.1 for OFHC copper, which will be utilized as a model material in the present study. As in [10], recovery processes are ignored ($\dot{N}_{rec} = 0$) due to the short time scales of interest ($< 1\mu$s), which inhibit many thermally-activated processes such as climb. The consequence of ignoring these recovery processes is that strain rate history effects are not captured.

Both heterogeneous and homogeneous nucleation of new dislocation loops are discussed at length by Austin and McDowell [10, 49]. Homogeneous nucleation requires a very large shear stress on the order of $\mu/10$, which is likely to be achieved only momentarily under shock compression conditions. Heterogeneous nucleation is more likely to occur in the vicinity of dynamically growing voids. Note that if these voids nucleated at stress concentrations, e.g. triple junctions and inclusions, these stress

Table 3.1: Material properties and substructure parameters corresponding to OFHC copper.

Material properties			Substructure parameters		
μ	48.4	GPa	α_0	1.0	
ρ	8,924	kg m^{-3}	δ_{mult}	42	mm^{-1}
c_s	2.33	km s^{-1}	α_{ann}	0.5	
b	0.256	nm	α_{dis}	0.012	

concentrators are no longer available to assist heterogeneous dislocation nucleation as the void grows. Heterogeneous nucleation may still occur if the local shear stresses are large enough to emit dislocations from the surface of voids [64, 65, 67, 68, 70, 109], but this mechanism likely requires very large pressures (∼5 GPa for copper). Due to the extremely high pressures likely required we choose to ignore dislocation emission in this chapter, and thus neglect both heterogenous and homogeneous nucleation, i.e. $\dot{N}_{nuc} = 0$. We revisit the issue of dislocation emission in chapters 4 and 5 where we demonstrate the importance of this mechanism in governing extreme dynamic failure of ductile metals.

3.4 Dynamic void growth governed by dislocation kinetics

Consider a spherical void of radius a embedded within an otherwise solid sphere of radius r_o, as shown in Fig. 3.3. The spherical shell is subjected to a *dynamic* loading of the pressure p_o on the boundary of the spherical shell, i.e. $\dot{p}_o >> 0$ at $r = r_o$. We develop a micromechanics-based model in this section to describe the rate at which this spherical void grows, i.e. $\dot{a}$. The void growth rate is constrained by micro-inertia, dislocation kinetics, and rate of substructure evolution. All of these elements are addressed in the development of our micromechanical dynamic void growth model.

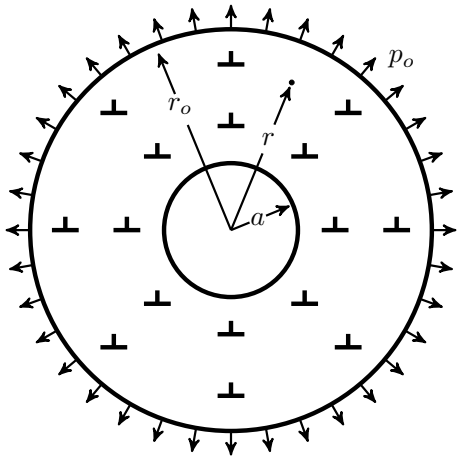

Fig. 3.3: Schematic of a spherical void of radius a embedded within an otherwise solid sphere of radius r_o. Yielding of the spherical shell occurs above a threshold pressure, i.e. $p_o \geq \mathcal{R}_{cr}$.

3.4.1 Kinematics

Following the approach laid out by Knowles and Jakub [82] for an incompressible spherical shell, consider a spherically symmetric motion of the form

$$\mathbf{x}(\mathbf{X},t) = r(R,t)\mathbf{e_r}, \tag{3.11}$$

where x is the spatial position at time t of the material particle that was located at X in the reference configuration, and r and R denote the radial coordinates in the deformed and reference configurations, respectively. The material is assumed to be plastically and elastically incompressible so that the current volume is equal to the reference volume, i.e.

$$r(R,t)^3 - a(t)^3 = R^3 - A^3, \tag{3.12}$$

where A denotes the radius of the spherical void in the reference configuration, and $a(t) = r(A,t)$ denotes the inner radius of the spherical shell at time t. Eq. (3.12) implies that the motion of the spherical shell, $r(R,t)$, is completely determined once the inner radius of the spherical shell is known as a function of time, $a(t)$. The corresponding deformation gradient tensor, $\mathbf{f} \triangleq \text{Grad}\mathbf{x}$, is obtained through spatial differentiation of Eq. (3.11) (after substitution of Eq. (3.12)), i.e.

$$\mathbf{f} = \frac{R^2}{r^2}\mathbf{e_r} \otimes \mathbf{e_r} + \frac{r}{R}(\mathbf{e}_\theta \otimes \mathbf{e}_\theta + \mathbf{e}_\phi \otimes \mathbf{e}_\phi). \tag{3.13}$$

A multiplicative split of the total deformation gradient tensor is assumed such that $\mathbf{f} = \mathbf{f}^e\mathbf{f}^p$, where $\mathbf{f}^p$ is the plastic deformation gradient and $\mathbf{f}^e$ is the corresponding

elastic deformation gradient. Consistent with dislocation-based plasticity theory, we take the plastic deformation to be incompressible, i.e. $\det(\mathbf{f^p}) = 1$, implying

$$r_p(R,t)^3 - a_p(t)^3 = R^3 - A^3, \tag{3.14}$$

where r_p and a_p are the locations of material elements in the intermediate configuration (originally located in the reference configuration at R and A, respectively). By utilizing Eq. (3.14), the plastic part of the deformation gradient tensor is obtained as

$$\mathbf{f^p} = \frac{R^2}{r_p^2}\mathbf{e_r} \otimes \mathbf{e_r} + \frac{r_p}{R}(\mathbf{e}_\theta \otimes \mathbf{e}_\theta + \mathbf{e}_\phi \otimes \mathbf{e}_\phi). \tag{3.15}$$

The spatial velocity gradient $\mathbf{l}$ is given by

$$\mathbf{l} = \dot{\mathbf{f}}\mathbf{f}^{-1} = \dot{\mathbf{f}}^e\mathbf{f}^{e^{-1}} + \mathbf{f}^e\dot{\mathbf{f}}^p\mathbf{f}^{p^{-1}}\mathbf{f}^{e^{-1}} \triangleq \mathbf{l}^e + \mathbf{l}^p. \tag{3.16}$$

Therefore the rate of deformation tensor, $\mathbf{d} \triangleq \frac{1}{2}\left(\mathbf{l} + \mathbf{l^T}\right)$, is obtained as

$$\mathbf{d} = -2\frac{\dot{r}}{r}\mathbf{e_r} \otimes \mathbf{e_r} + \frac{\dot{r}}{r}(\mathbf{e}_\theta \otimes \mathbf{e}_\theta + \mathbf{e}_\phi \otimes \mathbf{e}_\phi). \tag{3.17}$$

The plastic rate of deformation tensor $\mathbf{d^p}$ is the symmetric part of $\mathbf{l}^p \triangleq \mathbf{f}^e\dot{\mathbf{f}}^p\mathbf{f}^{p^{-1}}\mathbf{f}^{e^{-1}}$ and is given by

$$\mathbf{d^p} = -2\frac{\dot{r}_p}{r_p}\mathbf{e_r} \otimes \mathbf{e_r} + \frac{\dot{r}_p}{r_p}(\mathbf{e}_\theta \otimes \mathbf{e}_\theta + \mathbf{e}_\phi \otimes \mathbf{e}_\phi). \tag{3.18}$$

Recall that the plastic rate of deformation tensor is governed by the dislocation-based viscoplasticity model described in section 3.3. For the purpose of the present analysis, the assumption is made that upon yielding the plastic rate of deformation is much larger than the elastic rate of deformation, i.e. $\mathbf{d} \approx \mathbf{d^p}$.

To maintain consistency with Austin and McDowell [10] it proves convenient to introduce a non-standard scalar equivalent strain rate defined as

$$\dot{\varepsilon} \triangleq \sqrt{\frac{3}{2}\dot{\mathbf{e}}' : \dot{\mathbf{e}}'}, \tag{3.19}$$

where $\mathbf{e} \triangleq \ln\sqrt{\mathbf{f}^{\mathbf{T}}\mathbf{f}}$ is the logarithmic finite Hencky strain tensor and $\mathbf{e}'$ is the deviatoric part of the strain tensor. Notice that our definition of equivalent strain rate differs from the standard definition by a factor of ⅔. It is also worth noting that for symmetric deformation gradient tensors (as in the present case), the logarithmic Hencky strain rate tensor is identical to the rate of deformation tensor, i.e. $\dot{\mathbf{e}} = \mathbf{d}$, thus Eq. (3.17) may be utilized in evaluating Eq. (3.19) to obtain $\dot{\varepsilon} = 3\dot{r}/r$. This expression for the strain rate may be expanded by obtaining $\dot{r}$ from the time differentiation of Eq. (3.12) resulting in

$$\dot{\varepsilon} = \frac{a^3}{r^3}\frac{3\dot{a}}{a} = \frac{a^3}{r^3}\dot{\tilde{\varepsilon}}, \tag{3.20}$$

where we have introduced here a short hand notation for referencing variables evaluated on the void surface, e.g. $\dot{\tilde{\varepsilon}} \triangleq \dot{\varepsilon}|_{r=a} = 3\dot{a}/a$.

Substitution of Orowan's relation, i.e. $\dot{\varepsilon} = bN_m v_\perp$, into Eq. (3.20) provides an expression for the spatial distribution of the dislocation velocity, i.e.

$$v_\perp = \frac{a^3}{r^3}\frac{\dot{\tilde{\varepsilon}}}{bN_m} = \frac{\tilde{N}_m}{N_m}\frac{a^3}{r^3}\tilde{v}_\perp \tag{3.21}$$

where the void surface notation just defined has been applied to the mobile dislocation density and the dislocation velocity.

3.4.2 Dynamics

For the spherically symmetric motion only the radial balance of momentum in the current configuration is nontrivial, i.e.

$$\frac{\partial \sigma_{rr}}{\partial r} - \frac{2}{r}(\sigma_{\theta\theta} - \sigma_{rr}) = \rho \ddot{r}. \tag{3.22}$$

For this spherically symmetric stress state the maximum shear stress, $\tau \triangleq \frac{1}{2}\sqrt{\frac{3}{2}\boldsymbol{\sigma}' : \boldsymbol{\sigma}'}$, may be expressed as $\tau = \frac{1}{2}\left|\sigma_{\theta\theta} - \sigma_{rr}\right|$. Under tensile loading $\sigma_{\theta\theta} > \sigma_{rr}$, thus Eq. (3.22) may be rewritten as

$$\frac{\partial \sigma_{rr}}{\partial r} - \frac{4}{r}\tau = \rho \ddot{r}. \tag{3.23}$$

Based on the findings of Wu et al. [91], we assume isothermal conditions due to the extremely fast thermal diffusion associated with the small length scales of void growth; therefore, solving the energy equation is unnecessary. Substituting Eq. (3.12) into the right hand side of Eq. (3.23), the balance of radial momentum becomes

$$\frac{\partial \sigma_{rr}}{\partial r} - \frac{4}{r}\tau = -\rho \frac{\partial \psi}{\partial r}, \tag{3.24}$$

where ψ is the acceleration potential introduced in [83] as

$$\psi = \frac{a^2 \ddot{a}}{r} + \frac{2a\dot{a}^2}{r} - \frac{a^4 \dot{a}^2}{2r^4}. \tag{3.25}$$

Integrating Eq. (3.24) with respect to the spatial variable r in the current configuration over the entire spherical shell from $r = a(t)$ to $r = r_o(t)$, where $r_o(t)$ is the outer radius of the spherical shell as a function of time, we have

$$\sigma_{rr}\big|_{r=a}^{r=r_o} - \int_a^{r_o} \frac{4}{r}\tau dr = -\rho\, \psi\big|_{r=a}^{r=r_o}. \tag{3.26}$$

Eq. (3.26) may be further simplified by applying the appropriate boundary conditions and evaluating the acceleration potential, ψ, on the boundaries. Ignoring surface tension, the appropriate boundary conditions for the problem at hand are $\sigma_{rr}|_{r=a(t)} = 0$ and $\sigma_{rr}|_{r=r_o(t)} = p_o(t)$, as shown in Fig. 3.3. Substitution of the boundary conditions and the evaluation of the acceleration potential results in the general integro-differential equation governing the dynamics of a spherical void embedded within an otherwise intact spherical shell [82], i.e.

$$\underbrace{\rho\left(1-\frac{a}{r_o}\right)a\ddot{a}}_{\mathcal{R}^{\rho}_{tr}}+\underbrace{\rho\left(\frac{3}{2}-2\frac{a}{r_o}+\frac{1}{2}\left(\frac{a}{r_o}\right)^4\right)\dot{a}^2}_{\mathcal{R}^{\rho}_{ss}}=p_o(t)-\underbrace{\int_a^{r_o}\frac{4}{r}\tau dr}_{\mathcal{R}_{cr}+\mathcal{R}^{v_\perp}_{dd}}, \tag{3.27}$$

where $\mathcal{R}^{\rho}_{tr}$ and $\mathcal{R}^{\rho}_{ss}$ are the components of the inertial resistance to deformation associated with transient growth ($\ddot{a} \neq 0$) and steady state growth ($\ddot{a} = 0, \dot{a} \neq 0$), respectively. The spatial integral on the right hand side of Eq. (3.27) may be decomposed into a term dependent on the quasi-static flow strength (and any elastic deformation outside the plastic zone), i.e. $\mathcal{R}_{cr}$, and a term associated with the rate-sensitivity of the over-stress, $\mathcal{R}^{v_\perp}_{dd}$, which is given by

$$\mathcal{R}^{v_\perp}_{dd} = \int_a^{r_o}\frac{4}{r}\left(\tau-\tau_\mu\right)dr = \int_a^{r_o}\frac{4}{r}\frac{B_0 c_s}{b}\frac{v_\perp/c_s}{1-(v_\perp/c_s)^2}dr, \tag{3.28}$$

where Eq. (3.4) and Eq. (3.5) have been utilized. This formulation is used here because the rate-sensitivity of the shear stress is derived from the associated dislocation dynamics in this chapter.

Initial conditions, namely $a|_{t=0} = A$, $\dot{a}|_{t=0} = 0$, $N^0_m(R)$, $N^0_{im}(R)$, and $\vartheta|_{t=0}$, complete the set of equations. The particular challenge associated with numerically in-

tegrating Eq. (3.27) arises from the spatial integrals, e.g. Eq. (3.28), that must be numerically solved at each time step. In the following section, we will propose a number of closed form approximations to $\mathcal{R}_{dd}^{v_\perp}$ that significantly reduce the computational complexity associated with solving Eq. (3.27). Similar approximations for $\mathcal{R}_{cr}$ have been previously studied, e.g. [58, 83, 89–91]. These approximations are essential when it comes to implementing the micromechanical model in large-scale computations, e.g. [110, 111].

3.5 Numerical analysis and discussion

The dynamics of void growth at very high strain rates is a complex process involving the confluence of micro-inertia, dislocation dynamics, and substructure evolution. In order to best demonstrate how each of these contribute to dynamic void growth, we present a systematically chosen set of numerical results intended to reveal the underlying physics. We begin by discussing the influence of dislocation kinetics under constant dislocation substructure. Following this, we incorporate the evolving dislocation substructure, and demonstrate its role in constraining void kinetics at large deformation. Lastly, we discuss the implications of dislocation kinetics and evolving substructure as they pertain to experimental observations of spall fracture surfaces.

3.5.1 Influence of dislocation dynamics under constant substructure

We first study the characteristics of the resistance associated with dislocation dynamics ($\mathcal{R}_{dd}^{v_\perp}$) under temporally-constant, and spatially-varying dislocation substructures. Here we are able to develop a number of analytic expressions and approximations that provide a deeper understanding of the void growth kinetics. We demonstrate in particular the relative insensitivity of void kinetics to the particular spatial dependence of the dislocation substructure, which is important in developing closed-form approximations to $\mathcal{R}_{dd}^{v_\perp}$. We also demonstrate the temperature dependence of the dislocation dynamics resistance term and discuss how this may affect void kinetics.

We first discuss a family of analytic solutions to the dislocation dynamics resistance term $\mathcal{R}_{dd}^{v_\perp}$. Given that the substructure evolves in a non-linear manner

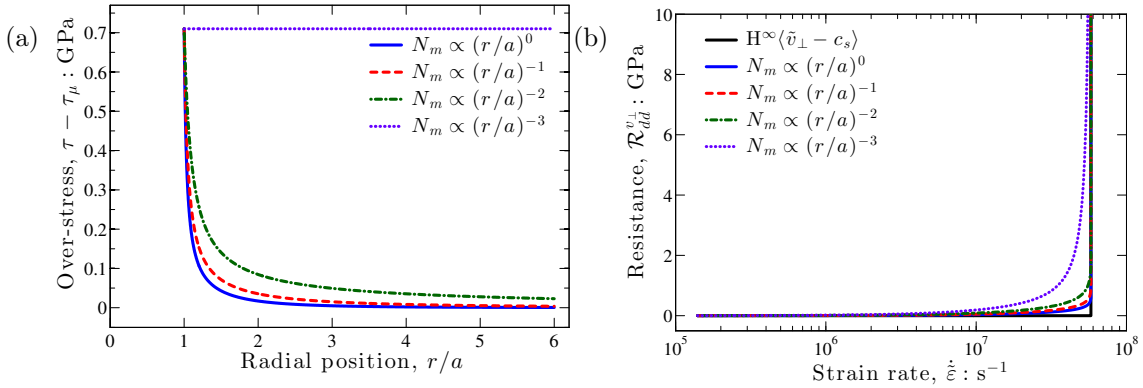

Fig. 3.4: (a) Spatial distributions of the over-stress, $\tau - \tau_\mu$, for $\tilde{v}_\perp = 0.9 \times c_s$. (b) The corresponding rate dependence of the dislocation dynamics resistance term, $\mathcal{R}_{dd}^{v_\perp}$.

(Eq. (5.18)–Eq. (3.10)) with respect to plastic deformation, it follows that the mobile dislocation density around a growing void will also develop a non-linear radial spatial dependence. Unfortunately, there are currently no experimental observations of this spatial dependence of the mobile dislocation density. This is one area where advanced in-situ characterization techniques are particularly needed. Although the precise form depends on the details of the evolution equations, we consider the radial spatial variation of the mobile dislocation density using the particular class of functions $N_m = \tilde{N}_m(r/a)^\eta$. Substitution of this class of functions into Eq. (3.21) gives the expression for the corresponding spatial dependence of the dislocation velocity:

$$v_\perp = \tilde{v}_\perp \left(\frac{a}{r}\right)^{\eta+3} = \frac{\dot{\tilde{\varepsilon}}}{b\tilde{N}_m}\left(\frac{a}{r}\right)^{\eta+3}. \tag{3.29}$$

For all cases of $\eta > -3$ the dislocation velocity decays with distance from the surface of the void, while $\eta = -3$ results in a spatially constant dislocation velocity. For $\eta > -3$ the dislocation velocity achieves its maximum value at the void surface, and the physical constraint that $v_\perp < c_s$ is satisfied everywhere throughout the spherical shell so long as it is satisfied at the void surface, i.e. $\tilde{v}_\perp < c_s$. We note that the cases of $\eta > 0$ correspond to the mobile density increasing with distance from the void surface, a possibility that we will address later.

The associated spatial dependence of the over-stress, $\tau - \tau_\mu$ is obtained by applying Eq. (3.29) to Eq. (3.4), for which numerical evaluations are presented in Fig. 3.4(a) with $v_\perp$ taken to be $0.9 \times c_s$. For $\eta > -3$ the over-stress decays even more rapidly with distance from the void surface than does the dislocation velocity, and the over-stress

at the void surface is much greater than at any other location. This is a result of the highly non-linear dependence of $v_\perp$ on B, and thus $\tau - \tau_\mu$, within the relativistic regime ($v_\perp \gtrsim 0.8 \times c_s$), see Eq. (3.4) and Eq. (3.5). The importance of the rapid spatial decay of the over-stress becomes evident in the examination of the characteristics of $\mathcal{R}_{dd}^{v_\perp}$ Utilization of Eq. (3.29) permits an exact solution to Eq. (3.28) expressed as

$$\mathcal{R}_{dd}^{v_\perp} = \begin{cases} \frac{2}{\eta+3}\frac{B_0 c_s}{b} \ln\left(\frac{c_s+\tilde{v}_\perp}{c_s-\tilde{v}_\perp} \times \frac{c_s-\tilde{v}_\perp \varphi^{\eta/3+1}}{c_s+\tilde{v}_\perp \varphi^{\eta/3+1}}\right) & \text{for } \eta \neq -3 \\ \frac{4}{3}\frac{B_0 c_s}{b}\frac{\tilde{v}_\perp/c_s}{1-(\tilde{v}_\perp/c_s)^2} \ln \varphi & \text{for } \eta = -3, \end{cases} \tag{3.30}$$

where $\varphi \triangleq a^3/r_o^3$ is the spherical shell porosity. Fig. 3.4(b) presents numerical evaluations of Eq. (3.30) as a function of both $v_\perp/c_s$ and $\dot{\tilde{\varepsilon}}$ with $\tilde{N}_m = 10^{14}$ m^{-2} and $\varphi = 0.5\%$. The value of $\mathcal{R}_{dd}^{v_\perp}$ is negligible ($<< \mathcal{R}_{cr}$) for $v_\perp \lesssim 0.15 \times c_s$ ($\dot{\tilde{\varepsilon}} \lesssim 10^7$ s^{-1} for $\tilde{N}_m = 10^{14}$ m^{-2}), which is well outside the relativistic regime. At the other end of the spectrum, as $v_\perp \to c_s$ the dislocation dynamics resistance becomes infinite ($\mathcal{R}_{dd}^{v_\perp} \to \infty$). The details of how $\mathcal{R}_{dd}^{v_\perp}$ transitions from the negligible regime ($v_\perp \lesssim 0.15 \times c_s$) to the infinite regime ($v_\perp \to c_s$) are governed by the specific manner in which the mobile dislocation density is spatially distributed. Reexamining Fig. 3.4(a), notice how rapidly $\tau - \tau_\mu$ decays with distance from the void surface for $\eta \nsim -3$, and how much greater the over-stress is near the void surface than anywhere else in the shell. The consequence of this is that (for $\eta \nsim -3$) the contribution to $\mathcal{R}_{dd}^{v_\perp}$ from $\tau - \tau_\mu$ near the void surface is far greater than from anywhere else, and thus in order for $\mathcal{R}_{dd}^{v_\perp}$ to achieve a significant value the over-stress at the void surface must be quite large. For example, in order to generate dislocation dynamics resistance

($\mathcal{R}_{dd}^{v_\perp}$) on the same order as the critical resistance ($\mathcal{R}_{cr}$), the dislocation velocity at the surface ($\tilde{v}_\perp$) must reach $\sim 0.98 \times c_s$ (far into the relativistic regime) for $\eta = -1$, corresponding to $\tilde{\tau} - \tilde{\tau}_\mu \sim 5$ GPa. This, however, is not the case for $\eta = -3$ where achieving the same level of dislocation dynamics resistance only requires $v_\perp \sim 0.5 \times c_s$ (outside the relativistic regime), corresponding to $\tilde{\tau} - \tilde{\tau}_\mu \sim 0.5$ GPa. This special-case results because for $\eta = -3$ the over-stress is spatially constant, and thus the entire spherical shell contributes to the dislocation dynamics resistance, while for $\eta \nsim -3$ only a small fraction of the spherical shell contributes significantly to the resistance, and the relativistic domain must be reached in order to achieve non-negligible dislocation dynamics resistance.

Thus a simple, yet effective, approximation to $\mathcal{R}_{dd}^{v_\perp}$ for cases in which $\eta \nsim -3$ is $\mathcal{R}_{dd}^{v_\perp} \sim \mathrm{H}^\infty\langle \tilde{v}_\perp - c_s \rangle$, where $\mathrm{H}^\infty\langle\cdot\rangle$ is the product of the standard Heaviside function $\mathrm{H}\langle\cdot\rangle$ and ∞. Physically, the approximation assumes that $\mathcal{R}_{dd}^{v_\perp}$ is negligible when $\tilde{v}_\perp < c_s$, then instantaneously transitions to an infinite value when $\tilde{v}_\perp = c_s$. The agreement of $\mathrm{H}^\infty\langle \tilde{v}_\perp - c_s \rangle$ with Eq. (3.30) is shown in Fig. 3.4(b). Notice that the approximation is particularly accurate for $\eta = 0$, and (although not shown) becomes even more accurate for $\eta > 0$, i.e. the mobile density increases with distance from the void surface. In the subsequent section on substructure evolution, this will become a hallmark of the later-stage void growth.

Using this approximation, $\mathcal{R}_{dd}^{v_\perp}$ can be written as

$$\mathcal{R}_{dd}^{v_\perp} = \mathrm{H}^\infty\langle \tilde{v}_\perp - c_s \rangle = \mathrm{H}^\infty\langle \dot{\tilde{\varepsilon}} - b\tilde{N}_m c_s \rangle, \tag{3.31}$$

provided that the mobile dislocation density does not decay stronger than inverse cubic, i.e. $\eta > -3$. Eq. (3.31) constitutes a lower bound on the dislocation dynamics resistance term, as it only accounts for the relativistic behavior of dislocations and ignores the contribution of dislocation drag.

What are the implications of this approximation on the dynamics? Consider the application of an instantaneous tensile pressure p_o to the outer surface of the spherical shell shown in Fig. 3.3. As this spherical shell deforms, it generates inertial and non-inertial forces that resist this deformation such that $p_o = \mathcal{R}_{cr} + \mathcal{R}_{dd}^{v_\perp} + \mathcal{R}_{tr}^{\rho} + \mathcal{R}_{ss}^{\rho}$, as discussed in the previous section. Here we aim to first isolate the contribution of dislocation dynamics resistance to the overall resistance, and therefore, we set $\mathcal{R}_{tr}^{\rho} = \mathcal{R}_{ss}^{\rho} = 0$ for the moment. For this case, manipulation of Eq. (3.31) yields $\tilde{v}_\perp = c_s \mathrm{H}\langle p_o - \mathcal{R}_{cr}\rangle$, which may be substituted into Eq. (3.21) to obtain an upper bound on the void growth rates, i.e.

$$\dot{a} < \frac{1}{3} a b \tilde{N}_m c_s. \tag{3.32}$$

Eq. (3.32) may be integrated exactly to obtain the corresponding (relativistic) upper bound on the current void size (assuming $p_o > R_{cr}$ for $t > t_{cr}$), i.e.

$$a < A \exp\left(\frac{1}{3} b \tilde{N}_m c_s \langle t - t_{cr}\rangle\right). \tag{3.33}$$

Manipulation of Eq. (3.33) results in an expression for the minimum required surface mobile dislocation density ($\tilde{N}_m$) to achieve a particular growth factor ($\Gamma \triangleq$

a/A) within a given time increment (Δt):

$$\tilde{N}_m > \frac{3}{bc_s\Delta t}\ln\Gamma. \tag{3.34}$$

According to Reina et al. [69] spall of metals at extreme rates may require some voids to grow two orders of magnitude in $\sim 0.1 - 10$ ns. For $\Gamma = 10^2$ and $\Delta t = 10$ ns, the minimum required surface mobile densities are $\tilde{N}_m > 1.5 \times 10^{15}$ m^{-2} and $\tilde{N}_m > 2.3 \times 10^{15}$ m^{-2} for aluminum and copper, respectively. Clearly, the mobile dislocation densities must be very large to achieve such rapid growth rates. Furthermore, as will be discussed in the proceeding subsection, even if the mobile dislocation density is sufficiently high there are still strong constraints imposed by micro-inertia, i.e. $\mathcal{R}^{\rho}_{tr}$ and $\mathcal{R}^{\rho}_{ss}$. These constraints contribute to the extreme rate-sensitivity of spall strength shown in Fig. 3.1(a).

3.5.1.1 Temperature dependence of $\mathcal{R}^{v_\perp}_{dd}$

Reina et al. [69] also discuss at length the importance of temperature in the void growth kinetics and spall strength of metals at extreme rates; we therefore examine the temperature dependence of $\mathcal{R}^{v_\perp}_{dd}$. The temperature dependence of $\mathcal{R}^{v_\perp}_{dd}$ arises from the temperature dependence of the over-stress, $\tau - \tau_\mu$. Recall that within the drag regime, the over-stress resulting from a particular glide velocity increases linearly with temperature due to increased phonon damping. Therefore, if all dislocations within the spherical shell are confined to the drag regime, then $\mathcal{R}^{v_\perp}_{dd}$ will assume the same linear temperature dependence. On the other hand, if the dislocations near the surface

of the void are in the relativistic regime then $\mathcal{R}_{dd}^{v_\perp}$ is well approximated by $\mathrm{H}^\infty\langle\tilde{v}_\perp - c_s\rangle$. In this case, the temperature dependence of $\mathcal{R}_{dd}^{v_\perp}$ is mostly governed by the temperature dependence of the shear wave speed ($\partial c_s/\partial\vartheta < 0$). Higher temperatures effectively shift the curves shown in Fig. 3.4(b) to the left.

In contrast to $\mathcal{R}_{dd}^{v_\perp}$, the critical resistance ($\mathcal{R}_{cr}$) decreases with temperature due to thermal softening of the quasi-static shear strength. For many materials the temperature dependence of the quasi-static shear strength decreases nearly linearly with the homologous temperature, $\vartheta_h \triangleq (\vartheta - \vartheta_0)\,/\,(\vartheta_m - \vartheta_0)$, where $\vartheta_0 = 300$ K and ϑ_m are reference and melting temperatures, respectively. A simple model for the temperature dependence of the critical resistance would follow this same functional dependence, i.e. $\mathcal{R}_{cr} = \mathcal{R}_{cr}^0(1 - \vartheta_h)$.

Fig. 3.5 shows numerical evaluations of the dependence of the total non-inertial

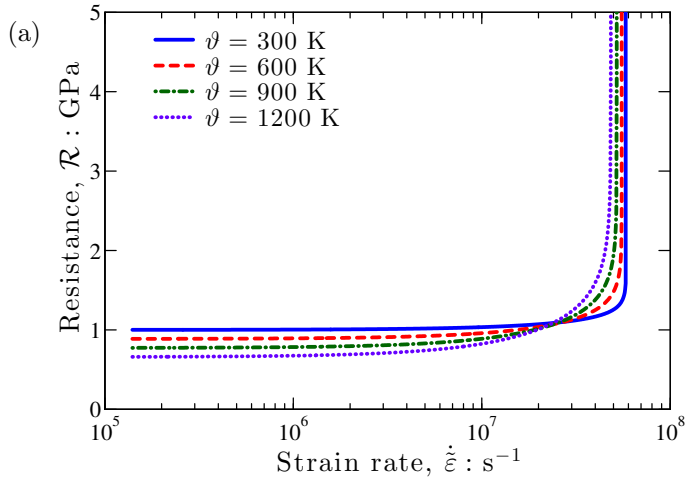

Fig. 3.5: Temperature dependence of total non-inertial resistance, $\mathcal{R}_{cr}+\mathcal{R}_{dd}^{v_\perp}$ with spatial dependence of the dislocation density characterized by $\eta = 0$. ($\tilde{N}_m = 10^{14}$; $\mathcal{R}_{cr}^0 =$ 1 GPa).

resistance, i.e. $\mathcal{R} = \mathcal{R}_{cr} + \mathcal{R}_{dd}^{v_\perp}$ on the applied strain rate for a number of temperatures, ϑ. Notice the cross-over that occurs in the temperature dependence. Below some particular transition strain rate the non-inertial resistance decreases with increasing temperature because it is dominated by $\mathcal{R}_{cr}$. Above this transition strain rate the non-inertial resistance is instead dominated by $\mathcal{R}_{dd}^{v_\perp}$ and thus increases with increasing temperature. These trends are consistent with the plate impact experiments of Kanel et al. [100], who observed an apparent transition in the temperature dependence of spall strength at volumetric strain rates of about 3×10^6 s^{-1}. Higher mobile dislocation densities shift the transition strain rate to higher values.

Recalling that tensile stress relaxation and spall strength are governed by both the number of voids and their growth rates [101], the temperature dependence of spall strength is complicated by the kinetics of vacancy clustering. While higher temperatures may result in slower void growth rates at very high strain rates, there are also likely to be more vacancy clusters generated due to the enhanced vacancy mobility at higher temperatures [69]. It is not immediately clear which of these mechanisms is more important to the overall stress relaxation. The temperature dependence at very high strain rates may depend on the particular microstructure. For example, a low-purity metal or alloy with numerous second-phase particles may be relatively unaffected by the number of vacancy clusters. The spall strength of such a material may exhibit a stronger anomalous temperature dependence than that of the high-purity aluminum shown in Fig. 3.1(b).

3.5.2 Influence of inertia and dislocation kinetics on void dynamics

The previous subsection analyzed the characteristics of $\mathcal{R}_{dd}^{v_\perp}$, while ignoring inertial effects, i.e. $\mathcal{R}_{tr}^{\rho}$ and $\mathcal{R}_{ss}^{\rho}$. Here we incorporate these effects into the analysis, with particular attention given to comparing the different mechanisms. However, the present analysis is limited to constant dislocation density, i.e. $\dot{N}_m = \dot{N}_{im} = 0$, in order to isolate the effects of dislocation kinetics. It will be shown that dislocation kinetics constrain the early growth rates of sub-micron voids, but micro-inertia eventually takes over as the dominant constraint.

Consider the steady state dynamics ($\ddot{a} = 0$) of the spherical shell shown in Fig. 3.3, ignoring the additional constraints imposed by dislocation dynamics, i.e. $\mathcal{R}_{dd}^{v_\perp} = 0$. Manipulation of the associated momentum balance ($p_o = \mathcal{R}_{cr} + \mathcal{R}_{ss}^{\rho}$) leads to a relation for the steady state growth rate previously derived by Molinari and Wright [105]:

$$\dot{a} = \sqrt{\xi \rho^{-1} \langle p_o - \mathcal{R}_{cr} \rangle}, \tag{3.35}$$

where $\xi = 2/3$ in steady state. For loading conditions in which $\ddot{a} \geq 0$, Eq. (3.35) serves as an upper bound on the velocity when constrained by micro-inertia. This micro-inertia upper bound complements the similar dislocation dynamics upper-bound established in Eq. (3.32). Taking the minimum of the two independent upper bounds, one obtains a bounding expression that accounts for both micro-inertia and disloca-

tion kinetics:

$$\dot{a} < \min\left(\frac{1}{3}ab\tilde{N}_m c_s, \sqrt{\xi\rho^{-1}\langle p_o - \mathcal{R}_{cr}\rangle}\right). \tag{3.36}$$

The dynamics transition from the dislocation dynamics dominated regime ($\mathcal{R}^{v_\perp}_{dd} > \mathcal{R}^{\rho}_{ss}$) to the micro-inertia dominated regime ($\mathcal{R}^{\rho}_{ss} > \mathcal{R}^{v_\perp}_{dd}$) for voids sizes greater than some critical transition size. This transition void size may be approximated through the manipulation of Eq. (3.36), and is expressed as

$$a|_{\text{transition}} = \frac{3}{b\tilde{N}_m c_s}\sqrt{\xi\rho^{-1}\langle p_o - \mathcal{R}_{cr}\rangle}. \tag{3.37}$$

This transition void size is presented in Fig. 3.6 as a function of the mobile dislocation density for two different overpressures. The lines for each overpressure separate out the domains where the dislocation dynamics dominates ($\mathcal{R}^{v_\perp}_{dd} > \mathcal{R}^{\rho}_{ss}$) or the micro-inertia dominates ($\mathcal{R}^{\rho}_{ss} > \mathcal{R}^{v_\perp}_{dd}$). Notice that dislocation dynamics governs the dynamics of void growth of small voids with lower mobile dislocation densities. On the other hand, micro-inertia dominates for larger voids with larger mobile dislocation densities.

Returning to the spherical shell shown in Fig. 3.3, we now consider the instantaneously applied pressure to be balanced by the total resistance, i.e. $p_o = \mathcal{R}_{cr} + \mathcal{R}^{v_\perp}_{dd} + \mathcal{R}^{\rho}_{tr} + \mathcal{R}^{\rho}_{ss}$ as in Eq. (3.27). Assuming a spatial distribution of the mobile dislocation density characterized by $\eta = -3$, we present numerical solutions of the full Eq. (3.27) in terms of the void surface velocity (void growth rate) as a function of the void size in Fig. 3.7(a) for several initial void sizes (the blue, red and green curves). Following a brief (size-dependent) transient period, the void growth rates

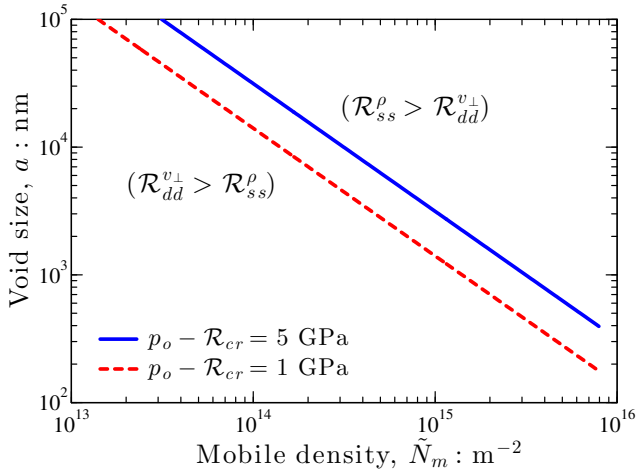

Fig. 3.6: A map demonstrating the division between the dislocation dynamics dominated regime ($\mathcal{R}^{v_\perp}_{dd} > \mathcal{R}^{\rho}_{ss}$) and the micro-inertia dominated regime ($\mathcal{R}^{\rho}_{ss} > \mathcal{R}^{v_\perp}_{dd}$).

quickly approach the upper bound expressed in Eq. (3.36) and shown here by the black curve. In the dislocation-dynamics-dominated regime the void velocity is linearly proportional to the current void size. The void growth then transitions into the micro-inertia-dominated regime and quickly achieves a steady state velocity governed by Eq. (3.35). The transition between the two regimes occurs at $a \sim 400$ nm, roughly in accordance with Eq. (3.37). The void velocities in the dislocation dynamics dominated regime are approximately 20% slower than the upper bound expressed by Eq. (3.36). This is due to the additional resistance associated with dislocation drag that is important for $\eta = -3$ but not accounted for in Eq. (3.36).

To better understand the competition between these resistance terms, we examine the contribution of each independent resistance term to the overall supercritical resistance ($\mathcal{R}^{v_\perp}_{dd} + \mathcal{R}^{\rho}_{tr} + \mathcal{R}^{\rho}_{ss}$) for voids of different initial sizes. Fig. 3.7(b) shows the fractional resistance breakdown for the $A = 10$ nm void as a function of the current

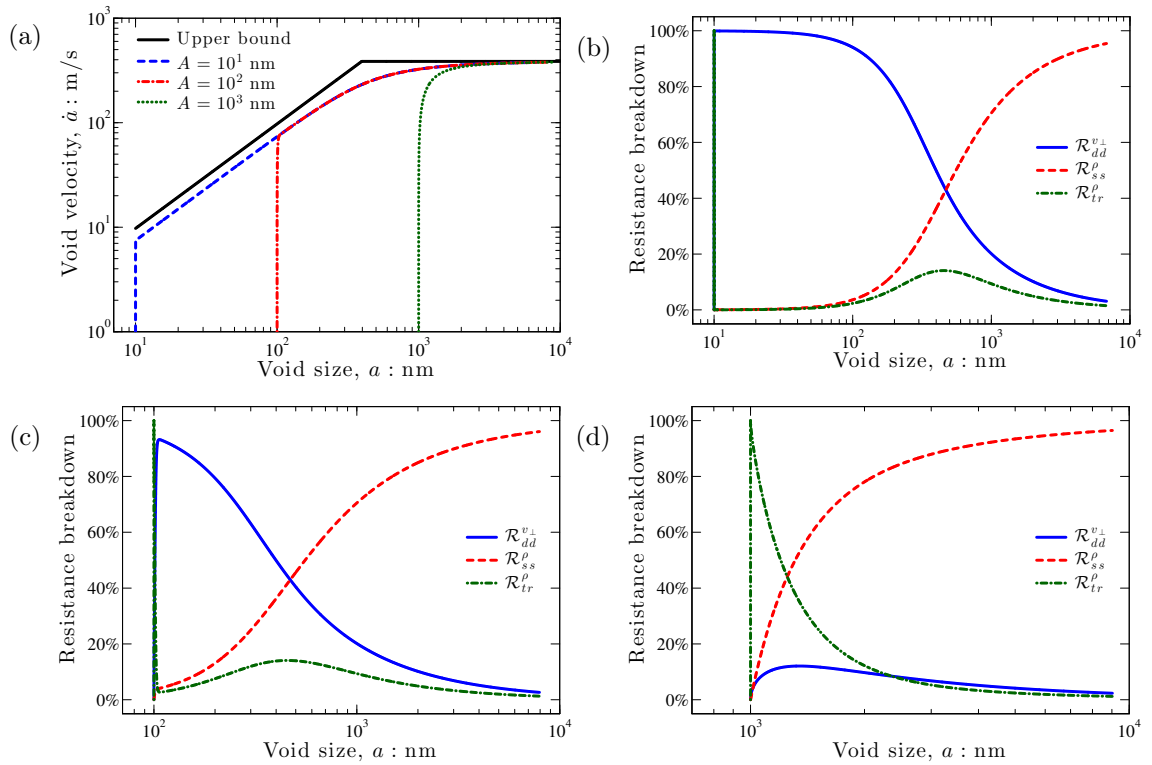

Fig. 3.7: (a) Evolution of void velocity resulting from the application of an instantaneous far-field pressure $p_o - \mathcal{R}_{cr} = 2$ GPa. Evolution of resistance breakdown for three initial void sizes: (b) $A = 10$ nm, (c) $A = 100$ nm, and (d) $A = 1$ μm. ($\tilde{N}_m = 5 \times 10^{15}$ m^{-2}; $\eta = -3$).

void size. The green line represents the transient inertial resistance, the red line is the steady state inertial resistance, and the blue line shows the dislocation dynamics resistance. For this very small initial void, there is an extremely brief period (the initial green spike) where the transient resistance constrains the void growth. Following this, the dynamics are governed mostly by the constraints imposed by dislocation kinetics. Then micro-inertia takes over as the dominant mechanism when the void size reaches about 400 nm, roughly in accordance with Eq. (3.37). The fractional breakdown for the $A = 10^2$ nm void is shown in Fig. 3.7(c) . Here the transient pe-

riod lasts slightly longer due to the larger initial void size. Dislocation dynamics then becomes the dominant resistance until the void grows to the transition size, following which micro-inertia takes over as the dominant resistance. Similarly, Fig. 3.7(d) shows the fractional breakdown for the $A = 1$ μm void. Since this void is larger than the transition void size, dislocation dynamics never plays a dominant role. Instead, the dynamics of these micron-sized voids (with large mobile dislocation densities) are governed almost entirely by micro-inertia.

Recall that the results shown in Fig. 3.7 are for a particular spatial distribution of the mobile dislocation density ($\eta = -3$). We now consider a typical case where $\eta \nsim -3$ (specifically $\eta = 0$). In this case Fig. 3.8(a) shows that the void velocities in the dislocation dynamics dominated regime are well approximated by the upper bound. This is associated with the dislocation dynamics resistance being largely governed by relativistic dislocations near the void surface for $\eta \nsim -3$. Recall that for $\eta \nsim -3$, $\mathcal{R}_{dd}^{v_\perp}$ is well approximated by $\mathrm{H}^\infty\langle \tilde{v}_\perp - c_s \rangle$. The contributions of the various resistance terms are shown in Fig. 3.8(b) for $\eta = 0$ and for the $A = 10$ nm void. Here the transition between micro-inertia dominant and dislocation dynamics dominant regimes is much steeper than in Fig. 3.7(b). Larger values of η result in even steeper transitions between regimes. Also note that the small discrepancy between the upper bound and the computed void dynamics shown in Fig. 3.8(b) is associated with $\mathcal{R}_{tr}^{\rho} \neq 0$ in the transition regime where $\ddot{a} \neq 0$. It is interesting to observe that typically either micro-inertia is dominant or dislocation dynamics is dominant, but they tend

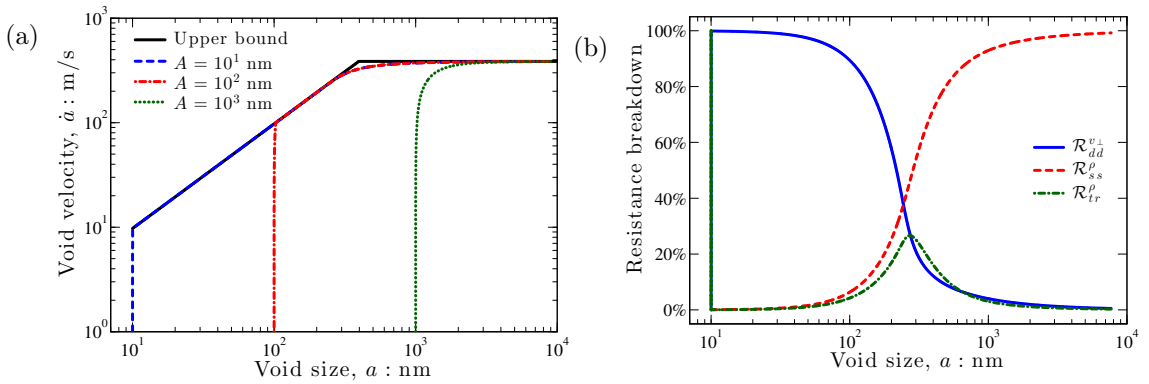

Fig. 3.8: (a) Evolution of void velocity resulting from the application of an instantaneous far-field pressure $p_o - \mathcal{R}_{cr} = 2$ GPa. (b) Evolution of resistance breakdown for $A = 10$ nm. ($\tilde{N}_m = 5 \times 10^{15}$ m^{-2}; $\eta = 0$).

not to cooperatively constrain void growth at the same time. This contributes to the agreement of Eq. (3.36) with the computed void dynamics presented in Fig. 3.8(a). It may be possible to observe many of the characteristic features of Fig. 3.8(a) *in situ* with a dynamic TEM.

3.5.3 Influence of dislocation substructure evolution on void dynamics

We now consider the added complexity of an evolving dislocation substructure around a dynamically growing void. Extremely high dislocation densities have been observed in the vicinity of deformed voids Lubarda et al. [65]. The critical question here is, what proportion of this high dislocation density is mobile? At high dislocation densities, the mean free path between (trapping) forest dislocations is very small. Thus, mobile dislocations may only glide a very short distance before becom-

ing immobilized. The consequence of this is that at some point in the deformation the population of mobile dislocations may collapse and thereby substantially limit the void growth rates.

The immobile and mobile dislocation densities evolve non-linearly with deformation according to the substructure evolution equations presented in section 3.3. Numerical evaluations of the mobile dislocation density evolution (Eq. (5.18) – Eq. (3.10); Eq. (3.21)) are shown in Fig. 3.9(a) which shows the mobile dislocation density at the surface of the void (initial void size $A = 10$ nm) as a function of the relative void size for three different initial immobile dislocation densities. In all cases, the mobile dislocation density first increases with plastic deformation due to multiplication; however, at some point ($a/A \sim 10 - 100$) the mobile dislocation density collapses. This collapse is associated with the immobile dislocation density growing to such large values that trapping of mobile segments by the forest network overtakes the multiplication mechanism, i.e. $\dot{N}_{trap} >> \dot{N}_{mult}$. Collapse of the curves thus occurs earlier for larger initial immobile dislocation densities. Recalling the linear relationship between $\tilde{N}_m$ and the maximum void velocity ($\dot{a} < ab\tilde{N}_m c_s/3$), it is clear that this collapse in mobile dislocation density will give rise to a corresponding collapse in the void velocity.

To see this, consider again the spherical shell shown in Fig. 3.3, with the instantaneously applied pressure balanced by both non-inertial and inertial resistance, i.e. $p_o = \mathcal{R}_{cr} + \mathcal{R}_{dd}^{v_\perp} + \mathcal{R}_{tr}^{\rho} + \mathcal{R}_{ss}^{\rho}$, but now we permit the dislocation substructure to evolve

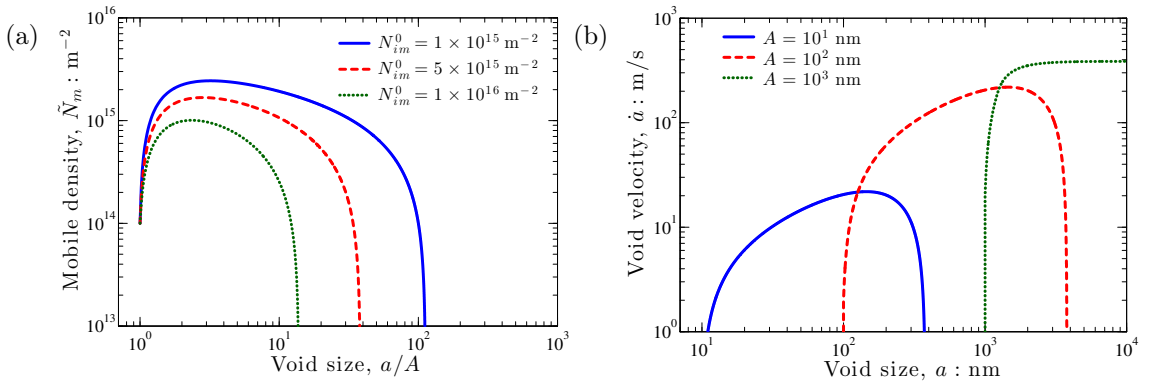

Fig. 3.9: (a) Evolution of mobile dislocation density at the void surface ($\tilde{N}_m$) with deformation. (b) Evolution of void velocity resulting from the application of an instantaneous far-field pressure $p_o - \mathcal{R}_{cr} = 2.0$ GPa with $N^0_{im} = 5 \times 10^{15}$ m^{-2}. ($N^0_m = 10^{14}$ m^{-2}; $\eta_0 = 0$).

with deformation, i.e. $\dot{N}_m \neq 0; \dot{N}_{im} \neq 0$. We show in Fig. 3.9(b) the computed void dynamics resulting from the application of an instantaneous, constant over-pressure ($p_o - \mathcal{R}_{cr} = 2.0$ GPa) for three initial void sizes. Consider first the dynamics of the $A = 10$ nm void shown in Fig. 3.9(b). Initially, the behavior is similar to the constant substructure behavior shown in Fig. 3.7(a), with the void velocity increasing with void size. However, unlike the behavior shown in Fig. 3.7(a), the void velocity is not linearly proportional to the void size since the mobile dislocation density also evolves with plastic deformation. After sufficient deformation ($a/A \sim 30$) the void velocity collapses in accordance with the collapse in mobile dislocation density shown in Fig. 3.9(a). The consequence of this collapse in the void velocity due to evolving substructure is essentially an upper bound on the maximum growth factor ($a/A \lesssim 10 - 100$) that can be achieved by dynamically growing voids. For the $A = 100$ nm void, the dynamics shown in Fig. 3.9(b) are similar to those of the smaller

void. The void dynamics of these sub-micron voids are governed nearly entirely by dislocation dynamics. Notice that the transition void size (see Fig. 3.6) is about a micron when the mobile dislocation density achieves its maximum value. Therefore, the largest void size considered in Fig. 3.9(b) ($A = 1$ μm) experiences void dynamics governed instead by micro-inertia. Notice that the void velocity quickly achieves the constant steady state value governed by Eq. (3.35).

We now re-examine the transition void size (Fig. 3.6) that divides the dislocation dynamics dominated regime ($\mathcal{R}_{dd}^{v_\perp} > \mathcal{R}_{ss}^{\rho}$) from the micro-inertia dominated regime ($\mathcal{R}_{ss}^{\rho} > \mathcal{R}_{dd}^{v_\perp}$) for the more general problem with evolving substructure. The variable that was plotted on the horizontal axis of Fig. 3.6 ($\tilde{N}_m$) is now a function of the void growth factor (a/A) as shown by Fig. 3.9(a). In Fig. 3.10 we have replaced the horizontal axis of Fig. 3.6 with the growth factor (a/A) and re-computed the transition void sizes for $p_o - \mathcal{R}_{cr} = 2$ GPa for several initial immobile dislocation densities. For relatively small growth factors $a/A \lesssim 10$ the transition void size is about $1 - 3$ microns depending on the magnitude of the initial immobile dislocation density. However, as the mobile dislocation density collapses at large deformation, the transition void size substantially increases. At this point, the low mobile dislocation density does not permit further growth regardless of the void size.

It is now worth revisiting the approximation on the dislocation dynamics resistance term, i.e. $\mathcal{R}_{dd}^{v_\perp} \approx \mathrm{H}^{\infty}\langle \tilde{v}_\perp - c_s \rangle$. In subsection 3.5.1 we established that the accuracy of the approximation depends on the particular distribution of the mobile dislocation

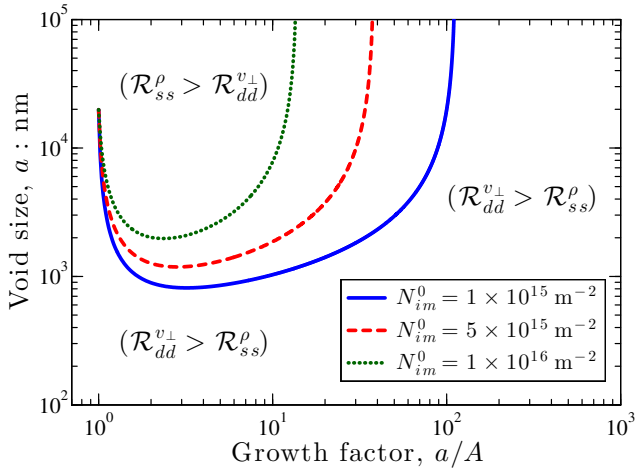

Fig. 3.10: A map demonstrating the division between the dislocation dynamics dominated regime ($\mathcal{R}^{v_\perp}_{dd} > \mathcal{R}^{\rho}_{ss}$) and the micro-inertia dominated regime ($\mathcal{R}^{\rho}_{ss} > \mathcal{R}^{v_\perp}_{dd}$) for $p_o - \mathcal{R}_{cr} = 2.0$ GPa. ($N^0_m = 10^{14}$ m^{-2}; $\eta_0 = 0$).

density. If the mobile density decays cubically with distance from the void surface ($\eta = -3$) then $\mathrm{H}^{\infty}\langle \tilde{v}_\perp - c_s \rangle$ under-predicts $\mathcal{R}^{v_\perp}_{dd}$. However, if the mobile density decays weaker than cubic (or increases) with distance from the void surface then $\mathrm{H}^{\infty}\langle \tilde{v}_\perp - c_s \rangle$ is an excellent approximation to $\mathcal{R}^{v_\perp}_{dd}$. The question now is, does the spatial distribution of the mobile dislocation density evolve in such a way as to permit this approximation on $\mathcal{R}^{v_\perp}_{dd}$? This approximation substantially reduces the computational cost associated with computing the void dynamics, because spatial discretization is no longer required, and the problem effectively reduces to a set of non-linear ordinary differential equations.

The evolving spatial distributions of the mobile dislocation density around a growing void are shown in Fig. 3.11(a) and Fig. 3.11(b) for two different initial mobile dislocation densities (greater in Fig. 3.11(b)). We see that the non-linear evolution

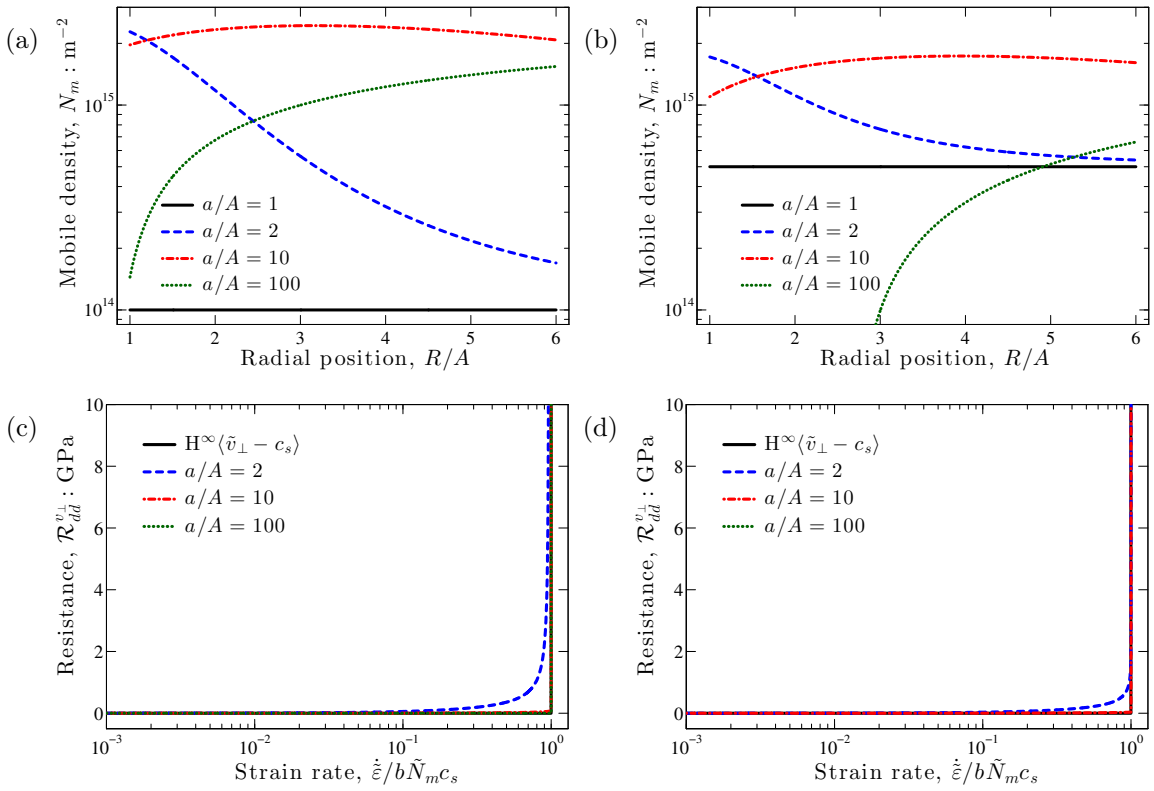

Fig. 3.11: Evolution of spatial distribution of mobile dislocation density as a function of deformation, a/A, for (a) $N_m^0 = 10^{14}$ m^{-2} and (b) $N_m^0 = 5 \times 10^{14}$ m^{-2}. Associated evolution of $\mathcal{R}_{cr}$ as a function of deformation, a/A, for (c) $N_m^0 = 10^{14}$ m^{-2} and (d) $N_m^0 = 5 \times 10^{14}$ m^{-2}. ($N_{im}^0 = 10 \times N_m^0$; $\eta_0 = 0$).

of the mobile dislocation density leads to a complex and changing spatial dependence of the dislocation density as the void grows (that is, as a/A increases). As shown in Fig. 3.11(a), the mobile dislocation density first ($a/A \sim 1 - 3$) decays spatially, in a similar manner to the cases of $\eta \sim -2$ to $\eta \sim -3$. In accordance with the earlier observations, such a spatial decay causes the dislocation velocity to be nearly constant throughout the spherical shell, and thus not entirely dominated by the relativistic behavior on the surface of the void. Therefore, within this deformation regime ($a/A \sim 1 - 3$) the dislocation dynamics resistance term $\mathcal{R}_{dd}^{v_\perp}$ is somewhat underesti-

mated by the closed-form lower bound $\mathrm{H}^{\infty}\langle\tilde{v}_{\perp} - c_s\rangle$, see Fig. 3.11(c). On the other hand, outside of this regime ($a/A \gtrsim 3$) the lower bound $\mathrm{H}^{\infty}\langle\tilde{v}_{\perp} - c_s\rangle$ approximates the dislocation dynamics resistance term $\mathcal{R}_{dd}^{v_{\perp}}$ extremely well, see Fig. 3.11(c). This is governed by the change in the spatial distribution of the mobile dislocation density. After sufficient deformation ($a/A \sim 3 - 5$) the mobile dislocation density is nearly spatially constant, i.e. $\eta \sim 0$, and further deformation results in a complete reversal of the spatial distribution, with N_m actually increasing with distance from the surface of the void, i.e. $\eta > 0$. As was discussed in detail in subsection 3.5.1, these spatial distributions cause the dislocation dynamics resistance to be dominated by the relativistic behavior of dislocations near the surface of the void, and hence the excellent agreement with the approximation. The agreement is even better for materials with higher initial immobile dislocation densities due to shorter mean free paths and enhanced trapping rates. This can be seen by comparison of Fig. 3.11(c) with Fig. 3.11(d). Therefore, $\mathcal{R}_{dd}^{v_{\perp}} \approx \mathrm{H}^{\infty}\langle\tilde{v}_{\perp} - c_s\rangle$ is perhaps most accurate and useful in problems involving shock compression (producing high initial immobile dislocation densities) prior to dynamic void growth, such as in the spall failure problem.

3.5.4 Characteristics of void size distributions

Currently, there are a limited set of experimental observations that may be utilized to validate dynamic void growth models (*in situ* observations of dynamic void growth rates would be ideal for these purposes). Lacking these *in situ* observations,

we must resort to *post-mortem* observations of the void size distributions to provide some measure of model validation. Through extensive fractographic analysis of aluminum and copper spall surfaces, Seaman et al. [112] observed that regardless of the extent of damage the void size distribution was well approximated by the exponential distribution

$$\zeta(a) = \frac{1}{\bar{a}} \exp\left(-\frac{a}{\bar{a}}\right), \tag{3.38}$$

where $\bar{a}$ is the associated mean void radius. It is beyond the scope of the current chapter to address how this particular distribution arises from the underlying microstructure. However, an interesting consequence of Seaman et al. [112]'s observation is that the void size distribution maintains its general shape regardless of the extent of deformation. An implication of this observation is that dynamic void growth may, to some degree, be self-affine. In other words, two arbitrary voids of different initial size, i.e. A_j and A_k, will differ in size by about the same factor after an arbitrary amount of deformation, i.e. $a_j/a_k \approx A_j/A_k$. It will be shown here that dynamic void growth governed only by micro-inertia is not consistent with this observation. In contrast, dynamic void growth governed by dislocation dynamics does possess this characteristic.

We first attempt to obtain an analytic expression for the void size history when the problem is governed by dislocation dynamics. Utilizing the approximations discussed in subsection 3.5.3, the set (Eq. (5.18) – Eq. (3.10); Eq. (3.27); Eq. (3.28)) of second-order integro-differential equations is effectively reduced to a set of first-order ordinary

differential equations:

$$\begin{cases} \dot{a} = \frac{1}{3} a b \tilde{N}_m c_s \\ \\ \tilde{N}_m = \langle \tilde{N}_m^0 + g(\varepsilon) \rangle, \end{cases} \tag{3.39}$$

where $\varepsilon = 3\ln(a/A)$ as before, and $g(\varepsilon)$ is the function that describes the change in mobile dislocation density with deformation. If the immobile dislocation density is much greater than the mobile dislocation density, then the rate of trapping will far exceed the rate of dislocation annihilation, i.e. ($\dot{N}_{trap} >> \dot{N}_{ann}$). Under these circumstances $g(\varepsilon) \approx c_1\varepsilon + c_2\varepsilon^2$ is consistent with the dislocation density evolution equations discussed in section 3.3, and it may be shown that $bc_1 = \delta_{mult} - \alpha_{dis}\sqrt{\tilde{N}_{im}^0}$ and $c_2 = -(\alpha_{dis}/2b)^2$. With this approximation to $g(\varepsilon)$, an analytic solution to Eq. (3.39) is obtained as

$$a = A \times \exp\left(\frac{\tilde{N}_m^0}{-\frac{3}{2}c_1 + 3c_3 \coth bc_s c_3 \langle t - t_{cr} \rangle} \right) \tag{3.40}$$

where $p_o > \mathcal{R}_{cr}$ for $t > t_{cr}$ and $c_3 \triangleq \sqrt{c_1^2/4 - \tilde{N}_m^0 c_2}$. Eq. (3.40) makes clear that dynamic void growth governed by dislocation dynamics alone is indeed self-affine. That is, voids of all size will experience the same growth factor (a/A) regardless of the initial void size. On the other hand, if the void dynamics where governed only by micro-inertia, then all voids would quickly become approximately the same size. This is apparent from Fig. 3.12(a), where numerical solutions of Eq. (3.27) are provided for $p_o - \mathcal{R}_{cr} = 2$ and $\mathcal{R}_{dd}^{v_\perp} = 0$. Over the course of a few nanoseconds, voids that initially differed in size by orders of magnitude become nearly identical in size (a similar result was pointed out by Wu et al. [90]). This is particularly true

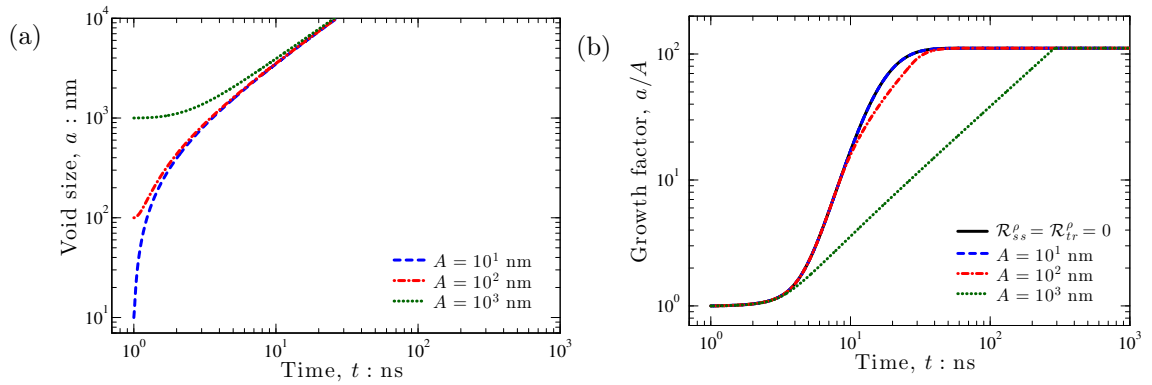

Fig. 3.12: Dynamics of void growth (a) governed by micro-inertia alone, i.e. $\mathcal{R}^{v_\perp}_{dd} = 0$, and (b) governed by both micro-inertia and dislocation kinetics. ($p_o - \mathcal{R}_{cr} = 2.0$ GPa for $t > 1$ ns; $N^0_m = 10^{14}$ m^{-2}; $N^0_{im} = 10^{15}$ m^{-2}; $\eta_0 = 0$)

of sub-micron voids. In contrast, when both micro-inertia and dislocation dynamics are relevant (Fig. 3.12(b), with $\mathcal{R}^{v_\perp}_{dd} \neq 0$), the void growth factors a/A are distinctly different functions of time for different initial void sizes. The solid line in Fig. 3.12(b) shows the evolution of the growth factor (a/A) without accounting for micro-inertia, consistent with Eq. (3.40). Clearly, micro-inertia may be neglected all together when analyzing voids that are initially tens of nanometers or smaller, because these voids are dominated by dislocation dynamics throughout their entire growth history. This is important because Reina et al. [69] have proposed that vacancy clusters in this size range may be critical to spall failure at extreme rates. The dynamic growth of these vacancy clusters may be well approximated by Eq. (3.40) (or more generally Eq. (3.39) for alternative dislocation density evolution models).

The vertical axis of Fig. 3.12(b) is plotted as the growth factor (a/A) in order to highlight the self-affinity characteristics. It is interesting to observe that there are regions where the dynamics are self-affine and other regions where they are not

self-affine. These regions are consistent with the mechanism map shown in Fig. 3.10. The void dynamics of the two smallest voids considered (10 and 100 nm) are initially smaller than the minimum transition void size ($\sim$ 700 nm), see Fig. 3.10. The voids are therefore initially governed by dislocation dynamics, and self-affinity is observed. At some point the 100 nm void becomes larger than the transition size. At this point the dynamics of the 100 nm void are now governed by micro-inertia and self-affinity is lost. The 1 μm void was initially larger than the transition size, and thus begins its growth in the micro-inertia dominated regime. Eventually the mobile dislocation density collapses at large growth factors and void growth shuts down. This collapse of the mobile dislocation density is independent of the initial void size and only depends on the growth factor. These results indicate that when both micro-inertia and dislocation dynamics are accounted for then some degree of self-affinity is predicted, and it is dependent on extent of deformation, the initial void sizes, and the initial immobile dislocation density. It should be possible to observe this characteristic through fractographic analysis of spall surfaces. The growth factor a/A of voids that nucleated from second-phase particles may be approximated by the ratio of void dimple diameter to particle diameter. According to the current analysis, this ratio should be smaller than about $10-100$ regardless of particle size. This ratio may also be dependent on the magnitude of the compressive shock stress. Higher shock stresses would generate higher immobile dislocation densities, which should result in smaller growth factors and smaller dimple-particle size ratios, see Fig. 3.9(a).

Although inertia-dominated void growth is observed in some low-rate spall experiments, as discussed by Wu et al. [91], the very high-strain rate experimental observations of Moshe et al. [113] are inconsistent with this void size characteristic of micro-inertia dominated void growth. The spall surface of copper obtained in laser shock experiments was presented by Moshe et al. [113] and is reproduced here in Fig. 3.13(a). Experimentally the void sizes in Fig. 3.13(a) differ by up to two orders of magnitude, i.e. $a \sim 100\text{nm} - 10\mu\text{m}$. A quantitative comparison of our predicted and measured void size distributions is presented in Fig. 3.13(b); where we have seeded the material with the exponential void size distribution suggested in Seaman et al. [112], i.e. Eq. (3.38). We find that an initial mean void size of $\bar{A} = 100$ nm results in predicted mean void sizes similar to those of Fig. 3.13(a). An initial mean void size of 100 nm is assumed to correspond with the size distribution of second-phase particles and vacancy clusters from which voids nucleate. After application of a constant over-

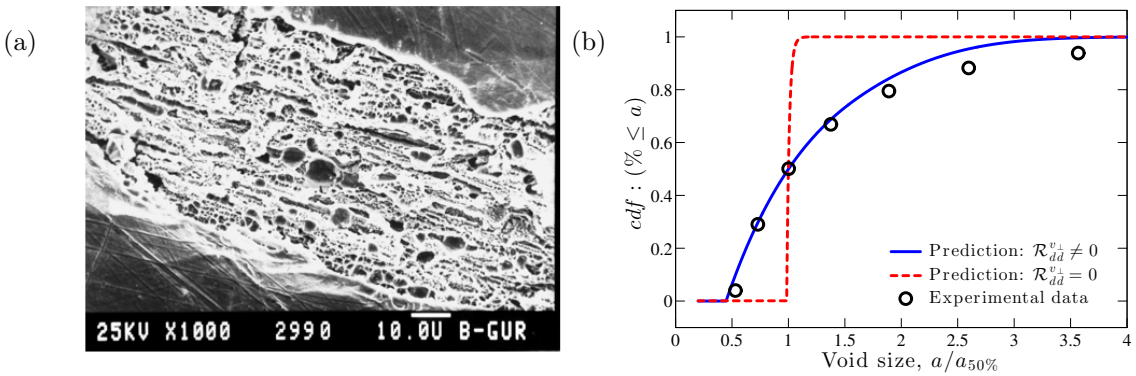

Fig. 3.13: (a) Spall fracture surface reported in Moshe et al. [113] showing final void sizes ranging from $a \sim 100\text{nm} - 10\mu\text{m}$. (b) Comparison of experimentally observed void distribution to theoretical predictions. ($p_o - \mathcal{R}_{cr} = 2.0$ GPa; $N_m^0 = 1 \times 10^{14}$ m^{-2}; $N_{im}^0 = 1 \times 10^{15}$ m^{-2}; $\eta_0 = 0$).

pressure $p_o - R_{cr} = 2.0$ GPa for a duration of 5 ns (approximate over-pressure and pulse duration associated with laser-induced shock compression), the predicted void size cumulative distribution functions are plotted in Fig. 3.13(b) for both the purely inertial resistance case and the full resistance case. Notice that the void size distribution predicted by micro-inertia dominated void growth ($\mathcal{R}_{dd}^{v_\perp} = 0$) has collapsed into essentially a Delta function centered around the average void size, i.e. $a \sim a_{50\%}$. However, accounting for dislocation kinetics results in the void size distribution maintaining its broad shape characterized by the exponential distribution, in accordance with the claims of Seaman et al. [112]. For comparison, we have used image processing techniques to extract the void size distribution associated with the spall surface shown in Fig. 3.13(a). Also for comparison purposes, we have removed all voids smaller than 200 nm from the predicted distribution, because these voids are not observable at the particular magnification of the SEM image shown in Fig. 3.13(a). The correlation between the experimental void size distributions and our predicted void size distribution (with both micro-inertial and dislocation dynamics resistances) is quite satisfactory, particularly given the uncertainties in the precise initial void sizes and the experimental loading conditions within these complex experiments. The comparison shown in Fig. 3.13(b) clearly demonstrates the need to account for both dislocation drag and relativistic effects in future dynamic void growth and high strain rate ductile failure models for such very high strain rate applications.

3.6 Summary of key findings

We have examined the consequences of dislocation kinetics and substructure evolution on dynamic void growth under very high strain rates, and we have developed a methodology for accounting for these effects in a computationally efficient manner. It was shown that dislocation kinetics and micro-inertia are both important to dynamic void growth and high strain rate tensile failure. Models need to account for both of these phenomena. We have described a simple approach for accounting for both in an efficient manner.

It was shown that while micro-inertia governs the growth of voids larger than about a micron, smaller voids in most metals are instead governed by dislocation kinetics at these very high strain rates. In particular, the relativistic constraint that dislocations must glide at speeds slower than the wave speed is significant. For many loading conditions the void dynamics are well approximated by the simple relation reported in Eq. (3.36), which is most accurate for voids that are initially sub-micron and have high initial immobile dislocation densities. This approximation substantially reduces the costs associated with accounting for dislocation dynamics and void dynamics in high strain rate-ductile failure modeling.

This study sheds light on a few key experimental observations related to the dynamic tensile failure of metals. First, the current analysis discusses a mechanism (relativistic dislocation drag) that may account for the dramatic change in spall strength rate-sensitivity observed by Moshe et al. [99]. It is likely that all ductile metals will

exhibit this behavior to some degree. Second, we briefly discuss the anomalous temperature dependence of spall strength observed by Kanel et al. [100]. We find that the temperature dependence of the dislocation drag coefficient is relatively unimportant, but the temperature dependence of the wave speed may give rise to an anomalous temperature dependence of spall strength at extreme strain rates. The kinetics of vacancy clustering further complicates matters, and likely results in the temperature dependence being a function of the purity level of the metal. Third, we have discussed some features that are observable through fractographic analysis of the spall surface. The current model predicts a broad distribution of void sizes on the spall surface under some conditions, similar to the experimental observations shown in Fig. 3.13(a). Furthermore, the model predicts that for voids that nucleate from second-phase particles there should be some upper limit on the ratio of dimple size to particle diameter, as demonstrated in Fig. 3.12(b).

Chapter 4

A criterion for dislocation emission in porous materials

In chapter 3 we explored the role that dislocation kinetics and substructure evolution play in constraining the rate of void growth. It was shown that (under very high tensile stresses) void growth rates are highly constrained by the effects of relativistic dislocation drag. In chapter 5 we will explore the consequences of these constrained void growth rates on the spall response of ductile FCC metals. However, as spall response is governed by both void nucleation and void growth, it is first necessary to build upon the current level of understanding regarding void nucleation, in particular at very high tensile stresses. The traditional view of void nucleation is associated with interface debonding at second-phase particles. Here, we motivate an alternative mechanism, namely vacancy clustering followed by void growth governed by dislo-

cation emission. This mechanism only becomes active at very large tensile stresses, and thus it is desirable to establish a closed-form criterion for the macroscopic stress required to activate this mechanism in porous materials. This chapter provides an analysis of dislocation emission from which such a critical stress criterion is derived. This criterion is validated against a number of molecular dynamics simulations.

4.1 Introduction and background

Failure of ductile metals has long been attributed to the microscopic processes of void nucleation, growth, and finally coalescence leading to fracture [52–56]. Some of the earliest investigations regarded void nucleation as a cavitation instability in an otherwise homogeneous elastic-perfectly plastic [57, 58], non-linear elastic [59], or power-law hardening medium [60]. However, these types of continuum analyses fail to predict bifurcation and spontaneous nucleation when surface energy is properly accounted for [69]. The more accepted view of void nucleation is that it occurs at some material defects. Traditionally, these void nucleating material defects have been associated with second-phase particles [71, 72]. For example, hard inclusions, such as carbide and oxide particles, may either crack or debond from the ductile metal matrix, see [73–75]. Voids have also been seen to nucleate within soft inclusions, e.g. sulfides [76]. However, much of this understanding of void nucleation at second-phase particles has been gleaned from observations of quasi-static fracture surfaces. At high

enough tensile stresses, e.g. levels achievable in laser shock experiments and related applications, second-phase particles may not necessarily be the dominant source of void nucleating material defects, and the recent observations of Pedrazas et al. [114] seem to support this assertion.

A number of investigators have hypothesized the existence of nanoscale voids (on the order of 1 nm in size) in shocked metals, see for example [65, 115]. Vacancy clustering is one potential mechanism for the formation of these nanovoids. Reina et al made use of lattice kinetic monte carlo simulations to demonstrate that the timescales associated with this process are in fact feasible (see section 4.2). Assuming the existence of these nanovoids, numerous atomistic studies have computed the level of tensile stress ($\sim \mu/10$) required to effectively grow these voids by emitting dislocation loops from the void surface [62–64, 66–68, 70, 115]. These levels of tensile stresses ($\sim \mu/10$) have been achieved in a number of laser shock experiments, e.g. reports of [98, 99, 114] reproduced here in Fig. 3.1(a), implying that such dislocation emission may be an important mechanism of void growth at these extreme loading rates. Given the potential importance of this mechanism, it is desirable to establish a closed-form criterion for the macroscopic stress required for dislocation emission in porous materials.

Through a simple dislocation analysis, Lubarda et al. [65] derived such a closed-form criterion for the critical far-field hydrostatic stress required to emit a straight edge dislocation from an infinitely extended cylindrical void in an otherwise homo-

geneous, linearly elastic, isotropic infinite medium. Although this analysis does not capture the actual geometry associated with the physical problem of interest, i.e. dislocation loops emitted from a spherical void in an anisotropic medium, favorable comparisons with atomistic simulations demonstrated the utility of such an analysis. Recently, Lubarda [11] extended this analysis to account for a far-field biaxial stress state, further increasing the utility of the theoretical model. In order to make the criterion more useful for the continuum level prediction of dynamic ductile failure (the focus of chapter 5), we provide a number of further extensions to the analysis of Lubarda [11] accounting for the following:

- a general three-dimensional macroscopic stress state, $\mathbf{\Sigma}$
- a particular void size distribution, $g(a)$
- finite porosity, φ
- finite surface energy, γ_{se}
- a temperature- and pressure-dependent shear modulus, μ
- a temperature-dependent dislocation core size, $w_{\perp}$.

The present chapter is organized as follows. Section 4.2 provides further motivation for the role of vacancy clustering and subsequent dislocation emission in the dynamic failure of metals at extreme strain rates ($\gtrsim 10^6$ s^{-1}). In section 4.3, we approximate the stress fields and Peach-Koehler forces experienced by a dislocation near

a void surface in a porous material. Here the porous material is composed of a particular void size distribution $g(a)$ with an associated finite porosity φ, and is subject to a general three-dimensional stress state. Our strategy involves the construction of an auxiliary problem associated with this physical problem, but simple enough to analytical solutions. These Peach-Koehler forces are then utilized in section 4.4 to establish a criterion for dislocation emission based on the stability arguments first proposed by Rice and Thomson [116] (placed in a somewhat more physical context here). Section 4.4 also provides a rather detailed discussion of the role of various parameters and physics on the criterion for dislocation emission. In section 4.5 we provide a fairly extensive validation of the emission criteria against molecular dynamics predictions of dislocation emission under various stress states and geometries. In addition to the validation effort, we provide a strategy for approximately calibrating the dislocation emission criterion parameters against atomistic calculations of homogeneous dislocation nucleation. Having calibrated and to some degree validated our emission criterion, we utilize the criterion in section 4.6 to predict some interesting anomalous behaviors associated with high surface energies and nonlinear stiffness. Lastly, a brief summary of the key findings is provided in section 4.7.

4.2 Motivating the role of vacancy clustering and subsequent dislocation emission in extreme dynamic failure

Pedrazas et al. [114] performed a number of laser shock experiments to measure the spall response of aluminum at very high strain rates ($\sim 2 - 4 \times 10^6$ s^{-1}) as a function of microstructure and purity level, i.e. an aluminum alloy containing 3 wt% magnesium, a 99% commercially pure aluminum, and a 99.999% high purity aluminum. One interesting observation from this set of experiments was that the highest purity aluminum exhibited the highest spall strength ($\sim 3-4$ GPa), with the aluminum-magnesium alloy exhibiting the lowest spall strength ($\sim 2 - 3$ GPa). Of course, the opposite trend is associated with yield strength of these materials. This somewhat non-intuitive inverse relationship between spall strength and the impurity content may be attributed to a larger population of void nucleating second-phase particles, and is explored in much greater detail in chapter 5.

In examining the spall fracture surface of the commercially pure aluminum under scanning electron microscopy (SEM), reproduced here in Fig. 4.1(a), Pedrazas et al. [114] clearly show the correlation between the spacing of second-phase particles and voids. However, this relationship vanishes in the case of the 99.999% high purity aluminum with the SEM images (Fig. 4.1(b)) revealing second-phase particles within

(a) 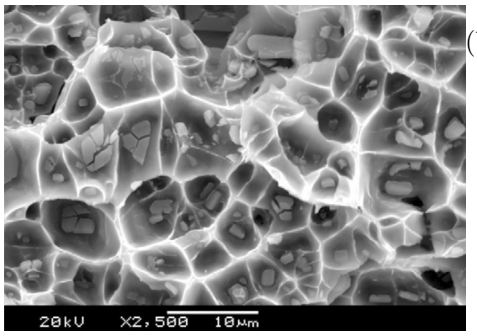

(b) 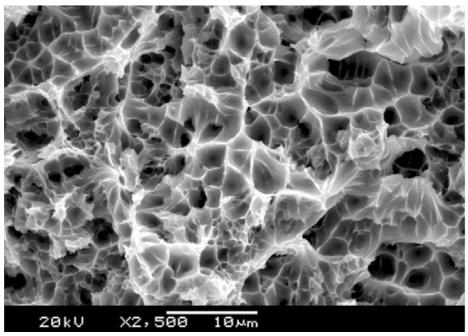

Fig. 4.1: SEM images of spall fracture surfaces reported in [114] for (a) a 99% commercially-pure aluminum and (b) a 99.999% high-purity aluminum. Most of the voids in the commercially-pure aluminum shown in (a) nucleate from second-phase particles, e.g. Al_3Fe, where as for the high-purity aluminum only a very small fraction of the dimples (∼5%) contained second-phase particles, implying that the bulk of these voids nucleate by an alternative mechanism, e.g. vacancy clustering and subsequent growth by dislocation emission.

the centers of only a very small fraction of the dimples (∼5%). The bulk of the voids (∼95%) must have nucleated from some material defect that is not visible at these particular resolutions (∼100 nm). One potential source is simply nucleation from a distribution of fine-scale second-phase particles and precipitates with sizes ranging from perhaps a few nanometers to less than ∼100 nm. Through a more detailed microscopy analysis at higher magnifications it may be possible to determine if the voids shown in Fig. 4.1(b) do in fact nucleate from such fine-scale second-phase particles. However, these fine-scale precipitates often have coherent interfaces that are extremely resistant to debonding. An alternative source of these void nucleating material defects is associated with the clustering of vacancies.

Extreme dynamic ductile failure, e.g. spall failure, is most often preceded by an intense shock wave that generates a preponderance of defects in the material. Inter-

secting dislocations may produce a large number of jogs, which when dragged along the glide plane (as a result of the associated high shear stresses in the shock front) contribute to a nonequilibrium superconcentration of vacancies c_v^{ne}, which may be approximated by the following phenomenological relationship [117–120]:

$$c_v^{ne} = A_v \varepsilon^p + \exp \frac{-E_v^f}{k_b \vartheta}, \tag{4.1}$$

where ε^p is the accumulated plastic strain, and $A_v \sim 10^{-4}$ is a fitting parameter obtained from shock experiments. The second term in Eq. (4.1) is the stress-dependent equilibrium concentration of vacancies with $k_b\vartheta$ being the thermal energy and E_v^f being a vacancy formation energy that decreases with increasing local tensile elastic strain [121]. Both high tensile stresses and relatively large plastic strains may be achieved in a number of dynamic ductile failure processes, e.g. spall failure and shaped charge jet breakup, for which a superconcentration of vacancies is likely.

In this superconcentrated state there may be enough time for these vacancies to cluster together, forming something of a *void embryo* of several angstroms to perhaps a few nanometers. The mechanism appears even more plausible when one considers the enhanced vacancy mobility ($\propto \exp -1/\vartheta$) that results from the associated shock temperature rise $\Delta\vartheta$. However, the vacancy mobility also increases as a result of the high tensile stress experienced during spall failure, see for example [121]. Incorporating these temperature- and stress-dependent vacancy mobilities into Lattice Kinetic Monte Carlo (LKMC) simulations, Reina et al. [69] was able to demonstrate that this mechanism of nanovoid formation through vacancy clustering is in fact feasible

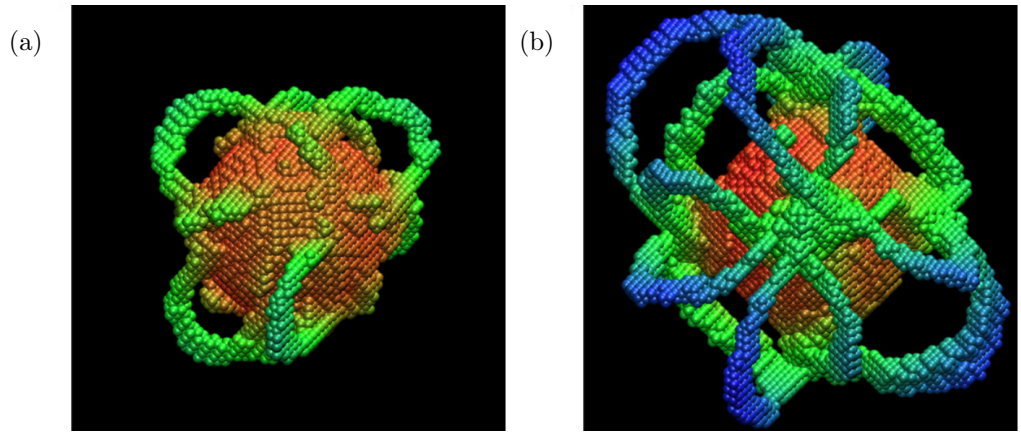

Fig. 4.2: Sequence of dislocation emission process typically observed in molecular dynamics simulations [115]. The dislocation line segments are identified by their centrosymmetry parameter and are visualized here in green and blue with the void surface visualized as red.

on the timescales associated with spall failure. Furthermore, the LKMC simulations of Reina et al. [69] do not account for *pipe diffusion* of vacancies along dislocation cores [122]. Since shocked materials possess extremely high dislocation densities, pipe diffusion may significantly accelerate the kinetics of vacancy clustering.

Once a vacancy cluster reaches a certain critical size (∼1 nm) it may now be possible to grow the void further by dislocation-based mechanisms. However, traditional dislocation-based growth mechanisms (similar to those studied in chapter 3) are unlikely due to the extremely small length scales associated with these vacancy clusters. The presence of a Frank-Read or single-arm source (to replenish the local mobile dislocation density) in the vicinity of these vacancy clusters is statistically unlikely. Dislocation emission is an alternative growth mechanism that may be capable of growing these vacancy clusters from their critical size (∼1 nm) to the sizes observed

in Fig. 4.1(b) ($\sim 0.1 - 1\mu$m). The process of dislocation emission carries matter from the void surface into the bulk of the material, permitting void growth. This process can be seen in Fig. 4.2, and is discussed in more detail elsewhere [11, 115].

Having provided some degree of motivation for the role of vacancy clustering and subsequent dislocation emission in extreme dynamic ductile failure, we now proceed with an analysis of dislocation emission.

4.3 Stress fields and Peach-Koehler forces experienced by a dislocation near a void surface in a porous material

The aim of this section is to set the stage for the derivation of a closed-form model that approximates the critical macroscopic stress state required to initiate dislocation emission in a porous material subject to a general stress state, extending the work of Lubarda et al. [65]. Since the analyses of Lubarda et al. [65] and Lubarda [11] are for a single void in an infinite medium, their emission criteria are independent of porosity (void volume fraction). Here we rectify this shortcoming by making use of averaging concepts from classical micromechanics. The porous emission model finally obtained in section 4.4 predicts that the critical macroscopic stress required for emission decays monotonically with increasing porosity. In addition, the new emission model accounts

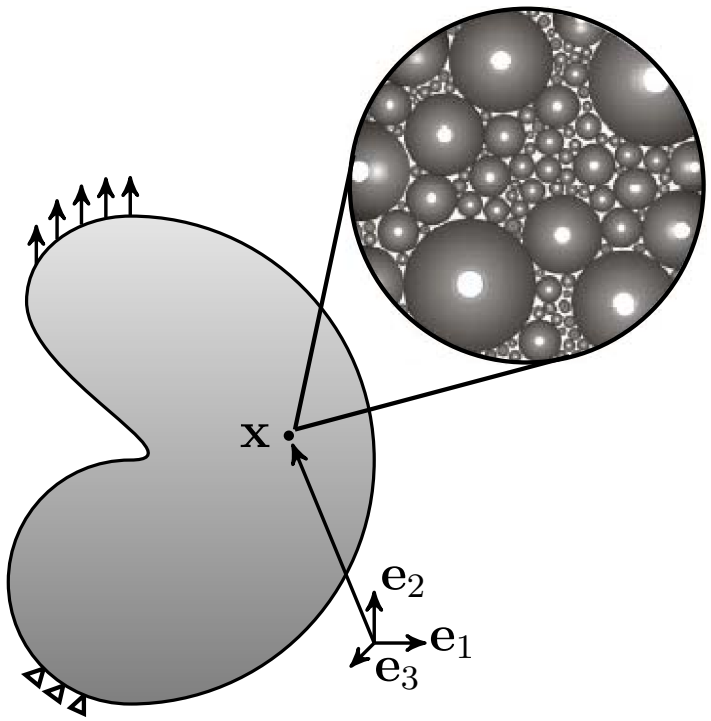

Fig. 4.3: Schematic of a general porous macroscopic body subject to mixed traction-displacement boundary conditions. On the microscale, the porosity φ is composed of a distribution of spherical voids characterized by the void size distribution $g(a)$ and mean void spacing $\bar{\ell}_v$ (inset adapted from [123]).

for the effects of surface energy and finite temperatures, while also providing a simple approximate method for extending the biaxial emission criterion of Lubarda [11] to general stress states.

Consider a general porous macroscopic body subject to mixed traction-displacement boundary conditions as shown in Fig. 4.3. At a particular macroscopic material point $\mathbf{x}$ the material possesses a porosity of $\varphi(\mathbf{x})$ and is subject to a general three-

dimensional macroscopic stress field, i.e.

$$\boldsymbol{\Sigma}(\mathbf{x}) = \begin{bmatrix} \Sigma_{11} & \Sigma_{12} & \Sigma_{13} \\ \Sigma_{21} & \Sigma_{22} & \Sigma_{23} \\ \Sigma_{31} & \Sigma_{32} & \Sigma_{33} \end{bmatrix}, \tag{4.2}$$

where the matrix is expressed with respect to the macroscopic physical coordinate system $\{\mathbf{e}_1, \mathbf{e}_2, \mathbf{e}_3\}$. Throughout the present chapter $\boldsymbol{\Sigma}$ is prescribed by the loading condition. However, chapter 6 provides an appropriate porous constitutive model that may be implemented into a computational framework to compute $\boldsymbol{\Sigma}(\mathbf{x})$ under general, mixed traction-displacement loading conditions such as those shown in Fig. 4.3.

On the microscale, the local porosity φ is composed of a distribution of spherical voids of varying radius a, see Fig. 4.3. The void population is characterized by a size distribution $g(a)$ and the number of voids per unit volume of solid material N_v. The mean void size $\bar{a}$ may be computed as $\bar{a} = \int_0^\infty g(a)a \; da$, and a measure of the mean center-to-center spacing between voids $\bar{\ell}_v$ may be defined such that

$$\varphi = \left(2\bar{a}/\bar{\ell}_v\right)^3. \tag{4.3}$$

From the above definitions, it follows that

$$\frac{\varphi}{1-\varphi} = \frac{4}{3}\pi N_v \int_0^\infty g(a)a^3 da. \tag{4.4}$$

In order to obtain the desired closed-form approximation for the critical stress required to activated dislocation emission, it is necessary to consider two auxiliary

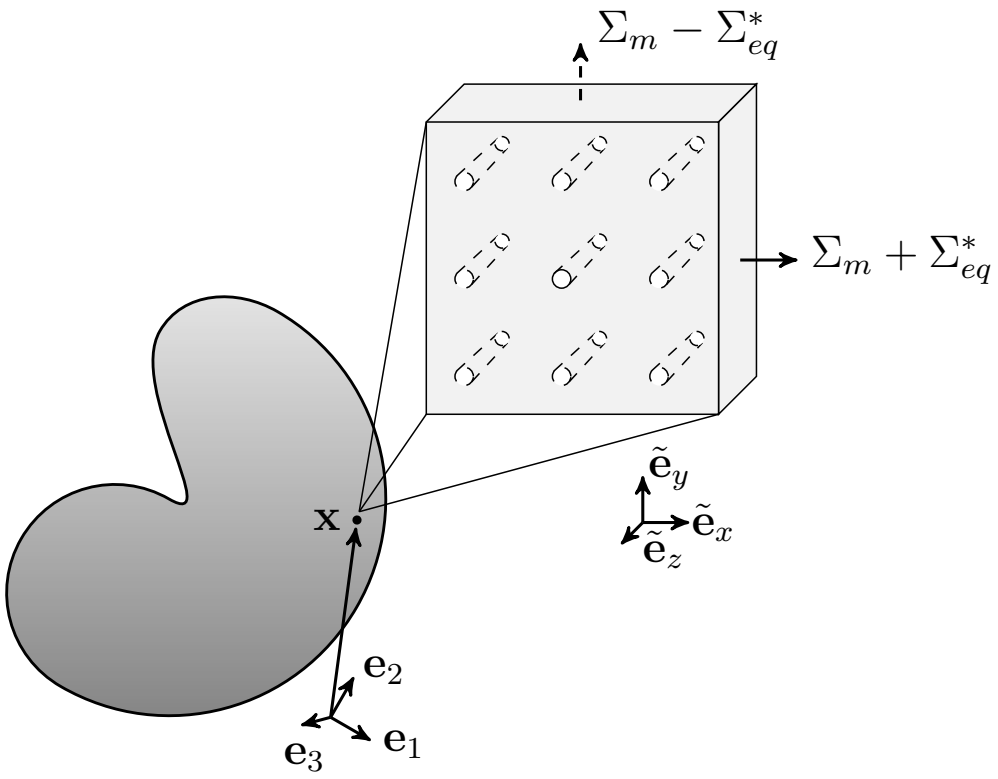

Fig. 4.4: Schematic of the first auxiliary problem corresponding to a general porous macroscopic body. On the microscale, the auxiliary porosity φ is composed of cylindrical voids characterized by the same void size distribution $g(a)$ as the corresponding physical problem shown in Fig. 4.3. The cylindrical voids are aligned along $\tilde{\mathbf{e}}_z$, where $\tilde{\mathbf{e}}_z$ is the principal stress direction associated with the principal stress component of Eq. (4.2) that is neither the maximum nor minimum principal stress component. The microscale RVE is subject to a simplified effective stress state that preserves the first stress invariant Σ_m and the second deviatoric stress invariant $\left(\Sigma^*_{eq}\right)^2$ of the general stress tensor $\boldsymbol{\Sigma}$ in the physical problem shown in Fig. 4.3.

problems alongside the physical one. The auxiliary problems are purposefully constructed to be simple enough to permit analytic stress analysis, yet still capture the most important governing physics. Consider first the auxiliary problem shown in Fig. 4.4 corresponding to a porous material with a distribution of cylindrical voids.

At each macroscopic material point $\mathbf{x}$ there is assumed to exist a corresponding auxiliary representative volume element (RVE). The auxiliary RVE is constructed in a manner to preserve the most important aspects of the geometry and general stress-state of the physical problem (Fig. 4.3). The alignment of the cylindrical voids in the auxiliary RVE is chosen based on the principal stress directions, and the geometry is constructed to preserve void size distribution and mean spacing (with one consequence being that the physical porosity φ is not necessarily preserved). The details of this procedure are discussed below.

Here the geometry of the auxiliary RVE is constructed in a manner that preserves the number of voids per unit volume of solid material N_v as well as the void size distribution $g(a)$, with a now corresponding to the radii of the auxiliary cylindrical voids. Preserving the void size distribution $g(a)$ is particularly crucial since the critical stress for dislocation emission is strongly size-dependent, as discussed in [11, 65]. An unknown geometric parameter in the auxiliary RVE is the length of the auxiliary cylinders. Here the length of each cylinder is taken to be $\bar{\ell}_v$, the mean spacing between voids in the physical problem. One consequence of this assumption is the preservation of the nearest neighbor spacing for the special case in which the physical RVE consists of an array of spherical voids equally spaced on a cubic lattice, which essentially transforms into infinitely extended cylindrical voids on a corresponding two-dimensional square lattice.

From these relations it follows that the total auxiliary void volume fraction (aux-

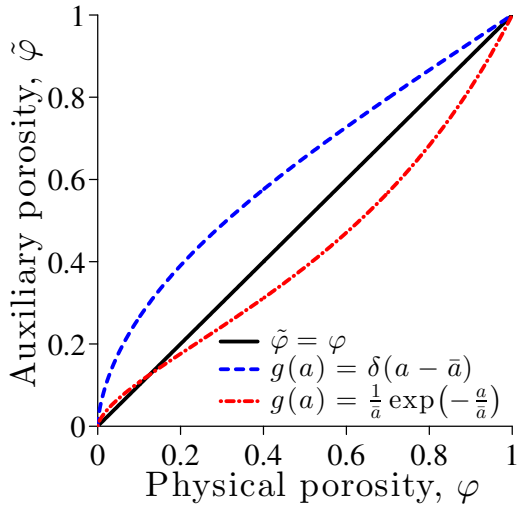

Fig. 4.5: Auxiliary porosity $\tilde{\varphi}$ as a function of the physical porosity φ as computed from Eq. (4.6) with $\zeta_g = 1$ for the delta distribution and $\zeta_g = 3$ for the exponential distribution. The auxiliary porosity corresponds to the cylindrical voids in the auxiliary problem shown in Fig. 4.4, and the physical porosity corresponds to the spherical voids in the physical problem shown in Fig. 4.3.

iliary porosity) is expressed as

$$\frac{\tilde{\varphi}}{1-\tilde{\varphi}} = \pi N_v \bar{\ell}_v \int_0^\infty g(a) a^2 da, \tag{4.5}$$

Eqs. (4.3) – (4.5) may be combined to obtain an expression that relates the physical porosity to the auxiliary porosity through the void size distribution alone, i.e.

$$\frac{1}{\tilde{\varphi}} = 1 + \frac{2}{3}\left(\frac{1}{\sqrt[3]{\varphi^2}} - \sqrt[3]{\varphi}\right) \underbrace{\frac{\int_0^\infty g(a) a^3 da}{\int_0^\infty g(a) \bar{a} a^2 da}}_{\triangleq \zeta_g} \tag{4.6}$$

Note that $\zeta_g = 1$ for the case in which all voids are of equal size, i.e. $g(a) = \delta(a - \bar{a})$ with $\delta(\cdot)$ being the Dirac delta distribution, and $\zeta_g = 3$ for an exponential distribution, i.e. $g(a) = \bar{a}^{-1} \exp(-a/\bar{a})$. The variation of the auxiliary porosity $\tilde{\varphi}$ as a function of the physical porosity φ is shown in Fig. 4.5. Notice that the limits are reproduced

correctly, i.e. $\tilde{\varphi} = 0$ for $\varphi = 0$ and $\tilde{\varphi} = 1$ for $\varphi = 1$, and for the delta distribution the auxiliary porosity is always equal to or greater than the physical porosity. The auxiliary porosity $\tilde{\varphi}$ associated with an exponential distribution is generally lower than the physical porosity ($\tilde{\varphi} < \varphi$), with the exception being for small porosity where $\tilde{\varphi} > \varphi$ for the exponential distribution. The observed difference between the two distributions is related to the more efficient packing of cylindrical voids enabled by a broad void size distribution (e.g. exponential) as compared with the infinitely narrow delta distribution.

In order to obtain the desired closed-form approximation for the emission criterion it is necessary to define an effective macroscopic auxiliary stress tensor $\tilde{\mathbf{\Sigma}}$. The effective macroscopic auxiliary stress tensor must be simple enough to permit an analytic stress analysis similar to [11], and yet be able to capture the most important driving forces governing dislocation emission. Here this effective auxiliary stress tensor is defined such that the first stress invariant and second deviatoric stress invariant are preserved, i.e. $I_1 = \tilde{I}_1$ and $J_2 = \tilde{J}_2$, which may be equivalently expressed as

$$\Sigma_m = \tilde{\Sigma}_m \qquad \text{and} \qquad \Sigma_{eq} = \tilde{\Sigma}_{eq}, \tag{4.7}$$

where the subscript m denotes the mean stress, i.e. $\Sigma_m \triangleq {}^1\!/\!_3 I_1 = {}^1\!/\!_3 \mathrm{tr}\mathbf{\Sigma}$ and the subscript eq denotes the equivelent von Mises stress, i.e. $\Sigma_{eq} \triangleq \sqrt{3J_2} = \sqrt{{}^3\!/\!_2 \mathbf{\Sigma}' : \mathbf{\Sigma}'}$ with $\mathbf{\Sigma}' \triangleq \mathbf{\Sigma} - \Sigma_m \mathbf{I}$. Eq. (4.7) also preserves the macroscopic stress triaxiality defined as $\tilde{\chi}_T = \chi_T \triangleq \Sigma_m / \Sigma_{eq}$. Here we utilize the following simple first and second invariant

preserving stress transformation expressed in matrix notation as

$$\tilde{\boldsymbol{\Sigma}} = \begin{bmatrix} \Sigma_m + \Sigma_{eq}^* & 0 & 0 \\ 0 & \Sigma_m - \Sigma_{eq}^* & 0 \\ 0 & 0 & \Sigma_m \end{bmatrix}, \tag{4.8}$$

where $\Sigma_{eq}^* \triangleq \Sigma_{eq}/\sqrt{3}$ and the matrix is expressed with respect to the auxiliary macroscopic coordinate system $\{\tilde{\mathbf{e}}_x, \tilde{\mathbf{e}}_y, \tilde{\mathbf{e}}_z\}$. As shown in Fig. 4.4, the coordinate system is constructed such that the array of auxiliary cylindrical voids are aligned along $\tilde{\mathbf{e}}_z$. The maximum and minimum principal auxiliary stresses are aligned with $\mathbf{e}_x$ and $\mathbf{e}_y$, respectively. As such, the maximum auxiliary shear stress lies within the xy-plane, thus maximizing the likelihood of dislocation emission in the auxiliary problem shown in Fig. 4.4.

Having established a relationship between the general macroscopic stress tensor $\boldsymbol{\Sigma}$ of the physical problem (Fig. 4.3) and the effective macroscopic stress tensor $\tilde{\boldsymbol{\Sigma}}$ for the auxiliary problem (Fig. 4.4), it proves useful to draw a connection to the auxiliary microscopic stress field $\tilde{\boldsymbol{\sigma}}$ that varies throughout the auxiliary RVE shown in Fig. 4.4. Utilizing the generalized Gauss theorem along with the local equilibrium condition $\boldsymbol{\nabla} \cdot \tilde{\boldsymbol{\sigma}} = \mathbf{0}$ it may be shown that the volumetric average of the auxiliary microscopic stress tensor $\tilde{\boldsymbol{\sigma}}$ over the microscale domain Ω_{micro} is equal to the effective macroscopic stress tensor $\tilde{\boldsymbol{\Sigma}}$ for the first auxiliary problem, i.e.

$$\Omega_{micro}^{-1} \iiint_{\Omega_{micro}} \tilde{\boldsymbol{\sigma}} d\Omega_{micro} = \tilde{\boldsymbol{\Sigma}}. \tag{4.9}$$

The microscale domain may be additively decomposed into a microscale domain that only includes the auxiliary cylindrical voids Ω^{void}_{micro} and a microscale domain that only includes the solid material Ω^{solid}_{micro} such that $\Omega_{micro} = \Omega^{v}_{micro} + \Omega^{s}_{micro}$. This additive domain decomposition permits the following decomposition of the volumetric average expressed in Eq. (4.9):

$$\underbrace{\frac{\Omega^{v}_{micro}}{\Omega_{micro}}\,\Omega^{v^{-1}}_{micro}\iiint_{\Omega^{v}_{micro}}\tilde{\boldsymbol{\sigma}}\,d\Omega^{v}_{micro}}_{\triangleq\langle\tilde{\boldsymbol{\sigma}}\rangle^{v}} + \underbrace{\frac{\Omega^{s}_{micro}}{\Omega_{micro}}\,\Omega^{s^{-1}}_{micro}\iiint_{\Omega^{s}_{micro}}\tilde{\boldsymbol{\sigma}}\,d\Omega^{s}_{micro}}_{\triangleq\langle\tilde{\boldsymbol{\sigma}}\rangle} = \tilde{\boldsymbol{\Sigma}}, \tag{4.10}$$

where $\langle\cdot\rangle$ denotes a volumetric average over the solid material only and $\langle\cdot\rangle^{v}$ denotes a volumetric average over the voids. Noting that ${}^{\Omega^{s}_{micro}}\!/_{\Omega_{micro}} = 1-\tilde{\varphi}$ by definition and that voids are necessarily stress-free, i.e. $\langle\tilde{\boldsymbol{\sigma}}\rangle^{v} = 0$, Eq. (4.10) may be recast in the following compact form:

$$(1-\tilde{\varphi})\,\langle\tilde{\boldsymbol{\sigma}}\rangle = \tilde{\boldsymbol{\Sigma}}. \tag{4.11}$$

The expression in Eq. (4.11) implies that $(1-\tilde{\varphi})^{-1}$ is essentially a stress concentration factor that governs the average amplification of the microscopic stress field in the solid material above the applied macroscopic stress.

The second auxiliary problem under consideration is that of the unit cell corresponding to the first auxiliary problem: a single infinitely extended cylindrical void of radius a embedded within an *infinite* isotropic linear-elastic medium subject to some effective far-field stress state $\tilde{\boldsymbol{\sigma}}^{\infty}$, see Fig. 4.6. The auxiliary microscopic stress field $\tilde{\boldsymbol{\sigma}}$ is, of course, locally perturbed by the presence of the void; however, it is required to asymptotically approach the far-field stress state at relative distances far from the

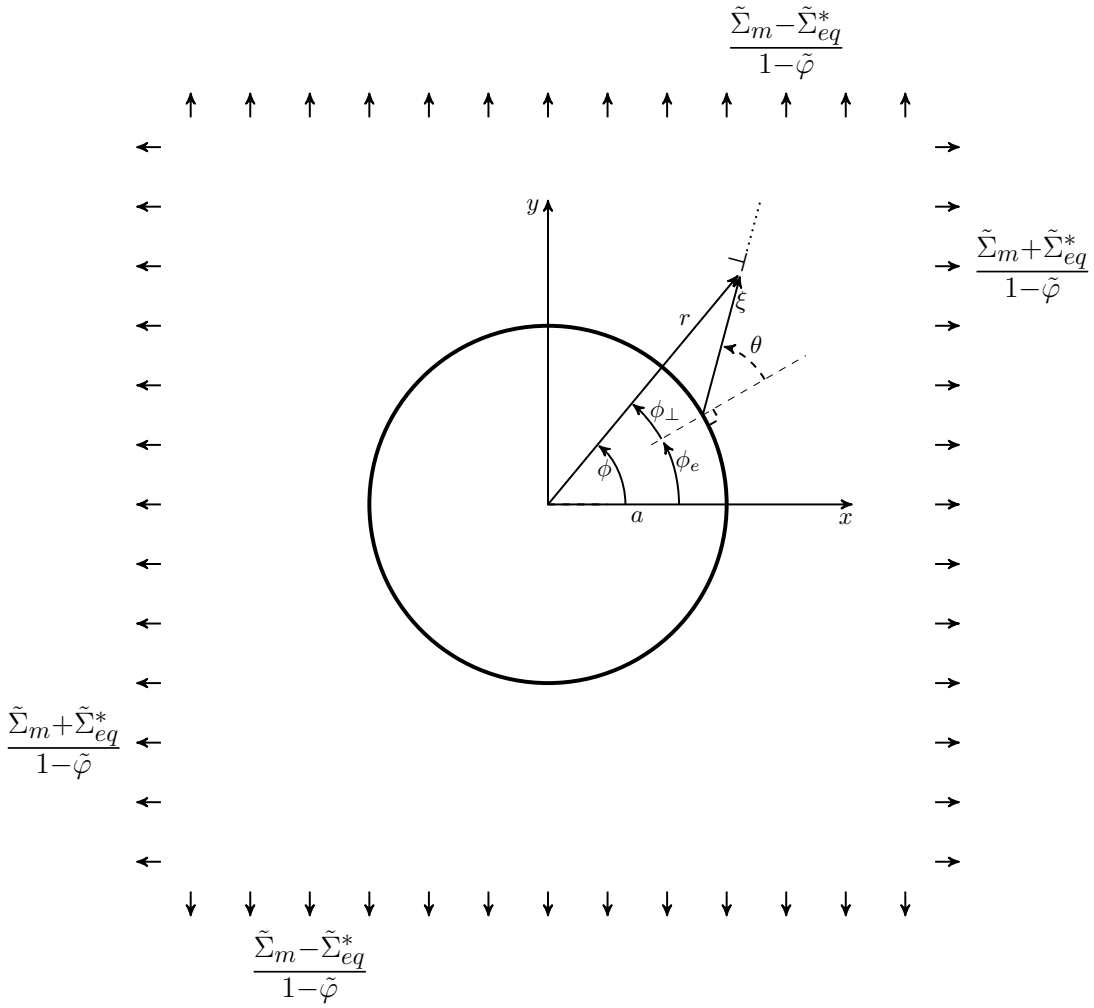

Fig. 4.6: Schematic of the second auxiliary problem corresponding to an infinitely extended cylindrical void in an infinite isotropic linear-elastic medium. The infinite medium is subject to a far-field effective stress state that preserves the first and second stress invariants corresponding to a particular macroscopic point x in the physical problem shown in Fig. 4.3. In addition, the far-field stress state accounts for the effect of finite porosity φ. The corresponding microscopic stress field is given in Eqs. (4.14) to (4.16) expressed in terms of the polar coordinate system (r, ϕ). A second set of polar coordinates (ξ, θ) are utilized to define the position of a dislocation $\perp$ on a particular glide plane of interest (dotted line) with respect to the mutual intersection of the glide plane with the void surface and corresponding surface normal (dashed line) at $(r = a, \phi = \phi_e)$ with $\phi = \phi_e + \phi_\perp$.

void surface, i.e. $\tilde{\boldsymbol{\sigma}}|_{\frac{r}{a}\to\infty} \to \tilde{\boldsymbol{\sigma}}^{\infty}$. Therefore, $\tilde{\boldsymbol{\sigma}}$ is asymptotically close to $\tilde{\boldsymbol{\sigma}}^{\infty}$ over an infinite domain Ω_{∞} implying that the volumetric average of the auxiliary microscopic stress field throughout the solid material $\langle\tilde{\boldsymbol{\sigma}}\rangle$ is identical to the effective far-field stress state $\tilde{\boldsymbol{\sigma}}^{\infty}$, i.e.

$$\tilde{\boldsymbol{\sigma}}|_{\frac{r}{a}\to\infty} \to \tilde{\boldsymbol{\sigma}}^{\infty} = \langle\tilde{\boldsymbol{\sigma}}\rangle, \tag{4.12}$$

with $\langle\tilde{\boldsymbol{\sigma}}\rangle = (1-\tilde{\varphi})^{-1}\,\tilde{\boldsymbol{\Sigma}}$ by Eq. (4.11). For voids or stress-free inclusions, the asymptotic boundary condition defined by Eq. (4.12) is essentially equivalent to the celebrated micromechanical assumptions of Mori and Tanaka [124].

Combining the asymptotic boundary condition expressed in Eq. (4.11) along with the stress concentration factor given by Eq. (4.12) and the effective stress transformation Eq. (4.8) it follows that

$$\tilde{\boldsymbol{\sigma}}|_{\frac{r}{a}\to\infty} \to \begin{bmatrix} \frac{\Sigma_m+\Sigma^*_{eq}}{1-\tilde{\varphi}} & 0 & 0 \\ 0 & \frac{\Sigma_m-\Sigma^*_{eq}}{1-\tilde{\varphi}} & 0 \\ 0 & 0 & \frac{\Sigma_m}{1-\tilde{\varphi}} \end{bmatrix}, \tag{4.13}$$

with the matrix expressed in the auxiliary macroscopic coordinate system $\{\mathbf{e}_x, \mathbf{e}_y, \mathbf{e}_z\}$. Applying the asymptotic boundary condition Eq. (4.13) along with a traction free boundary condition at the void surface, i.e. $\tilde{\boldsymbol{\sigma}}|_{r=a} \cdot \mathbf{n}_v = \mathbf{0}$ with $\mathbf{n}_v$ being the unit normal to the void surface, the in-plane solution to the local equilibrium equation

$\boldsymbol{\nabla} \cdot \tilde{\boldsymbol{\sigma}} = \mathbf{0}$ may be expressed as

$$\tilde{\sigma}_r^{app} = \frac{\Sigma_m}{1-\tilde{\varphi}}\left(1-\frac{a^2}{r^2}\right) + \frac{\Sigma_{eq}^*}{1-\tilde{\varphi}}\left(1-4\frac{a^2}{r^2}+3\frac{a^4}{r^4}\right)\cos 2\phi \tag{4.14}$$

$$\tilde{\sigma}_\phi^{app} = \frac{\Sigma_m}{1-\tilde{\varphi}}\left(1+\frac{a^2}{r^2}\right) - \frac{\Sigma_{eq}^*}{1-\tilde{\varphi}}\left(1+3\frac{a^4}{r^4}\right)\cos 2\phi \tag{4.15}$$

$$\tilde{\sigma}_{r\phi}^{app} = -\frac{\Sigma_{eq}^*}{1-\tilde{\varphi}}\left(1+2\frac{a^2}{r^2}-3\frac{a^4}{r^4}\right)\sin 2\phi, \tag{4.16}$$

with the angle ϕ defined in Fig. 4.6 and the superscript *app* indicates that the auxiliary microscopic stress results from the applied macroscopic loading. In the limit of $\tilde{\varphi} \to 0$ the stress fields utilized by Lubarda [11] are recovered. However, for finite porosity the local auxiliary microscopic stress $\tilde{\boldsymbol{\sigma}}^{app}$ increases monotonically with increasing porosity φ, implying that the likelihood of dislocation emission increases with increasing porosity (for a given macroscopic stress state $\boldsymbol{\Sigma}$). Under pure hydrostatic macroscopic loading, i.e. $\Sigma_{eq}^* = 0$ or $\chi_T = \pm\infty$, Eqs. (4.14) and (4.15) reduce to

$$\tilde{\sigma}_r^{app} = \frac{\Sigma_m}{1-\tilde{\varphi}}\left(1-\frac{a^2}{r^2}\right) \tag{4.17}$$

$$\tilde{\sigma}_\phi^{app} = \frac{\Sigma_m}{1-\tilde{\varphi}}\left(1+\frac{a^2}{r^2}\right) \tag{4.18}$$

with $\tilde{\sigma}_{r\phi} = 0$. The asymptotic boundary condition $\tilde{\boldsymbol{\sigma}}|_{\frac{r}{a}\to\infty} \to \langle\tilde{\boldsymbol{\sigma}}\rangle$ expressed in Eq. (4.12) may be confirmed by explicitly computing the volumetric average of Eq. (4.17), i.e.

$$\langle\tilde{\sigma}_r^{app}\rangle = \lim_{r_o/a\to\infty} \frac{1}{\pi\left(r_o^2-a^2\right)} \int_0^{2\pi}\int_a^{r_o} r\tilde{\sigma}_r^{app} dr d\phi = \lim_{r_o/a\to\infty} \frac{\Sigma_m}{1-\tilde{\varphi}}\left(1+\frac{\ln a/r_o}{r_o^2/a^2-1}\right) = \frac{\Sigma_m}{1-\tilde{\varphi}}, \tag{4.19}$$

and comparing it with the asymptotic value

$$\tilde{\sigma}_r^{app}|_{\frac{r}{a}\to\infty} = \lim_{r/a\to\infty} \frac{\Sigma_m}{1-\tilde{\varphi}}\left(1-\frac{a^2}{r^2}\right) = \frac{\Sigma_m}{1-\tilde{\varphi}}. \tag{4.20}$$

Having established the auxiliary microscopic stress fields that result from the applied loading, we now turn our attention to the auxiliary stress fields generated by the surface tension. For nano-sized voids it may be necessary to account for surface tension. Applying the variational analysis outlined in the appendix of [69] the traction on the surface of the cylindrical void is obtained here as

$$\tilde{\boldsymbol{\sigma}}|_{r=a} \cdot \mathbf{n}_v = \frac{\gamma_{se}}{a}\mathbf{n}_v, \tag{4.21}$$

where γ_{se} is the surface energy. Note that the surface tension for cylindrical voids as expressed in Eq. (4.21) is a factor of 2 smaller than that for spherical voids due to the alternative geometry. Applying the boundary condition expressed in Eq. (4.21) the effective microscopic stress field associated with the surface energy is expressed as

$$\tilde{\sigma}_r^{se} = \frac{\gamma_{se}}{a}\left(\frac{a^2}{r^2}\right) \tag{4.22}$$

$$\tilde{\sigma}_\phi^{se} = -\frac{\gamma_{se}}{a}\left(\frac{a^2}{r^2}\right) \tag{4.23}$$

with $\tilde{\sigma}_{r\phi} = 0$. Notice that Eqs. (4.22) and (4.23) contain the physical length scale a, which inversely scales the auxiliary microscopic stress field associated with the surface energy, i.e. $\tilde{\sigma}_r^{se} \to \infty$ and $\tilde{\sigma}_\phi^{se} \to -\infty$ as $a \to 0$. With the general stress fields in hand, we are now in a position to consider the shear stresses acting on a dislocation near the void surface.

Consider the edge dislocation located on a glide plane of interest shown as the dotted line in Fig. 4.6. A second set of polar coordinates (ξ, θ) are utilized to define the position of the edge dislocation $\perp$ on the glide plane of interest (dotted line) with respect to the mutual intersection of the glide plane with the void surface and corresponding surface normal (dashed line) at $(r = a, \phi = \phi_e)$ with $\phi = \phi_e + \phi_\perp$. Since the driving force for this edge dislocation is the local auxiliary in-plane shear shear stress $\tilde{\sigma}_{\xi\theta} \triangleq \tilde{\tau}$ on the glide plane of interest, it is useful to obtain $\tilde{\tau}$ through a stress transformation of Eqs. (4.14) to (4.16), i.e.

$$\tilde{\tau} \triangleq \tilde{\sigma}_{\xi\theta} = -\frac{1}{2}\left(\tilde{\sigma}_r - \tilde{\sigma}_\phi\right)\sin 2(\theta - \phi_\perp) + \tilde{\sigma}_{r\phi}\cos 2(\theta - \phi_\perp), \tag{4.24}$$

where the two coordinate systems (r, ϕ) and (ξ, θ) are related to one another through the following geometric relationships:

$$r^2 = a^2 + \xi^2 + 2a\xi\cos\theta \tag{4.25}$$

$$\tan(\phi_\perp) = \frac{\xi\sin\theta}{a + \xi\cos\theta}. \tag{4.26}$$

Substitution of Eqs. (4.14) to (4.16) in Eq. (4.24) results in the following expressions for the auxiliary microscopic shear stresses due to the applied stress and the effects

of surface tension:

$$\begin{aligned}\tilde{\tau}^{app} =& \frac{\Sigma_m}{1-\tilde{\varphi}}\left(\frac{a^2}{r^2}\right)\sin 2(\theta-\phi_\perp) \\ &- \frac{\Sigma^*_{eq}}{1-\tilde{\varphi}}\left(1-2\frac{a^2}{r^2}+3\frac{a^4}{r^4}\right)\cos 2\phi \sin 2(\theta-\phi_\perp) \\ &- \frac{\Sigma^*_{eq}}{1-\tilde{\varphi}}\left(1+2\frac{a^2}{r^2}-3\frac{a^4}{r^4}\right)\sin 2\phi \cos 2(\theta-\phi_\perp).\end{aligned} \tag{4.27}$$

$$\tilde{\tau}^{se} = -\frac{\gamma_{se}}{a}\frac{a^2}{r^2}\sin 2(\theta-\phi_\perp). \tag{4.28}$$

Utilizing the angle sum and difference trigonometric identities, i.e. $\sin(\alpha \pm \beta) = \sin(\alpha)\cos(\beta) \pm \sin(\beta)\cos(\alpha)$, Eq. (4.27) may be expressed more compactly as

$$\begin{aligned}\tilde{\tau}^{app} =& \frac{\Sigma_m}{1-\tilde{\varphi}}\left(\frac{a^2}{r^2}\right)\sin 2(\theta-\phi_\perp) - \frac{\Sigma^*_{eq}}{1-\tilde{\varphi}}\sin 2(\theta+\phi_e) \\ &- \frac{\Sigma^*_{eq}}{1-\tilde{\varphi}}\left(3\frac{a^4}{r^4}-2\frac{a^2}{r^2}\right)\sin 2(\theta-\phi_e-2\phi_\perp).\end{aligned} \tag{4.29}$$

With $\tilde{\tau}$ being the driving force for edge dislocations on the glide plane of interest, one may assume that the most favorable plane for dislocation emission is the one that maximizes $\tilde{\tau}$ near the void surface. Noting that the intersection of the glide plane and the void surface is located at $r = a$, $\phi = \phi_e$, and $\phi_\perp = 0$ substitution into Eqs. (4.27) and (4.28) gives the angular dependence of the auxiliary shear stress at the intersection of the void surface and glide plane (which is a driving force for emission), i.e.

$$\tilde{\tau}^{app}_{vs} = \frac{\Sigma_m}{1-\tilde{\varphi}}\sin 2\theta - 2\frac{\Sigma^*_{eq}}{1-\tilde{\varphi}}\cos 2\phi_e \sin 2\theta \tag{4.30}$$

$$\tilde{\tau}^{se}_{vs} = -\frac{\gamma_{se}}{a}\sin 2\theta, \tag{4.31}$$

where the subscript vs denotes the corresponding shear stress evaluated at the void surface ($r = a$). The angular dependence of the magnitude of the combined applied and surface energy shear stresses at the void surface, i.e. $|\tilde{\tau}^{app}_{vs} + \tilde{\tau}^{se}_{vs}|$, is plotted in Fig. 4.7 (normalized by Σ^{*}_{eq}). The critical emission angle ϕ^{cr}_{e} that maximizes $|\tilde{\tau}^{app}_{vs} + \tilde{\tau}^{se}_{vs}|$ is independent of θ and may be expressed as $\phi^{cr}_{e} = \pm n_i \pi/2$ with n_i being any odd integer for $\Sigma_m > (1-\tilde{\varphi})\gamma^{se}/a$ and being otherwise equal to any even integer, see Fig. 4.7(a). The glide angles θ that maximize $|\tilde{\tau}^{app}_{vs} + \tilde{\tau}^{se}_{vs}|$ at any critical emission angle, i.e. $\phi^{cr}_{e} = \pm n_i \pi/2$, are found to be $\theta^{cr} = \pm\pi/4$. The critical glide angles of $\theta = \pm 3\pi/4$ are neglected on the physical grounds that these angles represent glide planes defined inside the void, see Fig. 4.6.

Notice that the magnitude of the combined applied and surface energy shear stresses $|\tilde{\tau}^{app}_{vs} + \tilde{\tau}^{se}_{vs}|$ is greater for a compressive applied loading, i.e. $\Sigma_m < 0$, as compared to a tensile loading, i.e. $\Sigma_m > 0$, see Fig. 4.7(b). One consequence of this is that dislocation emission from the surface of nanovoids may be noticeably easier under compressive loading as compared with tensile loading. This effect is discussed further in section 4.6.

Consider now the straight dislocation located at (r, ϕ) as shown in Fig. 4.6. The Burgers vector of the dislocation is $\mathbf{b}$ and the line sense is $\mathbf{e}_z$. The corresponding Peach-Koehler forces associated with the applied loading and surface energy are given by $\tilde{\boldsymbol{\mathcal{F}}}^{app} = (\tilde{\boldsymbol{\sigma}}^{app} \cdot \mathbf{b}) \times \mathbf{e}_z$ and $\tilde{\boldsymbol{\mathcal{F}}}^{se} = (\tilde{\boldsymbol{\sigma}}^{se} \cdot \mathbf{b}) \times \mathbf{e}_z$, respectively. For an edge dislocation the Burgers vector is $\mathbf{b} = \pm b\mathbf{e}_\xi$, where b is the magnitude of the Burgers

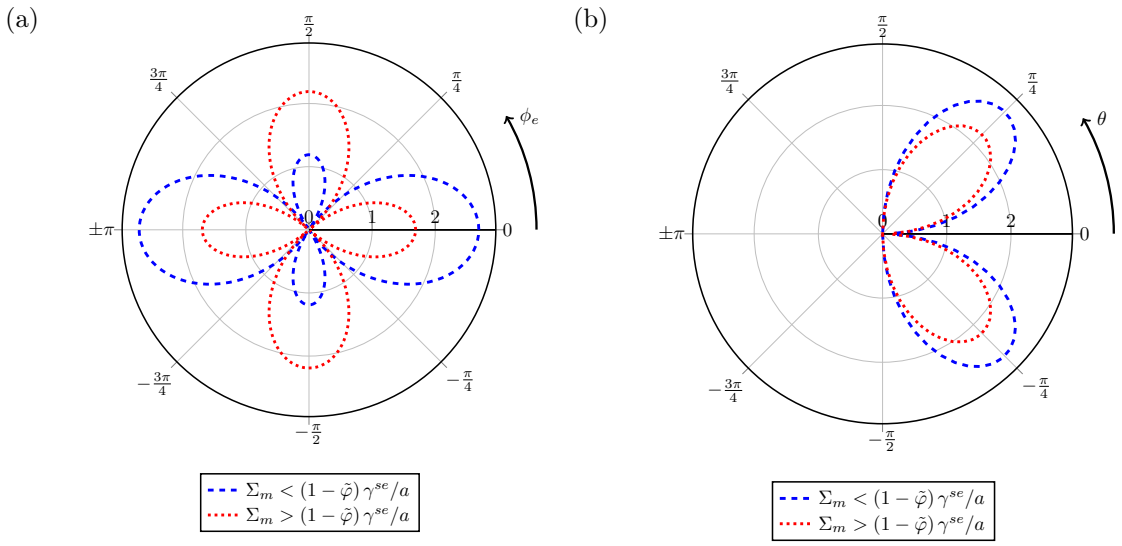

Fig. 4.7: Polar plots showing the angular dependence of the combined normalized applied and surface energy shear stresses at the void surface, i.e. $\left|\tilde{\tau}^{app}_{vs}/\Sigma^{*}_{eq} + \tilde{\tau}^{se}_{vs}/\Sigma^{*}_{eq}\right|$, with respect to (a) φ_e holding θ constant and (b) θ holding φ_e constant. Numerical calculations are computed from Eqs. (4.30) and (4.31) with $\Sigma_m = \pm\Sigma^{*}_{eq}/2$ and $(1-\tilde{\varphi})\gamma^{se}/a = \Sigma^{*}_{eq}/4$.

vector. The component for each of these two Peach-Koehler forces that is aligned with the slip direction is given as $\tilde{\mathcal{F}}^{app}_{\xi} \triangleq \tilde{\boldsymbol{\mathcal{F}}}^{app} \cdot \mathbf{e}_{\xi} = \pm\tilde{\tau}^{app} b$ and $\tilde{\mathcal{F}}^{se}_{\xi} \triangleq \tilde{\boldsymbol{\mathcal{F}}}^{se} \cdot \mathbf{e}_{\xi} = \pm\tilde{\tau}^{se} b$. The interaction of the emitted dislocation with the infinitely compliant cylindrical void generates an image force $\tilde{\boldsymbol{\mathcal{F}}}^{image}$, which acts to pull the dislocation towards the void surface. The component of the image Peach-Koehler force aligned with the slip direction is defined as $\tilde{\mathcal{F}}^{image}_{\xi} \triangleq -\left|\tilde{\tau}^{image}\right| b \triangleq \tilde{\boldsymbol{\mathcal{F}}}^{image} \cdot \mathbf{e}_{\xi}$ with $\left|\tilde{\tau}^{image}\right|$ being the magnitude of the image shear stress. This ξ-component of the image force may be determined from the Airy stress functions derived by Dundurs and Mura [125] and

Table 4.1: Thermoelastic properties of aluminum and copper taken from [127].

Property	Units	Copper	Aluminum
Reference shear modulus, μ_0	GPa	46.8	26.0
Pressure dependence of modulus, $\partial\mu/\partial p$	–	1.25	1.79
Temperature dependence of modulus, $\partial\mu/\partial\vartheta$	GPa / kK	17.7	16.8
Absolute melting temperature, ϑ_m	K	1358	933
Poisson ratio, ν	–	0.355	0.33

recently revisited by Lubarda [126], from which the following expression was obtained

$$\left|\tilde{\tau}^{image}\right| = \frac{\mu^*}{2}\frac{b}{a}\left(\frac{a^3}{r^3}\right)\left(\frac{r^4}{a^2r^2-a^4} - 2\frac{r^2-a^2}{r^2}\sin^2\theta\right)\cos(\theta-\phi_\perp), \tag{4.32}$$

where $\mu^* \triangleq \mu/\pi(1-\nu)$ with μ and ν being the shear modulus and Poisson ratio, respectively. Since dislocation emission is expected to occur at very high stresses, it is useful to account for the pressure dependence and temperature dependence of the shear modulus, i.e.

$$\mu = \mu_0 + \frac{\partial\mu}{\partial\vartheta}p + \frac{\partial\mu}{\partial\vartheta}\left(\vartheta-\vartheta_0\right), \tag{4.33}$$

where for most materials $\partial\mu/\partial\vartheta < 0$ and $\partial\mu/\partial p > 0$ with μ_0 being the shear modulus at ambient conditions and reference temperature, i.e. $p = 0$ and $\vartheta_0 = 300$K. Representative values for these parameters are provided in Table 4.1.

Notice that Eq. (4.32) contains a physical length scale b/a, which scales the magnitude of the image force. In addition, Eq. (4.32) is always positive, and hence the

image force always acts to pull the dislocation towards the void surface. The resulting net Peach-Koehler force along the slip direction is given as $\tilde{\mathcal{F}}_\xi^{net} = \tilde{\mathcal{F}}_\xi^{app} + \tilde{\mathcal{F}}_\xi^{se} + \tilde{\mathcal{F}}_\xi^{image}$. Combining Eqs. (4.28), (4.29), and (4.32) the net Peach-Koehler force acting along the slip direction of the dislocation is expressed as

$$\begin{aligned}\tilde{\mathcal{F}}_\xi^{net} = &\pm b\left(\frac{\Sigma_m}{1-\tilde{\varphi}} - \frac{\gamma_{se}}{a}\right)\frac{a^2}{r^2}\sin 2(\theta-\phi_\perp) \mp b\frac{\Sigma_{eq}^*}{1-\tilde{\varphi}}\sin 2(\theta+\phi_e) \\ &\mp b\frac{\Sigma_{eq}^*}{1-\tilde{\varphi}}\left(3\frac{a^4}{r^4} - 2\frac{a^2}{r^2}\right)\sin 2(\theta-\phi_e-2\phi_\perp) \\ &- b\frac{\mu^*}{2}\frac{b}{a}\left(\frac{a^3}{r^3}\right)\left(\frac{r^4}{a^2r^2-a^4} - 2\frac{r^2-a^2}{r^2}\sin^2\theta\right)\cos(\theta-\phi_\perp).\end{aligned} \tag{4.34}$$

In addition to governing dislocation emission, the net Peach-Koehler forces described in Eq. (4.34) drive the dynamics of emitted dislocations as they glide away from the void surface.

4.4 A critical stress criterion for dislocation emission in porous materials

Consider now a void suface of discrete atoms undergoing random thermal vibrations. In the present context, such a surface may be thought of as being composed of a very large number of discrete dislocation nuclei that are constantly attempting to escape the void surface with an attempt frequency given by ν_G. Nearly all of the escape attempts fail, because the dislocation is unable to overcome the image forces that pull it back towards the void surface. However, in the rare event that a thermal

vibration momentarily excites the dislocation nuclei to a position far enough from the void surface that the net force on a corresponding full dislocation (along a slip direction away from the surface of the void) becomes positive, i.e. $\tilde{\mathcal{F}}_{\xi}^{net} > 0$, then the dislocation embryo finds itself in an unstable position. Upon reaching this point of instability, the dislocation nuclei may form into either a partial or full dislocation and rapidly glide away from the surface of the void. This process constitutes a single dislocation emission event.

4.4.1 The porous critical emission surface

The radius of a dislocation core, $w_{\perp}$, may be taken as a reasonable upper bound on the maximum distance from the void surface (measured along the slip direction on the glide plane) that may be momentarily achieved in a rare thermal excitation of the dislocation nuclei. In this sense, our assumed conditions for dislocation emission are mathematically consistent with that of Rice and Thomson [116] for emission from cracks and Lubarda et al. [65] for emission from voids, although the atomistic processes governing emission are viewed somewhat differently in the present case. The critical condition for emission on a given glide plane defined by θ and ϕ_e is obtained by substituting $\xi = w_{\perp}$ in Eqs. (4.25) and (4.26), while making use of Eq. (4.34) with

$\tilde{\mathcal{F}}_{\xi}^{net} = 0$, i.e.

$$\tilde{\mathcal{F}}_{\xi}^{net} = 0 = -h_1\left(\frac{\Sigma_m}{1-\tilde{\varphi}} - \frac{\gamma_{se}}{a}\right) + h_2\frac{\Sigma_{eq}^*}{1-\tilde{\varphi}} \pm \frac{\mu^*}{2}\frac{b}{a}\left(\frac{a^3}{r_{cr}^3}\right)\left(\frac{r_{cr}^4}{a^2 r_{cr}^2 - a^4} - 2\frac{r_{cr}^2 - a^2}{r_{cr}^2}\sin^2\theta\right)\cos(\theta - \phi_{\perp}^{cr}), \tag{4.35}$$

where the $\pm$ corresponds to an edge dislocation with $\mathbf{b} = \mp b\mathbf{e}_{\xi}$. The critical radial position r_{cr} is defined by

$$r_{cr}^2 = a^2 + w_{\perp}^2 + 2aw_{\perp}\cos\theta \tag{4.36}$$

and the critical angle $\phi_{\perp}^{cr}$ is defined by

$$\tan(\phi_{\perp}^{cr}) = \frac{w_{\perp}\sin\theta}{a + w_{\perp}\cos\theta} \tag{4.37}$$

The non-dimensional length scales h_1 and h_2 utilized in Eq. (4.35) are respectively termed the mean and deviatoric stress modifiers and are expressed as

$$h_1 \triangleq \frac{a^2}{r_{cr}^2}\sin 2(\theta - \phi_{\perp}^{cr}) \tag{4.38}$$

$$h_2 \triangleq \sin 2(\theta + \phi_e) + \left(3\frac{a^4}{r_{cr}^4} - 2\frac{a^2}{r_{cr}^2}\right)\sin 2(\theta - \phi_e - 2\phi_{\perp}^{cr}). \tag{4.39}$$

Eq. (4.35) may be minimized to obtain the critical angles θ and ϕ_e that minimize the required applied stress for emission, see for example Lubarda [11]. However, the emission of dislocations is likely restricted to a discrete set of closed packed planes in FCC metals, which in general will not necessarily correspond with the critical angles obtained from the minimization of Eq. (4.35). Furthermore, such a minimization results in an algebraically complex emission criterion that may not be easily expressed

in a closed-form. An algebraically simpler closed-form emission criterion may be obtained by assuming that the glide planes most likely to first emit dislocations are those with the highest resolved shear stress at the void surface. Rather than explicitly track the crystallography, here we take the critical angles to be those corresponding to the maximum applied shear stress at the void surface, i.e. $\phi_e^{cr} = \pm n_i \pi/2$ and $\theta^{cr} = \pm\pi/4$ as discussed earlier (Fig. 4.7). Under these conditions, the closed-form expression for the critical image shear stress along the glide plane is obtained as

$$\left|\tilde{\tau}_{cr}^{image}\right| = \frac{\mu^*}{4}\frac{b}{w_\perp}\left\{\frac{\sqrt{2}a + 2w_\perp}{\sqrt{2}a + w_\perp} - \frac{a^2 w_\perp^2\left(\sqrt{2}a + w_\perp\right)\left(\sqrt{2}a + 2w_\perp\right)}{\left(a^2 + w_\perp^2 + \sqrt{2}a w_\perp\right)^3}\right\}^{\dagger}. \tag{4.40}$$

and the closed-form emission criterion may be compactly expressed as

$$\Phi_{Em} = h_1\left|\frac{\Sigma_m}{1-\tilde{\varphi}} - \frac{\gamma_{se}}{a}\right| + \left(\frac{h_2}{\sqrt{3}}\frac{\Sigma_{eq}}{(1-\tilde{\varphi})}\right) - \left|\tilde{\tau}_{cr}^{image}\right|, \tag{4.41}$$

where the subscript Em denotes the dislocation emission process which is active for $\Phi_{Em} \geq 0$. The last term on the right hand side of Eq. (4.41) provides the resistance to emission. The first and second terms provide the driving force for dislocation emission respectively resulting form the applied mean and deviatoric stresses. The non-dimensional length scales h_1 and h_2 utilized in Eq. (4.41) are the stress modifiers,

[†]In the limit of $a \to \infty$ Eq. (4.40) is consistent with the image force associated with a dislocation located some distance d from a planar surface, i.e. $-\mu^* b^2/4d$, see for example Hirth and Lothe [13].

which are obtained as

$$h_1 = \frac{a^3\left(a+\sqrt{2}w_\perp\right)}{\left(a^2+w_\perp^2+\sqrt{2}aw_\perp\right)^2} \tag{4.42}$$

$$h_2 = 1 + \frac{a^2\left(a^2-2w_\perp^2-2\sqrt{2}aw_\perp\right)\left(a^4-w^4+2\sqrt{2}a^3w_\perp-2\sqrt{2}aw_\perp^3\right)}{\left(a^2+w_\perp^2+\sqrt{2}aw_\perp\right)^4}, \tag{4.43}$$

from the evaluation of their definitions given in Eqs. (4.38) and (4.39) for $\phi_e^{cr} = \pm n_i\pi/2$ and $\theta^{cr} = \pm\pi/4$. In the limit of large void sizes relative to the dislocation core size, i.e. $a >> w_\perp$, it is clear from Eqs. (4.42) and (4.43) that $h_1 \to 1$ and $h_2 \to 2$, in which case the critical emission surface simplifies to

$$\Phi_{Em} = \left|\frac{\Sigma_m}{1-\tilde{\varphi}} - \frac{\gamma_{se}}{a}\right| + \left(\frac{2}{\sqrt{3}}\frac{\Sigma_{eq}}{(1-\tilde{\varphi})}\right) - \left(\frac{\mu^*}{4}\frac{b}{w_\perp}\right). \tag{4.44}$$

The emission criterion represented by Eq. (4.41) is far simpler than any criterion that results from the minimization of Eq. (4.35). Furthermore, it is entirely possible that dislocation emission actually occurs at the location on the void surface corresponding to the maximum applied shear stress. Detailed molecular statics calculations may shed more light on the governing mechanism. Nevertheless, we proceed with Eq. (4.41) as a suitable closed-form emission criterion.

One disadvantage of the derived emission surface expressed in Eq. (4.41) is that it has a number of sharp corners, which are often undesirable in computational frameworks. This may be remedied by augmenting Eq. (4.41) with a fictitious smoothing exponent η, i.e.

$$\Phi_{Em} = \left\{h_1^\eta\left|\frac{\Sigma_m}{1-\tilde{\varphi}} - \frac{\gamma_{se}}{a}\right|^\eta + \left(\frac{h_2}{\sqrt{3}}\frac{\Sigma_{eq}}{(1-\tilde{\varphi})}\right)^\eta - \left|\tilde{\tau}_{cr}^{image}\right|^\eta\right\}^{1/\eta}, \tag{4.45}$$

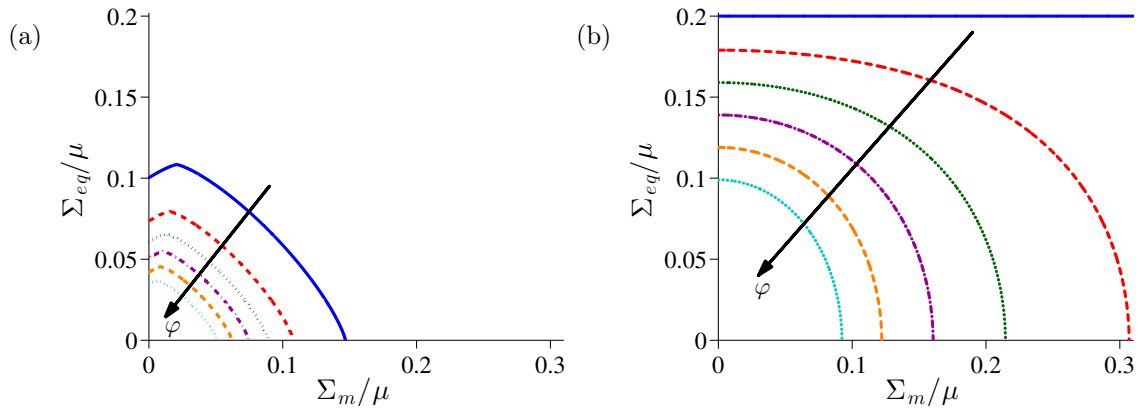

Fig. 4.8: Comparison of (a) our porous *critical emission surface*, i.e. Eq. (4.45), with (b) the *ideal* Gurson yield surface associated with homogeneous dislocation nucleation, i.e. Eq. (4.46) with $\sigma_y = \mu/5$, in hydrostatic-equivalent stress space. The arrows indicate increasing physical porosity varying as $\varphi = \{0; 0.1; 0.2; 0.3; 0.4; 0.5\}$. ($b = 2.55\text{Å}; w_\perp = b; a = 2$ nm; $\gamma_{se} = 2$ J/m^2; $\nu = 1/3; g(a) = \delta(a - \bar{a}); \eta = 1.3$).

where Eq. (4.41) and Eq. (4.45) are equivalent for $\eta = 1$; however, for $2 \leq \eta\infty$ Eq. (4.45) has the advantage of being a completely smooth surface with no sharp corners. The corners are completely smoothed for cases in which $\eta \geq 2$. In addition to providing smoothing, η may be thought of as a parameter that governs the shape of the emission surface.

In order to establish the proper context it is useful to compare our critical emission surface for porous materials with the celebrated porous yield surface of Gurson [77], i.e.

$$\Phi_G = \left(\frac{\Sigma_{eq}}{\sigma_y}\right)^2 + 2\varphi \cosh\left(\frac{3\Sigma_m}{2\sigma_y}\right) - \left(1 + \varphi^2\right), \tag{4.46}$$

with the subscript G denoting Gurson [77] yield surface and σ_y being the yield strength of the solid material surrounding the voids. Setting this solid material yield strength to its ideal value, i.e. $\sim \mu/5$, gives an approximation (albeit a poor one) for the condi-

tions required to induce void growth by homogenous nucleation of dislocations in the solid material. Hence, $\sigma_y = \mu/5$ in Eq. (4.46) serves as a somewhat suitable comparison to our emission criterion expressed in Eq. (4.45). Fig. 4.8 provides a comparison of these two surfaces as a function of porosity. Clearly, the critical emission surface shown in Fig. 4.8(a) easily fits within the *ideal* Gurson yield surface indicating that void growth by dislocation emission is easier than growth by homogeneous dislocation nucleation. This is not necessarily the case for extremely small voids that are only a few vacancies in size, as will be discussed further in subsection 4.4.2; nor is it necessarily the case for some void size distributions at large porosities as discussed in subsection 4.4.3.

Notice that the critical emission surface is asymmetric, while the *ideal* Gurson yield surface is symmetric with respect to the mean stress Σ_m. Here this tension-compression asymmetry is driven by the surface tension at the void surface with the peak of the critical emission surface shown in Fig. 4.8(a) occurring at $\Sigma_m = (1-\tilde{\varphi})\gamma_{se}/a$ (always on the tensile side of the surface for $\gamma_{se} > 0$). Interestingly, spontaneous emission of dislocations is theoretically possible if the surface energy is high enough. Subsection 4.6.3 provides a discussion of this curious mechanism. In subsection 4.6.4 we revisit the concept of a tension-compression asymmetry in the critical emission surface considering a pressure-dependent shear modulus, and a predicted anomalous temperature-dependence of the emission surface is studied in subsection 4.6.5.

The shapes of the two surfaces are also somewhat different, particularly at low porosities where the classic Gurson [77] yield surface becomes elongated with respect to the mean stress Σ_m. The shapes of the two surfaces are most similar for cases in which the fictitious smoothing exponent (or shape exponent) η assumes a value of about 2, compare Fig. 4.14 and Fig. 4.8(b), for example. Interestingly, in section 4.5 it is shown that $\eta = 2$ also brings the critical emission surface in close agreement with predictions of molecular dynamics simulations.

4.4.2 Length scales and size effects associated with the criterion for dislocation emission

The porous critical emission surface contains several important physical and non-dimensional length scales that govern the size effects associated with dislocation emission. The length scales and associated expected ranges include:

- The physical void size, a, $\mathcal{O}(1\text{Å}-1\text{mm})$
- The non-dimensional length scale, $0.5 \lesssim b/w_\perp \lesssim 2$
- The non-dimensional length scale, $a/w_\perp$, $\mathcal{O}(1 - 10^7)$
- The non-dimensional stress modifiers, $0 \leq h_1 \leq 1$, and $1 \lesssim h_2 \leq 2$

The physical length scale a enters into the emission criterion only through the surface tension term in Eq. (4.45). If surface tension is negligible than this physical length

scale does not play a significant role. The non-dimensional length scale, $b/w_\perp$, is vital as it linearly scales the magnitude of the critical image shear stress $|\tilde{\tau}_{cr}^{image}|$, see Eq. (4.40). The smaller the dislocation core size in relation to the magnitude of the Burgers' vector b, the larger the image shear stress and thus the material is more resistant to dislocation emission.

Fig. 4.9 demonstrates this linear dependence of $b/w_\perp$ on the critical stress required for dislocation emission under pure macroscopic hydrostatic tension and compression, i.e. $\Sigma_m > 0$ and $\Sigma_m < 0$ with $\Sigma_{eq} = 0$, and under pure macroscopic hydrostatic loading, i.e. $\Sigma_m = 0$. For simplicity Fig. 4.9 ignores the effects of surface tension, i.e. $\gamma_{se} = 0$. Fig. 4.9 also demonstrates that generally speaking the smaller the void the more resistant the material is to dislocation emission. One might assume that the void size dependencies shown in Fig. 4.9 are simply governed by the size dependence of $|\tilde{\tau}_{cr}^{image}|$. However, this size dependence is fairly mild (as shown in Fig. 4.10). Instead, these void size effects are to be governed primarily by the size effect associated with surface tension as well as the stress modifiers h_1 and h_2 (as shown in Fig. 4.10). Furthermore, the unbounded resistance to dislocation emission under hydrostatic loading (Fig. 4.9(a)) will be discussed and attributed to the behavior of h_1, and the peculiar void size effects under pure deviatoric loading (Fig. 4.9(b)) will be attributed to a similar anomalous size dependence of h_2.

The non-dimensional length scale $a/w_\perp$ enters the emission criterion in a number of places. For example, it enters the the critical image shear stress $|\tilde{\tau}_{cr}^{image}|$. In Eq. (4.40)

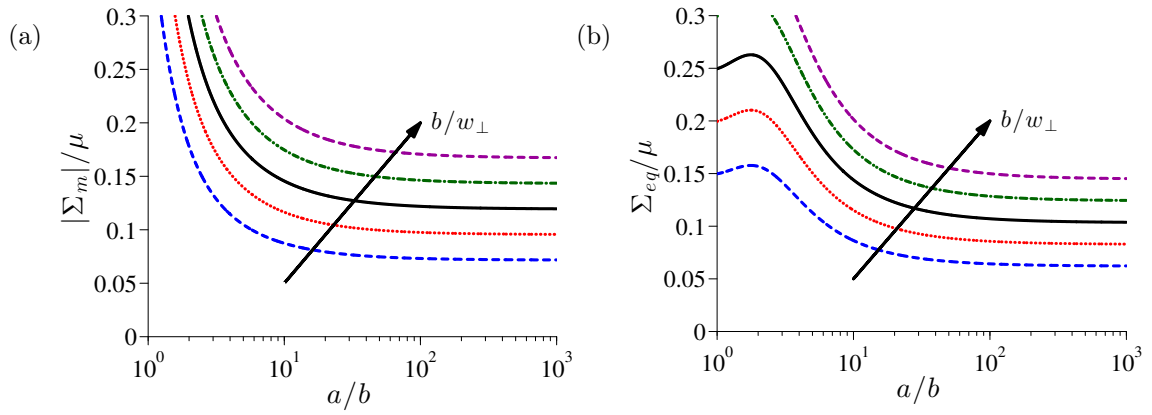

Fig. 4.9: Size effect associated with the critical stress required for dislocation emission (a) under pure macroscopic hydrostatic tension and compression, i.e. $\Sigma_m > 0$ and $\Sigma_m < 0$ with $\Sigma_{eq} = 0$, and (b) under pure macroscopic hydrostatic loading, i.e. $\Sigma_m = 0$, ignoring the effects of surface tension, i.e. $\gamma_{se} = 0$. The arrows indicate increasing non-dimensional inverse core size varying as $b/w_\perp = \{0.6; 0.8; 1.0; 1.2; 1.4\}$. ($b = 2.86$Å$; \mu = 26$ GPa$; \nu = 1/3; \tilde{\varphi} = 0$).

$a/w_\perp$ governs the size effect of $|\tilde{\tau}_{cr}^{image}|$ associated with the curvature of the void, i.e. $1/a^2$. As $a/w_\perp$ becomes smaller the critical image shear stress increases. However, this size effect is rather mild, see for example the solid (blue) curve in Fig. 4.10.

The major impact of $a/w_\perp$ comes in its relationship to the non-dimensional length scales h_1 and h_2, defined in Eqs. (4.42) and (4.43). As $a/w_\perp$ varies from very large values, i.e. $a/w_\perp \gtrsim 10^2$, to very small values, i.e. $a/w_\perp \lesssim 3$, the mean stress modifier h_1 monotonically decays from a value of 1 to 0, while the deviatoric stress modifier h_2 decays non-monotonically from a value of 2 to 1, see Fig. 4.10. Note that the size dependence of h_1 is stronger than that of h_2 for small values of $a/w_\perp$. The size dependence of the mean stress modifier h_1 is similar to that of the surface tension γ_{se}/a as shown in Fig. 4.10.

Physically, each stress modifier converts the respective macroscopic applied stress into a local shear stress on the glide plane of interest at a finite distance from the void surface $\xi = w_\perp$. Recall from Eq. (4.29) that the resolved shear stresses generated by the applied mean stress decay as a^2/r^2. Therefore, the shear stress will be highest on the void surface ($\xi = 0$) and somewhat smaller at ($\xi = w_\perp$). When $a/w_\perp >> 1$ the two shear stresses at $\xi = 0$ and $\xi = w_\perp$ are for all practical purposes equivalent. However, when $a/w_\perp$ is $\mathcal{O}(1)$ the applied shear stress at the critical emission point ($\xi = w_\perp$) is significantly lower than the applied shear stress at the void surface ($\xi = 0$). As such, the mean stress modifier takes on a lower value for low values of $a/w_\perp$ as shown in Fig. 4.10. A similar argument holds for the deviatoric stress with the main exception being that the shear stress field generated by the applied deviatoric stress has a component that is constant with respect to the radial position (the second term of Eq. (4.29)). So unlike h_1 the deviatoric stress modifier approaches 1 rather than 0 for small values of $a/w_\perp$.

These size dependencies of the non-dimensional length scales h_1 and h_2 are vital as these stress modifiers respectively scale the magnitude of the average mean stress in the solid material, i.e. $\Sigma_m/(1-\tilde{\varphi})$, and surface tension, i.e. γ_{se}/a, as well as the average equivalent stress in the solid material, i.e. $\Sigma_{eq}/(1-\tilde{\varphi})$, as shown in Eq. (4.45). Therefore the smaller the value of h_1 and h_2 the larger the critical macroscopic load required to overcome the image stresses experienced by a dislocation attempting to escape the void surface. Since h_2 always takes on a non-zero value the critical stress

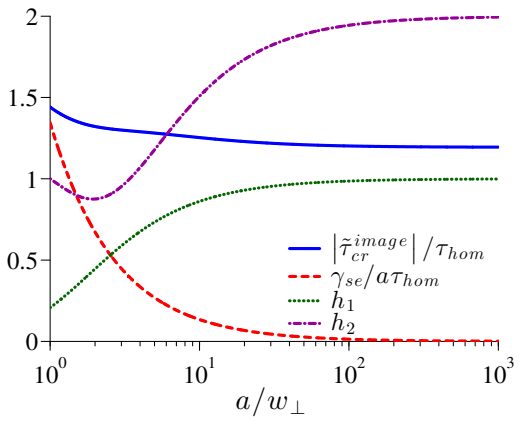

Fig. 4.10: Various physical and non-dimensional length scales that govern the size effects associated with the critical macroscopic stress required for dislocation emission, i.e. Eq. (4.45). Here $\tau_{hom} = \mu/10$ is utilized as a normalizing parameter for for the surface tension term (γ_{se}/a) and the critical image shear stress $|\tilde{\tau}_{cr}^{image}|$ defined in Eq. (4.40) (with $b = w_\perp$ here). The non-dimensional stress modifiers h_1 and h_2 govern the magnitude of the local stresses at a distance $w_\perp$ from the void surface, and are defined in Eqs. (4.42) and (4.43).

for emission under (nearly) pure deviatoric loading, i.e. $\Sigma_{eq} >> |\Sigma_m|$, is expected to remain finite in the limit of infinitesimally small voids. This is not true for purely hydrostatic loading since $h_1 \to 0$ in the limit of $a/w_\perp \to 0$. With $h_1 = 0$ an infinite mean stress is required for emission. These trends are shown in Fig. 4.9.

When surface tension is ignored, i.e. $\gamma_{se} = 0$, the void size effect associated with the critical stress for dislocation emission (shown in Fig. 4.9) is primarily governed by the non-dimensional length scales h_1, h_2, and $b/w_\perp$. The non-dimensional length scale $a/w_\perp$ plays an important role only through h_1 and h_2 with the size effects associated with the critical image shear stresses being fairly negligible in comparison. The dominant role of the mean stress modifiers on the void size effect may also be inferred from comparisons of the shape of the curves reported in Fig. 4.9(b) and the shape

of the curve for h_2 reported in Fig. 4.10. The shape of the curves appear to be near reflections of one another. Similarly, the void size effect associated with dislocation emission under pure hydrostatic loading is dominated by the mean stress modifier h_1 (when surface energy is ignored). Such details of the underlying physics governing the size effect for dislocation emission have not been discussed in the previous literature.

Lastly, it should also be noted that if the physical length scale $b/w_\perp$ is treated as an arbitrary fitting parameter, as in Fig. 4.9, than the emission criterion can be somewhat arbitrarily brought into agreement with experimentally observed or atomistically computed critical stresses. To alleviate some of this arbitrariness, a strategy for obtaining more realistic values of $b/w_\perp$ is outlined in subsection 4.5.2.

4.4.3 Role of the void size distribution and finite porosity

One of the primary advancements of the current dislocation emission analysis over previous analyses, e.g. Lubarda [11], is the ability to treat dislocation emission in porous materials with finite porosities. In subsection 4.5.6 it will be shown that this is a critical addition necessary to understanding the failure response of ductile materials whose void growth is governed by dislocation emission. The role of the auxiliary porosity $\tilde{\varphi}$ on the critical stress for dislocation emission is rather clear from Eq. (4.45), with the critical macroscopic stress essentially decaying linearly with aux-

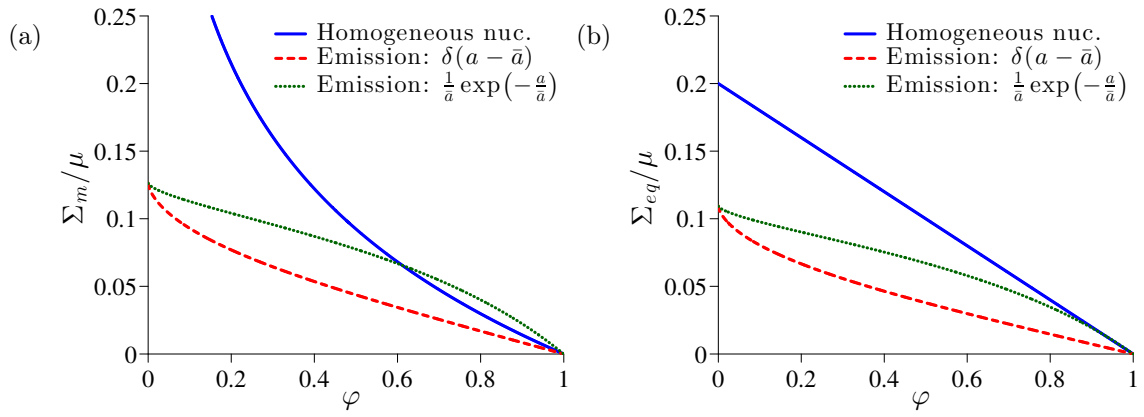

Fig. 4.11: Role of porosity and void size distribution on critical stress required for dislocation emission under (a) pure hydrostatic tension and (b) pure deviatoric stress. These critical stresses are compared with the ideal Gurson model demonstrating that homogeneous dislocation nucleation requires more stress than dislocation emission for most realistic conditions. ($\sigma_y = \mu/5; b = 2.55\text{Å}; w_\perp = b; a = 2$ nm; $\gamma_{se} = 2$ J/m^2; $\nu = 1/3$).

iliary porosity. However, the relationship between the critical macroscopic stress and the physical porosity φ is not immediately clear since $\varphi \neq \tilde{\varphi}$.

Fig. 4.11 demonstrates how the critical macroscopic stress for dislocation emission decays with increasing physical porosity φ. Notice that the softening response is somewhat non-linear and dependence on the particular void size distribution. For realistic values of physical porosity, i.e. $\varphi \lesssim 60\%$, we predict that the critical stress required for dislocation emission in a material possessing an exponential distribution of void sizes, i.e. $g(a) = \bar{a}^{-1} \exp(-a/\bar{a})$, will decrease nearly linearly with increasing physical porosity φ. On the other hand, we predict that the critical stress will decay faster than linearly with increasing porosity for a material possessing a delta distribution of void sizes, i.e. $g(a) = \delta(a - \bar{a})$.

Fig. 4.11 also provides a comparison of our porous critical emission surface with the *ideal* Gurson yield surface associated with homogeneous dislocation nucleation, i.e. Eq. (4.46) with $\sigma_y = \mu/5$. For the void size considered, Fig. 4.11(b) implies that dislocation emission is easier than homogeneous dislocation nucleation under (nearly) pure deviatoric loading, i.e. $\Sigma_{eq} >> |\Sigma_m|$, across the entire range of porosities. However, Fig. 4.11(a) implies that under (nearly) hydrostatic loading it may be possible for homogeneous dislocation nucleation to be easier than dislocation emission at very large porosity. It would be interesting to study the response of a nanoporous material possessing at least a few different void sizes utilizinglar dynamics simulations. This would allow us to test the predicted dependence on void size distribution. Unfortunately, this is beyond the scope of the current work. However, subsection 4.5.5 provides some degree of validation of the porosity dependence associated with a delta distribution of void sizes, i.e. $g(a) = \delta\left(a - \bar{a}\right)$.

4.5 Utilization of molecular dynamics simulations for the calibration and validation of the porous critical emission surface

Prior to detailed discussion of the implications of our critical emission surface, which constitutes the remainder of this chapter, it is worthwhile comparing the emis-

sion criterion with predictions of molecular dynamics simulations. Of course the molecular dynamics simulations are necessarily nonequilibrium in nature, while the emission criterion expressed in Eq. (4.45) is an equilibrium calculation. Nevertheless, the comparison is useful in examining the general trends associated with the dependence of stress state, void size, porosity, and temperature on the critical stress required for dislocation emission.

4.5.1 Overview of molecular dynamics simulations

The molecular dynamics simulations utilize an embedded-atom method (EAM) potential representative of face-centered-cubic (FCC) copper [128, 129]. Unless otherwise noted, the simulations probe the stress-strain response of a three-dimensional cube of single crystal copper material constructed such that the {100} planes are aligned with the faces of the simulation cube. Under equilibrium conditions the side length of the simulation cube is ℓ and the radius of the spherical void is a with the associated physical porosity being φ. The simulations make use of periodic boundary conditions that are, to some degree, equivalent to an infinitely extended array of equi-sized spherical voids positioned on cubic lattice. As such, $g(a) = \delta(a - \bar{a})$ in the remainder of this chapter. Constant velocity gradients are applied, which are equivalent to a constant engineering strain rate $\dot{\epsilon}$ that may be systematically varied. By independently applying the strain rates along the three principle directions the molecular dynamics simulations can probe different loading conditions. For example,

uniaxial deformation, biaxial deformation, and triaxial deformation are respectively achieved by increasing the simulation cube dimension in one, two, or three directions while holding the other dimensions fixed. These types of simulations make use of either an NVT or NVE ensemble, i.e. a system composed of a fixed number (N) of discrete atoms/molecules/particles at a fixed undeformed volume (V) and either a fixed temperature (T) or fixed energy (E). Alternatively, a uniaxial stress or biaxial stress condition may be achieved through the use of a NPT or NPE ensemble, where the pressure on two (or four) parallel faces is held constant at ambient conditions. Note that a thermostat is required to fix the temperature by exchanging thermal energy with a heat bath. For fixed energy (E) calculations, the temperature is allowed to evolve as a result of the thermoelastic effect or inelastic dissipation.

It is difficult to define stress at the atomistic length scales. One measure of the stress tensor volumetrically averaged over the entire simulation cube, i.e. Ω_{micro}, may be obtained from the virial method [130], i.e.

$$\Omega_{micro}^{-1} \iiint_{\Omega_{micro}} \boldsymbol{\sigma} d\Omega_{micro} = -\Omega_{micro}^{-1} \sum_{\alpha=1}^{n_{atoms}} \left(\frac{\mathbf{p}^{(\alpha)} \otimes \mathbf{p}^{(\alpha)}}{m^{(\alpha)}} + \sum_{\beta>\alpha}^{n_{atoms}} \mathbf{r}^{(\alpha \leftrightarrow \beta)} \otimes \mathbf{f}^{(\alpha \leftrightarrow \beta)} \right), \tag{4.47}$$

where m^{α} and $\mathbf{p}^{\alpha}$ is the mass and momentum of the α-th atom with n_{atoms} being the total number of atoms in the simulation domain. The interatomic forces between the α-th atom and the β-th atom are denoted as $\mathbf{f}^{(\alpha \leftrightarrow \beta)}$ with their corresponding interatomic separation denoted as $\mathbf{r}^{(\alpha \leftrightarrow \beta)}$. By definition this virial stress is equivalent to our macroscopic stress tensor $\boldsymbol{\Sigma}$ defined in Eq. (4.9), hence comparisons of the virial

stress tensor with our macroscopic critical stress criterion for dislocation emission, i.e. Eq. (4.45), and the macroscopic criterion for homogeneous dislocation nucleation, i.e. Eq. (4.46) with $\sigma_y = \mu/5$, are sensible.

The macroscopic signature of dislocation emission is typically associated with a rapid collapse of the macroscopic stress, see for example Fig. 1 and Fig. 2 of [66]. However, it is theoretically possible for dislocation emission to occur prior to this rapid collapse of the stress. Therefore, a careful analysis of the centrosymmetry parameter is very helpful in identifying the precise stress at which dislocation nucleation first occurs. For FCC metals, the centrosymmetry parameter for the α-th atom is defined as

$$\zeta_{cs}^{(\alpha)} = \sum_{\beta=1}^{6} \left| \mathbf{R}^{(\alpha \leftrightarrow \beta)} + \mathbf{R}^{(\alpha \leftrightarrow \beta+6)} \right|^2, \tag{4.48}$$

where $\mathbf{R}^{(\alpha \leftrightarrow \beta)}$ is set of 12 vectors that define the interatomic separation between the α-th atom and its 12 nearest neighbors. The set of nearest neighbor vectors is assembled such that $\mathbf{R}^{(\alpha \leftrightarrow \beta)} = -\mathbf{R}^{(\alpha \leftrightarrow \beta+6)}$ for a perfect FCC crystal. Thus, $\zeta_{cs} = 0$ for a perfect crystal. Various defects, e.g. partial dislocations, full dislocations, stacking faults, grain boundaries, and surface atoms may be identified by their centrosymmetry parameter. In the event that a careful centrosymmetry analysis is not performed than we resort to comparing the critical emission surface with the observed peak stresses.

4.5.2 Calibration of the temperature dependence of the dislocation core size

The greatest unknown in the criterion for dislocation emission is the dislocation core size $w_\perp$. In the literature, the core size has been traditionally treated as a fitting parameter. This approach unnecessarily constricts the predictive power of the derived criterion for dislocation emission and may lead to some confusion in the analysis of dislocation emission. It is therefore desirable to be able to at least approximately calibrate the dislocation core size independently of the atomistic calculations used to validate the theoretical model. One way to do this is to simply measure the dislocation core size under high resolution transmission electron microscopy. From these observations, one could obtain a reference core size as well as its temperature dependence. However, we are not actually interested the dislocation core per se, but rather the maximum displacement that a dislocation nuclei may be perturbed from equilibrium by a rare thermal excitation. We have assumed that this maximum thermal excitation is of similar magnitude as the dislocation core size, but strictly speaking it is not identical to the dislocation core size. Therefore, it may be more appropriate to calibrate the *dislocation core size* with another critical dislocation phenomena.

Consider, for example, the homogeneous nucleation of a single dislocation loop. In an idealized two-dimensional view, the process of dislocation loop nucleation may

Table 4.2: Measures of dislocation size for aluminum and copper.

Property	Units	Copper	Aluminum
Burgers vector magnitude, b	Å	2.55	2.86
Absolute zero core size, $w_{\perp}^{0\mathrm{K}}$	Å	2.88	2.15
Temperature dependence of core size, q_0	–	0.59	0.43

be mechanistically thought of as a perfect plane of atoms continuously attempting to split into two opposite-signed full dislocations (on the same glide plane). Nearly all of these split attempts fail, because the two dislocation nuclei are unable to overcome their mutual attraction. However, a nucleation event may occur in the rare event that a thermal excitation perturbs the two dislocation nuclei enough to overcome their mutual attraction. In the same spirit as our criterion for dislocation emission, each dislocation may be perturbed by a maximum displacement given by $w_{\perp}$, resulting here in a total separation distance of $d = 2 \times w_{\perp}$. The magnitude of the attractive line force between two opposite-signed dislocation is given as $\mu^* b^2/2d$. The magnitude of the line force that results from the applied loading is τb. An unstable equilibrium position is achieved when these two forces balance, and thus a simple criterion for homogeneous dislocation nucleation may be expressed as

$$\tau_{hom} = \frac{\mu^* b}{4 w_{\perp}}. \tag{4.49}$$

At room temperature ($\vartheta = 300\mathrm{K}$) the critical shear stress required for homogeneous

dislocation was observed to be $\tau_{hom} = 2.2$ GPa and $\tau_{hom} = 1.8$ GPa for copper and aluminum, respectively, according to molecular dynamics calculations reported in [131]. The dislocation core sizes that bring Eq. (4.49) into agreement with the observed homogeneous nucleation shear stresses are $w_\perp = 1.3 \times b$ and $w_\perp = 0.87 \times b$ for copper and aluminum, respectively. Likewise, $w_\perp = 1.13 \times b$ and $w_\perp = 0.75 \times b$ result in a good agreement of Eq. (4.49) and the corresponding molecular dynamics simulations at absolute zero ($\vartheta = 0$K), when the temperature dependence of the shear modulus is properly accounted for, i.e. Eq. (4.55). The core size used in the analysis of dislocation emission at room temperature and absolute zero should be fairly similar to these values corresponding to homogeneous dislocation nucleation.

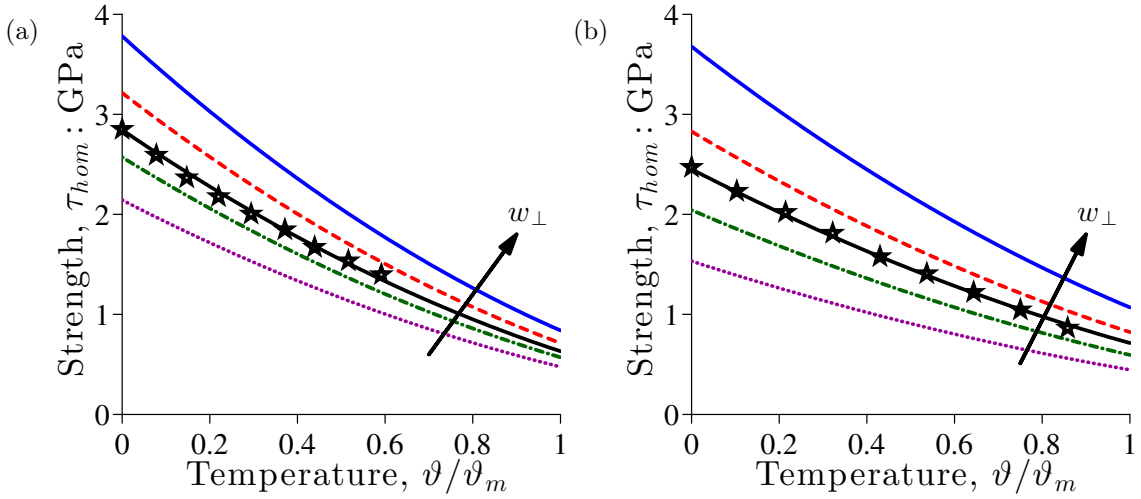

Fig. 4.12: Calibration of temperature-dependent dislocation core size for (a) copper and (b) aluminum. The arrows indicate increasing absolute zero dislocation core size varying as $w_\perp^{0\text{K}}/b = \{0.85; 1.0; 1.13; 1.25; 1.5\}$ in (a) and as $w_\perp^{0\text{K}}/b = \{0.5; 0.65; 0.75; 0.9; 1.2\}$ in (b). The symbols correspond to molecular dynamics simulations reported in [131]. Appropriate thermoelastic properties are provided in Table 4.1 with core size parameters provided in Table 4.2.

The temperature dependence of the core size may be obtained by fitting a simple temperature-dependent function to $w_\perp$, e.g.

$$\frac{1}{w_\perp} = \frac{1}{w_\perp^{0\mathrm{K}}}\left(1 - q_0\frac{\vartheta}{\vartheta_m}\right), \tag{4.50}$$

where $w_\perp^{0\mathrm{K}}$ is the value of the dislocation core size at absolute zero, q_0 is fitting constant, and ϑ_m is the absolute melting temperature. Accounting for the temperature dependence of both the shear modulus and the core size in Eq. (4.49), we find that $q_0 = 0.59$ and $q_0 = 0.43$ brings the theoretical model into good agreement with the molecular dynamics predictions reported in [131], as shown in Fig. 4.12.

4.5.3 Validation of hydrostatic tension-compression asymmetry and minor adjustment of absolute zero core size

As discussed in subsection 4.6.4 a tension-compression asymmetry is expected in the critical mean stress required to emit dislocations. The resulting tension-compression asymmetry is governed by a competition between the pressure-dependence of the shear modulus, i.e. $\partial\mu/\partial p$, and a finite surface energy γ_{se}. It is not immediately clear which mechanism will win out. If the pressure-dependence of the shear modulus is dominant than dislocation emission will require a higher stress magnitude in compression compared with tension. On the other hand, if the surface tension is

dominant than dislocation emission will require a higher stress magnitude in tension as compared with compression. Therefore, capturing the correct tension-compression asymmetry provides some measure of validation of our criterion for dislocation emission.

The author is aware of two molecular dynamics studies that investigated the critical stress required to emit dislocations under both tensile and compressive hydrostatic stresses. Both investigations make use of a careful centrosymmetry analysis to determine the stress at which point the dislocation is first emitted. This is particularly important for analyzing dislocation emission in compression as the stress never collapses and the macroscopic stress-strain response is fairly unaffected by emission.

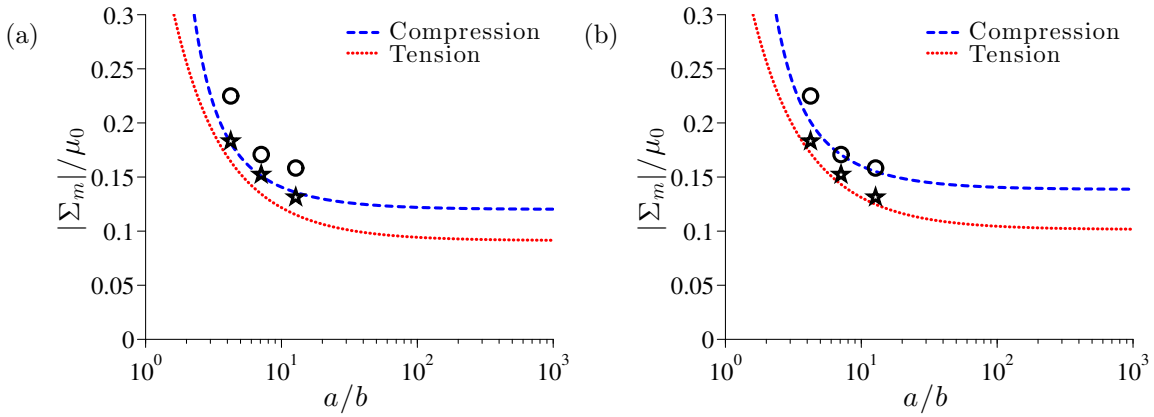

Fig. 4.13: Observed and predicted tension-compression asymmetry associated with the critical stress required for dislocation emission from a void of size a considering a pressure and temperature-dependent shear modulus (Table 4.1) and a finite surface energy $\gamma_{se} = 1.8$ J/m^2. The symbols represent molecular dynamics predictions of the critical emission mean stress at absolute zero ($\vartheta = 0$K) reported in [132] (open circles for compression and stars for tension). (a) makes use of the calibrated dislocation absolute zero core size of $w_\perp^{0\mathrm{K}} = 2.88$Å, while (b) makes use of a slightly adjusted value of $w_\perp^{0\mathrm{K}} = b = 2.55$Å that brings the theory in closer agreement with MD calculations.

One of these studies [115] probed the behavior of tantalum and observed a discernible tension-compression asymmetry. These MD calculations predicted that dislocation emission in compression requires a mean stress magnitude that is about 10% higher than in the case of tensile loading. A similar observation was reported in [132] for dislocation emission in copper at absolute zero ($\vartheta = 0$K). These MD calculations investigated a number of void sizes, and a comparison of the MD calculations and the theoretical predictions (Eq. (4.45) with $\gamma_{se} = 1.8$ J/m^2 [133] and appropriate thermoelastic properties taken from Table 4.1) is provided in Fig. 4.13. The same general trend is observed in both cases with compression requiring a high stress magnitude.

In Fig. 4.5.3 we make use of the absolute zero core size of $w_{\perp}^{0\text{K}} = 2.88$Å that was calibrated by fitting Eq. (4.49) to the MD calculations of homogeneous dislocation nucleation reported in [131]. Although the general trend is captured with this calibrated core size, an even better agreement can be had by slightly adjusting the value of the absolute zero core size to $w_{\perp} = 2.55$Å as shown in Fig. 4.5.3. This adjusted absolute zero core size will be utilized in the remainder of this chapter along with a surface energy of $\gamma_{se} = 1.8$ J/m^2.

4.5.4 Comparison of emission surface with multi-axial MD calculations and calibration of the shape exponent η

In addition to validating the tension-compression asymmetry, subsection 4.5.3 also provides a validation (to some degree) of the size of the emission surface. Here we turn our attention to the general shape of the emission surface, which is primarily governed by the shape exponent η. Investigating the shape of the emission surface requires a comparison with multi-axial MD calculations. A systematic study of this multi-axial response was studied by Seppälä et al. [66] for copper with an initial undeformed average temperature of $\langle \vartheta \rangle = 300\text{K}$ set by a thermostat. Unfortunately, a careful centrosymmetry analysis was not provided, so we resort to comparing our porous critical emission surface with the peak macroscopic stresses reported for the MD calculations. All simulations were performed under tensile loading, so the peak stress is easily discernible, see for example Fig. 1 and Fig. 2 of [66]. That said, the peak stresses are strongly dependent on the imposed strain-rate. As such, the peak stresses should be treated as upper bounds on the critical stress required for emission with the theoretical critical emission surface lying below these upper bounds.

Fig. 4.14 provides a comparison of the porous critical emission surface, i.e. Eq. (4.45) with the peak stresses predicted by the MD calculations reported in [66]. Extrapolating the rate-sensitivity by eye it appears that $\eta = 2$ gives the best agreement with our

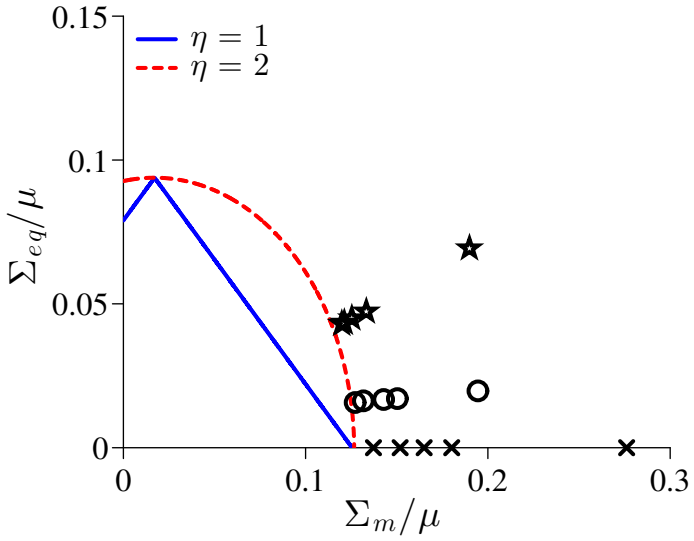

Fig. 4.14: Peak stresses predicted by molecular dynamics simulations for nanoporous copper subject to different stress states (with stars indicating uniaxial extension, open circles representing biaxial extension, and crosses marking triaxial extension) and various macroscopic engineering strain rates of $10^7, 10^8, 5 \times 10^8, 10^9$ and 10^{10} s^{-1} [66]. These MD calculations are compared with our equilibrium porous emission surface, i.e. Eq. (4.45). The plot demonstrates that $\eta = 2$ results in a good agreement between our emission surface and the MD calculations. Material properties are representative of copper and are provided in Table 4.1 with $\bar{a} = 2.16$ nm and $\varphi = 0.42\%$.

critical emission surface. From a computational standpoint this is very convenient as $\eta = 2$ results in a smooth emission surface with no sharp corners. $\eta = 2$ is utilized in the remainder of this chapter. It should also be noted that the *ideal* Gurson yield surface, i.e. Eq. (4.46), significantly over predicts the stress required for dislocation nucleation. As such, it should not be considered a suitable model for these purposes.

4.5.5 Validation of size effect and porosity dependence under uniaxial tension

Investigating a large range of void sizes is computationally demanding for full three-dimensional MD calculations. The computational expense may be significantly reduced by considering cylindrical voids that pierce through a relatively thin square plate of material. Such MD calculations were performed to study the emission of dislocations from cylindrical voids [134]. These particular MD calculations make use of an NPT ensemble to load the material under conditions of uniaxial tension, i.e. $\Sigma_{11} > 0$ with all other macroscopic stresses equal to zero, and the average temperature fixed to absolute zero ($\langle \vartheta \rangle = 0\text{K}$) by a thermostat.

The void size a, as well as the porosity, was systematically varied over a large range. As expected, the critical macroscopic stress required for emission decreases with increasing void size and porosity. Here, since the MD calculations essentially amount to a periodic array of cylindrical voids, this porosity is identical to the auxiliary porosity $\tilde{\varphi}$ in our porous critical emission surface. Fig. 4.15 provides a comparison of the size effect and porosity dependence associated with dislocation emission as predicted by MD calculations and our porous critical emission surface, i.e. Eq. (4.45). The MD calculations made use of the centrosymmetry parameter in determining the critical stress associated with incipient dislocation emission. As such, the agreement between the MD calculations and the theory is remarkable.

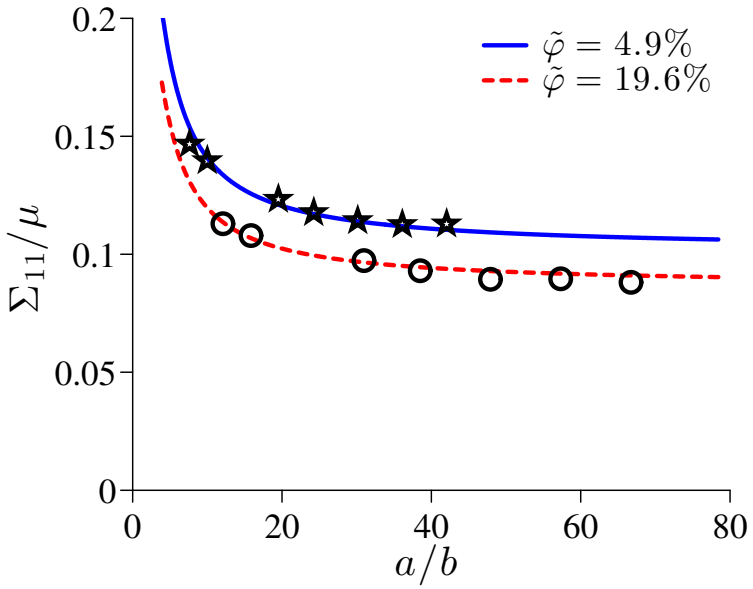

Fig. 4.15: Size effect and porosity dependence associated with the critical stress required for dislocation emission in copper under uniaxial stress conditions. Here the auxiliary porosity is directly known, because these particular MD simulations are for an array of cylindrical voids rather than the array of spherical voids studied elsewhere in this chapter. Material properties are representative of copper and are provided in Table 4.1 with $w_{\perp}^{0\mathrm{K}} = b = 2.55\text{Å}$.

4.5.6 Evolution of critical emission surface with deformation

At this point, our porous critical emission surface has been calibrated and validated (to some degree) through comparisons with molecular dynamics simulations. Up to this point we have primarily focused on the critical stress required to emit the first set of dislocations from the void surface. However, it is (at least theoretically) possible that the critical stress required to emit subsequent dislocations may be substantially different than the stress required to emit the first set of dislocations.

For example, the first set of dislocations could leave behind sharp ledges that may produce local stress concentrators that make subsequent emission easier. If this is the case, then our derived critical emission surface would need to be augmented to account for these effects, otherwise the critical emission surface would be of limited practical use.

In order to address these concerns, we compare our dislocation critical emission surface to molecular dynamics simulations deformed (in extension) well beyond the point at which the first set of dislocations are emitted. As the material continues to deform, the void size increases by approximately a Burgers vector magnitude with each emission event. Additionally, the physical porosity continuously increases with deformation, see for example Fig. 8 of [66]. As a result of the evolution of these two geometric parameters, the critical stress for dislocation emission is continuously reduced. Since Seppälä et al. [66] report the porosity as a function of the current engineering strain it is a simple matter to compute the critical emission surface as a function of this porosity and compare it with the current macroscopic stress in the MD calculations. Such a comparison is provided in Fig. 4.16, where the solid (blue) line accounts for the combined effect of both evolving porosity and void size on the evolution of the critical emission surface. The current equivalent spherical void size may be computed from the current porosity through the following relation:

$$\varphi \frac{1-\varphi_0}{1-\varphi} = \frac{4\pi}{3}\frac{a^3}{\ell^3}, \tag{4.51}$$

where $\varphi_0 = 0.42\%$ is the initial (undeformed) porosity and $\ell = 21.6$ nm are the

simulation cube side lengths prior to deformation. These values correspond to the particular MD calculations considered here. The current porosity and the computed equivalent spherical void size at each time point considered are reported in the top right corner of each subfigure in Fig. 4.16. Notice that the theoretical predictions agree reasonably well with the MD calculations early in the deformation. Although, not shown here the theory predicts a larger critical emission stress than the MD calculations at late stages in the deformation. This would seem to imply that at some point the material becomes significantly less resistant to dislocation emission. This effect may be attributed to the rise in temperature with deformation in the MD calculations, which is not explicitly accounted for here.

Recall that the molecular dynamics simulations utilized here make use of an NVE ensemble rather than an NVT ensemble. As a result the temperature undergoes considerable evolution. The evolution of the average temperature $\langle\vartheta\rangle$ is reported in Fig. 7 of [66]. Prior to the first emission event, the deformation is totally elastic and the temperature decrease due to the thermoelastic effect, see chapter 6 for more details on this. When dislocation emission becomes active, the associated inelastic dissipation results in a temperature rise that typically overtakes the temperature decrease associated with the thermoelastic effect.

Furthermore, Ariza et al. [70] demonstrated in their hot quasi-continuum simulations that once dislocation emission becomes active the local temperature near the void surface may be considerably higher than the average temperature, i.e. $\vartheta_{vs} > \langle\vartheta\rangle$,

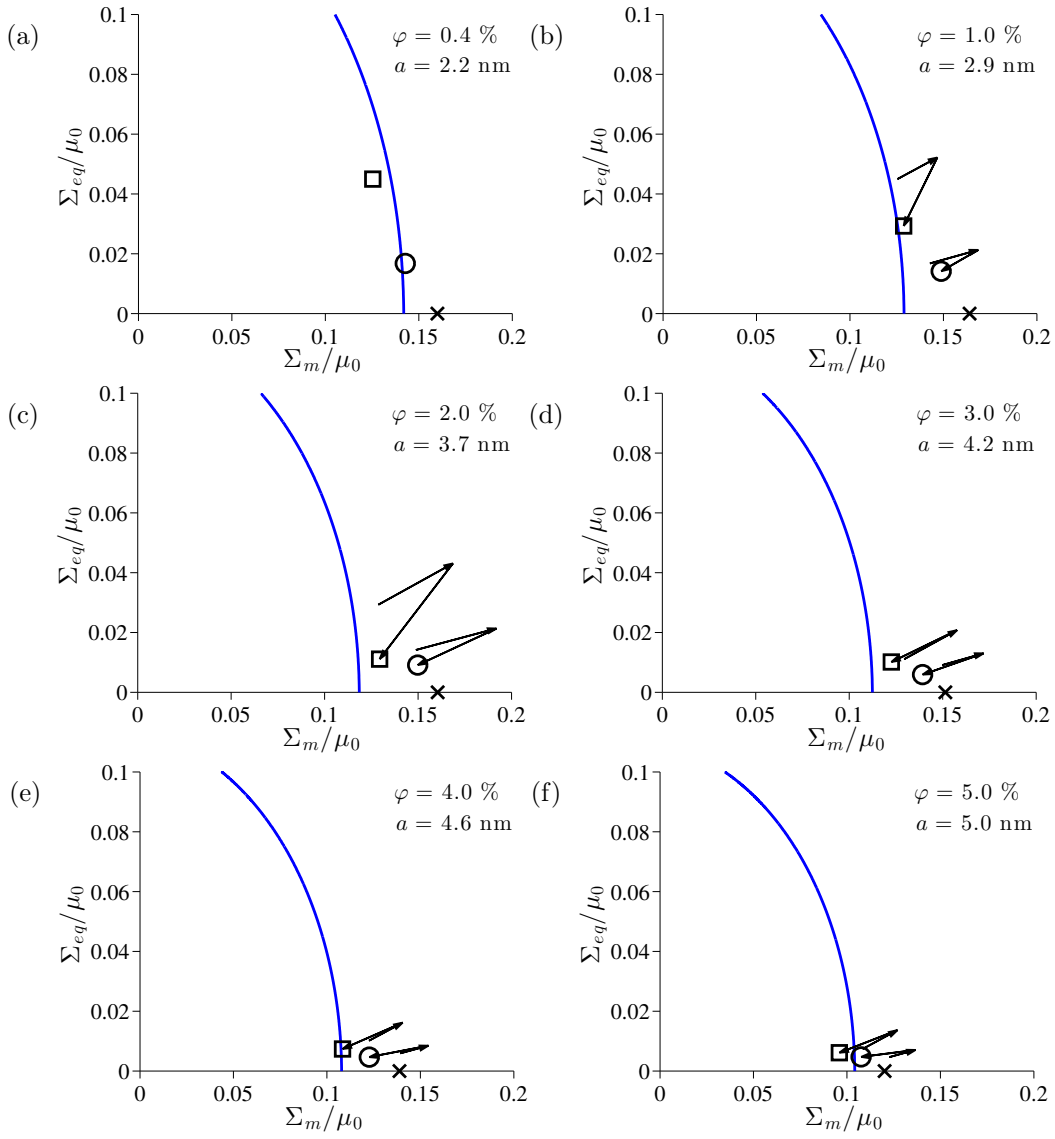

Fig. 4.16: Evolution of our critical emission surface (lines) with tensile deformation compared with MD calculations [66] of the corresponding current macroscopic stress (with squares, circles, and crosses representing uniaxial, biaxial, and triaxial extension, respectively). The solid (blue) lines account for the emission surface softening associated with increasing void size a and porosity φ. The arrows indicate the direction of inelastic flow. Material properties are given in Table 4.1 with the undeformed void size and porosity given as $\bar{a} = 2.16$ nm and $\varphi = 0.41\%$.

provided that the loading timescales are shorter than those required for thermal equilibration (typically the case for MD calculations). Explicitly accounting for the evolution of this nonequilibrium temperature field in our theoretical analysis may bring the predictions into closer agreement with NVE MD calculations at large deformations.

Lastly, it is interesting to examine the relationship between the normal of the emission surface and the direction of inelastic flow (inward pointing arrows in Fig. 4.16). If the two are correlated, than it may be possible to utilize a simple associative flow law to predict the evolution of the emission surface for arbitrary loading paths. The inelastic flow direction is computed by first computing a purely elastic step (the outward pointing arrows in Fig. 4.16) corresponding to the total deformation applied between two subfigures, i.e. $\Delta\boldsymbol{\Sigma} = \mathbb{C}\Delta\boldsymbol{\epsilon}$, where $\mathbb{C}$ is the fourth-order elasticity tensor with elastic constants C_{11}, C_{12}, and C_{44} provided in [66]. The inelastic flow direction is simply the arrow that connects the purely elastic step to the actual stress level computed in the MD calculations. It is clear, from Fig. 4.16 that the norm of the emission surface and the inelastic flow directions are uncorrelated (at least early on in the deformation). This observation implies that a non-associative flow law is required to accurately describe the evolution of the emission surface for an arbitrary loading path. It may be possible to derive such a non-associative flow law by considering the particular kinematics associated with dislocation loop emission. However, this analysis is beyond the scope of the current chapter.

4.6 Some theoretically predicted anomalous behavior induced by high surface energies and nonlinear elasticity

In section 4.4 and section 4.5 the role of surface energy and nonlinear stiffness on dislocation emission was not particularly emphasized. Here we revisit this issue, and demonstrate that a number of anomalous behaviors are (at least theoretically) possible if the material possesses a high enough surface energy. In addition to being an academic curiosity, some of these anomalous behaviors may have technological significance, especially if a greater level of control over surface energy is achieved in the near future through novel materials engineering and alloying strategies. We first focus on the effects of surface energy alone and hold the shear modulus constant. In subsection 4.6.4 and subsection 4.6.5 we revisit the anomalous behaviors considering a pressure and temperature dependent shear modulus.

4.6.1 Tension-compression asymmetry

One interesting prediction of our proposed criterion for dislocation emission, i.e. Eq. (4.45), is a surface-energy induced tension-compression asymmetry. Examining Eq. (4.45) it is clear that the role of a finite surface energy is simply to shift the center of the emission surface from the origin (all macroscopic stresses equal to zero) by some

finite amount in the direction of positive mean stress. This is clearly shown in the comparison of Fig. 4.17(a) with ($\gamma_{se} = 0$) and Fig. 4.17(b) with ($\gamma_{se} > 0$). The critical emission surface is symmetric in Fig. 4.17(a) with ($\gamma_{se} = 0$), while it is shifted towards positive mean stresses in Fig. 4.17(b) with ($\gamma_{se} > 0$). The effect is negligible for larger void sizes, i.e. $a/b \gtrsim 10^2$, which corresponds to the collapse of the surface tension term γ_{se}/a as can be seen in the dashed (red) curve of Fig. 4.10. This tension-compression asymmetry will be revisited considering a pressure-dependent shear modulus in subsection 4.6.4, where it will be shown that for most metals the pressure-dependence of the shear modulus dominates the tension-compression asymmetry for nearly hydrostatic loading conditions, i.e. $|\Sigma_m| >> \Sigma_{eq}$. However, the tension-compression asymmetry associated with nearly pure deviatoric loading states, i.e. $\Sigma_{eq} >> |\Sigma_m|$, is still expected to behave somewhat similarly to Fig. 4.17(b) with the material being somewhat stronger in tension as compared with compression at small void sizes. In addition, if there so happens to be a material that exhibits negligible pressure dependence on its shear modulus, then the tension-compression asymmetry would again be dominated by the surface tension, and a behavior similar to Fig. 4.17(b) would expected.

4.6.2 *Smaller is sometimes weaker*

A second interesting prediction of our proposed criterion for dislocation emission, i.e. Eq. (4.45), is a potential anomalous size effect, with materials becoming less resis-

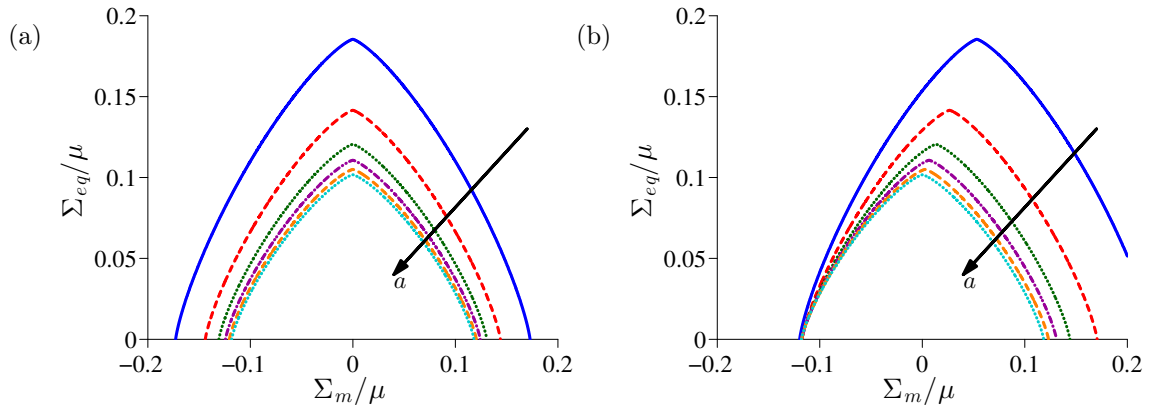

Fig. 4.17: Size dependence of porous critical emission surface, i.e. Eq. (4.45), with (a) no surface energy, i.e. $\gamma_{se} = 0$, and (b) finite surface energy $\gamma_{se} = 2$ J/m^2. The arrows indicate increasing void size varying as $a/b = \{3, 5, 10, 25, 100, 1000\}$. ($b = 2.86$Å$; w_\perp = b; \mu = 26$ GPa$; \nu = 1/3; \tilde{\varphi} = 0; \eta = 1.3$).

tant to dislocation emission at small void sizes. This type of behavior was observed to some degree in Fig. 4.9(b) with the critical stress for emission under (nearly) pure deviatoric loading mildly decreasing with void size below $2 - 3b$. Note that these are extremely small voids, essentially vacancy clusters composed of several vacancies at most. Interestingly, a very similar anomalous size-dependence has been recently observed for dislocation emission in magnesium under pure shear loading [135]. From our analysis, it appears that this is associated with the non-monotonic decay of the resolved shear stress with distance from the void surface, c.f. the second and third terms of Eq. (4.27). Essentially, there is something of a deviatoric stress shielding effect that occurs at $\xi \sim a$, which becomes important when a and $w_\perp$ are or similar magnitude.

The *smaller is weaker* behavior that is the focus of the current subsection is

induced by surface energy rather than the size dependence of h_2. Recall again that surface energy essentially shifts the center of the emission surface by some finite amount in the positive mean stress direction, see Fig. 4.17(b). The higher the surface tension γ_{se}/a the greater this shift. At some point, γ_{se}/a may in principle be so large that its size effects dominate the behavior rather than the size effects associated with mean and deviatoric stress modifiers (h_1 and h_2). In this case, it is possible for the material to be less resistant to dislocation emission at low triaxialities, i.e. $\chi_T \lesssim 0$. Such a behavior is demonstrated in Fig. 4.18 for the highest surface energy considered ($\gamma_{se} = 4$ J/m^2). At high triaxialities, this anomalous size effect of *smaller is weaker* vanishes regardless of the surface energy. This anomalous size effect is revisited in subsection 4.6.4 considering a pressure-dependent shear modulus, and it is shown that

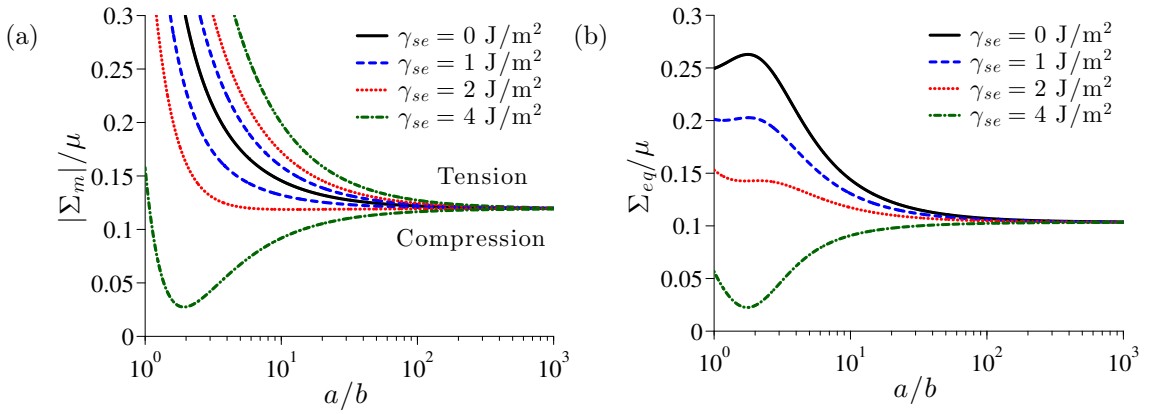

Fig. 4.18: Size effect associated with the critical stress required for dislocation emission (a) under pure macroscopic hydrostatic tension and compression, i.e. $\Sigma_m > 0$ and $\Sigma_m < 0$ with $\Sigma_{eq} = 0$, and (b) under pure macroscopic hydrostatic loading, i.e. $\Sigma_m = 0$. The plots demonstrate that for the most part *smaller is stronger*. However, it is (at least theoretically) possible that *smaller is weaker* for low triaxialities and high surface energies. ($b = 2.86$Å$; w_\perp = b; \mu = 26$ GPa$; \nu = 1/3; \tilde{\varphi} = 0$).

this anomalous size effect may persist provided the surface energy is large enough.

4.6.3 Spontaneous dislocation emission

The final anomalous emission behavior considered here is the possibility of dislocations spontaneously emitting from the surface of dislocations in order to reduce the total energy of the material system. Consider again Fig. 4.17(b), and the shift in the emission surface caused by the surface tension term γ_{se}/a. If this surface tension is large enough, than it is (at least theoretically) possible for the entire emission surface to shift past the origin (defined by all stresses equal to zero). In this case, the point of zero applied macroscopic loading lies outside the critical emission surface and dislocation emission occurs spontaneously. Furthermore, this spontaneous collapse would be unstable if the surface tension γ_{se}/a driving emission increases faster with decreasing void size a than does the critical resistance, i.e. $h_1^{-1}\,|\tilde{\tau}_{cr}^{image}|$. Such a spontaneous collapse of nanovoids by dislocation emission is likely very rare, otherwise it would have most likely been observed by one of the numerous molecular dynamics investigations involving nanovoids.

The condition for spontaneous dislocation emission may be obtained by setting all macroscopic stresses equal to zero in the critical emission surface (Eq. (4.45) with $\Phi_{Em} = 0$), i.e.

$$\frac{\gamma_{se}}{b\mu^*} = \frac{1}{4h_1}\frac{a}{w_\perp}\left\{\frac{\sqrt{2}a + 2w_\perp}{\sqrt{2}a + w_\perp} - \frac{a^2 w_\perp^2\left(\sqrt{2}a + w_\perp\right)\left(\sqrt{2}a + 2w_\perp\right)}{\left(a^2 + w_\perp^2 + \sqrt{2}aw_\perp\right)^3}\right\}, \tag{4.52}$$

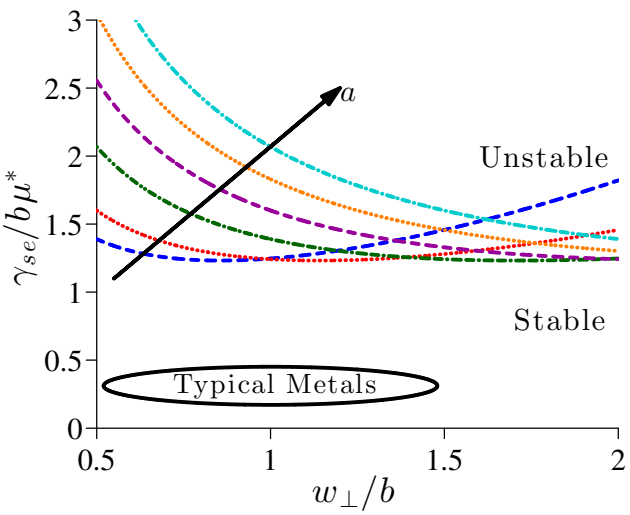

Fig. 4.19: A stability map identifying the regions in which vacancy clusters and nanovoids may spontaneously emit dislocations and collapse unstably under no applied macroscopic loading. The conditions for spontaneous emission depend strongly on the dislocation core size $w_\perp$, the surface energy γ_{se}, and the elastic modulus μ^*. For reference, the typical properties associated with pure FCC metals fall within the indicated ellipse, c.f. [136]. The arrow denotes increasing void size varying as $a/b = \{1.5, 2, 3, 4, 5, 6\}$.

where the right hand side of this criterion for spontaneous emission is simply a combination of the various physical and non-dimensional length scales associated with dislocation emission. Fig. 4.19 provides a stability map for spontaneous dislocation emission computed from Eq. (4.52). The area above (below) the various curves in Fig. 4.19 identifies regions where the material parameter $\gamma_{se}/b\mu^*$ is (not) large enough to permit spontaneous dislocation emission. For reference, the typical properties associated with pure FCC metals fall within the indicated ellipse in Fig. 4.19, c.f. [136]. The authors are unaware of any materials possessing the particular properties necessary for spontaneous emission. On the one hand, this is consistent with the lack of

observations of spontaneous emission in the experimental as well as molecular dynamics literature. On the other hand, it is unfortunate that the design of these materials does not currently appear feasible based on our simple emission criterion. At the very least, our findings should motivate a suite of atomistic investigations attempting to discover possible materials and configurations where spontaneous emission can occur for currently achievable surface energies. Furthermore, it may possible to engineer alloys with the desired combination of surface energy and stiffness characterized by $\gamma_{se}/b\mu^*$. The design of such alloys could be advantageous to a number of applications in the aerospace, defense, and semiconductor industries.

4.6.4 Tension-compression asymmetry revisited considering a pressure-dependent shear modulus

Most materials exhibit a nonlinear shear modulus behavior such that the shear modulus increases with increasing local compressive hydrostatic pressure and decreases with increasing hydrostatic tension, i.e. $\partial\mu/\partial p > 0$, with p being the local hydrostatic compressive pressure (in the second auxiliary problem), i.e. $p = -\tilde{\boldsymbol{\sigma}} : \boldsymbol{I}/3$. It is interesting to revisit the tension-compression asymmetry discussed in subsection 4.4.2 considering this pressure dependence of the shear modulus, e.g.

$$\mu = \mu_0 + \frac{\partial \mu}{\partial p} p, \tag{4.53}$$

where μ_0 is shear modulus at ambient conditions, i.e. $p = 0$, with representative provided in Table 4.1.

In subsection 4.4.2, we analyzed a tension-compression asymmetry in the macroscopic stress required for dislocation emission. This particular tension-compression asymmetry was induced by a non-negligible surface tension. A second source of tension-compression asymmetry results from the pressure dependence of the shear modulus. In our analysis of dislocation emission the shear-modulus scales the magnitude of the image shear stress $|\tilde{\tau}_{cr}^{image}|$ associated with the interaction of the emitting dislocation and the void surface, see Eq. (4.40). Since the image shear stress provides the primary resistance to dislocation emission, a higher applied macroscopic load is naturally required to overcome a higher image shear stress. With $\partial\mu/\partial p > 0$, a higher shear modulus and thus a higher image shear stress $|\tilde{\tau}_{cr}^{image}|$ is induced by a local compressive hydrostatic pressure, i.e. $p > 0$. On the other hand, a lower shear modulus and thus a lower image shear stress is induced by a local tensile pressure, i.e. $p < 0$. Therefore, ignoring for the moment the effects of surface energy, a somewhat lower macroscopic load is required for dislocation emission when the local pressure at $\xi = w_\perp$ is tensile, i.e. $p < 0$, as compared with compressive, i.e. $p > 0$.

The relationship between the local compressive pressure at $\xi = w_\perp$ and the macroscopic loading may be obtained by examining Eqs. (4.14) – (4.16) and making use of Eq. (4.36), i.e.

$$p = -\frac{\Sigma_m}{1-\tilde{\varphi}} + \frac{4}{3}\frac{a^2\cos 2\phi_{cr}}{a^2 + w_\perp^2 + \sqrt{2}aw_\perp}\frac{\Sigma_{eq}^*}{1-\tilde{\varphi}}. \tag{4.54}$$

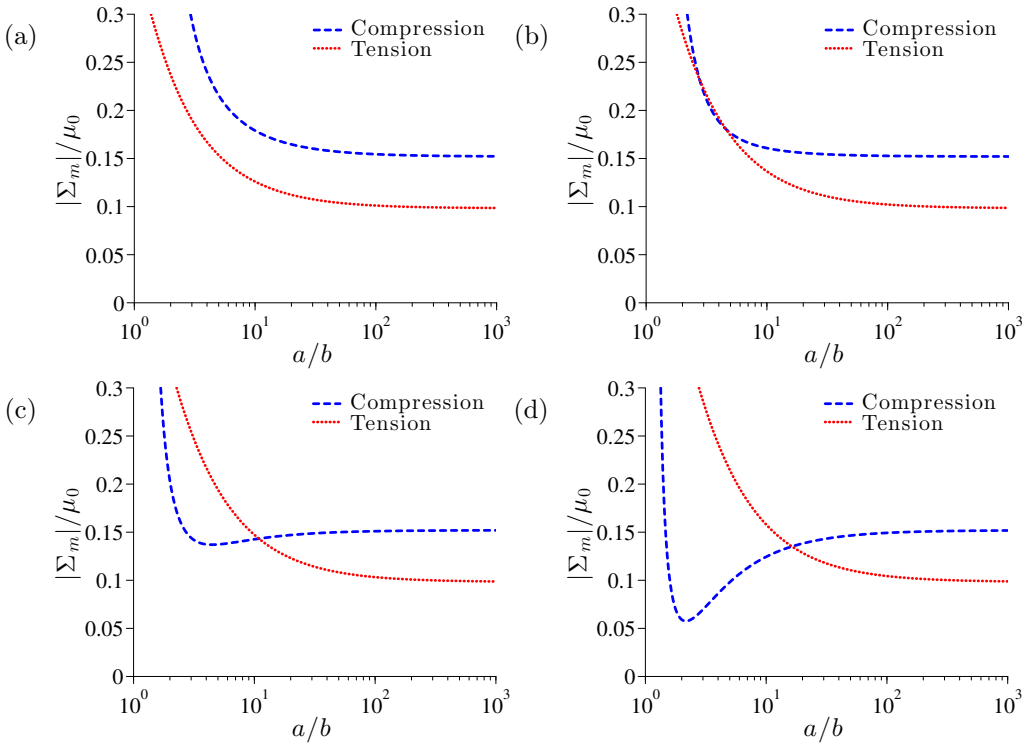

Fig. 4.20: Size effect associated with the tension-compression asymmetry in the critical stress required for dislocation emission considering a pressure-dependent shear modulus, i.e. $\partial\mu/\partial p = 1.8$, and four different surface energies (a) $\gamma_{se} = 1$ J/m^2; (b) $\gamma_{se} = 2$ J/m^2; (c) $\gamma_{se} = 3$ J/m^2; and (d) $\gamma_{se} = 4$ J/m^2. ($b = 2.86$Å$; w_\perp = b; \mu_0 = 26$ GPa$; \nu = 1/3; \tilde{\varphi} = 0$).

It should be noted that the stress field associated with the surface energy does not contribute to the local hydrostatic pressure, see Eqs. (4.22) and (4.23). Therefore, the conditions required for spontaneous dislocation emission (discussed in subsection 4.6.3) are unaffected by the pressure-dependence of the shear modulus.

Surface tension and the pressure-dependence of the shear modulus effect the tension-compression asymmetry of dislocation emission in different ways. Recall from subsection 4.4.2 that surface energy tends to shift the center of the emission surface

in the tensile mean stress direction. The result of this is that dislocation emission requires a somewhat larger macroscopic load in tension as a result of surface tension and a somewhat smaller load in compression, see Fig. 4.18(a). The tendency is opposite for the effects of the pressure-dependence of the shear modulus, with tension being weaker than compression. Considering the effects of both surface tension and a pressure-dependent shear modulus it is not immediately clear which mechanism will govern the tension-compression symmetry. Fig. 4.20 demonstrates this competition between the surface tension induced and pressure-dependent shear modulus induced tension-compression asymmetry associated with dislocation emission as a function of void size for four different surface energies. As expected, for high surface energies and very small voids the material is more resistant to dislocation emission (stronger) in tension as compared with compression. However, for larger void sizes (regardless of surface energy) or for lower surface energies (regardless of the void size) the material is more resistant to dislocation emission (stronger) in compression as compared with tension. For most realistic values of γ_{se} and $\partial\mu/\partial p$ the tension-compression asymmetry associated with dislocation emission is dominated by the pressure-dependence of the shear modulus, and thus we should generally expect for materials to be more resistant to dislocation emission in compression rather than tension.

4.6.5 Temperature dependence of emission criterion

In addition to the pressure-dependence discussed in subsection 4.6.4, the shear modulus of most materials softens with increasing local absolute temperature ϑ, e.g.

$$\mu = \mu_0 + \frac{\partial \mu}{\partial \vartheta} p + \frac{\partial \mu}{\partial \vartheta} (\vartheta - \vartheta_0) , \tag{4.55}$$

where $\partial \mu / \partial \vartheta < 0$ and μ_0 is the shear modulus at ambient conditions and reference temperature, i.e. $p = 0$ and $\vartheta_0 = 300\text{K}$. Representative values for these parameters are provided in Table 4.1. Similarly to the pressure-dependence of the shear modulus, the temperature dependence of the shear modulus results in a reduction of the magnitude of the image shear stress with increasing temperature. Since the image shear stress provides the primary resistance to dislocation emission, a lower applied macroscopic load is naturally required to overcome the reduced image shear stress. The temperature dependence of Eq. (4.55) alone results in the perhaps expected monotonic linear decrease in the macroscopic stress required for emission. However, it is commonly observed that the temperature-dependence of the emission strength of most metals decays faster with temperature than does the shear modulus. Similarly, molecular dynamics simulations have shown a similar behavior with respect to the shear stress required for homogeneous nucleation of dislocation. In subsection 4.5.2 it was shown that this stronger temperature dependence may be accounted for in the present analysis through a temperature dependent dislocation core size, i.e.

$$\frac{1}{w_\perp} = \frac{1}{w_\perp^{0\text{K}}} \left(1 - q_0 \frac{\vartheta}{\vartheta_m} \right) , \tag{4.56}$$

where $w_\perp^{0\mathrm{K}}$ is the dislocation core size at $\vartheta = 0\mathrm{K}$ and q_0 is a fitting parameter such that $0 < q_0 \leq 1$ and $w_\perp = w_\perp^{0\mathrm{K}}/(1-q_0)$ at the melting temperature $\vartheta = \vartheta_m$. In subsection 4.5.2 it was shown that this fitting parameter q_0 is fundamentally related to the temperature dependence associated with the critical stress for homogeneous nucleation, i.e.

$$\tau_{hom} = \tau_{hom}^{0\mathrm{K}} \left(1 + \frac{1}{\mu_0}\frac{\partial \mu}{\partial \vartheta}\left(\vartheta - \vartheta_0\right)\right)\left(1 - q_0 \frac{\vartheta}{\vartheta_m}\right), \tag{4.57}$$

where $\tau_{hom}^{0\mathrm{K}}$ is the critical stress required for homogeneous nucleation at absolute zero, i.e. $\vartheta = 0\mathrm{K}$.

For very large void sizes, i.e. $a/w_\perp \gtrsim 10^3$, the critical macroscopic stress required for emission is simply proportional to the ratio of the shear modulus and the disloca-

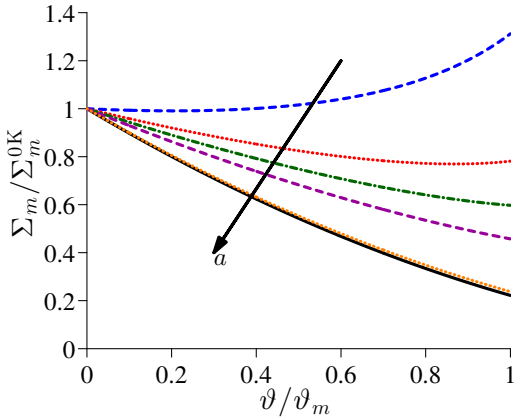

Fig. 4.21: Size effect associated with the temperature dependence of the critical stress required for dislocation emission under pure macroscopic hydrostatic tension, i.e. $\Sigma_m > 0$ with $\Sigma_{eq} = 0$. The arrow indicates the various void sizes considered ranging from $a/b = \{1; 2; 3; 5; 100; \infty\}$. The plots demonstrate an anomalous temperature dependence for very small voids under pure hydrostatic loading conditions. ($b = 2.55\text{Å}; w_\perp^{0\mathrm{K}} = b; \mu_0 = 46.8$ GPa$; \nu = 0.355; \gamma_{se} = 2$ J/m$^2; \partial\mu/\partial\vartheta = 0.51 \times \mu_0/\vartheta_m; \vartheta_m = 1358\mathrm{K}; q_0 = 0.59$).

tion core size, see Eq. (4.40). As a consequence, the temperature dependence of the critical macroscopic stress required for dislocation emission from large voids is identical to that of homogeneous nucleation, i.e. $\propto \left(\mu_0 + \partial\mu/\partial\vartheta\,(\vartheta - \vartheta_0)\right)(1 - q_0\vartheta/\vartheta_m)$. However, in the case of very small voids, i.e. $a \sim w_\perp$, a somewhat nonintuitive, anomalous temperature dependence of the critical emission stress is predicted as a consequence of the temperature dependent core size characterized by Eq. (4.56). This anomalous temperature dependence is shown in Fig. 4.21 for the case of pure macroscopic hydrostatic tension, i.e. $\Sigma_m > 0$ with $\Sigma_{eq} = 0$. Under conditions in which the magnitude of the triaxiality is high, i.e. $|\chi_T| \gtrsim 10$, the anomalous temperature dependence is significant, with extremely small voids, i.e. $a \sim 1 - 2b$, actually becoming more resistant to dislocation emission at higher temperatures. This result is quite unexpected and it would be interesting to perform a suite of atomistic calculations in order to definitely prove this finding. Interestingly, this anomalous temperature dependence vanishes for cases in which the magnitude of the triaxiality is low, i.e. $|\chi_T| \sim 0$.

4.7 Summary of key findings and features

Here we have outlined an extension of the Lubarda [11] criterion for dislocation emission to account for the effects of:

- ✦ a general three-dimensional macroscopic stress state, $\boldsymbol{\Sigma}$

- a particular void size distribution, $g(a)$
- finite porosity, φ
- finite surface energy, γ_{se}
- a temperature- and pressure-dependent shear modulus, μ
- a temperature-dependent dislocation core size, $w_{\perp}$.

Through this extension, we are able to construct a simple porous *critical emission surface* suitable for continuum-level predictions of dynamic ductile failure. Five key features of our porous critical emission surface include:

- *Predictiveness:* a large set of atomistic data is captured by the emission surface with a single fitting parameter ($w_{\perp}$), which is somewhat bounded by the homogeneous nucleation stress
- *Softening response:* a monotonic, nonlinear collapse of the emission surface with increasing porosity φ and temperature ϑ
- *Simplicity:* a simple algebraic form is derived that is trivial to implement in computational schemes
- *Smoothness:* a smooth emission surface with no sharp corners further simplifies computational implementation
- *Non-associative flow:* the normal to the emission surface does not correlate with the plastic flow direction, hence a non-associative flow law is required.

In addition to increasing the utility of the criterion for dislocation emission, we also provide a discussion of some interesting and perhaps non-intuitive predicted behavior induced by high surface energies, e.g.

- *Tension-compression asymmetry:* with materials resisting dislocation emission differently in compression and tension depending on the competition between surface tension and nonlinear stiffness
- *Smaller is weaker:* under certain conditions dislocation emission is predicted to be more difficult with increasing void size
- *Spontaneous dislocation emission:* extremely high surface tensions may permit the spontaneous emission of dislocations resulting in an unstable collapse of any pre-existing voids.

From a purely scientific standpoint, dislocation emission is a fascinating subject full of examples of counter intuitiveness. From an engineering standpoint, dislocation emission now seems to be an important mechanism in the failure response of ductile metals subject to extreme loading conditions. The present chapter has, to some degree, attempted to emphasize both of these view points.

Chapter 5

Simple scaling laws for the role of pre-existing and shock-induced microstructure on spall strength

5.1 Introduction

For the past few decades there has been an intense effort to understand and control the mechanical response of metals subjected to high strain rates, i.e. $10^3 - 10^8$ s^{-1}. A number of applications stand to benefit from such understanding, e.g. personal and vehicular protection, nuclear stockpile reliability, spacecraft shielding, vehicular crashworthiness, and advanced manufacturing. Recent advances in computational capabilities have permitted multiscale modeling to play a greater role in this effort.

Our aim here is to make use of our multiscale mechanism-based framework to provide a deeper understanding of the role of pre-existing and shock-induced microstructure on the dynamic tensile strength of ductile metals.

Ductile failure of metals is known to be governed by the microscopic processes of void nucleation, growth, and finally coalescence leading to fracture [52–56]. The earliest investigations regarded void nucleation as a cavitation instability in an otherwise homogenous elastic-perfectly plastic [57, 58], non-linear elastic [59], or power-law hardening medium [60]. However, these types of continuum analyses fail to predict bifurcation and spontaneous nucleation when accounting for surface energy. The more accepted view of void nucleation is that it occurs at some material defect.

In this thesis we have emphasized the role of a hierarchy of void nucleation sites. Voids may nucleate at second-phase particles along grain boundaries or within grains [71, 72]. Void nucleation at second-phase particles along grain boundaries is often preferred, with high-angle grain boundaries (misorientations between 25° and 50°) being most susceptible [137]. It is currently unclear whether these high-angle grain boundaries are preferred nucleation sites due to stress concentrations at these boundaries or because these boundaries are simply inherently weaker. Second-phase inclusions that are hard in relation to the metal matrix, e.g. carbide and oxide particles, may either internally crack or debond from the matrix [73–75]. Voids may also nucleate within soft inclusions, e.g. sulfides [76]. In addition to these well understood void nucleation sites, voids may also nucleate at vacancy clusters, [69] provided the tensile stresses

are high enough to activate dislocation emission ($\sim \mu/10$) [64–70]. In this chapter it will be shown that this hierarchy of void nucleation sites governs, to a large extent, the rate-dependence of dynamic ductile failure of metals.

Numerous experimental investigations have demonstrated the strong strain rate-dependence of dynamic tensile failure of metals (e.g. through spallation). Consider for example Fig. 5.1, which shows the dependence of the spall strength on tensile strain rate for the case of commercially pure aluminum. Although the results in this figure are derived from two very different experimental techniques (plate impact and laser shock) and there are some subtleties associated with the analysis of each experimental type, it is apparent that the spall strength of commercially pure aluminum increases rapidly with increasing rate of deformation at volumetric strain rates $\dot{\varepsilon}_v$ larger than 10^7 s^{-1}. Defining the rate-sensitivity of spall strength as $m^* \triangleq \partial \ln \sigma^* / \partial \ln \dot{\varepsilon}_v$, where σ^* is the spall strength, Kanel et al. [96] observed that the spall strength rate-

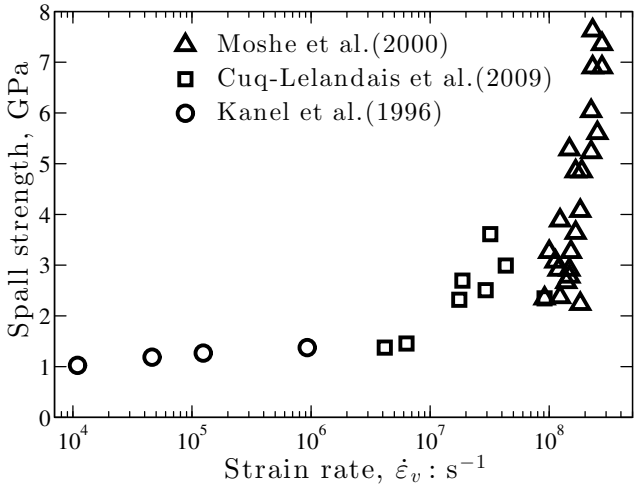

Fig. 5.1: Dramatic change in the observed rate-sensitivity of spall strength in aluminum at extreme loading rates.

sensitivity for commercially pure aluminum is approximately equal to $m^* \approx 0.06$ over the strain rate range of 10^4 s$^{-1} \leq \dot{\varepsilon}_v \leq 10^6$ s^{-1}, see Fig. 5.1. A similar rate-sensitivity was observed by Fortov et al. [97] for aluminum foil over the same strain rate range. The laser shock experiments of Cuq-Lelandais et al. [98] examined higher strain rates and suggests slightly higher rate sensitivity of the spall strength. The highest strain rates were achieved by Moshe et al. [99], who used laser shock experiments with ultrashort pulses of $20 - 100$ picoseconds to experimentally measure spall strength at the extreme strain rates of $\dot{\varepsilon}_v \gtrsim 10^8$ s^{-1}. Over this range, the measurements of Moshe et al. [99] show a spall strength rate-sensitivity of about $m^* \sim 1$ for aluminum foil, see Fig. 5.1. Such a dramatic change in the spall strength rate-sensitivity is suggestive of a transition in the underlying dominant mechanism.

Wilkerson and Ramesh [50] attributed this change in mechanism to a transition in the mechanism governing void growth, i.e. from a micro-inertia dominated regime to a regime governed by the constraints imposed by relativistic glide of dislocations. In this chapter it will be shown that this transition is also associated with a transition in the dominant void nucleation site, i.e. from nucleation at second-phase particles to nucleation from vacancy clusters. This claim is somewhat supported by the spall strength predictions of Wright and Ramesh [101] (with dynamic void growth governed by micro-inertia), who assumed a potential void nucleation site density of 10^{15} m^{-3}. With this nucleation site density they were able to successfully predict the rate-sensitivity of spall strength of pure copper over a range of strain rates

10^3 s^{-1} $\leq \dot{\varepsilon}_v \leq 3 \times 10^5$ s^{-1}. However, keeping this nucleation site density constant, their model substantially over-predicts the experimentally measured spall strength of copper subject to the extreme strain rates $\dot{\varepsilon}_v \geq 10^7$ s^{-1} generated in laser-induced shock loading experiments. A void nucleation site density of $\sim 10^{17}$ m^{-1} is required to bring the model predictions into agreement with the experimental measurements. These arguments support the hypothesis that a second family of void nucleation sites becomes active at the high tensile stresses generated by extreme strain rates $\dot{\varepsilon}_v \geq 10^6$ s^{-1}.

Further supporting evidence for the role of vacancy clustering in spall failure was provided by Pedrazas et al. [114], who performed a number of laser shock experiments to measure the spall response of aluminum at very high strain rates ($\sim 2 - 4 \times 10^6$ s^{-1}) as a function of microstructures and purity level (an aluminum alloy containing 3 wt% magnesium, a 99% commercially pure aluminum, and a 99.999% high purity aluminum). In examining the spall fracture surface of the commercially pure aluminum under scanning electron microscopy (SEM), reproduced here in Fig. 5.2(a), Pedrazas et al. [114] clearly show the correlation between the spacing of second-phase particles and voids. However, this relationship vanishes in the case of the 99.999% high purity aluminum with the SEM images (Fig. 5.2(b)) revealing second-phase particles within the centers of only a very small fraction of the dimples (∼5%). The bulk of the voids (∼95%) must have nucleated from some material defect that is not visible at these particular resolutions (∼100 nm). One potential source of these void

(a) 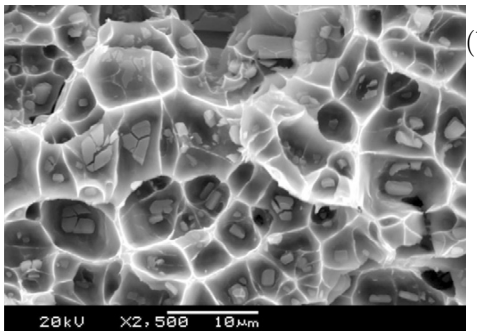

(b) 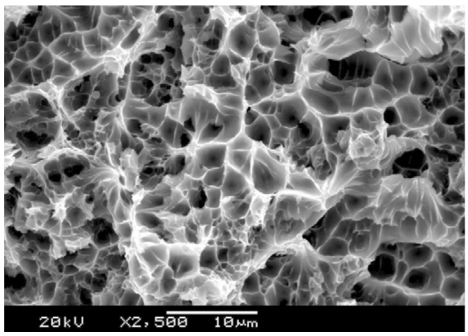

Fig. 5.2: SEM images of spall fracture surfaces reported in [114] for (a) a 99% commercially-pure aluminum and (b) a 99.999% high-purity aluminum. Most of the voids in the commercially-pure aluminum shown in (a) nucleate from second-phase particles, e.g. Al_3Fe, where as for the high-purity aluminum only a very small fraction of the dimples ($\sim$5%) contained second-phase particles, implying that the bulk of these voids nucleate by an alternative mechanism, e.g. vacancy clustering and subsequent growth by dislocation emission.

nucleating material defects is the clustering of vacancies.

The chapter is organized as follows. Section 5.2 begins with the description of a general mechanism-based model for ductile failure, making use of the dynamic void growth model established in chapter 3 and the porous emission criterion developed in chapter 4. Next, section 5.3 introduces a number of simplifications that lead to an idealized, yet highly instructive, set of simple scaling laws for spall strength. Scaling behaviors and comparisons of model predictions with experiments are provided in section 5.4 for single crystal and polycrystal spall strength. For single crystals we discuss the role of purity-level and some peculiar behaviors that arise when the spall failure is dominated by voids that grow from shock-induced vacancy clusters. For polycrystals we provide predictions of the rate-sensitivity and an anomalous grain size dependence of spall strength. Lastly, a brief summary of the key findings is

provided in section 5.5.

5.2 A general mechanism-based model for dynamic ductile failure

5.2.1 Macroscale stress-strain relations for a porous material

Consider a porous macroscopic body subject to mixed traction-displacement boundary conditions as shown in Fig. 5.3. At a particular macroscopic material point $\mathbf{x}$ the material possesses a porosity of $\varphi(\mathbf{x})$ and is subject to a general three-dimensional macroscopic stress field, i.e.

$$\boldsymbol{\Sigma}(\mathbf{x}) = \begin{bmatrix} \Sigma_{11} & \Sigma_{12} & \Sigma_{13} \\ \Sigma_{21} & \Sigma_{22} & \Sigma_{23} \\ \Sigma_{31} & \Sigma_{32} & \Sigma_{33} \end{bmatrix}, \tag{5.1}$$

where the matrix is expressed with respect to the macroscopic physical coordinate system $\{\mathbf{e}_1, \mathbf{e}_2, \mathbf{e}_3\}$. At any point in the body this macroscopic stress may be related to the macroscopic elastic strain tensor $\boldsymbol{\varepsilon}^e$ through an effectively homogenized stress-strain relation. Assuming a linearly isotropic homogenized material, the stress-strain relation may be expressed as

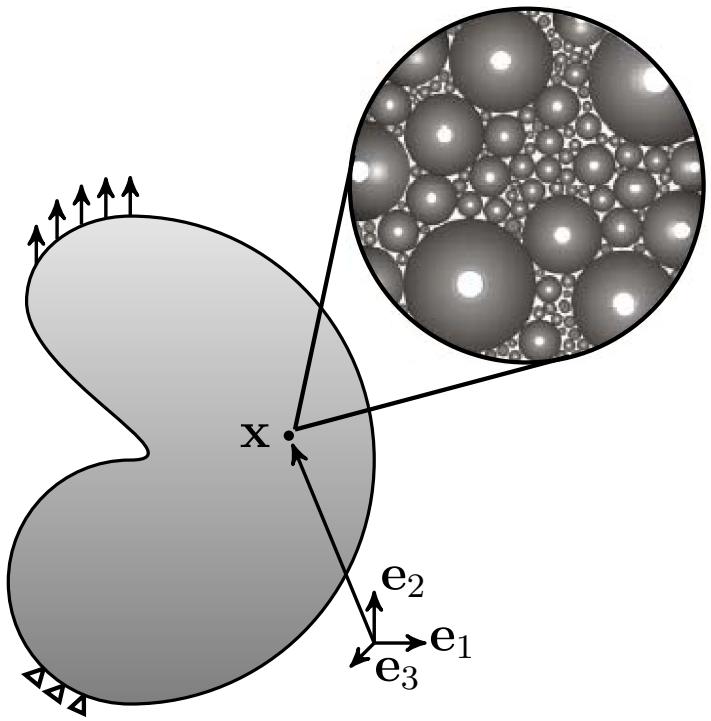

Fig. 5.3: Schematic of a general porous macroscopic body subject to mixed traction-displacement boundary conditions. On the microscale, the porosity φ is composed of a distribution of spherical voids characterized by the void size distribution $g(a)$ and mean void spacing $\bar{\ell}_v$ (inset adapted from [123]).

$$\boldsymbol{\Sigma} = K_{\varphi}\boldsymbol{\varepsilon}^{e} : \mathbf{I} + 2\mu_{\varphi}\boldsymbol{\varepsilon}^{e'}, \tag{5.2}$$

where K_{φ} and μ_{φ} are the effective isotropic elastic constants and $\boldsymbol{\varepsilon}^{e'} \triangleq \boldsymbol{\varepsilon}^{e} : \mathbf{I} - 1/3\boldsymbol{\varepsilon}^{e} : \mathbf{I}$ is the deviatoric part of the macroscopic elastic strain tensor. Classical micromechanics provides a number of analytic approximations for these effective isotropic elastic constants, see for example [138]. The Mori and Tanaka [124] method is one popular micromechanical approximation predicting closed-form relations for the effective

elastic constants, i.e.

$$K_\varphi = K + \frac{(1-\varphi)(3K+4\mu)}{3(1-\varphi)+4\mu/K} \tag{5.3}$$

and

$$\mu_\varphi = \mu + \frac{5\mu(1-\varphi)(3K+4\mu)}{6\varphi(K+2\mu)-5(3K+4\mu)}, \tag{5.4}$$

where K and μ are respectively the isotropic bulk and shear moduli of the solid material. Notice that the effective elastic constants decay monotonically and nonlinearly from the solid stiffness to zero stiffness as the porosity φ increases from zero to one.

The total strain $\boldsymbol{\varepsilon}$ maybe decomposed into elastic, plastic, and porous parts following an additive or multiplicative decomposition. In chapter 6 we make use of the presumably more accurate multiplicative decomposition of the total deformation gradient tensor $\mathbf{F}$. Here, for simplicity, we make use of an additive decomposition, i.e.

$$\boldsymbol{\varepsilon} = \boldsymbol{\varepsilon}^e + \boldsymbol{\varepsilon}^p + \boldsymbol{\varepsilon}^\varphi, \tag{5.5}$$

where the plastic and porous parts of the macroscopic strain tensor are denoted as $\boldsymbol{\varepsilon}^p$ and $\boldsymbol{\varepsilon}^\varphi$. The porous strain tensor $\boldsymbol{\varepsilon}^\varphi$ is defined such that it only captures the dilatational deformation associated with spherical void growth. As such, the porous strain tensor represents pure dilatational deformation, i.e. $\boldsymbol{\varepsilon}^{\varphi'} = 0$. Consistent with dislocation-based plasticity theory, the volumetric part of the plastic strain tensor is taken to be zero, i.e. $\boldsymbol{\varepsilon}^p : \mathbf{I} = 0$. The evolution of $\boldsymbol{\varepsilon}^p$ and $\boldsymbol{\varepsilon}^\varphi$ are discussed further in the following subsections.

5.2.2 Pure dilatation approximation

Generally an appropriate porous flow law is required to describe the evolution of the plastic part of the macroscopic strain tensor $\boldsymbol{\varepsilon}^p$. However, spall failure induced by plate impact is one particular loading path that is well approximated by a pure dilatation macroscopic deformation approximation, i.e. $\boldsymbol{\varepsilon}' = 0$, as described in [101, 102]. Since the deviatoric and volumetric parts of the elastic macroscopic strain tensors are decoupled and the porous strain tensor is isotropic, it follows from the additive decomposition of the strain tensors that $\boldsymbol{\varepsilon}^{p'} = 0$. Recalling that the volumetric part of the plastic strain tensor is also zero, i.e. $\boldsymbol{\varepsilon}^p : \mathbf{I} = 0$, the total plastic strain tensor is nil, i.e. $\boldsymbol{\varepsilon}^p = 0$. As such, a porous flow law for $\boldsymbol{\varepsilon}^p$ is not required for this particular idealized loading path.

Strictly speaking, the deformation associated with plate impact experiments employed in the study of spall failure is uniaxial deformation, i.e.

$$\boldsymbol{\varepsilon} = \begin{bmatrix} \varepsilon_{11} & 0 & 0 \\ 0 & 0 & 0 \\ 0 & 0 & 0 \end{bmatrix}, \tag{5.6}$$

with the resulting macroscopic stress tensor (for isotropic materials) expressed as

$$\boldsymbol{\Sigma} = \begin{bmatrix} \Sigma_{11} & 0 & 0 \\ 0 & \Sigma_{22} & 0 \\ 0 & 0 & \Sigma_{22} \end{bmatrix}. \tag{5.7}$$

The corresponding macroscopic equivalent stress for this stress tensor follows as

$\Sigma_{eq} \triangleq \sqrt{3/2 \boldsymbol{\Sigma}' : \boldsymbol{\Sigma}'} = |\Sigma_{11} - \Sigma_{22}|$. Typically, the mean stress $\Sigma_m \triangleq 1/3 \boldsymbol{\Sigma} : \mathbf{I}$ greatly exceeds the equivalent stress by as much as an order of magnitude, i.e. $\Sigma_m >> \Sigma_{eq}$. Nevertheless, these effects are not always negligible (consider for example materials with high shear strengths) and chapter 6 provides a more generalized framework to account for the macroscopic deviatoric stress that is generated in plate impact as well as more complex loading situations.

Ignoring the macroscopic deviatoric stress and strains the relevant stress-strain relations may be expressed by a simple scalar relation, i.e.

$$\Sigma_m = K_\varphi \left(\varepsilon_v - \varepsilon_v^\varphi \right), \tag{5.8}$$

where $\varepsilon_v \triangleq \boldsymbol{\varepsilon} : \mathbf{I}$ and $\varepsilon_v^\varphi \triangleq \boldsymbol{\varepsilon}^p : \mathbf{I}$ are the volumetric parts of the total macroscopic strain tensor and the macroscopic porous strain tensor, respectively.

Making use of a logarithmic finite Hencky strain tensor, the volumetric part of the porous strain tensor may be expressed as

$$\varepsilon_v^\varphi = \ln \left(\frac{1 - \varphi_0}{1 - \varphi} \right), \tag{5.9}$$

where φ_0 is the initial porosity. For relatively small porosities ($\varphi_0 \leq \varphi << 1$), a first order Taylor-series approximation of Eq. (5.9) results in

$$\varepsilon_v^\varphi = \varphi - \varphi_0. \tag{5.10}$$

For relatively small deformations and porosities, i.e. $|\varepsilon_v| \lesssim 1\%$ and $\varphi \lesssim 1\%$, the macroscopic stress-strain relation takes on the following reduced form

$$\Sigma_m = K \left(\varepsilon_v - \varphi + \varphi_0 \right). \tag{5.11}$$

Here the stress-strain relation is incredibly simple and the complexity arises through the dynamic evolution of the (small) porosity as described in the following subsection.

5.2.3 Dynamic void growth and porosity evolution

On the microscale, the local porosity φ at any material point $\mathbf{x}$ is composed of a distribution of spherical voids of varying radius a, as shown in Fig. 5.3. The void population is characterized by a size distribution $g(a)$ and the number of voids per unit volume of solid material N_v. The mean void size $\bar{a}$ may be computed as $\bar{a} = \int_0^\infty g(a)a \; da$, and a measure of the mean center-to-center spacing between voids $\bar{\ell}_v$ may be defined such that $\varphi = (2\bar{a}/\bar{\ell}_v)^3$. From the above definitions, it follows that

$$\frac{\varphi}{1-\varphi} = \frac{4}{3}\pi N_v \int_0^\infty g(a)a^3 da. \tag{5.12}$$

The void size distribution may be alternatively defined with respect to the initial void sizes A and the initial size distribution $\mathcal{G}(A)$, i.e.

$$\frac{\varphi}{1-\varphi} = \frac{4}{3}\pi N_v \int_0^\infty \mathcal{G}(A)\left(a(A)\right)^3 dA. \tag{5.13}$$

The main advantage of employing Eq. (5.13) over Eq. (5.12) is that $\mathcal{G}(A)$ is a constant function whereas $g(a)$ continuously evolves as some voids grow earlier and faster than others. From Eq. (5.13) it is clear that the dynamic evolution of porosity simply follows from the dynamic evolution of the discrete voids once the constants $\mathcal{G}(A)$ and N_v have been prescribed.

Chapter 3 provided a detailed derivation of such a dynamic void growth model that accounted for the constraints imposed by the inertial resistance of the accelerating solid material around a dynamically growing void. Here we make use of that dynamic void growth model, expressed here as

$$\rho\left(1-\sqrt[3]{\varphi}\right)a\ddot{a}+\rho\left(\frac{3}{2}-2\sqrt[3]{\varphi}+\frac{1}{2}\varphi^{4/3}\right)\dot{a}^2=\Sigma_m-\mathcal{R}_{cr}-\mathcal{R}_{dd}, \tag{5.14}$$

where ρ is the density of the solid material with $\mathcal{R}_{cr}$ and $\mathcal{R}_{dd}$ providing additional resistances to void growth. $\mathcal{R}_{cr}$ is simply the critical stress required to initiate quasi-static growth of the particular void under consideration. $\mathcal{R}_{cr}$ may be, for example,

- ✦ a critical mean stress required to debond a second-phase particle from the matrix
- ✦ a critical mean stress required to yield the matrix material around the void
- ✦ a critical mean stress required to activate dislocation emission from nanovoids.

$\mathcal{R}_{dd}$ is an additional resistance associated with a dynamic over-stress in the flow strength of the solid material surrounding the dynamically growing void.

Eq. (5.14) governs the dynamics of each discrete void in the void population. If the voids are all of equal size, i.e. $g(a)=\delta(a-\bar{a})$ with $\delta(\cdot)$ being a Dirac-delta distribution, then the dynamic evolution of porosity may be expressed as a single equation, i.e.

$$3\rho\ell_v^2\left(\frac{1-\sqrt[3]{\varphi}}{\left(\sqrt[5]{\varphi}-\varphi\sqrt[5]{\varphi}\right)^{5/3}}\ddot{\varphi}-\frac{1-12\varphi+11\varphi^{4/3}}{6\left(\sqrt{\varphi}-\varphi\sqrt{\varphi}\right)^{8/3}}\dot{\varphi}^2\right)=\Sigma_m-\mathcal{R}_{cr}-\mathcal{R}_{dd}, \tag{5.15}$$

The algebraic complexity of the functional form expressed in Eq. (5.15) is noteworthy. It would be impractical to attempt to obtain such an evolution equation from a fit to either experimental or simulation data. Furthermore, a physics-based model for dynamic evolution of porosity requires a length scale, i.e. ℓ_v, and a second-order differential equation on porosity, i.e. $\ddot{\varphi}$, in order to accurately capture the role of microinertia in dynamic ductile failure of metals. Often, this is not accounted for in models utilized in the failure analysis of structures subject to extreme dynamic loading conditions.

Chapter 3 also provided a derivation of the viscoplastic resistance term $\mathcal{R}_{dd}$ accounting for the effects of relativistic drag on dislocations gliding near the shear wave

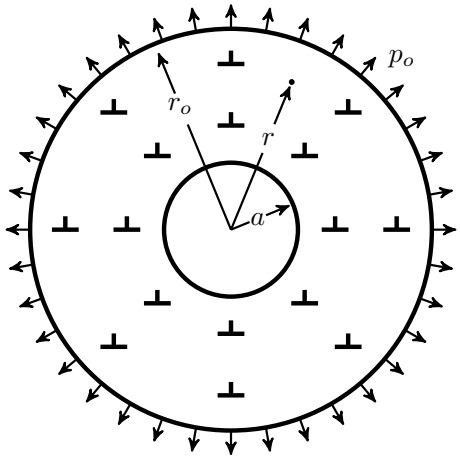

Fig. 5.4: Schematic of a spherical void of radius a embedded within an otherwise solid sphere of radius r_o.

speed, which is expressed generally as

$$\mathcal{R}_{dd} = \int_a^{r_o} \frac{4}{r} \frac{B_0 c_s}{b} \frac{v_\perp / c_s}{1 - (v_\perp / c_s)^2} dr, \tag{5.16}$$

with r and $r_o \triangleq a/\sqrt[3]{\varphi}$ respectively denoting the spatial radial variable and the outer radius of the spherical shell (see Fig. 5.4). The magnitude of the Burgers vector, shear wave speed, and nominal drag coefficient are denoted as b, c_s, and B_0, which was modeled by Leibfried [104] as $B_0 = 3k_b\vartheta z/20c_s b^2$, with z is the number of atoms per unit cell and $k_b\vartheta$ being the thermal energy. The spatial variable in Eq. (5.16) is the local dislocation velocity $v_\perp$, which was shown in Eq. (3.21) to directly depend on the spatial evolution of the mobile dislocation density N_m through Orowan's relation, i.e. $\dot{\varepsilon}^p = bN_m v_\perp$. The resulting relation may be expressed as $bN_m v_\perp = 3\dot{a}a^2/r^3$, which when substituted into Eq. (5.16) results in a expression for $\mathcal{R}_{dd}$ whose only unknown is the spatial variation of N_m, i.e.

$$\mathcal{R}_{dd} = 12\dot{a}a^2 \int_a^{r_o} \frac{B_0 N_m c_s^2 / r^4}{(bN_m c_s)^2 - (3\dot{a}a^2/r^3)^2} dr. \tag{5.17}$$

Substructure evolution equations that govern the spatial evolution of the mobile and immobile dislocations densities (N_m and N_{im}) with deformation were provided in section 3.3 based on the work of Austin and McDowell [10], i.e.

$$\dot{N}_m = \dot{N}_{nuc} + \dot{N}_{mult} - \dot{N}_{ann} - \dot{N}_{trap} \tag{5.18}$$

$$\dot{N}_{im} = \dot{N}_{trap} - \dot{N}_{rec}, \tag{5.19}$$

where the subscripts *nuc*, *mult*, *ann*, *trap*, and *rec* refer to dislocation nucleation, multiplication, annihilation, trapping, and recovery, respectively. The multiplication,

annihilation, and trapping terms follow from section 3.3 as

$$\dot{N}_{mult} = 3\delta_{mult}\frac{\dot{a}a^2}{br^3} \tag{5.20}$$

$$\dot{N}_{ann} = 3\alpha_{ann}N_m\frac{\dot{a}a^2}{r^3} \tag{5.21}$$

$$\dot{N}_{trap} = 3\frac{\dot{a}a^2}{b\Lambda r^3}, \tag{5.22}$$

where δ_{mult} and α_{ann} are model parameters and Λ is the effective mean free path of dislocations and decreases with increasing dislocation density, i.e. $\Lambda^{-1} = \alpha_{dis}\sqrt{N_{im} + N_m}$, see [10]. Representative material properties and model parameters are given in Table 3.1 for OFHC copper. As in [10], recovery processes are ignored ($\dot{N}_{rec} = 0$) due to the short time scales of interest ($< 1\mu$s), which inhibit many thermally-activated processes such as climb. The consequence of ignoring these recovery processes is that strain rate history effects are not properly captured.

Both heterogeneous and homogeneous nucleation of new dislocation loops are discussed at length by Austin and McDowell [10, 49]. Homogeneous nucleation requires very large shear stresses, which are likely to be achieved only momentarily under shock compression conditions and homogeneous nucleation is thus ignored in the present chapter. Heterogeneous nucleation is more likely to occur in the vicinity of dynamically growing voids. However, if the voids nucleate at stress concentrations, e.g. triple junctions and inclusions, these stress concentrators are no longer available to assist heterogeneous dislocation nucleation as the void grows. Heterogeneous nucleation may still occur if the local shear stresses are large enough to emit disloca-

tions from the surface of voids [64, 65, 67, 68, 70, 109], where the critical criterion for dislocation emission was provided in chapter 4 as

$$\Phi_{em} = \sqrt{h_1^2 \left| \frac{\Sigma_m}{1-\tilde{\varphi}} - \frac{\gamma_{se}}{a} \right|^2 + \left(\frac{h_2}{\sqrt{3}} \frac{\Sigma_{eq}}{(1-\tilde{\varphi})} \right)^2 - \left| \tilde{\tau}_{cr}^{image} \right|^2}, \tag{5.23}$$

where γ_{se} is the surface energy of the material, $\tilde{\varphi}$ is an auxiliary porosity defined Eq. (4.6), h_1 and h_2 are non-dimensional length scales expressed in Eqs. (4.42) and (4.43), with the magnitude of the critical image shear stress expressed here as

$$\left| \tilde{\tau}_{cr}^{image} \right| = \frac{\mu_s^*}{4} \frac{b}{w_\perp} \left\{ \frac{\sqrt{2}a + 2w_\perp}{\sqrt{2}a + w_\perp} - \frac{a^2 w_\perp^2 \left(\sqrt{2}a + w_\perp\right)\left(\sqrt{2}a + 2w_\perp\right)}{\left(a^2 + w_\perp^2 + \sqrt{2}a w_\perp\right)^3} \right\}, \tag{5.24}$$

where $w_\perp$ is a temperature-dependent dislocation core size calibrated in chapter 4 and modeled by Eq. (4.56). Here we are primarily concerned with the mean tensile stress Σ_m^{Em} required to activate dislocation emission, which may be expressed as

$$\Sigma_m^{Em} = (1-\tilde{\varphi}) h_1^{-2} \left| \tilde{\tau}_{cr}^{image} \right| + (1-\tilde{\varphi}) \frac{\gamma_{se}}{a}, \tag{5.25}$$

for most practical values of γ_{se} (see chapter 4 for more discussion on this).

The rate at which dislocation emission replenishes the mobile dislocation density may be modeled by an Arrhenius relation, i.e.

$$\dot{N}_{nuc} = \frac{\alpha_{em} \nu_D b}{\Omega} f\left(\frac{a}{r}\right) \exp\left\{ \frac{g_0 \mu b}{k_b \vartheta} \frac{\left(\Sigma_m - \Sigma_m^{Em}\right)}{\left| \tilde{\tau}_{cr}^{image} \right|} \right\} H(\Sigma_m - \Sigma_m^{Em}), \tag{5.26}$$

where α_{em} and g_0 are dimensionless material parameters with ν_D and Ω respectively denoting the Debye frequency and atomic volume. One of the current deficiencies of most dislocation-based plasticity models is their inability to capture flux of dislocation

density from one spatial location to another. Due to this deficiency, we introduce in Eq. (5.26) a spatial function $f(a/r)$ that models the spatial variation of the rate of change in mobile dislocation density associated with emission from the void surfaces. For the emission of prismatic loops, the spatial function may vary as $1/r^3$, since the line length of prismatic loops remain constant as they glide away from the void surface. On the other hand, shear loops expand as they glide from the void surface, leading to a different spatial variation that is perhaps nearly linear. Based on these arguments, one possible functional form for the spatial variation of $\dot{N}_{nuc}$ is

$$f\left(\frac{a}{r}\right) = \chi_s + \chi_p \frac{a^3}{r^3}, \tag{5.27}$$

where χ_s and χ_p are the fractions of emitted dislocation loops that are respectively characterized as either shear loops or prismatic loops with $\chi_s + \chi_p = 1$ by definition.

In general, the viscoplastic resistance term $\mathcal{R}_{dd}$, expressed on the right hand side of Eq. (5.14) must be numerically integrated at each time step (since N_m in Eq. (5.16) may take on any arbitrary radial spatial variation). This demands a discretization of the spatial variable r (in addition to time t), which substantially increases the computational cost of the problem at hand. This is particularly undesirable for the simulation of complex structures subject to dynamic failure governed by Eq. (5.14), see for example the work of [110, 111]. In the following section, we consider an idealized material for which some simple scaling laws may be derived. Despite their idealized nature, these simple scaling laws are able to shed light on some of the most important physics governing some of the more perplexing experimental observations

associated with spall failure.

5.3 Simple scaling laws for spall failure

5.3.1 Stress, porosity, and time at peak mean stress

Wright and Ramesh [101] demonstrated that the peak mean tensile stress Σ_m^* achieved during pure hydrostatic loading compares well with the spall strength of materials and that Σ_m^* is achieved at a relatively small porosity, $\mathcal{O}(0.1\% - 1\%)$. This peak stress porosity φ^* is substantially lower than the coalescence porosity $\varphi_c \sim 20\% - 60\%$ where fracture occurs and stresses are fully relaxed. Rather than being associated with coalescence of porosity, the peak mean tensile stress is associated with the rate of inelastic deformation overtaking the rate of total deformation and thus driving the stress down. This may be easily seen by considering the maximization of Eq. (5.11) with respect to time t for a constant applied strain rate, i.e.

$$\left.\frac{\partial \Sigma_m}{\partial t}\right|_{t=t^*} = K\left(\dot{\varepsilon}_v - \dot{\varphi}^*\right) = 0 \qquad \rightarrow \qquad \dot{\varepsilon}_v = \dot{\varphi}^*, \tag{5.28}$$

where t^* is the time at which the peak mean tensile stress is obtained and $\dot{\varphi}^*$ is the porosity growth rate at the corresponding time. For $t < t^*$ the rate of total deformation is greater than the rate of inelastic deformation, i.e. $\dot{\varepsilon}_v > \dot{\varphi}^*$, and the mean stress continues to climb according to Eq. (5.11). Beyond $t = t^*$, the rate of inelastic deformation overtakes the rate of total deformation, i.e. $\dot{\varphi}^* > \dot{\varepsilon}_v$, and the

mean stress collapses, see for example [101]. The transition between the two regimes occurs at $t = t^*$ and corresponds to the achievement of the peak mean tensile stress, which may be expressed by substituting Eq. (5.28) into Eq. (5.11), i.e.

$$\Sigma_m^* = K\left(\dot{\varepsilon}_v t^* - \varphi^* + \varphi_0\right), \tag{5.29}$$

where $\varphi^* = \varphi|_{t=t^*}$.

5.3.2 Scaling laws for ultra-high purity metals

Consider an idealized ultra-high purity metal with no second-phase particles. In this chapter, we assume that the only source of void nucleation in such a material is through vacancy clustering. As discussed in chapter 4, spall failure is preceded by an intense shock wave that generates a preponderance of defects in metals. Intersecting dislocations may produce a large number of jogs, which when dragged along the glide plane (as a result of the associated high shear stresses in the shock front) contribute to a nonequilibrium superconcentration of vacancies c_v^{ne}, which may be phenomenologically approximated as $c_v^{ne} \approx A_v \varepsilon^p$ with ε^p being the accumulated plastic strain and $A_v \sim 10^{-4}$ being a fitting parameter obtained from shock experiments [117–120]. The plastic strain accumulated as a result of shock compression and subsequent unloading may be approximated as $\varepsilon^p \approx \frac{4}{3} \ln V/V_0$, where V/V_0 is the relative specific volume in the shocked state [5]. The relative specific volume in the shock state and the magnitude of the shock stress Σ_{ss} may be related through an equation of state.

For an equation of state characterized by a linear relation between shock velocity U_s and particle velocity U_p, i.e. $U_s = C_0 + SU_p$ with C_0 and S being material parameters, we have

$$V/V_0 = 1 + \frac{K_0}{2S^2\Sigma_{ss}}\left(\sqrt{1+4S\frac{\Sigma_{ss}}{K_0}} + 2S(S-1)\frac{\Sigma_{ss}}{K_0} - 1\right), \tag{5.30}$$

where K_0 is the reference bulk modulus. Therefore, the concentration of vacancies just prior to the tensile loading stage approximately scales with shock stress as

$$c_v^{ne} = 1.3\times 10^{-4}\ln\left(1 + \frac{K_0}{2S^2\Sigma_{ss}}\left(\sqrt{1+4S\frac{\Sigma_{ss}}{K_0}} + 2S(S-1)\frac{\Sigma_{ss}}{K_0} - 1\right)\right). \tag{5.31}$$

Eq. (5.31) implies that the non-equilibrium concentration of vacancies is sensitive to the shock stress.

According to Reina et al. [69], the kinetics of vacancy clustering are fast enough for a small fraction of these superconcentrated vacancies to form divacancies, trivacancies, as well as larger vacancy complexes during the shock compression and release. The void size distribution $\mathcal{G}(A)$ associated with the vacancy clusters is assumed to be approximated by an exponential distribution, i.e.

$$\mathcal{G}(A) = \frac{1}{\bar{A}}\exp -\frac{A}{\bar{A}}, \tag{5.32}$$

with $\bar{A}$ characterizing the mean of the distribution and taken here to be equal to the radius of a single vacancy, i.e. $\frac{3}{4}\pi^{-1}\sqrt[3]{\Omega}$. In the future, it may be desirable to extract the discrete size distribution directly from vacancy clustering simulations similar to those of [69]; however, this is beyond the scope of the current chapter. Nevertheless, Eq. (5.32) captures the most important aspects, i.e. that single vacancies

vastly outnumber divacancies, and divancancies vastly outnumber trivacancies, etc., without introducing any unknown variables.

Now that the material has been seeded with a distribution of shock-induced void *embryos*, it may now be possible to substantially grow these voids further through a dislocation mechanism. As argued in chapter 4, these vacancy clusters are likely too small for traditional dislocation mechanisms (based on the activation of Frank-Read and single-arm sources) to be operative. However, if the stresses are large enough to activate dislocation emission, then this source will supply mobile dislocation segments to the plastic zone around the growing nanovoids. Recall from chapter 3, that micro-inertia is negligible for the dynamic growth of very small nanovoids ($\lesssim 100$ nm). As such, the void growth rate of these nanovoids is well approximated by

$$\dot{a} = \frac{1}{3} a b \tilde{N}_m c_s, \tag{5.33}$$

where $\tilde{N}_m$ is the mobile dislocation density near the void surface, i.e. $r = a$. In general, $\tilde{N}_m$ may arbitrarily evolve as the voids grow governed by the substructure evolution equations provided in the proceeding section. However, for the moment we assume $\tilde{N}_m$ approximately constant shortly after the activation of dislocation emission. The advantage of such an assumption is that the current void size then follows directly from the integration of Eq. (5.33), i.e.

$$a = A \exp\left(\frac{1}{3} b \tilde{N}_m c_s \langle t - t_{cr} \rangle\right), \tag{5.34}$$

where $\langle \cdot \rangle$ denote Macaulay brackets and t_{cr} is the time at which dislocation emission

becomes active for the particular void under consideration. t_{cr} is defined such that $\Sigma_m|_{t=t_{cr}} = \Sigma_m^{Em}(A)$, where $\Sigma_m^{Em}(A)$ is the size-dependent emission criterion expressed in Eq. (5.25).

The physical justification for taking $\tilde{N}_m$ to be a constant relates to the concept of a saturation dislocation density N_{sat}, typically assumed to be $\mathcal{O}(10^{16} - 10^{17}\ \mathrm{m}^{-2})$. Such a saturation density is is likely exhibited in most materials, and develops when all relevant nucleation sources are active and exactly balance the rate of annihilation $\dot{N}_{ann}$. The activation of dislocation emission generates an avalanche of dislocations that will quickly drive the total dislocation density to the saturation level ($N_{im} + N_m \rightarrow N_{sat}$). If one further assumes that the ratio of mobile to immobile dislocation densities (N_m/N_{im}) is approximately constant in this saturated state, then the mobile dislocation density in this saturated state may be approximated as

$$N_m = \chi_m N_{sat}, \tag{5.35}$$

where χ_m is a parameter $\mathcal{O}(1\% - 10\%)$ that characterizes the fraction of dislocation density that remains mobile in the saturated state. Based on these assumptions, the nanovoid velocities are quickly governed by the special relation

$$\dot{a} = \frac{1}{3} abc_s \chi_m N_{sat} \tag{5.36}$$

rather than the more general expression given in Eq. (5.33). Provided negligible dislocation-based void growth prior to attainment of the saturated state, integration

of Eq. (5.36) leads directly to

$$a = A \exp\left(\frac{1}{3} b \chi_m N_{sat} c_s \langle t - t_{cr} \rangle\right). \tag{5.37}$$

Following Eq. (5.13), the porosity at any time is given as

$$\frac{\varphi}{1-\varphi} = \frac{4}{3}\pi N_v \int_0^\infty \mathcal{G}(A) A^3 \exp\left(b \chi_m N_{sat} c_s \langle t - t_{cr} \rangle\right) dA, \tag{5.38}$$

where it is noted that in general the time t_{cr} at which emission is active for a particular void depends on that void's size A, see chapter 4. Provided that the porosity is small, i.e. $\varphi << 1$, the initial porosity φ_0 may be taken to be the shock-induced nonequilibrium vacancy concentration c_v^{ne} and Eq. (5.47) may be reconstructed to remove the unknown N_v, i.e.

$$\varphi = \frac{c_v^{ne}}{\zeta \bar{A}^3} \int_0^\infty \mathcal{G}(A) A^3 \exp\left(b \chi_m N_{sat} c_s \langle t - t_{cr} \rangle\right) dA, \tag{5.39}$$

where $\zeta = 6$ for an exponential distribution and $\zeta = 1$ for a delta distribution, i.e. $\mathcal{G}(A) = \delta(A - \bar{A})$. Notice that for this idealized ultra-high purity material the porosity φ scales directly with the shock-induced nonequilibrium vacancy concentration. Time differentiation of Eq. (5.39) gives the porosity growth rate for the idealized material, i.e.

$$\dot{\varphi} = \frac{c_v^{ne}}{\zeta \bar{A}^3} \int_0^\infty b \chi_m N_{sat} c_s \mathcal{G}(A) A^3 \exp\left(b \chi_m N_{sat} c_s \langle t - t_{cr} \rangle\right) dA. \tag{5.40}$$

Utilizing our stability criterion derived in Eq. (5.28), i.e. $\dot{\varepsilon}_v = \dot{\varphi}$ at $t = t^*$, an implicit relation for t^* is obtained as

$$\dot{\varepsilon}_v = \frac{c_v^{ne}}{\zeta \bar{A}^3} \int_0^\infty b \chi_m N_{sat} c_s \mathcal{G}(A) A^3 \exp\left(b \chi_m N_{sat} c_s \langle t^* - t_{cr} \rangle\right) dA. \tag{5.41}$$

Solving Eq. (5.41) for t^*, the peak mean stress then follows directly from substitution of a numerical solution for t^* into Eq. (5.39) and Eq. (5.29). Although this numerical procedure is more accurate, an instructive semi-explicit expression may be obtained by assuming that $\Sigma_m^* \approx K\dot{\varepsilon}_v t^*$, where t^* is still defined by the stability criterion ($\dot{\varepsilon}_v = \dot{\varphi}$), i.e.

$$\dot{\varepsilon}_v \approx \frac{c_v^{ne}}{\zeta \bar{A}^3} \int_0^\infty b\chi_m N_{sat} c_s \mathcal{G}(A) A^3 \exp\left(\frac{b\chi_m N_{sat} c_s}{K\dot{\varepsilon}_v} \langle \Sigma_m^* - \Sigma_m^{Em} \rangle\right) dA. \tag{5.42}$$

Eq. (5.41) may be explicitly inverted for the special case in which the vacancy cluster size distribution is a delta function, i.e. $\mathcal{G}(A) = \delta(A - \bar{A})$, from which it follows that

$$t^* = t_{cr} + \frac{1}{b\chi_m N_{sat} c_s} \ln\left(\frac{\dot{\varepsilon}_v}{c_v^{ne} b\chi_m N_{sat} c_s}\right). \tag{5.43}$$

Substitution into Eq. (5.39) and Eq. (5.29) results in a simple scaling law for the spall strength of ultra-high purity metals:

$$\Sigma_m^* = \Sigma_m^{Em} + K\left(\frac{\dot{\varepsilon}_v}{bc_s\chi_m N_{sat}}\right) \ln\frac{\varphi^*}{c_v^{ne}} - K(\varphi^* - c_v^{ne}), \tag{5.44}$$

with $\varphi^* = \max\left(c_v^{ne}, \dot{\varepsilon}_v / bc_s\chi_m N_{sat}\right)$. The first term on the right-hand side of Eq. (5.44) is the minimum spall strength for this idealized material and corresponds to the critical mean stress required to activate dislocation emission, the second term is the primary rate-dependent component that is governed by the relativistic glide of dislocations and the saturated mobile dislocation density $\chi_m N_{sat}$, and the last term is a derived correction factor that accounts for the accumulated inelastic strain prior to achieving the peak mean stress. Notice that Eq. (5.44) results in a rate-sensitivity for

spall strength of $m^* \sim 1$. Interestingly, a very similar rate-sensitivity was observed in the laser-shock experiments of Moshe et al. [99].

5.3.3 Scaling laws accounting for traditional void nucleation at second-phase particles

Consider now a metal containing a population of second-phase particles of various sizes A_p. Nucleation is assumed to occur by particle interface debonding such that the initial void size A is taken to be the particle size A_p for the particular void under consideration. The size distribution of these second-phase particles is denoted here as $\mathcal{G}_p(A_p)$. We may assume that the dynamics of these voids are governed by micro-inertia provided that the entire population of debonded second-phase particles are larger than the dislocation kinetics to micro-inertia transition size ($\sim$ 200 nm) discussed in chapter 3.

The growth rate of voids governed by micro-inertia is well approximated by the steady-state kinetics discussed in chapter 3, i.e.

$$\dot{a} = \sqrt{\frac{2}{3}\frac{\langle \Sigma_m - \mathcal{R}_{cr} \rangle}{\rho}}, \tag{5.45}$$

where R_{cr} is taken to be a constant critical resistance proportional to the flow strength of the shocked metal. The void size is obtained from time-integration of Eq. (5.45),

assuming Σ_m varies linearly with time from $t = t_{cr}$ to $t = t^*$ as $\Sigma_m \approx K\dot{\varepsilon}_v t$, i.e.

$$a = A_p + \frac{2}{3}\sqrt{\frac{2}{3}}\frac{\langle \Sigma_m - \mathcal{R}_{cr}\rangle^{3/2}}{K\dot{\varepsilon}_v\sqrt{\rho}}. \tag{5.46}$$

The porosity growth rate associated with these voids nucleating from second-phase particles follows from the time differentiation of Eq. (5.13) and making use of Eq. (5.45) and Eq. (5.46), i.e.

$$\dot{\varphi} = \bar{\ell}_p^{-3}\int_0^\infty \mathcal{G}_p(A_p)\left(A_p + \frac{2}{3}\sqrt{\frac{2}{3}}\frac{\langle \Sigma_m - \mathcal{R}_{cr}\rangle^{3/2}}{K\dot{\varepsilon}_v\sqrt{\rho}}\right)^2\sqrt{\frac{2}{3}\frac{\langle \Sigma_m - \mathcal{R}_{cr}\rangle}{\rho}}dA, \tag{5.47}$$

where $2\bar{\ell}_p$ is the average center-to-center spacing of the second-phase particles. Since we are only considering fairly coarse second-phase particles, it is reasonable to assume that $\mathcal{R}_{cr}$ is independent of void size over this range of sizes. In this case, making use of the stability condition ($\dot{\varepsilon}_v = \dot{\varphi}$) the scaling law may be expressed as

$$\dot{\varepsilon}_v = \sqrt{\frac{2}{3}\frac{\langle \Sigma_m^* - \mathcal{R}_{cr}\rangle}{\rho}}\frac{\bar{A}_p^2}{\bar{\ell}_p^3} + \frac{8}{9}\frac{\langle \Sigma_m^* - \mathcal{R}_{cr}\rangle^2}{\rho K\dot{\varepsilon}_v}\frac{\bar{A}_p}{\bar{\ell}_p^3} + \frac{8}{9}\sqrt{\frac{2}{3}}\frac{\langle \Sigma_m^* - \mathcal{R}_{cr}\rangle^{7/2}}{\rho^{3/2}K^2\bar{\ell}_p^3\dot{\varepsilon}_v^2}, \tag{5.48}$$

where $\bar{A}_p$ is the mean size of the second-phase particles and $\bar{A}_p^2$ is the mean square of the particle sizes. If the void growth factor is sufficiently large, i.e. $a/A_p \gtrsim 5 - 10$, than the last term in Eq. (5.48) will dominate and a closed form scaling expression follows as

$$\Sigma_m^* \approx \mathcal{R}_{cr} + K\left(\frac{\bar{\ell}_p\dot{\varepsilon}_v}{c_B}\right)^{6/7}. \tag{5.49}$$

For metals c_B is $\mathcal{O}(10^3$ m/s). With the exception of high-purity materials, $\bar{\ell}_p$ is typically $\mathcal{O}(1\ \mu m)$. Therefore, the ratio $c_B/\bar{\ell}_p$ is $\mathcal{O}(10^9\ \mathrm{s}^{-1})$, and thus according to Eq. (5.49) the spall strength may approach the bulk modulus, i.e. $\Sigma_m^* \approx K$, when $\dot{\varepsilon}_v$ is $\mathcal{O}(10^9\ \mathrm{s}^{-1})$.

Considering materials that possess a pre-existing microstructure, i.e. coarse second-phase particles, and a shock-induced microstructure, i.e. vacancy clusters, the approximate scaling behavior for a distribution of vacancy cluster sizes and second-phase particle sizes simply follows from the superposition of Eq. (5.48) and Eq. (5.42), i.e.

$$\dot{\varepsilon}_v \approx \sqrt{\frac{2}{3}\frac{\langle \Sigma_m^* - \mathcal{R}_{cr}\rangle}{\rho}}\frac{\bar{A}_p^2}{\bar{\ell}_p^3} + \frac{8}{9}\frac{\langle \Sigma_m^* - \mathcal{R}_{cr}\rangle^2}{\rho K \dot{\varepsilon}_v}\frac{\bar{A}_p}{\bar{\ell}_p^3} + \frac{8}{9}\sqrt{\frac{2}{3}}\frac{\langle \Sigma_m^* - \mathcal{R}_{cr}\rangle^{7/2}}{\rho^{3/2}K^2\bar{\ell}_p^3\dot{\varepsilon}_v^2} + \frac{c_v^{ne}}{\zeta \bar{A}^3}\int_0^\infty b\chi_m N_{sat} c_s \mathcal{G}(A) A^3 \exp\left(\frac{b\chi_m N_{sat} c_s}{K\dot{\varepsilon}_v}\langle \Sigma_m^* - \Sigma_m^{Em}\rangle\right) dA. \tag{5.50}$$

Assuming relatively large growth factors of voids nucleated from second-phase particles, i.e. $a/A_p \gtrsim 5-10$, at $t = t^*$ and a single dominant family of vacancy cluster sizes $\bar{A}$, the spall strength may be assumed to approximately scale as

$$\Sigma_m^* \approx \min\begin{cases} \mathcal{R}_{cr} + K\left(\frac{\bar{\ell}_p \dot{\varepsilon}_v}{c_B}\right)^{6/7} \\ \Sigma_m^{Em} + K\left(\frac{\dot{\varepsilon}_v}{b c_s \chi_m N_{sat}}\right)\ln\frac{\varphi^*}{c_v^{ne}} - K(\varphi^* - c_v^{ne}). \end{cases} \tag{5.51}$$

Notice that the rate-sensitivity of spall strength is expected to be $m^* \sim 6/7$ for the scaling behavior associated with void nucleation at coarse second-phase particle with void growth dynamics governed by micro-inertia. On the other hand, the rate-sensitivity is expected to be $m^* \sim 1$ when vacancy clustering and subsequent dislocation emission-mediated void growth dominate the strength. The strain rate at which the governing mechanism translates from pre-existing microstructure and micro-inertia to shock-induced microstructure and dislocation kinetics may be obtained by setting the two scaling laws in Eq. (5.51) equal to one another. The transitional strain-rate $\dot{\varepsilon}_v^{trans}$

may therefore be obtained from the solution of the following nonlinear equation:

$$\left(\frac{\bar{\ell}_p \dot{\varepsilon}_v^{trans}}{c_B}\right)^{6/7} - \left(\frac{\dot{\varepsilon}_v^{trans}}{bc_s\chi_m N_{sat}}\right) \ln \frac{\varphi^{trans}}{c_v^{ne}} = \frac{\Sigma_m^{Em} - \mathcal{R}_{cr}}{K} + \varphi^{trans} - c_v^{ne}, \tag{5.52}$$

with $\varphi^{trans} = \max\left(c_v^{ne}, \dot{\varepsilon}_v^{trans}/bc_s\chi_m N_{sat}\right)$.

Some aspects of the role of pre-existing and shock-induced microstructure on spall strength may be gleaned from Eq. (5.51). The dynamic component of the spall strength over the quasi-static critical value $(\Sigma_m^* - \mathcal{R}_{cr})$ scales with $\bar{\ell}_p^{6/7}$ implying that dynamic spall strength is strongly dependent on material microstructure with higher-purity metals being stronger than corresponding low-purity metals (provided that $\mathcal{R}_{cr}$ does not strongly scale with ℓ_p). In the regime where spall strength is governed by the shock-induced microstructure, the second term in Eq. (5.51) scales as the logarithm of the inverse shock-induced nonequilibrium vacancy concentration, i.e. $\ln(1/c_v^{ne})$. Such a scaling implies that the dynamic component of the spall strength in this regime $(\Sigma_m^* - \Sigma_m^{Em})$ is weakly dependent on c_v^{ne} with smaller c_v^{ne} resulting in larger dynamic spall strength. That said, spall strength is still highly sensitive to the shock-induced microstructure since Σ_m^{Em} strongly depends on the size of the vacancy clusters as discussed in chapter 4.

In the following section we examine these scaling behaviors further and make comparisons with experiments. The primary aim is to shed light on some of the most important factors influencing rate-sensitivity and microstructural sensitivity of spall strength.

5.4 Model predictions and comparison with experiments

Here we make use of the simple scaling laws derived in section 5.3 to shed some light on the most important mechanisms governing spall strength. Despite its extreme simplicity, the scaling relation expressed in Eq. (5.51) is very instructive for understanding some of the more perplexing experimentally-observed behavior. Therefore, we limit the scope of the present section to numerical analysis of Eq. (5.51). In general, Eq. (5.51) captures the behavior of an idealized material microstructure that is composed of a delta distribution of shock-induced vacancy clusters of size $\bar{A}$ and a delta distribution of second-phase particles with mean spacing characterized by $\bar{\ell}_p$.

5.4.1 *Ideal* spall strength of metals

It is useful to first examine the *ideal* spall strength of ultra-pure metals in the limit of $\bar{\ell}_p \to \infty$. For this case, Eq. (5.51) collapse to Eq. (5.44) with the spall strength governed entirely by the shock-induced microstructure, i.e. c_v^{ne} and $\bar{A}$, the resistance to dislocation emission Σ_m^{Em}, the saturated mobile dislocation density $\chi_m N_{sat}$, and the associated kinetic constraints imposed by dislocation relativistic effects.

The *ideal* spall strength may be thought of as an upper bound with the expectation that most experimentally measured spall strengths should lie below this upper bound. Two limiting cases that may approach this upper bound are ultra high-purity mate-

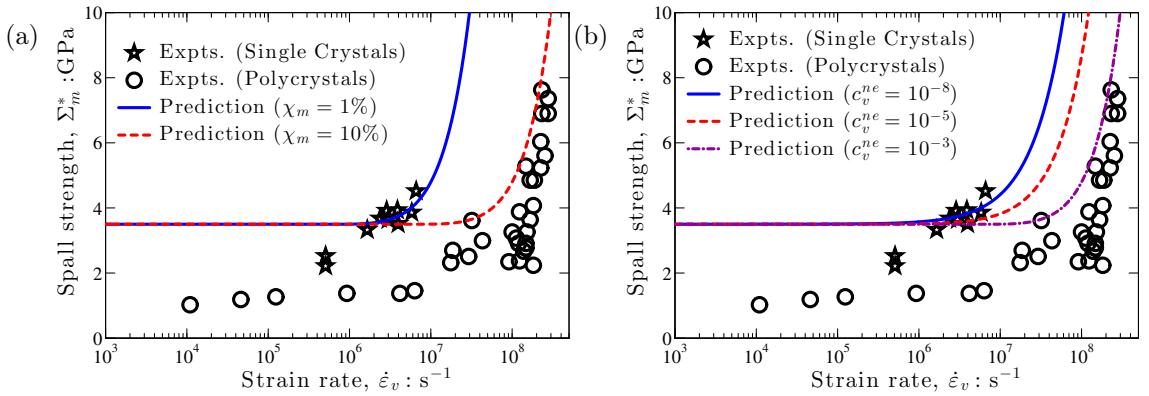

Fig. 5.5: *Ideal* spall strength of aluminum as predicted by Eq. (5.44) with (a) demonstrating the effect of the parameter χ_m that denotes the fraction of mobile dislocations in the saturated state, i.e. $N_m \to \chi_m N_{sat}$ and (b) the effect of vacancy cluster concentration c_v^{ne}. Unless otherwise noted the model parameters are $\chi_m = 10\%, N_{sat} = 10^{17}\text{m}^{-2}, c_v^{ne} = 10^{-3}, \bar{A} = 2$ nm, and $\Sigma_m^{Em}(\bar{A}) = 3.5$ GPa. Experimental measurements reported in [96, 98–100, 114].

rials with very large second phase particle spacings as well as more ordinary metals subject to the most extreme tensile strain rates generated by laser shock experiments. Fig. 5.5 provides predictions of the *ideal* spall strength of aluminum according to the scaling relation Eq. (5.44). Notice that for a large set of assumed material parameters the polycrystal experimental data falls below the upper bound, with its nearest approach occurring at the most extreme strain rates ($\gtrsim 10^8\text{s}^{-1}$). The single crystal data is for very high-purity aluminum crystals, and as such the scaling relation may be thought of as more of an approximation than an upper bound (at sufficiently high strain rates).

The agreement between the single crystal spall data and the model predictions depend strongly on the assumed model parameters. More detailed discrete defect

calculations are required to better understand how widely the material parameters may vary for realistic materials. For example, in Fig. 5.5(a) taking $\chi_m N_{sat} \sim 10^{15}\text{m}^{-2}$ with $c_v^{ne} = 10^{-3}$ results in a reasonable agreement between the predicted and observed rate-sensitivity for high-purity single crystal spall strength for strain rates $\gtrsim 3 \times 10^6\text{s}^{-1}$. However, a similar level of agreement may be had by assuming $\chi_m N_{sat} \sim 10^{16}\text{m}^{-2}$ with $c_v^{ne} = 10^{-8}$ as in Fig. 5.5(b). Chapter 8 provides some discussion of the kinds of discrete defect calculations that may be utilized to establish a more fundamental understanding of these model parameters.

It is also worthwhile to reemphasize here the importance of vacancy clustering kinetics. The results provided in Fig. 5.5 assume that there is enough time during the loading for a fraction of the superconcentrated vacancies to cluster together enough to form at least some nanovoids of size $\bar{A} = 2$ nm or greater. The curves in Fig. 5.5(b) all shift up by about 1.5 GPa if the clustering kinetics are only fast enough to form nanovoids of about 1 nm in size (recall from chapter 4 that dislocation emission is strongly size-dependent). Certainly, more detailed clustering kinetics simulations are desirable. Fig. 5.5 does however demonstrate the feasibility of vacancy clustering and dislocation emission as an important mechanism in governing the spall strength of high-purity metals as well as more ordinary metals subject to the most extreme loading conditions. It is also worth noting that since the nonequilibrium vacancy concentration scales with the magnitude of the shock stress Σ_{ss}, i.e. Eq. (5.31), we expect the *ideal* spall strength of materials to be dependent on the magnitude of Σ_{ss}.

5.4.2 Transition between dominant mechanisms

Consider now the general scaling relation Eq. (5.51) that models the spall strength of an idealized material microstructure that is composed of a delta distribution of shock-induced vacancy clusters of size $\bar{A}$ and a delta distribution of second-phase particles with mean spacing characterized by $\bar{\ell}_p$. Under what conditions will the shock-induced microstructure transition into the dominate mechanism? This question is addressed in the present subsection.

In Eq. (5.51) the pre-existing microstructure is characterized primarily by $\bar{\ell}_p$, which depends directly on the purity-level. Most spall strength experiments of single crystals happen to be performed on very high-purity single crystals, while the majority of spall strength measurements on polycrystals happen to make use of less pure materials. This should be kept in mind when comparing single crystal and polycrystal data. Here we assume $\bar{\ell}_p = 20\mu$m for high-purity single crystals and take it to be $\bar{\ell}_p = 2\mu$m for lower purity polycrystals. In addition to $\bar{\ell}_p$, void nucleation may be easier in lower-purity materials as compared with high-purity materials. As such, we assume that second-phase particles in high-purity single crystals are about twice as resistant to void nucleation as compared with lower-purity polycrystals, i.e. $\mathcal{R}_{cr} = 1$ GPa for polycrystals and $\mathcal{R}_{cr} = 2$ GPa for high-purity single crystals. This need not be the case for low-purity single crystals as demonstrated by Minich et al. [139] for single crystal copper doped with SiO_2 particles.

Utilizing these assumptions, Fig. 5.6 demonstrates the rate-dependence of spall

strength across the two regimes as predicted by Eq. (5.51). Below the transitional strain rate $\dot{\varepsilon}_v^{trans}$ (identified here by the knee in each curve) the rate-sensitivity of spall strength is governed by the nucleation of voids at second-phase particles whose subsequent growth dynamics are governed by micro-inertia, i.e. Eq. (5.49). Above the transition strain rate $\dot{\varepsilon}_v^{trans}$, the rate-sensitivity is governed by the clustering of vacancies and subsequent dislocation-emission mediated void growth, i.e. Eq. (5.44).

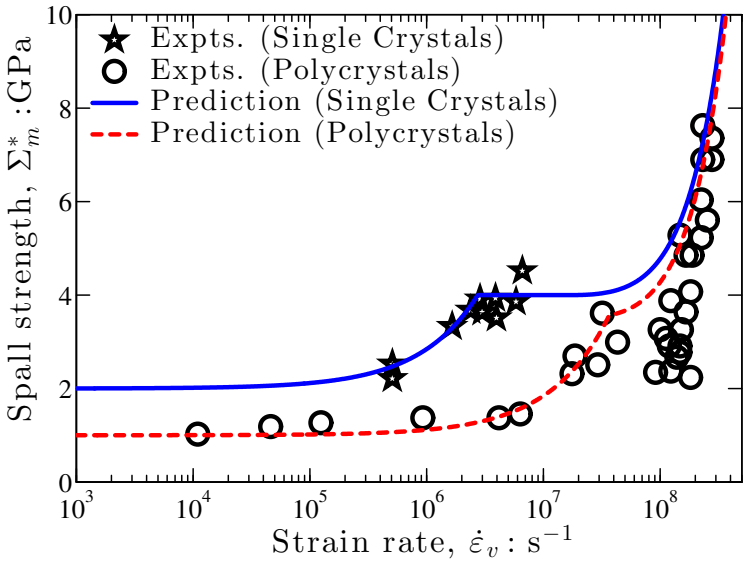

Fig. 5.6: Transition in dominant mechanism governing spall strength as predicted by Eq. (5.51). Below the transitional strain rate $\dot{\varepsilon}_v^{trans}$ (identified here by the knee in each curve) the rate-sensitivity of spall strength is governed by the nucleation of voids at second-phase particles whose subsequent growth dynamics are governed by micro-inertia, i.e. Eq. (5.49). Above the transition strain rate, the rate-sensitivity is governed by the clustering of vacancies and subsequent dislocation-emission mediated void growth, i.e. Eq. (5.44). The transitional strain rate $\dot{\varepsilon}_v^{trans}$ increases with decreasing ℓ_p and may be obtained directly from Eq. (5.52). Assumed model parameters for single crystals are $\mathcal{R}_{cr} = 2$ GPa, $\Sigma_m^{Em} = 4$ GPa, $\bar{\ell}_p = 20\mu$m, $c_v^{ne} = 0.2\%$, $\chi_m N_{sat} = 10^{16}\text{m}^{-2}$. Parameters for polycrystals are taken as $\mathcal{R}_{cr} = 1$ GPa, $\Sigma_m^{Em} = 3.5$ GPa, $\bar{\ell}_p = 2\mu$m, $c_v^{ne} = 0.2\%$, $\chi_m N_{sat} = 10^{16}\text{m}^{-2}$. Experimental measurements reported in [96, 98–100, 114].

It is rather remarkable that the simple scaling relation provided in Eq. (5.51) is able to capture most of the experimental data in Fig. 5.6. Notice that the transition to vacancy clustering and subsequent dislocation emission dominated spall behavior in single crystals occurs at about an order of magnitude lower transition strain rate than in polycrystals. In general, the transitional strain rate $\dot{\varepsilon}_v^{trans}$ is inversely related to $\bar{\ell}_p$ (provided that $\mathcal{R}_{cr}$ does not depend strongly on $\bar{\ell}_p$). The transitional strain rate $\dot{\varepsilon}_v^{trans}$ may be obtained directly from the solution of Eq. (5.52). In the following subsection, we explore further the role of pre-existing microstructure and discuss some strategies for engineering materials with enhanced spall strength.

5.4.3 Scaling laws for microstructural design

5.4.3.1 Limits to enhancement through purity refinement

Throughout this section we have emphasized the role of purity-level on spall strength. Generally speaking, the higher the purity-level the higher the spall strength. Is there a limit to this trend for high purity metals beyond which further reductions of impurity content fail to yield enhancements in spall strength? The present subsection addresses this question, demonstrating that such a limit is directly related to the transition in the dominant governing mechanism from pre-existing microstructure to shock-induced microstructure.

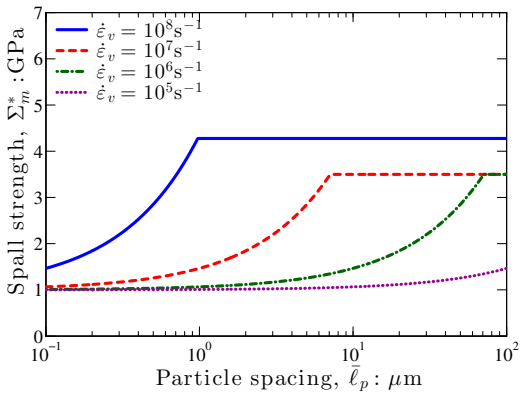

Fig. 5.7: Spall strength as a function of particle spacing $\bar{\ell}_p$ and strain rate $\dot{\varepsilon}_v$ according to Eq. (5.51). The plot demonstrates that spall strength is very sensitive to purity-level up to a point; however, once a critical (strain rate-dependent) purity-level has been achieved, further reductions of impurities does not improve the spall strength (as the spall strength of these ultra-pure metals is governed by the shock-induced microstructure). The knees in the plots identify transitions in the dominant mechanisms, and may be obtained directly from the solution of Eq. (5.53). Model parameters are taken to be $\mathcal{R}_{cr} = 1$ GPa, $\Sigma_m^{Em} = 3.5$ GPa, $c_v^{ne} = 0.2\%$, $\chi_m N_{sat} = 10^{16}\text{m}^{-2}$.

Fig. 5.7 provides a prediction of the spall strength of high-purity aluminum as a function strain rate $\dot{\varepsilon}_v$ and particle spacing $\bar{\ell}_p$ with larger $\bar{\ell}_p$ representing a higher purity material. Spall strength is highly sensitive to the impurity content for most cases. However, the spall strength of very high-purity materials, i.e. $\bar{\ell}_p \gtrsim 10^1 - 10^2$, is relatively insensitive to further reductions in the impurity content at very high strain rates ($\gtrsim 10^6 - 10^7 \text{s}^{-1}$). At such high purity levels the spall strength is approaching the ideal spall strength for relatively lower (but still high) applied strain rates.

We define a transitional mean second-phase particle spacing $\bar{\ell}_p^{trans}$ to be associated with the purity-level required for the dominant governing mechanism to transition from void growth at second-phase particles to void growth from the shock-induced

microstructure (at a particular strain rate). This transitional mean second-phase particle spacing may be obtained by setting the two scaling laws in Eq. (5.51) equal to one another, i.e.

$$\bar{\ell}_p^{trans} = \frac{c_B}{\dot{\varepsilon}_v}\left(\frac{\Sigma_m^{Em} - \mathcal{R}_{cr}}{K} + \left(\frac{\dot{\varepsilon}_v}{bc_s\chi_m N_{sat}}\right)\ln\frac{\varphi^*}{c_v^{ne}} + \varphi^* - c_v^{ne}\right)^{7/6} \tag{5.53}$$

Of course, in real-world applications high-purity single crystals are typically undesirable due to their low shear strength, in despite of their remarkably high resistance to spall failure. A more technologically relevant strategy for enhancing spall strength is through grain refinement, discussed in the proceeding subsection.

5.4.3.2 Enhancement through grain refinement

The experimental literature on the influence of grain size on spall strength is complex and often conflicting. Some studies have demonstrated an increase in spall strength with decreasing grain size, others have shown a decrease with decreasing grain size, and several others have reported no discernible effect at all. In the present chapter we demonstrate through our simple scaling relation that any of these behaviors may be expected depending on the grain size range investigated, the strain rate of interest, and the processing route utilized for grain refinement. The simple scaling laws presented here help establish a greater understanding of the role of grain size in spall failure. The traditional lack of understanding on the subject is one of the principle bottlenecks slowing the advancement of grain refinement as a strategy for enhancing spall strength of materials for relevant applications.

The complexity with the role of grain size on spall strength is primarily comes about through the fact that grain size may strongly influence both the first and second term on the right hand side of Eq. (5.49). The first term $\mathcal{R}_{cr}$ scales linearly with the yield strength σ_y, e.g. $\mathcal{R}_{cr} = 2/3\sigma_y \ln 1/\varphi$, which scales as the inverse square root of the grain size, i.e. $\sigma_y = \sigma_0 + k_{HP}/\sqrt{d_G}$, where k_{HP} is the Hall-Petch coefficient with σ_0 denoting a reference flow strength for a corresponding coarse-grained material. Accordingly, a scaling relation for the critical resistance to void nucleation (which is consistent with the so called incipient spall strength) follows as

$$\mathcal{R}_{cr} = \mathcal{R}^0_{cr}\left(1 + \frac{k_{HP}}{\sigma_0\sqrt{d_G}}\right), \tag{5.54}$$

with $\mathcal{R}^0_{cr}$ denoting a reference critical resistance for a corresponding coarse-grained material.

The second term in Eq. (5.49), i.e. $K\left(\bar{\ell}_p\dot{\varepsilon}_v/c_B\right)^{6/7}$, may depend strongly on grain size depending on the processing route. Grain refinement by ball milling introduces a significant number of impurities to achieve the desired ultra-fine grain or nanocrystalline structures. One would expect the spacing between second-phase particle spacing to decrease with decreasing grain size, for example

$$\bar{\ell}_p = \left(\frac{1}{\bar{\ell}^0_p} + \frac{1}{d_G}\right)^{-1}, \tag{5.55}$$

where $\bar{\ell}^0_p$ is the second-phase particle spacing prior to grain refinement. Grain refinement by severe plastic deformation (SPD), on the other hand, does not necessarily require the introduction of additional impurities. However, pre-existing second-phase

particles may fragment during the SPD processing, e.g. during the first few equal-channel angular pressing (ECAP) passes. As such, a different scaling relation between grain size and second-phase particle spacing likely holds for this processing method. For lack of any better model we assume here that the SPD process may be modeled as

$$\frac{\bar{\ell}_p}{d_p} = \frac{\bar{\ell}_p^0}{d_p^0}, \tag{5.56}$$

where d_p^0 and d_p denote the second-phase particle diameters before and after SPD-induced fragmentation. Here we assume d_p/d_p^0 to be about 10. Combining the scaling laws one may approximate the grain size dependence of spall strength (in the regime

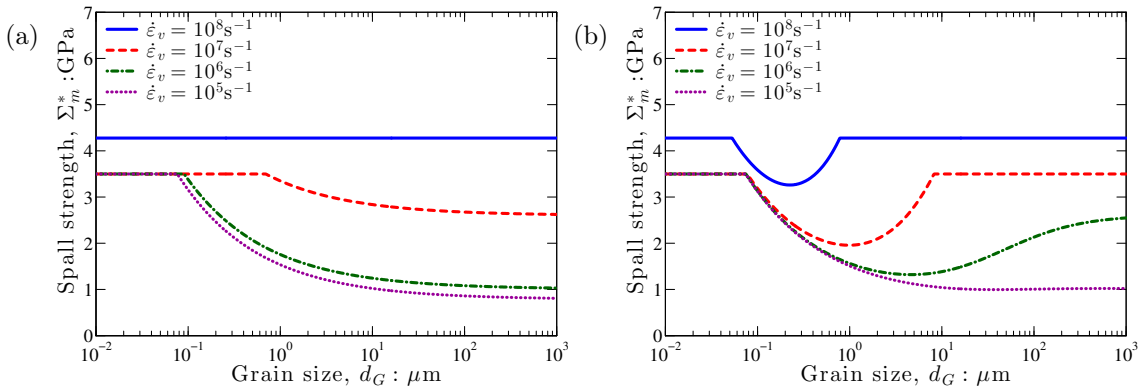

Fig. 5.8: Spall strength as a function of grain size d_G and strain rate $\dot{\varepsilon}_v$ for polycrystals processed by (a) severe plastic deformation (SPD) and (b) ball milling as predicted by Eq. (5.57) and Eq. (5.44). The plot demonstrates that spall strength may depend on grain-size in a complex manner that depends on the strain rate under consideration and the processing route. Either processing route produces a Hall-Petch type strengthening of the critical resistance to void growth, i.e. $\mathcal{R}_{cr} \propto 1/\sqrt{d_G}$. The difference is associated with the fact that ball milling introduces additional impurities to reduce grain size, i.e. $\ell_p \propto d_G$, whereas the purity content for SPD may be assumed to be approximately constant. Model parameters are taken to be $\mathcal{R}_{cr}^0 = 0.75$ GPa, $\Sigma_m^{Em} = 3.5$ GPa, $c_v^{ne} = 0.2\%$, $\chi_m N_{sat} = 10^{16}\mathrm{m}^{-2}$, $k_{HP}/\sigma_0 = 10^{-4}\sqrt{\mathrm{m}}$, and $\bar{\ell}_p = 50\mu$m.

dominated by pre-existing microstructure) as

$$\Sigma_m^* \approx \begin{cases} \mathcal{R}_{cr}^0 \left(1 + \frac{k_{HP}}{\sigma_0 \sqrt{d_G}}\right) + K \left(\frac{1}{\bar{\ell}_p^0} + \frac{1}{d_G}\right)^{-6/7} \left(\frac{\dot{\varepsilon}_v}{c_B}\right)^{6/7} & \text{for ball milling} \\ \mathcal{R}_{cr}^0 \left(1 + \frac{k_{HP}}{\sigma_0 \sqrt{d_G}}\right) + K \left(\frac{\bar{\ell}_p^0 d_p \dot{\varepsilon}_v}{d_p^0 c_B}\right)^{6/7} & \text{for SPD.} \end{cases} \tag{5.57}$$

Fig. 5.8 demonstrates the predicted grain size dependence of spall strength as a function of strain rate $\dot{\varepsilon}_v$. As emphasized throughout, shock-induced microstructure dominates the behavior at the highest strain rates, and pre-existing microstructure becomes irrelevant as shown in Fig. 5.8(a). Similar to the transitional mean second-phase particle spacing $\bar{\ell}_p^{trans}$ defined in Eq. (5.53), we may define a transitional grain size d_G^{trans} for materials processed by SPD. d_G^{trans} identifies the transition in dominant governing mechanism from grain structure to shock-induced microstructure (at a particular strain rate). This transitional grain size may be obtained by setting the SPD scaling law in Eq. (5.57) equal to the shock-induced scaling law Eq. (5.44), i.e.

$$d_G^{trans} = \frac{\left(\frac{R_{cr}^0 k_{HP}}{K \sigma_0}\right)^2}{\left(\frac{\Sigma_m^{Em}}{K} - \left(\frac{\bar{\ell}_p^0 d_p \dot{\varepsilon}_v}{d_p^0 c_B}\right)^{6/7} + \left(\frac{\dot{\varepsilon}_v}{b c_s \chi_m N_{sat}}\right) \ln \frac{\varphi^*}{c_v^{ne}} + \varphi^* - c_v^{ne}\right)^2} \tag{5.58}$$

Below the most extreme strain rates the spall strength may be highly sensitive to grain size. From Fig. 5.8(a) the behavior of the SPD aluminum is somewhat expected:

- ✦ coarse-grained (CG) structures ($\gtrsim 100\mu$m) being mostly insensitive to d_G
- ✦ fine-grained (FG) structures ($\sim 10\mu$m) being somewhat sensitive to d_G
- ✦ ultra-fine-grained (UFG) materials ($\lesssim 1\mu$m) exhibiting strong enhancement

- ✦ with enhancement saturated for nanocrystalline (NC) materials ($\lesssim$ 100 nm).

From Fig. 5.8(b) we see that the predicted behavior of materials processed by ball milling are similar for UFG and NC grain sizes. However, there is a notable difference at larger grain sizes with coarse-grained and fine-grained materials softening with decreasing grain size at very high strain rates. Additionally, the material processed by ball milling exhibits two transitional grain sizes which may be obtained directly from the numerical solution of

$$\frac{R^0_{cr} k_{HP}}{K\sigma_0\sqrt{d^{trans}_G}} + \left(\frac{1}{\bar{\ell}^0_p} + \frac{1}{d^{trans}_G}\right)^{-6/7} \left(\frac{\dot{\varepsilon}_v}{c_B}\right)^{6/7} = \frac{\Sigma^{Em}_m}{K} + \left(\frac{\dot{\varepsilon}_v}{bc_s\chi_m N_{sat}}\right) \ln\frac{\varphi^*}{c^{ne}_v} + \varphi^* - c^{ne}_v. \tag{5.59}$$

Although our analysis is quite simple, Fig. 5.8 clearly demonstrates the complexity associated with the relationship between grain size and spall strength. Detailed crystal plasticity calculations are planned for future work. In addition, further experimental investigations are needed, with particular emphasis given to the characterization of second-phase particle size distributions and spacings, grain size and morphology, and any relationships between the two. Such efforts are critical to improving our ability to harness grain refinement for the enhancement of spall strength.

5.5 Summary of key findings

The chapter has provided a mechanism-based ductile failure model capable of capturing the role of pre-existing and shock-induced microstructures on the spall

strength of metals. Making use of a few key simplifications, simple scaling laws were derived from the more general mechanism-based framework. Though simple, the derived scaling laws proved powerful in helping to shed light on some of the more perplexing experimental observations associated with spall failure.

The key findings and implications may be summarized as follows:

- ✦ Pre-existing microstructure, e.g. second-phase particle spacing and grain size, governs the spall strength of materials under most loading situations
- ✦ At extreme rates spall strength is governed by a shock-induced microstructure, e.g. vacancy clusters, with growth mediated by dislocation emission
- ✦ The transition to shock-induced dominated behavior occurs at slightly lower strain rates for high purity crystals
- ✦ Spall strength depends on grain-size in a complex manner that depends on loading rate and processing route
- ✦ Materials processed by severe plastic deformation (SPD) are predicted to strengthen with decreasing grain size
- ✦ Materials processed by ball milling are expected to first soften with decreasing grain size, then strength in the ultra-fine-grained regime.

Chapter 6

A thermodynamically consistent multiscale mechanism-based framework for dynamic failure of ductile FCC crystals

6.1 Introduction

The advancement of a number of technologies and applications critical to our safety and well-being (e.g. inertial confinement fusion, nuclear stockpile reliability, defense systems, spacecraft and hypersonic aircraft shielding, vehicular crashworthiness, and advanced manufacturing) depends on our capacity to predict the response

of metals subject to complex dynamic loading paths in extreme thermomechanical environments. Such extreme thermomechanical environments may include pressures on the order of the bulk modulus, shear stresses near the ideal strength, temperatures approaching melting, very high strain rates ($10^3 - 10^8$ s^{-1}), as well as large deformations and rotations. The current chapter aims to provide a thermodynamically consistent multiscale framework for modeling the deformation and failure of ductile FCC single crystals subject to complex, three-dimensional dynamic loading paths in these extreme thermomechanical environments.

One of the primary challenges associated with developing such a framework is the fact that dynamic failure is highly sensitive to the current stress state, temperature, loading rate, and material microstructure, as well as their histories, see for example [99, 140–142]. This is in stark contrast to thermoelasticity and the equation of state for solid materials, which are usually modeled quite successfully as functions of current elastic deformation and temperature only, with no direct dependence on loading rate or history of loading rate. Given this strong sensitivity of dynamic failure to a very large set of evolving parameters, it is unlikely that an empirical model with numerous *ad hoc* fitting parameters would be able to capture the rate-dependent failure envelope over a large set of stress states and strain rate histories. Furthermore, there are only a limited number of stress states accessible by fundamental experiments (e.g. uniaxial strain spall experiments) and thus there is insufficient data to even attempt such an empirical fit. Given these realities, we adopt a multiscale mechanism-based modeling

approach in which macroscopic failure evolution is governed by appropriate models of microscale processes occurring within the material.

The failure of ductile metals is known to be governed by the microscopic processes of void nucleation, growth, and finally coalescence leading to failure [52–56]. Void nucleation at second-phase particles that lie either along grain boundaries are within grains is well documented [71–76]. More recent work [64–70] suggests that under extremely high tensile stresses, voids may also nucleate from vacancy clusters. Accounting for this hierarchy of void nucleation sites is critical to the accurate prediction of the dynamic failure response of metals, which was the major discussion point of chapter 5.

The observed rate-dependence of dynamic ductile failure, e.g. [98–100, 113, 140], is associated with the rate-dependence of the microscopic processes of void nucleation, growth, and coalescence. In order to incorporate this rate-dependence in our multiscale mechanism-based framework, we explicitly account for the rate-dependence of dynamic void growth. The aspects of the rate-dependence associated with micro-inertia are accounted for by following the approach first laid out by Knowles and Jakub [82] and later extended by Carroll and Holt [83]. The additional void growth rate-dependence associated with the rate-dependence of thermally-activated dislocation glide is modeled similarly to Cortés [85, 86] and Tong and Ravichandran [93, 94]. However, this model is not necessarily appropriate at extreme strain rates where dislocation glide may be governed by relativistic drag [10, 49]. Within this regime, it is

necessary to impose the upper bounds on void growth velocity discussed in chapter 3 (as well as [50]). Lastly, at very high tensile pressures it may be possible for voids to grow by dislocation emission as discussed in chapter 4 as well as [64–70]. The parameterized dislocation emission mediated void growth model presented in chapter 4 is utilized here to account for this possible phenomenon.

A critical aspect of this multiscale mechanics-based approach is the recognition that the local microscopic stresses and temperatures drive microscopic failure processes, as opposed to macroscopic stresses and temperatures. Generally, the microscopic stress state is different from that at the macroscale. However, explicitly resolving the microscopic stress field is typically computationally infeasible. Therefore, we make use of a self-consistent micromechanics formulation that relates the microscopic stress and strain fields to those of the macroscale through fourth-order stress and strain concentration tensors, which are fundamentally derived from the Eshelby tensor [143], volume averaging concepts [138], and Mori-Tanaka assumptions [124]. This approach naturally leads to effective macroscopic thermoelastic properties that are generally nonlinear functions of porosity and are often regarded as more accurate than simple volumetric averaging.

It is just as important to such a multiscale mechanics-based formulation to provide a proper treatment of the thermodynamics, in order to accurately predict the complex temperature evolution associated with irreversible nonequilibrium shock compression, near isentropic release, and dissipation associated with plastic and inelastic work. Ac-

curate prediction of the temperature evolution is critical because it intimately affects the failure processes. The temperature dependence of quasi-static ductile failure processes has been well documented, with the most well-known example being the famous ductile-to-brittle transition temperature, e.g. [144]. Unfortunately, such a deep understanding does not currently exist for the role of temperature in dynamic ductile failure. However, Kanel and Razorenov [145] and Kanel et al. [100] have experimentally observed a complex temperature dependence of spall strength that appears to be dependent on the loading rate. Given this motivation for an accurate prediction of temperature evolution, we provide an extension of the rigorous thermodynamic formulation of Luscher et al. [146] to be applicable to porous single crystals.

This chapter is organized as follows. Section 6.2 provides an overview of the finite deformation kinematics associated with a material undergoing elastic, plastic, and porous deformations. Particular attention is given to a proper multiplicative decomposition into dilatational and isochoric parts of the elastic, plastic, and porous deformations. In section 6.3, we extend the rigorous thermodynamic formulation of Luscher et al. [146] to be applicable to porous crystals. Emphasis is placed on obtaining an accurate representation of the evolution of temperature in these materials subject to shock heating and inelastic dissipation. Section 6.4 outlines a micromechanical framework for relating macroscopic and microscopic stress and strains. The micromechanical framework naturally leads to effective macroscopic thermoelastic properties that are functions of the thermoelastic properties of the corresponding solid material.

This micromechanical framework is also utilized in section 6.5 to couple macroscopic inelastic deformations to microscale viscoplasticity and void dynamics. Following this approach, it is unnecessary to provide *ad hoc* macroscopic inelastic flow rules and hardening laws, which would undoubtedly introduce many unknown model parameters difficult to obtain from available experimental data. Lastly, a brief summary and key implications of the formulation are discussed in section 6.6.

6.2 Kinematics

A multiplicative decomposition (Fig. 6.1) of the total macroscopic deformation gradient tensor, $\mathbf{F}$, is assumed such that $\mathbf{F} = \mathbf{F}_e\mathbf{F}_p\mathbf{F}_\varphi$, where $\mathbf{F}_e$, $\mathbf{F}_p$, and $\mathbf{F}_\varphi$ correspond to the elastic, plastic, and porous parts of the macroscopic deformation gradient, respectively. The porous macroscopic deformation gradient tensor $\mathbf{F}_\varphi$ maps the reference configuration $\mathcal{B}_0$ into the intermediate porous configuration $\mathcal{B}_\varphi$, i.e. $\mathbf{x}_\varphi = \mathbf{F}_\varphi\mathbf{x}_0$. The plastic macroscopic deformation gradient tensor $\mathbf{F}_p$ maps the intermediate porous configuration $\mathcal{B}_\varphi$ into the intermediate plastic configuration $\mathcal{B}_p$, i.e. $\mathbf{x}_p = \mathbf{F}_p\mathbf{x}_\varphi$. The elastic macroscopic deformation gradient tensor $\mathbf{F}_e$ maps the intermediate porous configuration $\mathcal{B}_p$ into the current configuration $\mathcal{B}$, i.e. $\mathbf{x} = \mathbf{F}_e\mathbf{x}_p$. The multiplicative decomposition of the total macroscopic deformation gradient tensor

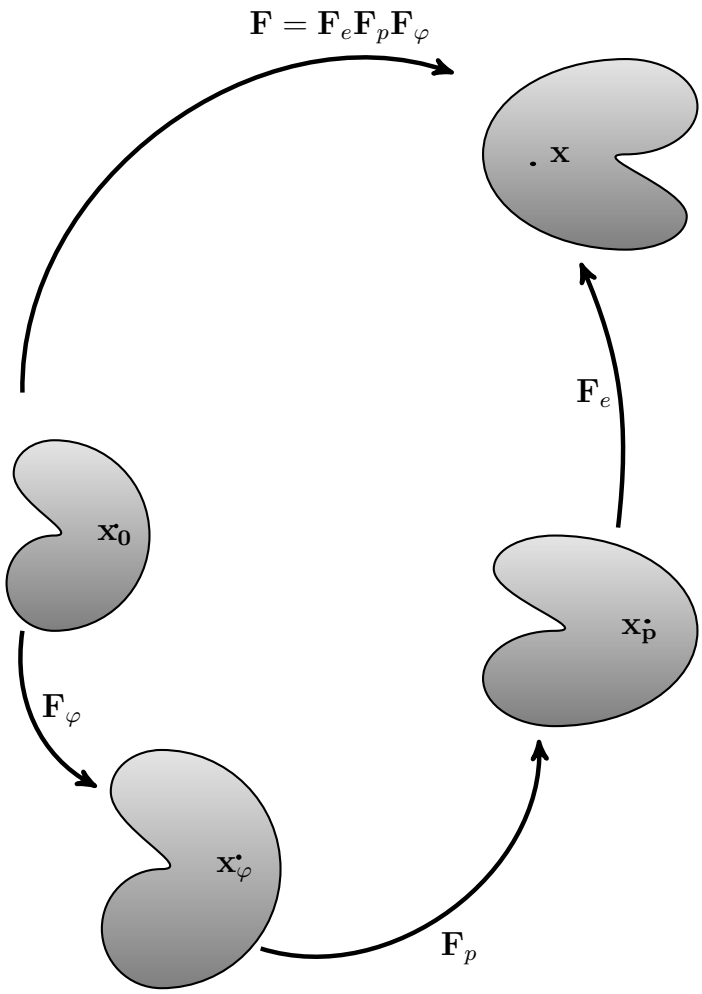

Fig. 6.1: Schematic showing a multiplicative decomposition of the total macroscopic deformation gradient tensor, $\mathbf{F}$, is assumed such that $\mathbf{F} = \mathbf{F}_e\mathbf{F}_p\mathbf{F}_\varphi$, where $\mathbf{F}_e$, $\mathbf{F}_p$, and $\mathbf{F}_\varphi$ correspond to the elastic, plastic, and porous parts of the macroscopic deformation gradient, respectively. The porous macroscopic deformation gradient tensor $\mathbf{F}_\varphi$ maps the reference configuration $\mathcal{B}_0$ into the intermediate porous configuration $\mathcal{B}_\varphi$, i.e. $\mathbf{x}_\varphi = \mathbf{F}_\varphi\mathbf{x}_0$. The plastic macroscopic deformation gradient tensor $\mathbf{F}_p$ maps the intermediate porous configuration $\mathcal{B}_\varphi$ into the intermediate plastic configuration $\mathcal{B}_p$, i.e. $\mathbf{x}_p = \mathbf{F}_p\mathbf{x}_\varphi$. The elastic macroscopic deformation gradient tensor $\mathbf{F}_e$ maps the intermediate porous configuration $\mathcal{B}_p$ into the current configuration $\mathcal{B}$, i.e. $\mathbf{x} = \mathbf{F}_\varphi\mathbf{x}_p$.

leads to a multiplicative decomposition of the macroscopic relative expansion, i.e.

$$J \triangleq \det \mathbf{F} = \underbrace{\det \mathbf{F}_e}_{\triangleq J_e} \underbrace{\det \mathbf{F}_p}_{\triangleq J_p} \underbrace{\det \mathbf{F}_\varphi}_{\triangleq J_\varphi}. \tag{6.1}$$

The macroscopic relative porous expansion relates the macroscopic reference volume, V_0, to the volume in the macroscopic intermediate porous configuration, V_φ, i.e. $J_\varphi = V_\varphi/V_0$. Similarly, the macroscopic relative plastic expansion relates the macroscopic porous volume, V_φ, to the volume in the macroscopic intermediate plastic configuration, V_p, i.e. $J_p = V_p/V_\varphi$. Consistent with dislocation-based plasticity, the macroscopic plastic deformation may be assumed to be incompressible, i.e. $J_p = 1$, and consequently $V_p = V_\varphi$. Therefore, the macroscopic elastic relative expansion relates the volume in the macroscopic intermediate porous configuration, V_φ, to the volume in the current configuration, V, i.e. $J_e = V/V_\varphi$. The macroscopic porosity, φ, is defined as the ratio of total macroscopic void volume in the intermediate porous configuration, V_φ^{void}, to the total macroscopic volume in the intermediate porous configuration, i.e. $\varphi = V_\varphi^{void}/V_\varphi$. This is related to the relative porous expansion through the expression

$$J_\varphi = \frac{1-\varphi_0}{1-\varphi}, \tag{6.2}$$

where φ_0 is the initial macroscopic porosity in the reference configuration. Invoking the conservation of mass, the density in each configuration is proportional to the ratio of the reference macroscopic density to the net macroscopic relative expansion in the

corresponding configuration, i.e.

$$\rho = J^{-1}\rho_0 = J_e^{-1}\underbrace{J_p^{-1}\overbrace{J_\varphi^{-1}\rho_0}^{\triangleq\rho_\varphi}}_{\triangleq\rho_p} \tag{6.3}$$

where the reference density ρ_0 is related to the density of the undeformed solid material ρ_0^s, i.e. $\rho_0 = (1-\varphi_0)\rho_0^s$. As stated previously, we take the plastic deformation to be incompressible, i.e. $J_p = 1$ (consistent with dislocation-based plasticity theory), and consequently $\rho_p = \rho_\varphi$. The macroscopic specific volumes in the reference, intermediate, and current configurations are inversely proportional to the corresponding macroscopic density, i.e. $\mathrm{v}_0 = \rho_0^{-1}; \mathrm{v}_\varphi = \rho_\varphi^{-1}; \mathrm{v} = \rho^{-1}$.

Under shock loading conditions materials may experience both large volumetric as well as large isochoric deformations, for which the usual additive decomposition of volumetric and deviatoric deformation may be insufficient [146]. Hence, we assume a multiplicative decomposition of the total deformation tensor into purely dilatational and purely isochoric parts, i.e. $\mathbf{F} = \sqrt[3]{J}\bar{\mathbf{F}}$, where $J \triangleq \det\mathbf{F}$ is the macroscopic relative expansion corresponding to pure dilatation and $\bar{\mathbf{F}}$ is the total macroscopic isochoric deformation gradient tensor corresponding to pure isochoric deformation, i.e. $\det\bar{\mathbf{F}} = 1$. The definition of the total macroscopic isochoric deformation tensor, i.e. $\bar{\mathbf{F}} \triangleq J^{-1/3}\mathbf{F}$, along with Eq. (6.1) leads to a multiplicative decomposition of the total macroscopic isochoric deformation gradient tensor, i.e.

$$\bar{\mathbf{F}} = \underbrace{J_e^{-1/3}\mathbf{F}_e}_{\triangleq\bar{\mathbf{F}}_e}\underbrace{J_p^{-1/3}\mathbf{F}_p}_{\triangleq\bar{\mathbf{F}}_p}\underbrace{J_\varphi^{-1/3}\mathbf{F}_\varphi}_{\triangleq\bar{\mathbf{F}}_\varphi}. \tag{6.4}$$

The elastic right Cauchy deformation tensor is defined as $\mathbf{C}_e \triangleq \mathbf{F}_e^T \mathbf{F}_e$, with the isochoric part of the elastic right Cauchy deformation tensor being similarly defined as $\bar{\mathbf{C}}_e \triangleq \bar{\mathbf{F}}_e^T \bar{\mathbf{F}}_e$. The corresponding total and isochoric elastic Green-Lagrange strain tensors are defined as $\mathbf{E}_e \triangleq \frac{1}{2}(\mathbf{C}_e - \mathbf{I})$ and $\bar{\mathbf{E}}_e \triangleq \frac{1}{2}(\bar{\mathbf{C}}_e - \mathbf{I})$. In the following subsection on thermodynamics, it proves useful to consider the partial derivative of the isochoric elastic Green-Lagrange strain tensor with respect to the total Green-Lagrange strain tensor, i.e.

$$\mathbb{M} \triangleq \frac{\partial \bar{\mathbf{E}}_e}{\partial \mathbf{E}_e} = \frac{\partial \bar{\mathbf{C}}_e}{\partial \mathbf{C}_e} = J_e^{-2/3} \left(\mathbf{I} \boxtimes \mathbf{I} - \frac{1}{3} \mathbf{C}_e \otimes \mathbf{C}_e^{-1} \right), \tag{6.5}$$

where the operator $\boxtimes$ obeys the property $[\mathbf{A} \boxtimes \mathbf{B}]_{ijkl} = A_{ik} B_{jl}$. Consequently $[\mathbf{I} \boxtimes \mathbf{I}]_{ijkl} = \delta_{ik}\delta_{jl}$, where δ_{ik} is the usual Kronecker delta function. The partial derivative of the elastic relative expansion with respect to the total Green-Lagrange strain tensor also proves useful:

$$\frac{\partial J_e}{\partial \mathbf{E}_e} = 2 \frac{\partial}{\partial \mathbf{C}_e} \sqrt{\det(\mathbf{C}_e)} = J_e \mathbf{C}_e^{-1}. \tag{6.6}$$

Consider now the elastic-plastic-porous decomposition of the total macroscopic velocity gradient, $\mathbf{L} \triangleq \dot{\mathbf{F}} \mathbf{F}^{-1}$, and the total macroscopic rate of deformation tensor, $\mathbf{D} \triangleq \frac{1}{2}\left(\mathbf{L} + \mathbf{L}^T\right)$. The multiplicative decomposition of the total macroscopic deformation gradient tensor, $\mathbf{F} = \mathbf{F}_e \mathbf{F}_p \mathbf{F}_\varphi$, leads to additive decompositions of both the total macroscopic velocity gradient as well as the total macroscopic rate of deformation tensor, i.e.

$$\mathbf{L} = \underbrace{\dot{\mathbf{F}}_e \mathbf{F}_e^{-1}}_{\triangleq \mathbf{L}_e} + \underbrace{\mathbf{F}_e \dot{\mathbf{F}}_p \mathbf{F}_p^{-1} \mathbf{F}_e^{-1}}_{\triangleq \mathbf{L}_p} + \underbrace{\mathbf{F}_e \mathbf{F}_p \dot{\mathbf{F}}_\varphi \mathbf{F}_\varphi^{-1} \mathbf{F}_p^{-1} \mathbf{F}_e^{-1}}_{\triangleq \mathbf{L}_\varphi}, \tag{6.7}$$

and

$$\mathbf{D} = \underbrace{\tfrac{1}{2}\left(\mathbf{L}_e + \mathbf{L}_e^T\right)}_{\triangleq \mathbf{D}_e} + \underbrace{\tfrac{1}{2}\left(\mathbf{L}_p + \mathbf{L}_p^T\right)}_{\triangleq \mathbf{D}_p} + \underbrace{\tfrac{1}{2}\left(\mathbf{L}_\varphi + \mathbf{L}_\varphi^T\right)}_{\triangleq \mathbf{D}_\varphi}. \tag{6.8}$$

In the present formulation $\mathbf{F}_p$ encapsulates the isochoric deformation associated with non-spherical void growth. $\mathbf{F}_\varphi$ is defined such that it only captures the dilatational deformation associated with spherical void growth. The resulting porous deformation tensor that generates the desired relative porous expansion is simply given by $\mathbf{F}_\varphi = \sqrt[3]{J_\varphi}\mathbf{I}$, and the corresponding porous velocity gradient and rate of deformation tensors are given by $\mathbf{L}_\varphi = \mathbf{D}_\varphi = \frac{1}{3}\frac{\dot{\varphi}}{1-\varphi}\mathbf{I}$. Note that this relation holds only for our definition of $\mathbf{F}_\varphi$ which captures the dilatational deformation associated with spherical void growth with non-sphercial void growth captured in $\mathbf{F}_p$.

As a consequence of the additive decomposition of the rate of deformation tensor, a similar additive decomposition of the macroscopic internal stress power per unit mass naturally follows, i.e.

$$\mathcal{P} \triangleq \frac{\boldsymbol{\Sigma} : \mathbf{D}}{\rho} = \frac{\boldsymbol{\Sigma} : \mathbf{D}_e}{\rho} + \frac{\boldsymbol{\Sigma} : \mathbf{D}_p}{\rho} + \frac{\boldsymbol{\Sigma} : \mathbf{D}_\varphi}{\rho}, \tag{6.9}$$

where ρ and $\boldsymbol{\Sigma}$ are respectively the macroscopic mass density and the macroscopic Cauchy stress in the current configuration. We also note that the macroscopic second Piola-Kirchhoff stress, $\mathbf{S} \triangleq J_e \mathbf{F}_e^{-1} \boldsymbol{\Sigma} \mathbf{F}_e^{-T}$, in the intermediate plastic configuration is a stress conjugate of the elastic Green-Lagrange strain rate tensor, i.e.

$$\frac{\boldsymbol{\Sigma} : \mathbf{D}_e}{\rho} = \frac{\mathbf{S} : \dot{\mathbf{E}}_e}{\rho_\varphi}, \tag{6.10}$$

where $\rho_\varphi = \rho_p$ is the mass density in both the intermediate porous and plastic configurations.

6.3 Thermodynamics

The strong form of the macroscopic energy balance may be expressed as

$$\rho\dot{\mathcal{E}} = \rho\mathcal{P} + \rho\mathcal{Q}_s - \nabla\cdot\mathbf{q}, \tag{6.11}$$

where $\mathcal{E}$ and $\mathcal{P}$ are the macroscopic internal energy and internal stress per unit mass, $\mathcal{Q}_s$ is the macroscopic heat supply per unit mass, and $\mathbf{q}$ is the macroscopic heat flux per unit mass. The macroscopic Helmholtz free energy per unit mass, Ψ, is defined as the energy available for doing useful work on the system at a constant absolute temperature Θ, i.e. $\Psi \triangleq \mathcal{E} - \mathcal{N}\Theta$, where $\mathcal{N}$ is the macroscopic internal entropy per unit mass. Time differentiation of the Helmholtz free energy combined with Eq. (6.11) results in an alternative form of the energy balance, i.e.

$$\rho\dot{\Psi} = \rho\mathcal{P} - \rho\dot{\mathcal{N}}\Theta - \rho\mathcal{N}\dot{\Theta} + \rho\mathcal{Q}_s - \nabla\cdot\mathbf{q}. \tag{6.12}$$

Considering the additive decomposition of the macroscopic internal stress power, Eq. (6.9), along with Eq. (6.10) results in the most useful form of the energy balance, i.e.

$$\rho\dot{\Psi} = J_e^{-1}\mathbf{S}_q : \dot{\mathbf{E}}_e + \underbrace{\boldsymbol{\Sigma}_q : \mathbf{D}_p + \boldsymbol{\Sigma}_q : \mathbf{D}_\varphi + \boldsymbol{\Sigma}_d : \mathbf{D}}_{\triangleq\rho\mathcal{P}_d} - \rho\dot{\mathcal{N}}\Theta - \rho\mathcal{N}\dot{\Theta} + \rho\mathcal{Q}_s - \nabla\cdot\mathbf{q}, \tag{6.13}$$

where we have assumed that the total macroscopic Cauchy stress may be additively decomposed into quasi-conservative and dissipative parts, i.e. $\boldsymbol{\Sigma} = \boldsymbol{\Sigma}_q + \boldsymbol{\Sigma}_d$, following the thermodynamic arguments of Ziegler [147]. The dissipative part of the total Cauchy stress, $\boldsymbol{\Sigma}_d$, captures the non-equilibrium irreversible departure from thermodynamic equilibrium typical of shock loading conditions. $\mathbf{S}_q \triangleq J_e \mathbf{F}_e^{-1} \boldsymbol{\Sigma}_q \mathbf{F}_e^{-T}$ is of course the macroscopic quasi-conservative second Piola-Kirchhoff stress, and $\mathcal{P}_d$ is the dissipative part of the internal stress power per unit mass.

Now consider the Helmholtz free energy to be a function of the relevant state variables, i.e.

$$\Psi = \Psi(\mathbf{E}_e, \Theta, \boldsymbol{\Xi}_1, \boldsymbol{\Xi}_2, \boldsymbol{\Xi}_3, ..., \boldsymbol{\Xi}_\kappa) \tag{6.14}$$

where $\boldsymbol{\Xi}_1, \boldsymbol{\Xi}_2, ..., \boldsymbol{\Xi}_\kappa$ is a finite set of κ internal state variables that may be represented by tensors of any order. Following the chain rule, time differentiation of Eq. (6.14) gives

$$\dot{\Psi} = \frac{\partial \Psi}{\partial \mathbf{E}_e} : \dot{\mathbf{E}}_e + \frac{\partial \Psi}{\partial \Theta} \dot{\Theta} + \sum_{k=1}^{\kappa} \frac{\partial \Psi}{\partial \boldsymbol{\Xi}_k} * \dot{\boldsymbol{\Xi}}_k, \tag{6.15}$$

where the operator $*$ generates the scalar product of two tensors of any rank. Substituting the expression for the rate of change of the Helmholtz free energy, Eq. (6.15), into the energy balance, Eq. (6.13), and rearranging like terms results in an expression for the rate of entropy production, i.e.

$$\rho \Theta \dot{\mathcal{N}} - \rho \mathcal{Q}_s + \nabla \cdot \mathbf{q} = \left(J_e^{-1} \mathbf{S}_q - \frac{\partial \Psi}{\partial \mathbf{E}_e} \right) : \dot{\mathbf{E}}_e - \rho \left(\mathcal{N} + \frac{\partial \Psi}{\partial \Theta} \right) \dot{\Theta} + \rho \mathcal{P}_d - \sum_{k=1}^{\kappa} \rho \frac{\partial \Psi}{\partial \boldsymbol{\Xi}_k} * \dot{\boldsymbol{\Xi}}_k. \tag{6.16}$$

Now consider the Clausius-Duhem inequality as an alternative form of the Second Law of thermodynamics, i.e.

$$\rho\Theta\dot{\mathcal{N}} - \rho\mathcal{Q}_s - \nabla\cdot\mathbf{q} \geq \mathbf{q}\cdot\frac{\nabla\Theta}{\Theta}. \tag{6.17}$$

Substitution of the rate of entropy production, Eq. (6.16), into the Clausius-Duhem inequality, Eq. (6.17), results in an alternative form of the Clausius-Duhem inequality, i.e.

$$\left(J_e^{-1}\mathbf{S}_q - \rho\frac{\partial\Psi}{\partial\mathbf{E}_e}\right) : \dot{\mathbf{E}}_e - \rho\left(\mathcal{N} + \frac{\partial\Psi}{\partial\Theta}\right)\dot{\Theta} + \rho\mathcal{P}_d - \sum_{k=1}^{\kappa}\rho\frac{\partial\Psi}{\partial\boldsymbol{\Xi}_k} * \dot{\boldsymbol{\Xi}}_k - \mathbf{q}\cdot\frac{\nabla\Theta}{\Theta} \geq 0. \tag{6.18}$$

Following the Coleman-Noll procedure, consider now a loading condition that prescribes an infinitesimal change in the elastic Green-Lagrange strain tensor holding all other quantities fixed, i.e. $\dot{\mathbf{E}}_e \neq 0$. Similarly, consider a loading condition that prescribes an infinitesimal change in the absolute temperature holding all other quantities fixed, i.e. $\dot{\Theta} \neq 0$. Under such loading conditions, the alternative form of the Clausius-Duhem inequality given in Eq. (6.18) reduces to the two following expressions

$$\left(J_e^{-1}\mathbf{S}_q - \rho\frac{\partial\Psi}{\partial\mathbf{E}_e}\right) : \dot{\mathbf{E}}_e \geq 0 \tag{6.19}$$

$$-\left(\mathcal{N} + \frac{\partial\Psi}{\partial\Theta}\right)\dot{\Theta} \geq 0. \tag{6.20}$$

Since both state variables, $\mathbf{E}_e$ and Θ, may be subject to either a positive or negative infinitesimal change while holding all other quantities fixed it must follow that the expressions contained within the parenthesis of Eq. (6.19) must be exactly equal to

zero, i.e.

$$\mathbf{S}_q = \rho_\varphi \frac{\partial \Psi}{\partial \mathbf{E}_e}; \qquad \mathcal{N} = -\frac{\partial \Psi}{\partial \Theta}. \tag{6.21}$$

Time differentiation of the above expression leads to a useful expression for the rate of intrinsic entropy production, i.e.

$$\dot{\mathcal{N}} = -\frac{d}{dt}\frac{\partial \Psi}{\partial \Theta} = \underbrace{-\frac{\partial^2 \Psi}{\partial \Theta^2}}_{=C_v^\varphi/\Theta}\dot{\Theta} - \frac{\partial^2 \Psi}{\partial \Theta \partial \mathbf{E}_e} : \dot{\mathbf{E}}_e - \sum_{k=1}^{\kappa} \frac{\partial^2 \Psi}{\partial \Theta \partial \boldsymbol{\Xi}_k} * \dot{\boldsymbol{\Xi}}_k, \tag{6.22}$$

where $C_v^\varphi \triangleq \Theta(\partial \mathcal{N}/\partial \Theta)$ is defined as the effective macroscopic specific heat at constant volume. Substitution of this expression for the rate of intrinsic entropy production, Eq. (6.22), into Eq. (6.16) and rearranging terms leads to the final general expression for the rate of temperature change, i.e.

$$\underbrace{\rho C_v^\varphi \dot{\Theta}}_{\substack{\text{temperature}\\ \text{change}}} = \underbrace{\rho \Theta \frac{\partial^2 \Psi}{\partial \Theta \partial \mathbf{E}_e} : \dot{\mathbf{E}}_e}_{\substack{\text{thermoelastic}\\ \text{coupling}}} + \underbrace{\rho \sum_{k=1}^{\kappa} \left(\Theta \frac{\partial^2 \Psi}{\partial \Theta \partial \boldsymbol{\Xi}_k} - \frac{\partial \Psi}{\partial \boldsymbol{\Xi}_k} \right) * \dot{\boldsymbol{\Xi}}_k}_{\text{rate of energy of internal state variables}} + \underbrace{\rho \mathcal{P}_d}_{\substack{\text{dissipative}\\ \text{power}}} + \underbrace{\rho \mathcal{Q}_s - \nabla \cdot \mathbf{q}}_{\substack{\text{heat supply}\\ \text{and conduction}}}. \tag{6.23}$$

At this point we postulate a particular functional form of the Helmholtz free energy consistent with Eq. (6.14). We assume that the macroscopic Helmholtz free energy may be additively decomposed into parts associated with the macroscopic elastic strain energy, the macroscopic thermal energy, and the microscopic elastic strain energy trapped by lattice defects and dislocation substructure, i.e.

$$\Psi = \Psi_e(\mathbf{E}_e, \Theta, \varphi) + \Psi_\Theta(\Theta, \varphi) + \Psi_\perp(\Theta, \rho_\perp), \tag{6.24}$$

where $\{\varphi, \rho_\perp\}$ constitute a set of two internal state variables corresponding to the total volume of voids per unit volume in the intermediate porous configuration and

the total dislocation line length per unit of solid volume in the intermediate plastic configuration. Note that the dislocation density $\rho_\perp$ may be phenomenologically related to the slip resistance through the Taylor hardening law, as in Eq. (6.65). The free energy associated with lattice defects accounts for the fraction of plastic work that is not converted to heat [148, 149], which has traditionally been treated with the phenomenological Taylor-Quinney parameter, $\beta_{TQ} \approx 0.9$, [150, 151]. We assume functional forms of Ψ_Θ and $\Psi_\perp$ consistent with Clayton [152], i.e.

$$\Psi_\Theta = -C_v^\varphi \Theta \ln \frac{\Theta}{\Theta_0}; \qquad \Psi_\perp = \frac{1}{2}\kappa_\perp \Omega_\perp \mu^s b^2 \frac{\rho_\perp}{\rho_0^s}, \tag{6.25}$$

where μ^s is the temperature-dependent and pressure-dependent effective shear modulus of the solid material, b is the magnitude of the Burgers' vector, and the product $\kappa_\perp \Omega_\perp$ is a proportionality constant. For a dilute concentration of straight screw dislocations this proportionality constant may be approximated as $\kappa_\perp \Omega_\perp \sim 2$, although real materials may take on different values [153]. Note that the macroscopic effective specific heat expressed in Eq. (6.25) is consistent with its thermodynamic definition, i.e. $C_v^\varphi \triangleq \Theta\,(\partial \mathcal{N}/\partial \Theta)$, provided that the macroscopic elastic strain energy and lattice defect energies are restricted to linear functions of temperature, i.e. $\partial^2 \Psi_e / \partial \Theta^2 = \partial^2 \Psi_\perp / \partial \Theta^2 = 0$, and that the macroscopic effective specific heat is constant with respect to temperature. In order to incorporate a temperature-dependent specific heat an alternative function is required for the pure thermal part of the Helmholtz free energy.

Following Luscher et al. [146], we assume that the part of the Helmholtz free

energy associated with elastic strain energy may be additively decomposed into a purely volumetric part that only depends on the volumetric deformation and a purely deviatoric part that only depends on the isochoric part of the deformation, i.e. $\Psi_e(\mathbf{E}_e, \Theta, \varphi) = \Psi_{vol}(J_e, \Theta, \varphi) + \Psi_{dev}(\bar{\mathbf{E}}_e, \Theta, \varphi)$. Making use of the chain rule, the macroscopic quasi-conservative second Piola-Kirchhoff stress given in Eq. (6.21) may be related to the volumetric and deviatoric parts of the Helmholtz free energy, i.e.

$$\mathbf{S}_q = \rho_\varphi \frac{\partial \Psi}{\partial \mathbf{E}_e} = \rho_\varphi \frac{\partial \Psi_{vol}}{\partial J_e}\frac{\partial J_e}{\partial \mathbf{E}_e} + \rho_\varphi \frac{\partial \Psi_{dev}}{\partial \bar{\mathbf{E}}_e}\frac{\partial \bar{\mathbf{E}}_e}{\partial \mathbf{E}_e} = \rho_\varphi J_e \frac{\partial \Psi_{vol}}{\partial J_e}\mathbf{C}_e^{-1} + \rho_\varphi \frac{\partial \Psi_{dev}}{\partial \bar{\mathbf{E}}_e} : \mathbb{M}, \quad (6.26)$$

where Eq. (6.5) and Eq. (6.6) have been utilized. The part (Ψ_{dev}) of Helmholtz free energy (per unit volume in the intermediate configurations) corresponding to isochoric elastic strain energy is assumed to depend quadratically on the isochoric elastic strain tensor, i.e.

$$\rho_\varphi \Psi_{dev} = \frac{1}{2}\bar{\mathbf{E}}_e : \mathbb{C}_\varphi : \bar{\mathbf{E}}_e, \quad (6.27)$$

where $\mathbb{C}_\varphi$ is the temperature-dependent macroscopic effective fourth order elasticity tensor (taken to cubic symmetry in the current work). The part of Helmholtz free energy (per unit volume in the intermediate configurations) corresponding to purely volumetric elastic strain energy is defined such that $P_q \triangleq -\mathrm{tr}(\mathbf{\Sigma}_q)/3 = -\rho_\varphi \partial \Psi_{vol}/\partial J_e$, where the macroscopic quasi-conservative pressure is given here by the Mie-Grüneisen equation of state for porous materials, i.e.

$$P_q = K_\varphi^0 \chi_e \frac{1 - \Gamma_\varphi \chi_e}{(1 - S_\varphi \chi_e)^2} + \rho_\varphi \Gamma_\varphi C_v^\varphi (\Theta - \Theta_0), \quad (6.28)$$

where $\chi_e \triangleq 1 - J_e$ is a scalar measure of volumetric strain, K_φ^0 is the macroscopic

effective bulk modulus at ambient conditions, i.e. $P = 0$ and $\Theta = \Theta_0$, $\Gamma_\varphi \triangleq \rho_\varphi \partial P_q / \partial \mathcal{E}$ is the macroscopic effective Grüneisen parameter, and $S_\varphi \triangleq dU_s/dU_p$ is the macroscopic effective linear Hugoniot slope coefficient with U_s being the shock wave speed associated with a particular particle velocity, U_p. The dissipative part of the total pressure $P_d \triangleq -\mathrm{tr}(\boldsymbol{\Sigma}_d)/3 = P - P_q$ is modeled by recourse to an artificial viscosity:

$$P_d = \begin{cases} K_\varphi^0 \, |\dot{\chi}_e| / \dot{\chi}_1 + K_\varphi^0 \left(\dot{\chi}_e / \dot{\chi}_2\right)^2 & \text{for } \dot{\chi}_e > 0 \\ \\ 0 & \text{for } \dot{\chi}_e \leq 0, \end{cases} \tag{6.29}$$

where $\dot{\chi}_1$ and $\dot{\chi}_2$ are material parameters. This phenomenologically accounts for the irreversible drag associated with the non-equilibrium trajectory between two near equilibrium thermodynamic states [146]. Furthermore, we assume that the deviatoric part of the macroscopic dissipative Cauchy stress is negligible, i.e. $\Sigma'_d = 0$, since the deviatoric stresses are not high enough for such effects to be important. With these constitutive assumptions in hand, the final expression for the rate of temperature change may be expressed as

$$\begin{aligned} \underbrace{\rho C_v^\varphi \dot{\Theta}}_{\substack{\text{temperature} \\ \text{change}}} &= \underbrace{-\rho_\varphi \Gamma_\varphi C_v^\varphi \Theta \dot{\mathrm{v}} + \Theta \frac{\partial \mathbb{C}_\varphi}{\partial \Theta} : \bar{\mathbf{E}}_e : \mathbb{M} : \dot{\mathbf{E}}_e}_{\text{thermoelastic coupling}} + \underbrace{\rho_\varphi P_q \dot{\mathrm{v}}_\varphi}_{\substack{\text{porous} \\ \text{dissipation}}} + \underbrace{\boldsymbol{\Sigma}_q : \mathbf{D}_p}_{\substack{\text{plastic} \\ \text{dissipation}}} + \underbrace{\rho P_d \dot{\mathrm{v}}}_{\substack{\text{nonequilibrium} \\ \text{dissipation}}} \\ &+ \underbrace{\frac{1}{2} \dot{\varphi} J_e^{-1} \bar{\mathbf{E}}_e : \left(\Theta \frac{\partial^2 \mathbb{C}_\varphi}{\partial \Theta \partial \varphi} - \frac{\partial \mathbb{C}_\varphi}{\partial \varphi} \right) : \bar{\mathbf{E}}_e}_{\text{deviatoric thermoporoelastic coupling}} + \underbrace{J_e^{-1} \dot{\varphi} \int_1^{1-J_e} \left(\frac{\partial^2 P_q}{\partial \Theta \partial \varphi} - \frac{\partial P_q}{\partial \varphi} \right) d\chi_e}_{\text{volumetric thermoporoelastic coupling}} \\ &+ \underbrace{\rho \Theta \frac{\partial C_v^\varphi}{\partial \varphi} \dot{\varphi}}_{\substack{\text{thermoporous} \\ \text{coupling}}} + + \underbrace{\frac{\rho}{\rho_0^s} \left(\Theta \frac{\partial \mu^s}{\partial \Theta} - \mu^s \right) b^2 \dot{\rho}_\perp^s}_{\text{lattice defect energy}} + \underbrace{\rho \mathcal{Q}_s - \nabla \cdot \mathbf{q}}_{\substack{\text{heat supply} \\ \text{and conduction}}}, \end{aligned} \tag{6.30}$$

where kinetic evolution laws for $\mathbf{D}_p$ and $\dot{\rho}^s_\perp$ are provided in subsection 6.5.1 and subsection 6.5.2, and dynamic evolution laws for $\ddot{\varphi}$ and $\dot{\varphi}$ will be addressed in subsection 6.5.3. We first turn our attention to bridging the microscale and macroscale through the use of stress and strain concentration tensors derived from the Eshelby tensor.

6.4 Micromechanics and effective properties

Consider a microscopic elastic deformation gradient tensor $\mathbf{f}_e$ in the solid material that corresponds to the macroscopic elastic deformation tensor $\mathbf{F}_e$ in the homogenized porous material. The generalized Gauss function may be utilized to demonstrate that the volumetric average of the microscopic elastic deformation gradient tensor $\mathbf{f}_e$ over the microscale domain Ω_{micro} at a particular macroscopic material point is equal to the macroscopic deformation gradient tensor $\mathbf{F}_e$, i.e.

$$\Omega_{micro}^{-1} \iiint_{\Omega_{micro}} \mathbf{f}_e d\Omega_{micro} = \mathbf{F}_e. \tag{6.31}$$

The microscale domain may be additively decomposed into a microscale domain that only includes voids Ω_{micro}^{void} and a microscale domain that only includes the solid material Ω_{micro}^{solid} such that $\Omega_{micro} = \Omega_{micro}^{v} + \Omega_{micro}^{s}$. This additive decomposition of the domains permits the following decomposition of the volumetric average expressed in

Eq. (6.31)

$$\frac{\Omega^v_{micro}}{\Omega_{micro}} \underbrace{\Omega^{v^{-1}}_{micro} \iiint_{\Omega^v_{micro}} \mathbf{f}_e d\Omega^v_{micro}}_{\triangleq \langle \mathbf{f}_e \rangle^v} + \frac{\Omega^s_{micro}}{\Omega_{micro}} \underbrace{\Omega^{s^{-1}}_{micro} \iiint_{\Omega^s_{micro}} \mathbf{f}_e d\Omega^s_{micro}}_{\triangleq \langle \mathbf{f}_e \rangle} = \mathbf{F}_e, \tag{6.32}$$

where $\langle \cdot \rangle$ denotes a volumetric average over the solid material only and $\langle \cdot \rangle^v$ denotes a volumetric average over the voids. Noting that ${}^{\Omega^v_{micro}}/_{\Omega_{micro}} = \varphi$ and ${}^{\Omega^s_{micro}}/_{\Omega_{micro}} = 1 - \varphi$ by definition, Eq. (6.32) may be recast in the following compact form

$$\varphi \langle \mathbf{f}_e \rangle^v + (1 - \varphi) \langle \mathbf{f}_e \rangle = \mathbf{F}_e. \tag{6.33}$$

Similar expressions relate the microscopic stress tensor $\boldsymbol{\sigma}$ and the macroscopic stress tensor $\boldsymbol{\Sigma}$, i.e.

$$\varphi \cancel{\langle \boldsymbol{\sigma} \rangle^v} + (1 - \varphi) \langle \boldsymbol{\sigma} \rangle = \boldsymbol{\Sigma}. \tag{6.34}$$

as well as the microscopic temperature ϑ and macroscopic temperature Θ, i.e.

$$\varphi \cancel{\langle \vartheta \rangle^v} + (1 - \varphi) \langle \vartheta \rangle = \Theta, \tag{6.35}$$

where it has been noted in Eq. (6.34) and Eq. (6.35) that the voids are stress free and assumed to be gas free at zero Kelvin, i.e. $\langle \boldsymbol{\sigma} \rangle^v = \langle \vartheta \rangle^v = 0$. Strictly speaking, Eq. (6.34) is exact only under mechanical equilibrium and in the absence of body forces, i.e. $\nabla \cdot \boldsymbol{\sigma} = 0$, see for example [138]. Under the dynamic loading conditions of interest here, Eq. (6.34) must be considered an approximation. Nevertheless, Eq. (6.34) will prove useful in defining effective elastic properties.

Notice that Eq. (6.34) and Eq. (6.35) provide unique relationships between the macroscopic quantities and the microscopic quantities averaged over the solid part of

the material. However, the concentration of elastic deformation in the void domain as compared to the solid domain is unknown and may not be determined by Eq. (6.33) alone. In order to rectify this elastic strain concentration tensors may be utilized to relate microscopic and macroscopic deformations, i.e.

$$\mathbb{A}_e^v : (\mathbf{F}_e - \mathbf{I}) = (\langle \mathbf{f}_e \rangle^v - \mathbf{I}) \tag{6.36}$$

$$\mathbb{A}_e^s : (\mathbf{F}_e - \mathbf{I}) = (\langle \mathbf{f}_e \rangle - \mathbf{I}) \,, \tag{6.37}$$

where $\mathbb{A}_e^v$ and $\mathbb{A}_e^s$ are elastic strain concentration tensors corresponding to elastic deformations in the void and solid parts of the material, respectively. Consistency of Eq. (6.33) with Eq. (6.36) and Eq. (6.37) requires that $\varphi \mathbb{A}_e^v + (1-\varphi)\mathbb{A}_e^s = \mathbb{I}$. These strain concentration tensors combined with Eq. (6.34) give rise to an effective linear elastic anisotropic stiffness tensor of the form

$$\mathbb{C}_\varphi = (1-\varphi)\, \mathbb{C}^s \mathbb{A}_e^s, \tag{6.38}$$

where $\mathbb{C}_\varphi$ is the effective linear elastic stiffness tensor of the homogenized porous material and $\mathbb{C}^s$ is the linear elastic stiffness tensor of the solid material containing with no voids. Eq. (6.38) provides a model for the degradation of the anisotropic stiffness tensor once $\mathbb{A}_e^s$ is determined.

Mori and Tanaka [124] proposed a method for approximating $\mathbb{A}_e^s$ by making use of the Eshelby tensor [143] along with an assumption for how voids elastically interact in an average sense. Utilization of their method results in the following approximation

for the strain concentration tensor

$$\mathbb{A}_e^s = \left(\varphi \mathbb{T}_e^v + (1-\varphi)\mathbb{I}\right)^{-1}, \tag{6.39}$$

where $\mathbb{T}_e^v$ relates the average deformation in the void to the average deformation in the solid material and was determined by [143] as

$$\mathbb{T}_e^v = (\mathbb{I} - \mathbb{S})^{-1} \tag{6.40}$$

with $\mathbb{S}$ being the Eshelby tensor. For spherical voids in an isotropic material a simple closed-form expression for the effective bulk modulus and shear modulus is easily obtainable from Eq. (6.38) and Eq. (6.39) as

$$K_\varphi = K^s + \frac{(1-\varphi)(3K^s + 4\mu^s)}{3(1-\varphi) + 4\mu^s/K^s} \tag{6.41}$$

and

$$\mu_\varphi = \mu^s + \frac{5\mu^s(1-\varphi)(3K^s + 4\mu^s)}{6\varphi(K^s + 2\mu^s) - 5(3K^s + 4\mu^s)} \tag{6.42}$$

Typically, the Eshelby tensor associated with anisotropic materials may only be obtained through numerical integration. One simple closed-form model for the anisotropic stiffness tensor is

$$\mathbb{C}_\varphi = \frac{\mu_\varphi}{\mu_0^s}\mathbb{C}_0^s, \tag{6.43}$$

provided that $\mathbb{C}_\varphi$ is only utilized to compute the deviatoric part of the stress tensor and an equation of state is utilized to compute the spherical part of the stress tensor (as in the present case). However, numerical calculations are required to support such an approximation.

Some of the effective properties associated with the Mie-Grüneisen equation of state are obtainable through classical micromechanics. For example, the effective Grüneisen parameter is related to the macroscopic effective thermal expansion coefficient α_T^{φ} through the following relation

$$\Gamma_{\varphi} = \mathrm{v}\frac{\partial P}{\partial \mathcal{E}} = \frac{\alpha_T^{\varphi} K_{\varphi}^0}{C_v^{\varphi}}, \tag{6.44}$$

where models for α_T^{φ} and C_v^{φ} have been established in [154]. Unfortunately, the macroscopic effective linear Hugoniot slope coefficient S_{φ} utilized in the Mie-Grüneisen equation of state may not be obtained through the classical micromechanics utilized for the linear elastic stiffness tensor. Nevertheless, one useful approximation has been provided in the literature [155] as

$$S_{\varphi} = \frac{S_s}{1 + \varphi\,(S_s - 1)}, \tag{6.45}$$

where S_s is the linear Hugoniot slope coefficient for the solid material with no voids.

This section has established a set of micromechanical models for approximating the effective thermomechanical properties of a porous crystal. The following section will provide evolution laws for the inelastic deformation, which along with the effective properties discussed in this section permit the calculation of the stress and temperature evolution discussed in section 6.3.

6.5 Dynamic porous crystal plasticity

Recently, a number of porous crystal plasticity models have been proposed, any of which could, in principle, be utilized to provide evolution laws for the inelastic parts of the macroscopic velocity gradient in the respective intermediate configurations, i.e. $\dot{\mathbf{F}}_p\mathbf{F}_p^{-1}$ and $\dot{\mathbf{F}}_\varphi\mathbf{F}_\varphi^{-1}$. However, these models are for the most part developed to account for the phenomena that is most relevant to quasi-static loading conditions, e.g. initial yield stress, complex anisotropic hardening, non-spherical void shapes, void growth in shear, etc. Here we propose an alternative macroscopic effective porous crystal plasticity model that is more appropriate for the physics associated with very high strain rates, i.e. $10^3 - 10^8$ s^{-1}. In this domain, voids may not interact with each other as strongly as they do in the quasi-static. Therefore, assumptions that are not necessarily valid in the quasi-static regime may be acceptable in the dynamic regime.

6.5.1 Microscale kinematics

Consider a multiplicative decomposition (Fig. 6.2) of the total microscopic deformation gradient tensor, $\mathbf{f} = \mathbf{f}_e\mathbf{f}_p\mathbf{f}_\varphi$, where $\mathbf{f}_e$ is the microscopic elastic deformation gradient tensor in the solid material that corresponds to the macroscopic elastic deformation in the homogenized porous material, i.e. $\mathbf{F}_e$. Similarly, $\mathbf{f}_p$ and $\mathbf{f}_\varphi$ are microscopic plastic deformation gradient tensors in the solid material that correspond to the macroscopic plastic and macroscopic porous deformation in the homogenized

porous material, i.e. $\mathbf{F}_p$ and $\mathbf{F}_\varphi$. The multiplicative decomposition of the microscopic deformation gradient tensor leads to an additive decomposition of the velocity gradient tensor similar to Eq. (6.7), i.e.

$$\mathbf{l} \triangleq \dot{\mathbf{f}}\mathbf{f}^{-1} = \underbrace{\dot{\mathbf{f}}_e\mathbf{f}_e^{-1}}_{\triangleq \mathbf{l}_e} + \underbrace{\mathbf{f}_e\dot{\mathbf{f}}_p\mathbf{f}_p^{-1}\mathbf{f}_e^{-1}}_{\triangleq \mathbf{l}_p} + \underbrace{\mathbf{f}_e\mathbf{f}_p\dot{\mathbf{f}}_\varphi\mathbf{f}_\varphi^{-1}\mathbf{f}_p^{-1}\mathbf{f}_e^{-1}}_{\triangleq \mathbf{l}_\varphi} \tag{6.46}$$

Consider the set of microscopic spatial coordinates $\{\mathbf{y}_0, \mathbf{y}_\varphi, \mathbf{y}_p, \mathbf{y}\}$ that define the position of material particles in the reference, intermediate porous, intermediate plastic, and current configurations, respectively. We postulate the following idealized inelastic microscopic motions

$$\mathbf{y}_e = \mathbf{f}_e\mathbf{y}_p, \qquad \mathbf{y}_p = \mathbf{f}_p\mathbf{y}_\varphi = \mathbf{F}_p\mathbf{y}_\varphi, \qquad \mathbf{y}_\varphi = \mathbf{f}_\varphi\mathbf{y}_0 = r_\varphi\mathbf{e}_\mathbf{r}, \tag{6.47}$$

where we have assumed that the microscopic plastic deformation gradient is unperturbed by the presence of voids and therefore equal to the macroscopic plastic deformation gradient, i.e. $\mathbf{f}_p = \mathbf{F}_p$. Note that a similar assumption lies at the heart of the Gurson [77] isotropic porous plasticity model, as well as its many subsequent derivatives.

Now consider the auxiliary problem of a spherical void of initial radius a_0 in the reference configuration embedded within an otherwise solid sphere of radius r_0^{out}. As shown in Fig. 6.3, the microscopic porous deformation gradient tensor $\mathbf{f}_\varphi$ maps the reference configuration into the intermediate porous configuration, where the spherical void now has a radius of a_φ and the outer radius of the spherical shell is denoted as r_φ^{out}. Consistent with dislocation-based plasticity, the solid material within the spherical

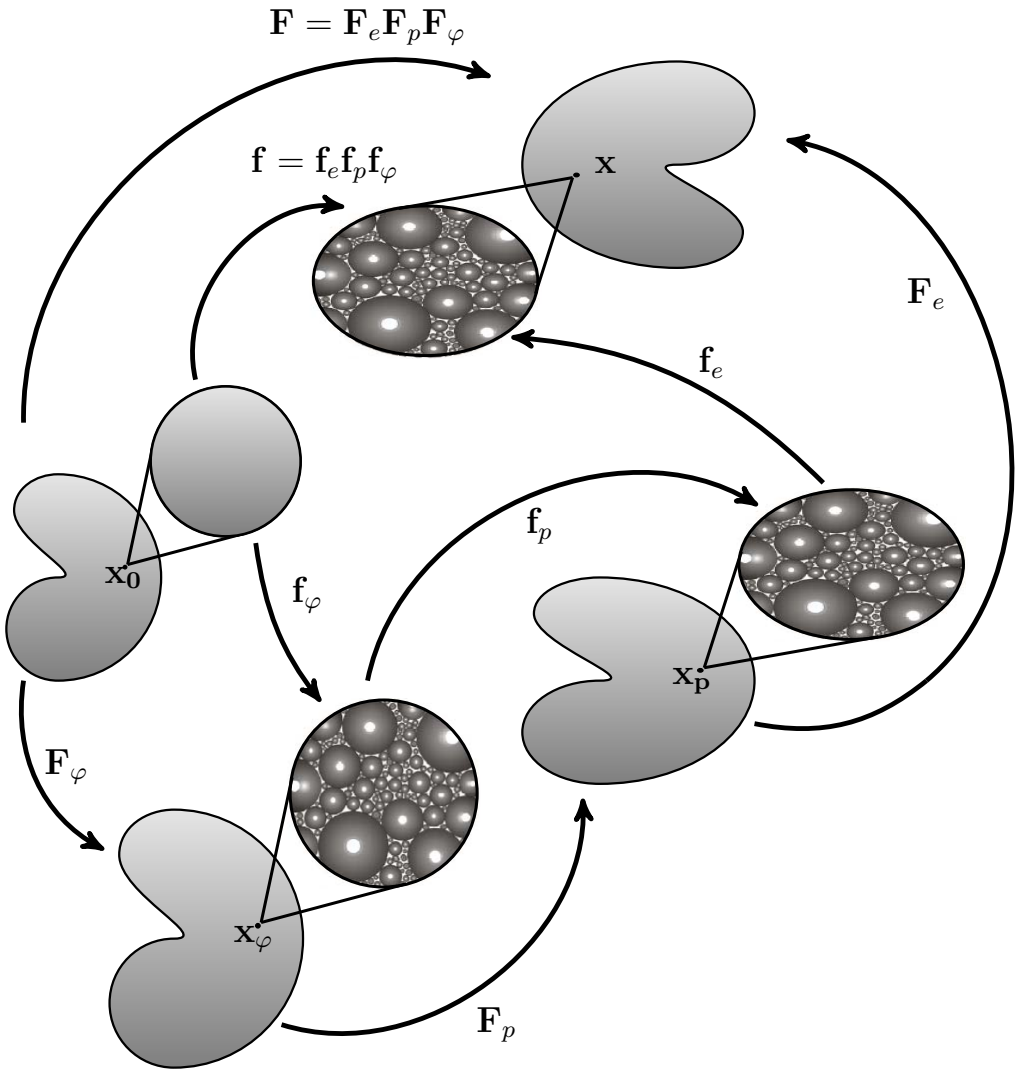

Fig. 6.2: Schematic showing a multiplicative decomposition of the total microscopic deformation gradient tensor, $\mathbf{f} = \mathbf{f}_e\mathbf{f}_p\mathbf{f}_\varphi$, where $\mathbf{f}_e$ is the microscopic elastic deformation gradient tensor in the solid material that corresponds to the macroscopic elastic deformation in the homogenized porous material, i.e. $\mathbf{F}_e$. Similarly, $\mathbf{f}_p$ and $\mathbf{f}_\varphi$ are microscopic plastic deformation gradient tensors in the solid material that correspond to the macroscopic plastic and macroscopic porous deformation in the homogenized porous material, i.e. $\mathbf{F}_p$ and $\mathbf{F}_\varphi$. On the microscale the voids are spherical in the intermediate porous configuration, and may be non-spherical in the intermediate plastic configuration as well as the current configuration.

shell is assumed to be plastically incompressible so that the volume of the spherical shell in the reference configuration is exactly equal to the volume in the intermediate porous configuration, i.e.

$$\left(r_{\varphi}^{out}\right)^3 - a_{\varphi}^3 = \left(r_0^{out}\right)^3 - a_0^3. \tag{6.48}$$

At this point it is convenient to revisit the notion of macroscopic porosity, φ, introduced in section 6.2. Based on the self-consistent arguments of Wright and Ramesh [101] the outer radius of every spherical shell in the intermediate porous configuration, r_{φ}^{out}, is chosen such that the macroscopic porosity is exactly equal to the void volume

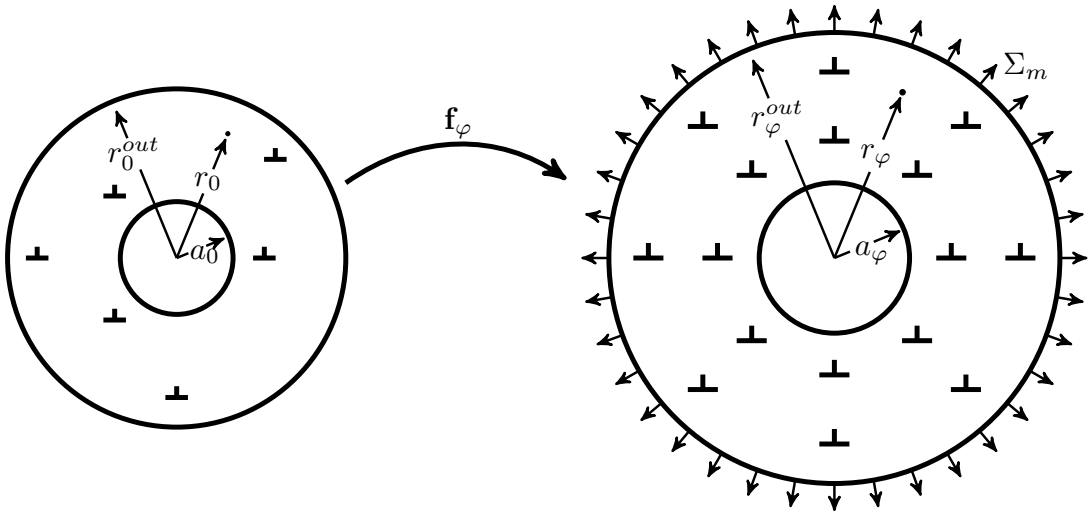

Fig. 6.3: Schematic showing the microscopic porous deformation gradient tensor $\mathbf{f}_\varphi$ mapping the reference configuration into the intermediate porous configuration. A unit cell in the reference configuration is represented by a spherical void of initial radius a_0 embedded within an otherwise solid sphere of radius r_0^{out}. A unit cell in the intermediate porous configuration is represented by a spherical void of radius a_φ embedded within an otherwise solid sphere of outer radius r_φ^{out}. The driving force for the porous deformation is the mean macroscopic stress Σ_m.

fraction of the spherical shell (or the local microscopic porosity), i.e. $\varphi = (a_\varphi / r_\varphi^{out})^3$. Therefore, the otherwise unknown outer radius may be removed from Eq. (6.48) in the alternative expression given by

$$a_\varphi^3 \left(\frac{1}{\varphi} - 1 \right) = a_0^3 \left(\frac{1}{\varphi_0} - 1 \right). \tag{6.49}$$

Time differentiation of Eq. (6.49) results in an expression that will prove useful in subsequent analysis, i.e.

$$3 \frac{\dot{a}_\varphi}{a_\varphi} = \frac{\dot{\varphi}}{\varphi - \varphi^2}. \tag{6.50}$$

Turning our attention to the microscopic spatial variation of the deformation in the intermediate porous configuration, the plastic incompressibility condition must hold for any arbitrary subdomain of the spherical shell, i.e.

$$r_\varphi^3 - a_\varphi^3 = r_0^3 - a_0^3, \tag{6.51}$$

where r_φ and r_0 denote the radial coordinates in the intermediate porous and reference configurations, respectively, as shown in Fig. 6.3. Therefore, Eq. (6.51) implies that the motion of the spherical shell in the intermediate porous configuration r_φ is completely determined once a_φ is known as a function of time.

The corresponding microscopic deformation gradient tensor in the intermediate porous configuration is obtained by spatial differentiation of Eq. (6.51), i.e.

$$\mathbf{f}_\varphi = \frac{r_0^2}{r_\varphi^2} \mathbf{e_r} \otimes \mathbf{e_r} + \frac{r_\varphi}{r_0} (\mathbf{e}_\theta \otimes \mathbf{e}_\theta + \mathbf{e}_\phi \otimes \mathbf{e}_\phi). \tag{6.52}$$

The corresponding porous parts of the microscopic velocity gradient and microscopic rate of deformation tensor, $\mathbf{d}_\varphi \triangleq (\mathbf{l} + \mathbf{l}^T)/2$ follows from time differentiation of

Eq. (6.52), i.e.

$$\mathbf{d}_\varphi = \mathbf{l}_\varphi = -2\frac{\dot{r}_\varphi}{r_\varphi}\mathbf{e}_\mathbf{r} \otimes \mathbf{e}_\mathbf{r} + \frac{\dot{r}_\varphi}{r_\varphi}(\mathbf{e}_\theta \otimes \mathbf{e}_\theta + \mathbf{e}_\phi \otimes \mathbf{e}_\phi). \tag{6.53}$$

For simplicity of the formulation, we assume an isotropic measure of the effective slip in the intermediate porous configuration. Such an approximation is likely invalid for nanovoids where discrete dislocation interactions may dominate. In accordance with J_2 isotropic plasticity theory

$$\mathbf{d}_\varphi = \frac{\dot{\gamma}_\varphi^{eq}}{\sqrt{2}}\mathbf{n}_\varphi^{eq}, \tag{6.54}$$

where $\mathbf{n}_\varphi^{eq}$ is the effective flow direction in the intermediate porous configuration. For isotropic J_2 associative flow, Drucker's maximum plastic dissipation postulate gives $\mathbf{n}_\varphi^{eq} = \boldsymbol{\sigma}'_\varphi/|\boldsymbol{\sigma}'_\varphi|$. A similar expression for the plastic part of the microscopic velocity gradient in the intermediate plastic configuration may be related to the sum of the microscopic plastic slip rates $\dot{\gamma}_p^{(\alpha)}$ on each of the n_s microscopic slip systems, i.e.

$$\dot{\mathbf{f}}_p\mathbf{f}_p^{-1} = \sum_{\alpha=1}^{n_s} \dot{\gamma}_p^{(\alpha)} \boldsymbol{m}_0^{(\alpha)} \otimes \boldsymbol{n}_0^{(\alpha)}, \tag{6.55}$$

where $\boldsymbol{m}_0^{(\alpha)}$ and $\boldsymbol{n}_0^{(\alpha)}$ are the microscopic slip direction and the microscopic unit normal to the slip plane for the α-th slip system in the reference configuration with n_s being the total number of slip systems. Note that based on our idealized motion, we also have $\dot{\mathbf{F}}_p\mathbf{F}_p^{-1} = \dot{\mathbf{f}}_p\mathbf{f}_p^{-1}$ and $\dot{\gamma}_p^{(\alpha)} = \langle\dot{\gamma}_p^{(\alpha)}\rangle$.

Returning to the intermediate porous deformation, substitution of Eq. (6.50), Eq. (6.51), and Eq. (6.53) into Eq. (6.54) followed by a contraction on itself results in

the following expressions for the microscopic spatial variation of the effective isotropic slip rate expressed as

$$\dot{\gamma}_{\varphi}^{eq} = 2\sqrt{3}\left(\frac{a_{\varphi}}{r_{\varphi}}\right)^{3}\frac{|\dot{a}_{\varphi}|}{a_{\varphi}} = \frac{2}{\sqrt{3}}\left(\frac{a_{\varphi}}{r_{\varphi}}\right)^{3}\frac{|\dot{\varphi}|}{\varphi-\varphi^{2}} \tag{6.56}$$

Notice that the isotropic slip rate is highest on the surface of the void (at $r_{\varphi} = a_{\varphi}$) and decays cubically with distance from the surface of the void. It will prove convenient in subsection 6.5.2 to compute the volume average of the effective isotropic slip rate over the entire spherical shell, i.e.

$$\langle\dot{\gamma}_{\varphi}^{eq}\rangle_{uc} \triangleq \frac{1}{V_{uc}}\int_{0}^{\pi}\int_{0}^{2\pi}\int_{a_{\varphi}}^{r_{\varphi}^{out}}\dot{\gamma}_{\varphi}^{eq}\sin(\phi)r_{\varphi}^{2}dr_{\varphi}d\theta d\phi, \tag{6.57}$$

where the subscript uc indicates that the volume averaging is occurring over a single unit cell (the spherical shell in this case) with $V_{uc} \triangleq \frac{4}{3}\pi\left(r_{\varphi}^{out}\right)^{3} - \frac{4}{3}\pi a_{\varphi}^{3}$ being the volume of associated unit cell. Making use of Eq. (6.56) the integral in Eq. (6.57) may be evaluated as

$$\langle\dot{\gamma}_{\varphi}^{eq}\rangle_{uc} = \frac{2}{\sqrt{3}}\frac{|\dot{\varphi}|}{(1-\varphi)^{2}}\ln\left(\frac{1}{\varphi}\right). \tag{6.58}$$

Notice that the effective isotropic slip rate in the intermediate porous configuration averaged over the unit cell expressed in Eq. (6.58) only depends on the macroscopic porosity φ and does not depend on any microscopic quantities unique to a particular unit cell, e.g. a_{φ}. Therefore, the effective isotropic slip rate averaged over the entire microscale (including all the spherical shells at a particular macroscopic material point) is identical to the corresponding quantity averaged over the unit cell, i.e. $\langle\dot{\gamma}_{\varphi}^{eq}\rangle = \langle\dot{\gamma}_{\varphi}^{eq}\rangle_{uc}$.

Lastly, it is convenient to introduce a measure of the volumetrically averaged net accumulated microscopic plastic strain, $\langle\gamma_{net}^{(\alpha)}\rangle$, on each slip system associated with both plastic and porous deformation. One difficulty with defining an appropriate model for $\langle\gamma_{net}^{(\alpha)}\rangle$ is the fact that the porous deformation (resulting in purely spherical void growth) requires slip on many different slip systems at different angular positions around the void. However, the porous deformation here has conveniently been characterized by an effective isotropic measure, i.e. γ_{φ}^{eq}, that does not discriminate between slip systems. A modified Taylor factor M_T^* may be utilized to relate the effective isotropic slip rates to a measure of the sum of slip on the active slip systems, i.e. $M_T^*\langle\dot{\gamma}_{\varphi}^{eq}\rangle = \langle\sum_{i=\alpha}^{n_s}\dot{\gamma}_{\varphi}^{(\alpha)}\rangle$. Our modified Taylor factor is related to the traditional Taylor factor, M_T, associated with polycrystal plasticity (and may be approximated as such, i.e. $M_T^* \triangleq M_T/\sqrt{3} \approx 3.06/\sqrt{3} \approx 1.77$). For purely spherical void growth (under pure hydrostatic loading) there are no preferred slip systems and thus each slip system may be assumed to be equally active, i.e. $n_s\langle\dot{\gamma}_{\varphi}^{(\alpha)}\rangle \approx \langle\sum_{i=\alpha}^{n_s}\dot{\gamma}_{\varphi}^{(\alpha)}\rangle$. Combining these two relations, we obtain an approximate relation for the slip rate on each slip system that results from the porous deformation, i.e. $\langle\dot{\gamma}_{\varphi}^{(\alpha)}\rangle \approx (M_T^*/n_s)\langle\dot{\gamma}_{\varphi}^{eq}\rangle$. We assume that the slip rates from both porous and plastic deformation may be additively combined to obtain the net microscopic slip rate expressed as

$$\langle\dot{\gamma}_{net}^{(\alpha)}\rangle = \left|\langle\dot{\gamma}_{p}^{(\alpha)}\rangle\right| + \frac{M_T^*}{n_s}\langle\dot{\gamma}_{\varphi}^{eq}\rangle, \tag{6.59}$$

with $\langle\gamma_{net}^{(\alpha)}\rangle \triangleq \int_0^t \langle\dot{\gamma}_{net}^{(\alpha)}\rangle dt$.

6.5.2 Microscale slip kinetics and hardening laws

The microscopic plastic slip rate $\dot{\gamma}_p^{(\alpha)}$ on the α-th slip system in the intermediate plastic configuration may be related to the corresponding microscopic shear stress resolved on the slip system in current configuration, $\tau^{(\alpha)} \triangleq \boldsymbol{\sigma} : (\boldsymbol{m}^{(\alpha)} \otimes \boldsymbol{n}^{(\alpha)})$, through the following phenomenological relation

$$\dot{\gamma}_p^{(\alpha)} = \dot{\gamma}_0 \left| \frac{\tau^{(\alpha)}}{\tau_c^{(\alpha)}} \right|^{1/m} \operatorname{sgn}\left(\tau^{(\alpha)}\right), \tag{6.60}$$

where m is the rate sensitivity parameter (that may be temperature dependent), $\dot{\gamma}_0$ is a reference strain rate and $\tau_c^{(\alpha)}$ is a temperature-dependent evolving slip resistance. The slip resistance may be additively decomposed into parts associated with the Peierls barrier $\tau_p^{(\alpha)}$, solid solution strengthening $\tau_{ss}^{(\alpha)}$, second phase particle and precipitation strengthening $\tau_{sp}^{(\alpha)}$, Hall-Petch strengthening in the presence of grain boundaries $\tau_{HP}^{(\alpha)}$, and strain hardening $\tau_\perp^{(\alpha)}$, i.e. $\tau_c^{(\alpha)} = \tau_p^{(\alpha)} + \tau_{ss}^{(\alpha)} + \tau_{sp}^{(\alpha)} + \tau_{HP}^{(\alpha)} + \tau_\perp^{(\alpha)}$.

Typically, $\tau_\perp^{(\alpha)}$ is a function of the local accumulated plastic deformation, and is thus usually allowed to have any arbitrary spatial variation regardless of the length scale of interest. However, the slip resistance associated with strain hardening is phenomenologically associated with an evolving dislocation density, $\rho_\perp$. This evolving dislocation density may only be defined over a sufficiently large volume of material. Due to the long range interacting stress fields generated by dislocations, this finite volume size may actually be of similar magnitude to the volume associated with the plastic zone developed around a growing void. Therefore, it may not necessarily be

appropriate to allow $\tau_{\perp}^{(\alpha)}$ to spatially vary on the microscale. Given this argument (and assuming that the other sources of slip resistance do not evolve with deformation) we restrict the evolving slip resistance $\tau_c^{(\alpha)}$ to be spatially constant with respect to the microscale spatial coordinates $\mathbf{y}$ and only spatially depend on the macroscale coordinate $\mathbf{x}$. Based on these arguments, we choose to recast Eq. (6.60) into an alternative, more convienent form that reflects these considerations, i.e.

$$\langle \dot{\gamma}_p^{(\alpha)} \rangle = \dot{\gamma}_0 \left| \frac{\langle \tau^{(\alpha)} \rangle}{\langle \tau_c^{(\alpha)} \rangle} \right|^{1/m} \operatorname{sgn}\left(\langle \tau^{(\alpha)} \rangle \right), \tag{6.61}$$

with $\langle \tau^{(\alpha)} \rangle \triangleq \langle \boldsymbol{\sigma} \rangle : \left(\langle \boldsymbol{m}^{(\alpha)} \rangle \otimes \langle \boldsymbol{n}^{(\alpha)} \rangle \right)$. These volumetric averages may be computed by making use of the elastic strain and stress concentration tensors discussed in section 6.4, i.e.

$$\begin{aligned} &\langle \boldsymbol{\sigma} \rangle = \mathbb{B}_e : \boldsymbol{\Sigma}; \\ &\langle \boldsymbol{m}^{(\alpha)} \rangle = \langle \mathbf{f}_e \boldsymbol{m}_0^{(\alpha)} \rangle = \langle \mathbf{f}_e \rangle \boldsymbol{m}_0^{(\alpha)} = \mathbb{A}_e^s : (\mathbf{F}_e - \mathbf{I})\, \boldsymbol{m}_0^{(\alpha)} + \boldsymbol{m}_0^{(\alpha)}; \\ &\langle \boldsymbol{n}^{(\alpha)} \rangle = \langle \boldsymbol{n}_0^{(\alpha)} \mathbf{f}_e^{-1} \rangle = \boldsymbol{n}_0^{(\alpha)} \langle \mathbf{f}_e^{-1} \rangle = \boldsymbol{n}_0^{(\alpha)} \left(\mathbb{A}_e^s : (\mathbf{F}_e - \mathbf{I}) + \mathbf{I} \right)^{-1}, \end{aligned} \tag{6.62}$$

noting that the microscopic slip directions and unit normals in the reference configuration are constant with respect to the microscale spatial coordinate, i.e. $\boldsymbol{m}_0^{(\alpha)} = \langle \boldsymbol{m}_0^{(\alpha)} \rangle$ and $\boldsymbol{n}_0^{(\alpha)} = \langle \boldsymbol{n}_0^{(\alpha)} \rangle$. A similar microscale slip kinetics law may be proposed for the plastic deformation associated with the microscopic porous deformation, i.e.

$$\dot{\gamma}_{\varphi}^{eq} = \frac{\dot{\gamma}_0}{M_T^*} \left(\frac{\tau_{\varphi}^{eq}}{\langle \tau_c^{eq} \rangle} \right)^{1/m}, \tag{6.63}$$

where $\tau_{\varphi}^{eq} \triangleq \sqrt{\frac{\boldsymbol{\sigma}'_{\boldsymbol{\varphi}} : \boldsymbol{\sigma}'_{\boldsymbol{\varphi}}}{2}}$ is an effective isotropic measure of the microscopically spatially varying stress in the intermediate porous configuration. The isotropic measure of the

slip resistance $\langle \tau_c^{eq} \rangle$ is taken to be a weighted average of the active slip resistances, i.e.

$$\langle \tau_c^{eq} \rangle = M_T^* \frac{\sum_{\alpha=1}^{n_s} \langle \tau_c^{(\alpha)} \rangle \langle \dot{\gamma}_{net}^{(\alpha)} \rangle}{\sum_{\alpha=1}^{n_s} \langle \dot{\gamma}_{net}^{(\alpha)} \rangle}, \tag{6.64}$$

with $\langle \dot{\gamma}_{net}^{(\alpha)} \rangle$ reflecting the net accumulated microscopic inelastic strain rate associated with both plastic and porous deformation volumetrically averaged over the entire microscale. One justification for the averaging utilized in Eq. (6.64) is that spherical void growth requires the activation of many different slip systems (similar to polycrystal plasticity) at different angular positions around the void. The isotropic measure of the slip resistance may also be related to the average dislocation density through the Taylor hardening relation, i.e.

$$\rho_\perp = \left(\sqrt{\rho_\perp^0} + \frac{\langle \tau_c^{eq} \rangle - \langle \tau_c^{eq} \rangle|_{t=0}}{\hat{\alpha} \mu^s b M_T^*} \right)^2, \tag{6.65}$$

where $\hat{\alpha} \approx 1/2$ is a proportionality constant and $\rho_\perp^0$ is the initial average dislocation density. Eq. (6.65) may be utilized in Eq. (6.25) to compute the evolving lattice defect energy, which in turn effects the temperature evolution governed by Eq. (6.30).

The strain hardening law on each slip system at room temperature is assumed to follow the usual form, i.e.

$$\langle \dot{\tau}_\perp^{(\alpha)} \rangle \Big|_{\vartheta=\vartheta_0} = \sum_{\beta=1}^{n_s} h_{\alpha\beta} \langle \dot{\gamma}_{net}^{(\beta)} \rangle, \tag{6.66}$$

where $h_{\alpha\beta}$ is the hardening matrix that captures both self-hardening and latent hardening. The evolution law for the hardening matrix is typically modeled after[156–158],

i.e.

$$h_{\alpha\beta} = qh + (1-q)h\delta_{\alpha\beta}, \tag{6.67}$$

where h is an evolving scalar hardness and the constant latent hardening ratio is denoted as q. Typically $q \sim 1.4$ for ductile FCC crystals Asaro and Needleman [159]. A modified version of the scalar hardening evolution law of Peirce et al. [157] is utilized here, i.e.

$$h = h_0 \, \mathrm{sech}^2 \left(\frac{h_0}{\tau_\perp^s - \tau_\perp^0} \sum_{\alpha=1}^{n_s} \langle \gamma_{net}^{(\alpha)} \rangle \right), \tag{6.68}$$

where h_0 is the initial scalar hardness with $\tau_\perp^0$ and $\tau_\perp^s$ representing the initial and saturated levels of the slip resistance associated with strain hardening.

The temperature and pressure dependence of the slip resistance is assumed to take the following form

$$\langle \tau_c^{(\alpha)} \rangle = \frac{\mu^s}{\mu_0^s} \left(\frac{\langle \vartheta \rangle - \vartheta_0}{\vartheta_m - \vartheta_0} \right)^{q^*} \langle \tau_c^{(\alpha)} \rangle \big|_{\vartheta=\vartheta_0}, \tag{6.69}$$

where q^* is the temperature dependence exponent and μ^s is the effective shear modulus taken to depend linearly on the microscopic average temperature and macroscopic compressive pressure, i.e. $\mu^s = \mu_0^s + (\langle \vartheta \rangle - \vartheta_0) \frac{\partial \mu^s}{\partial \vartheta} + P \frac{\partial \mu^s}{\partial P}$. Notice that Eq. (6.69) has made use of the volumetrically averaged microscopic temperature rather than the local, microscopically varying temperature field. Some justification for this assumption has been provided by Wu et al. [91], who showed that the microscopic thermal gradients around a dynamically growing void quickly equilibrate. This is particularly the case for sub-micron sized voids.

6.5.3 Microscale void dynamics in thermally-activated regime

For the spherically symmetric motion in the intermediate porous configuration only the radial balance of momentum is nontrivial, i.e.

$$\frac{\partial \sigma_{\varphi}^{rr}}{\partial r_{\varphi}} - \frac{2}{r_{\varphi}}(\sigma_{\varphi}^{\theta\theta} - \sigma_{\varphi}^{rr}) = \rho_0^s \ddot{r}_{\varphi}, \tag{6.70}$$

where ρ_0^s is the mass density of the solid material in the reference configuration. For this spherically symmetric stress state a scalar measure of the equivalent shear stress may be expressed as

$$\tau_{\varphi}^{eq} \triangleq \sqrt{\frac{\boldsymbol{\sigma}'_{\varphi} : \boldsymbol{\sigma}'_{\varphi}}{2}} = \frac{\left|\sigma_{\varphi}^{\theta\theta} - \sigma_{\varphi}^{rr}\right|}{2\sqrt{3}}. \tag{6.71}$$

Under tensile loading $\sigma_{\varphi}^{\theta\theta} > \sigma_{\varphi}^{rr}$ while under compressive loading $\sigma_{\varphi}^{\theta\theta} < \sigma_{\varphi}^{rr}$, thus Eq. (6.70) may be rewritten as

$$\frac{\partial \sigma_{\varphi}^{rr}}{\partial r_{\varphi}} - \frac{4\sqrt{3}}{r_{\varphi}}\tau_{\varphi}^{eq}\,\mathrm{sgn}(\dot{a}_{\varphi}) = \rho \ddot{r}_{\varphi}. \tag{6.72}$$

Integrating Eq. (6.72) (after substitution of Eq. (6.51)) with respect to the spatial variable r in the intermediate porous configuration over the entire spherical shell from $r = a_{\varphi}$ to $r = r_{\varphi}^{out}$, where r_{φ}^{out} is the outer radius of the spherical shell, we have the general integro-differential equation governing the dynamics of a spherical void

embedded within an otherwise intact spherical shell [82], i.e.

$$\rho_0^s \left(1 - \sqrt[3]{\varphi}\right) a_\varphi \ddot{a}_\varphi + \rho_0^s \left(\frac{3}{2} - 2\sqrt[3]{\varphi} + \frac{1}{2}\varphi^{4/3}\right) \dot{a}_\varphi^2 = \Sigma_m - \frac{2\gamma_{se}}{a_\varphi} - \underbrace{\int_{a_\varphi}^{r_\varphi^{out}} \frac{4\sqrt{3}}{r_\varphi} \tau_\varphi^{eq} \operatorname{sgn}(\dot{a}_\varphi) dr_\varphi}_{\triangleq \mathcal{R}_\varphi^{vp}}, \tag{6.73}$$

where Σ_m denotes the mean macroscopic stress and $\mathcal{R}_\varphi^{vp}$ is termed the viscoplastic resistance. Note that a similar expression was obtained in chapter 3 for an incompressible isotropic material. The appropriate boundary conditions for the problem at hand are the applied tensile pressure shown in Fig. 6.3, i.e. $\sigma_\varphi^{rr}|_{r_\varphi = r_\varphi^{out}} = p_\varphi^{out} = \Sigma_m$ (see [101]), and a term associated with the surface energy, γ_{se}, on the void surface, i.e. $\sigma_\varphi^{rr}|_{r_\varphi = a_\varphi} = 2a_\varphi/\gamma_{se}$ (see Reina et al. [69] for a detailed derivation).

In general, the viscoplastic resistance term $\mathcal{R}_{vp}$, expressed on the right hand side of Eq. (6.73), must be numerically integrated at each time step (since τ_φ^{eq} may take on any arbitrary radial spatial variation). This demands a discretization of the spatial variable r_φ (in addition to time t), which substantially increases the computational cost of the problem at hand. This is particularly undesirable for the simulation of complex structures subject to dynamic failure governed by Eq. (6.73). In subsection 6.5.2 we have provided necessary assumptions (many physically justified) that restrict τ_φ^{eq} to a particular set of radial spatial variations that permit analytic integration of the viscoplastic resistance term expressed on the right hand side of Eq. (6.73), i.e.

$$\mathcal{R}_\varphi^{vp} = \zeta_m \langle \tau_c^{eq} \rangle \frac{1 - \varphi^m}{(1 - \varphi)^m} \left(\frac{M_T^* \, |\dot{\varphi}|}{\dot{\gamma}_0 \varphi}\right)^m \operatorname{sgn}(\dot{a}_\varphi), \tag{6.74}$$

where $\zeta_m \triangleq 2^{2+m}3^{-(1+m)/2}m^{-1}$. Substituting Eq. (6.66) and Eq. (6.69) into Eq. (6.64) one may obtain an expression for the evolving isotropic measure of the slip resistance, i.e.

$$\langle \tau_c^{eq} \rangle = M_T^* \frac{\mu^s}{\mu_0^s} \left(\frac{\langle \vartheta \rangle - \vartheta_0}{\vartheta_m - \vartheta_0} \right)^{q^*} \left(\tau_c^0 + \frac{\sum_{\alpha=1}^{n_s} \sum_{\beta=1}^{n_s} \langle \dot{\gamma}_{net}^{(\alpha)} \rangle \int_0^t h_{\alpha\beta} \langle \dot{\gamma}_{net}^{(\beta)} \rangle dt}{\sum_{\alpha=1}^{n_s} \langle \dot{\gamma}_{net}^{(\alpha)} \rangle} \right), \tag{6.75}$$

where $\tau_c^0 \triangleq \tau_p + \tau_{ss} + \tau_{sp} + \tau_{HP} + \tau_\perp^0$ is the initial slip resistance on all n_s slip systems. The hardening matrix $h_{\alpha\beta}$ evolves according to Eq. (6.68) and the evolution of the average temperature $\langle \vartheta \rangle$ is governed by Eq. (6.30) and Eq. (6.30). The microscopic average of the net slip rate associated with both plastic and porous deformation is obtained by substituting Eq. (6.58) into Eq. (6.59), i.e.

$$\langle \dot{\gamma}_{net}^{(\alpha)} \rangle = \left| \langle \dot{\gamma}_p^{(\alpha)} \rangle \right| + \frac{2}{\sqrt{3}} \frac{M_T^*}{n_s} \frac{|\dot{\varphi}|}{(1-\varphi)^2} \ln \left(\frac{1}{\varphi} \right). \tag{6.76}$$

Closure of the model is provided by bridging the microscale void dynamics to the evolution of porosity on the macroscale. Consider a general distribution of void sizes characterized by $g(a_\varphi)$. The current porosity is then obtained by integrating the void volumes over this distribution, i.e.

$$\frac{\varphi}{1-\varphi} = \frac{4}{3}\pi N_{nuc} \int_0^\infty g(a_\varphi) a_\varphi^3 da_\varphi, \tag{6.77}$$

where the number of voids per unit volume in the reference configuration is denoted as N_{nuc} and may vary substantially depending on the material and loading conditions. Eq. (6.73) through Eq. (6.77) constitute a set of ordinary differential equations that govern the dynamics of a distribution of dynamically growing voids on the microscale

and the corresponding porosity (or void volume fraction) on the macroscale. The set of equations are analytic with respect to the microscale spatial coordinates, which substantially reduces the computational complexity associated with modeling these inherently multiscale failure processes.

As a brief aside, it is instructive to examine the special case in which all voids are the same size, i.e. $g(a_\varphi) = \delta(a_\varphi)$, with $\delta(\cdot)$ being the Dirac delta function. For this special case, Eq. (6.73) may be recast in the following functional form

$$3\rho_0^s \ell_v^2 \left(\frac{1-\sqrt[3]{\varphi}}{\left(\sqrt[5]{\varphi}-\varphi\sqrt[5]{\varphi}\right)^{5/3}}\ddot{\varphi} - \frac{1-12\varphi+11\varphi^{4/3}}{6\left(\sqrt{\varphi}-\varphi\sqrt{\varphi}\right)^{8/3}}\dot{\varphi}^2 \right) = \Sigma_m - 2\frac{\gamma_{se}}{\ell_v}\sqrt[3]{\frac{1-\varphi}{\varphi}} - \zeta_m \langle \tau_c^{eq} \rangle \frac{1-\varphi^m}{(1-\varphi)^m}\left(\frac{M_T^* \left|\dot{\varphi}\right|}{\dot{\gamma}_0 \varphi}\right)^m \operatorname{sgn}(\dot{a}_\varphi), \tag{6.78}$$

with $\ell_v \triangleq \left(\frac{4}{3}\pi N_{nuc}\right)^{-3}$ being a measure of the average center-to-center spacing between nucleated voids in the reference configuration. The algebraic complexity of the functional form expressed in Eq. (6.78) is noteworthy. It would be impractical to attempt to obtain such an evolution equation from a fit to either experimental or simulation data. Furthermore, a physics-based model for dynamic evolution of porosity requires a length scale, i.e. ℓ_v, and a second-order differential equation on porosity, i.e. $\ddot{\varphi}$, in order to accurately capture the role of microinertia in dynamic ductile failure of metals. Often, this is not accounted for in models utilized in the failure analysis of structures subject to extreme dynamic loading conditions.

6.5.4 Microscale void dynamics under extreme conditions

It is necessary to modify Eq. (6.73) in order to properly account for dynamic void growth in the relativistic drag regime discussed in chapter 3. Based on the analysis provided in section 3.5, in particular the effects of relativistic drag on void dynamics may be suitably accounted for by enforcing the appropriate limit on void velocity

$$|\dot{a}_\varphi| < \frac{1}{3} a_\varphi b \tilde{N}_m c_s, \tag{6.79}$$

where $\tilde{N}_m$ is the mobile dislocation density near the surface of the void. In section 3.5 the evolution of the mobile dislocation densities was modeled after Austin and McDowell [49] and is recast here as

$$\dot{\tilde{N}}_m = \dot{\tilde{N}}_{nuc} + \dot{\tilde{N}}_{mult} - \dot{\tilde{N}}_{ann} - \dot{\tilde{N}}_{trap} \tag{6.80}$$

$$\dot{\tilde{N}}_{im} = \dot{\tilde{N}}_{trap}, \tag{6.81}$$

where $\tilde{N}_{im}$ is the immobile dislocation density near the surface of the void and the subscripts *nuc*, *mult*, *ann*, *trap*, and *rec* refer to dislocation nucleation, multiplication, annihilation, and trapping, respectively. Recovery processes are ignored ($\dot{N}_{rec} = 0$) due to the short time scales of interest ($< 1\mu$s) inhibiting many thermally-activated processes such as climb. A physically-based framework proposed by [10] is assumed to sufficiently capture the correct physics and may be recast in the appropriate form

as

$$\dot{\tilde{N}}_{mult} = 3\frac{\delta_{mult}}{b}\frac{\dot{a}_\varphi}{a_\varphi} \tag{6.82}$$

$$\dot{\tilde{N}}_{ann} = 3\alpha_{ann}\tilde{N}_m\frac{\dot{a}_\varphi}{a_\varphi} \tag{6.83}$$

$$\dot{\tilde{N}}_{trap} = 3\frac{1}{b\tilde{\Lambda}}\frac{\dot{a}_\varphi}{a_\varphi}, \tag{6.84}$$

with δ_{mult} and α_{ann} being model parameters and $\tilde{\cdot}$ denoting the value of the respective quantity near the void surface. $\tilde{\Lambda}$ is the effective mean free path of dislocations near the surface of the void and decreases with increasing dislocation density, i.e. $\tilde{\Lambda}^{-1} = \alpha_{dis}\sqrt{\tilde{N}_{im} + \tilde{N}_m}$, see [10].

The limits imposed by Eq. (6.79) play an important role at very high tensile pressures in the range of $\mu/30 \lesssim \boldsymbol{\Sigma} : \mathbf{I}/3 \lesssim \mu/10$ as discussed in chapter 3 and chapter 5. However, at extremely high tensile pressures $\gtrsim \mu/10$ it may be possible to rapidly grow voids by emitting dislocations from the surface of the voids. This mechanism has been extensively studied recently [64, 65, 67, 68, 70, 109]. In chapter 4 we derived a critical stress criterion for the activation of dislocation emission in porous materials under general stress states, i.e.

$$\Phi_{em} = \sqrt{h_1^2\left|\frac{\Sigma_m}{1-\tilde{\varphi}} - \frac{\gamma_{se}}{a}\right|^2 + \left(\frac{h_2}{\sqrt{3}}\frac{\Sigma_{eq}}{(1-\tilde{\varphi})}\right)^2 - \left|\tilde{\tau}_{cr}^{image}\right|^2}, \tag{6.85}$$

where Σ_{eq} denotes the macroscopic deviatoric stress, γ_{se} is the surface energy of the material, $\tilde{\varphi}$ is an auxiliary porosity defined Eq. (4.6), h_1 and h_2 are non-dimensional length scales expressed in Eqs. (4.42) and (4.43), with the magnitude of the critical

image shear stress expressed here as

$$\left|\tilde{\tau}_{cr}^{image}\right| = \frac{\mu_s^*}{4}\frac{b}{w_\perp}\left\{\frac{\sqrt{2}a+2w_\perp}{\sqrt{2}a+w_\perp} - \frac{a^2w_\perp^2\left(\sqrt{2}a+w_\perp\right)\left(\sqrt{2}a+2w_\perp\right)}{\left(a^2+w_\perp^2+\sqrt{2}aw_\perp\right)^3}\right\}, \tag{6.86}$$

where $w_\perp$ is a temperature-dependent dislocation core size calibrated in chapter 4 and modeled by Eq. (4.56) and $\mu_s^* \triangleq \mu/\pi(1-\nu_s)$ with ν being the Poisson ratio of the solid material.

With dislocation emission active (Φ_{em}) the rate at which dislocation emission replenishes the mobile dislocation density in the vicinity of the void surface was modeled by an Arrhenius relation in chapter 5, i.e.

$$\dot{\tilde{N}}_{nuc} = \frac{\alpha_{em}\nu_D b}{\Omega}\exp\left\{\frac{g_0\mu b}{k_b\vartheta}\frac{\Phi_{em}}{\left|\tilde{\tau}_{cr}^{image}\right|}\right\}H(\Phi_{em}), \tag{6.87}$$

where α_{em} and g_0 are dimensionless material parameters with ν_D and Ω respectively denoting the Debye frequency and atomic volume.

6.6 Summary and implications

The aim of the current chapter has been to provide a thermodynamically consistent multiscale framework for modeling the deformation and failure of ductile FCC single crystals subject to complex, three-dimensional dynamic loading paths. The model accounts for a number of dynamic void growth mechanisms that account for the dominant governing physics across a broad range of strain-rates and stress states. The key mechanisms effecting void growth that are accounted for in the present model include:

- ✦ micro-inertia, which is explicitly accounted for
- ✦ thermally-activated glide accounted for through a power-law rate-sensitivity
- ✦ mean dislocations velocities are explicitly limited to shear wave speed
- ✦ dislocation emission governing void growth under the most extreme conditions.

Particular attention was paid to a proper treatment of the thermodynamics in order to provide an accurate description of the temperature evolution associated with irreversible nonequilibrium shock compression, near-isentropic release, and dissipation associated with plastic and inelastic work. In addition, a porous crystal plasticity framework was provided with emphasis placed on coupling the hardening associated with plastic and porous deformation. Unfortunately, it is beyond the scope of the current work to provide a rigorous validation of this framework. A suite of single crystal plasticity unit cell finite element calculations would provide the necessary data to provide some degree of validation of the various micromechanical assumptions made throughout this chapter. Nevertheless, the assumptions have been clearly stated throughout the chapter and justified as much as feasible. At the very least the chapter serves as a skeletal framework that may be improved upon over the next few years.

Chapter 7

A microstructurally informed thermal fatigue model and its application to surface evolution of near-Earth asteroids[†]

Throughout this dissertation we have explored the role of microstructure (see chapter 5), defect kinetics (chapters 2, 3, and 5), and nonequilibrium thermal transport (chapters 2 and 4) in governing the failure behavior of materials on extremely short timescales, i.e. $\lesssim 100$ ns. However, microstructure, defect kinetics, and nonequi-

[†]The present chapter is largely based on a collaborative work published by Delbo et al. [160]. The contribution of J.W. to this publication was significant as noted in [160].

librium thermal transport are equally important to the failure response of materials on extremely long timescales, i.e. $\gtrsim 10^6$ years. An excellent demonstration of this phenomena is the gradual surface evolution of near-Earth asteroids driven by the thermal radiation of the Sun due to thermal fatigue. Furthermore, this particular application involves an extreme range of pertinent length-scales from micron-sized cracks and mm-sized inclusions to m-sized boulders and km-sized asteroids, as well as relevant timescales from seconds to billions of years. The spirit of this dissertation has been the development of simple multiscale mechanics models that capture relevant physics in the most computationally efficient manner. Modeling the fine-scale surface evolution of km-sized asteroids over billions of years is one application where this approach is vital.

7.1 Introduction and background

Space missions [161, 162] and thermal infrared observations [163] have shown that small asteroids (km-sized and smaller) are covered by a layer of cm-sized or smaller particles, which constitute the regolith. Regolith generation has traditionally been attributed to the fall back of impact ejecta and the comminution of boulders by micrometeoroid impact [164, 165]. However, laboratory experiments [166] and impact models [164] show that crater ejecta velocities are typically larger than several tens of cm/s, which corresponds to the gravitational escape velocity of km-sized asteroids.

Therefore, impact debris cannot be the main source of regolith on small asteroids [164].

The collisional and gravitational reaccumulation processes by which small asteroids are formed likely result in the creation of surfaces composed of boulders [171]. These boulders are broken up by micrometeoroid impacts into the smaller particles constituting the regolith [164, 165]. A classical model [172] that calculates the time required to form regolith by fragmenting rocks of sizes between 1 and 10 cm by micrometeoroid impacts shows that these rocks on the Moon's surface will be broken down into smaller rocks in several million years [165, 172]. On asteroids, like on the Moon, regolith formation via breakup of rocks by micrometeoroid impacts is accomplished via two mechanisms: rupture and erosion [165]. On the Moon, rock survival time against micrometeoroid rupture is in the range of 2 – 20 Myr for rock diameters between 1 and 10 cm [172].

This survival time on asteroids can be calculated by means of the following method. First, given the relation between the rock diameter and the meteoroid impact energy required for the rock rupture [172] and assuming a density of 1 g cm^{-3} for cometary and 3.5 g cm^{-3} for asteroidal meteoroids, one can find that rocks of 1-10 cm in size are broken up by sub-millimetric meteoroids [165]. Meteoroids of this size dominate the zodiacal dust cloud [173, 174], which is believed to be constituted primarily of cometary dust [173]. Next, given the orbital distribution of these cometary particles [173], we use a classical method [174], but without imposing an impact ve-

locity cutoff, to calculate the average intrinsic impact probabilities (p, e.g. number of impacts per meteoroid on a circular cross section of 1 km of radius per year) and the average impact velocity (v_i) of meteoroids on the Moon, a typical NEA (a=1 AU, e=0.3, i=0.15 rad), and average MBA. We find $p = 8.0 \times 10^{-18}$, v_i=11 km/s for the Moon; $p = 9.5 \times 10^{-18}$, v_i=15 km/s for a typical NEA; $p \sim 1 \times 10^{-18}$, v_i=10 km/s for the average MBA. Neglecting the different impact velocities (since the energy for rock breakup, E_b, is a shallow function of the impact velocity, i.e. $E_b \propto v_i^{0.7}$ [172]), the rate of meteoroid impacts per unit time and unit surface (Φ) on the Moon, NEAs, and MBAs is proportional to p. We thus have that $\Phi_{NEA} \sim \Phi_{Moon} \sim 10 \times \Phi_{MBA}$.

Hence, the impact-driven rock survival time on NEAs is similar to that on the Moon, while on MBAs rocks survive somewhat longer. For rocks in the size range 1-10 cm, erosion removes in the order of 1 mm/Myr of surface [165, 172], requiring at least $\sim$ 10-100 Myr to comminute rocks on the Moon and on NEAs, and 0.1-1 Gyr on MBAs. Therefore, using the known [173] orbital distribution of micrometeoroids and a method [174] to calculate the impact probability of micrometeoroids with the Moon and asteroids (Methods), we find that the break-down of surface rocks requires about the same amount of time on near-Earth asteroids (NEAs, asteroids with a perihelion distance $q < 1.3$ AU) and on the Moon, while on Main-Belt asteroids (MBAs) this time is about 10 times longer than on the Moon. In the present chapter, we aim to demonstrate that our proposed mechanism of rock fragmentation by thermal fatigue is often orders of magnitude faster than by micrometeroid impact, the mechanism

(

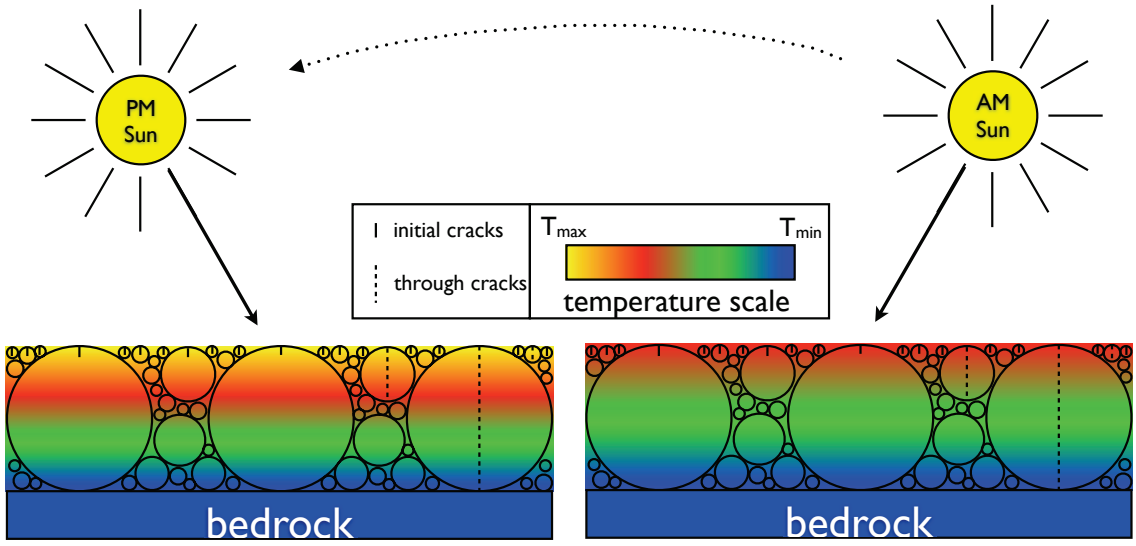

Fig. 7.1: Schematic of the gradual surface evolution of near-Earth asteroids resulting from fatigue crack growth driven by the thermal radiation of the Sun.

traditionally assumed to dominate surface evolution on planetary bodies.

The physical mechanism (Fig. 7.1) by which progressive thermal fatigue crack propagation may lead to fragmentation can have two observable effects: a) the flaking off of material from the surface of boulders, also invoked to explain characteristic regolith deposits observed near boulders in *ponds* on the surface of the NEA Eros [175], and b) the propagation of a crack across the entire diameter of rocks. The flaking mechanism is likely to be most applicable to large boulders that experience high thermal gradients because of their angular and/or highly sloped surfaces [176]. Alternatively, small cm-sized rocks, that experience more modest thermal gradients, are more likely to be fragmented by a crack that grows through the entire rock. We limit the scope of this work to the latter mechanism.

Delbo et al. [160] demonstrated that thermal fatigue [167–169], a mechanism of

rock weathering and fragmentation with no subsequent ejection, is the dominant process governing regolith generation on small asteroids. The model presented in this chapter will show that rocks larger than a few centimeters may break up faster by thermal fragmentation, induced by the diurnal temperature variations, than by micrometeoroid impacts. Our findings imply that thermal fragmentation may even be fast enough to contribute significantly to regolith generation on all asteroids, regardless of their size. Furthermore, production of fresh regolith originating from thermal fatigue fragmentation may be an important process for the rejuvenation of near-Earth asteroids' surfaces, as well as for explaining the observed shortage of low-perihelion carbonaceous near-Earth asteroids [170]. Along these lines, our model predictions imply that some near-Earth asteroids (NEAs) that pass within Mercury's orbit may be completely eroded by the thermal fragmentation processes in as little as a few million years.

7.2 Experimental methods and observations

Boulders on the surface of asteroids are also exposed to cyclic diurnal temperature variations, which cause mechanical stresses. In order to answer the question whether these stresses are large enough to induce thermal fatigue crack growth, Delbo et al. [160] performed laboratory experiments on two meteorites: a carbonaceous chondrite (CM2 Murchison) and an ordinary chondrite (LL3.2 Sahara 97210) considered the

closest available analogs of the C and S broad asteroid spectroscopic classes, respectively. The protocol shown in Fig. 7.2 consists of utilizing a climatic chamber to subject these meteorites to temperature cycles that approximate the day/night temperature variations experienced on NEA surfaces. The temperature cycle period was taken to be 2.2 hours, the fastest period permitted by the climatic chamber allowing a reasonable number of cycles within a month, while still subjecting meteorites to temperature rates of change typical of NEA surfaces. The magnitude of the temperature excursion, ΔT, was taken to be 190 K, equal of the ΔT of C-type NEAs at $\sim$0.7 AU from the Sun (see Fig. 7.3). After subjecting the meteorites to as few as 407 temperature cycles, Delbo et al. [160] utilized an X-ray tomography to observe (Fig. 7.4) and measure an increase in the length and in the width of several of the pre-existing cracks in both Murchison and Sahara 97210, thus confirming thermal fatigue. Additionally, small particles were found in the sample holder that had broken off from the surface or the Murchison sample as a result of temperature cycling (Fig. 7.5).

Measurements for 21 cracks for each meteorite are shown in Figs. 7.6 and 7.7. To image these cracks in the meteorites at three stages of thermal fatigue i.e. before the temperature cycles (t_0), after 76 cycles (t_1), and after 407 cycles (t_2), Delbo et al. [160] utilized a Phoenix Nanotom CT scanner that produces three-dimensional data cubes of approximately 1000^3 voxels or 2000^3 voxels depending on the spatial resolution, $\Delta\ell$. Specifically, for Murchison, $\Delta\ell$=12.5, 13, 13 μm and for Sahara $\Delta\ell$=3.75, 4, 4.5 μm, at

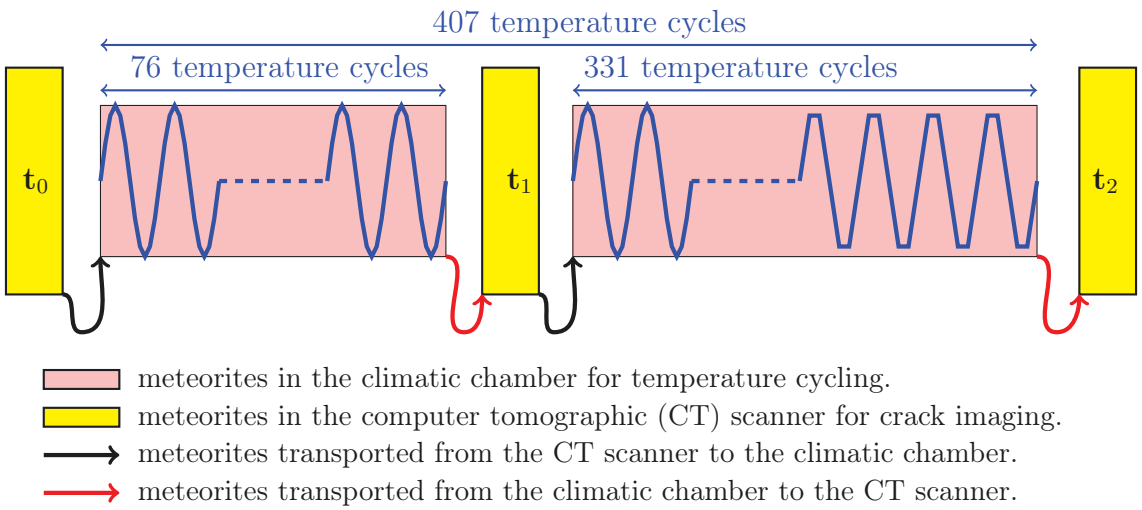

Fig. 7.2: Schematic of the experimental protocol for the thermal fatigue of meteorites [160]. The experimental protocol consists of placing samples of the meteorites Murchison and Sahara 97210 in a climatic chamber where the air temperature is forced to follow temperature cycles between 250 and 440 K at a nearly constant rate of change with a period of 2.2 h. The air in the climatic chamber is anhydrous and at a pressure of 1 bar. The samples have sizes of approximately 1 cm in diameter. Meteorites are analyzed by X-ray computer tomography before the temperature cycles begin (t_0), after 76 cycles (t_1), and after 407 cycles (t_2). From the tomographies we measure the increase of the volume and length of cracks as a function of the number of temperature cycles.

t_0, t_1, and t_2, respectively. The higher spatial resolution for Sahara 97210 is necessary because this meteorite has fewer and thinner cracks than Murchison. The orientation of each sample within the scanned volume varies between t_0, t_1, and t_2. Since the determination of crack growth requires the comparison of sizes of same cracks at t_0, t_1, and t_2, the meteorites were precisely aligned and scaled within the CT scans. To do this, several distinctive features in the meteorites, such as metal rich inclusions of a few voxels in volume, are visually identified at t_0, t_1, and t_2 and used as position markers. Because the objects are not initially aligned, the same marker does not necessarily

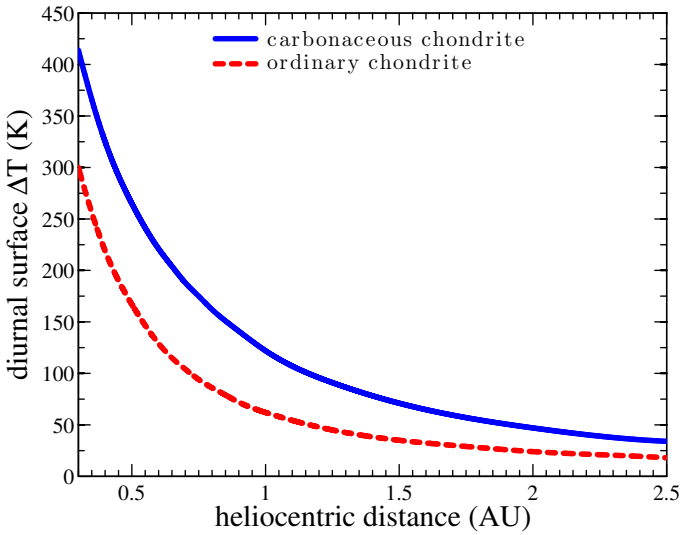

Fig. 7.3: Diurnal surface temperature excursions on asteroids as a function of the heliocentric distance.

have the same coordinates at t_0, t_1, and t_2. For each meteorite, the matrices that best transform the marker coordinates at t_1 and at t_2 to those at t_0 are computed, and a Monte Carlo method is employed to calculate the best transformation matrix by minimizing the square of the distance between the marker coordinates at t_0 and the transformed ones. The procedure TRANSFORM_VOLUME, written in IDL by Martin Downing, is then utilized to apply the transformations to align the CT volumes at t_1 and t_2 to those at t_0 (see www.idlcoyote.com/programs/transform_volume.pro; IDL is developed by Exelis Visual Information Solutions Incorporated. http://www.exelisvis.com/ProductsServices/IDL.aspx). The accuracy of the final alignment is of the order of 1 voxel.

Delbo et al. [160] developed a method for the determination of the volume and length of the cracks that is not sensitive to the absolute value of the voxel intensity.

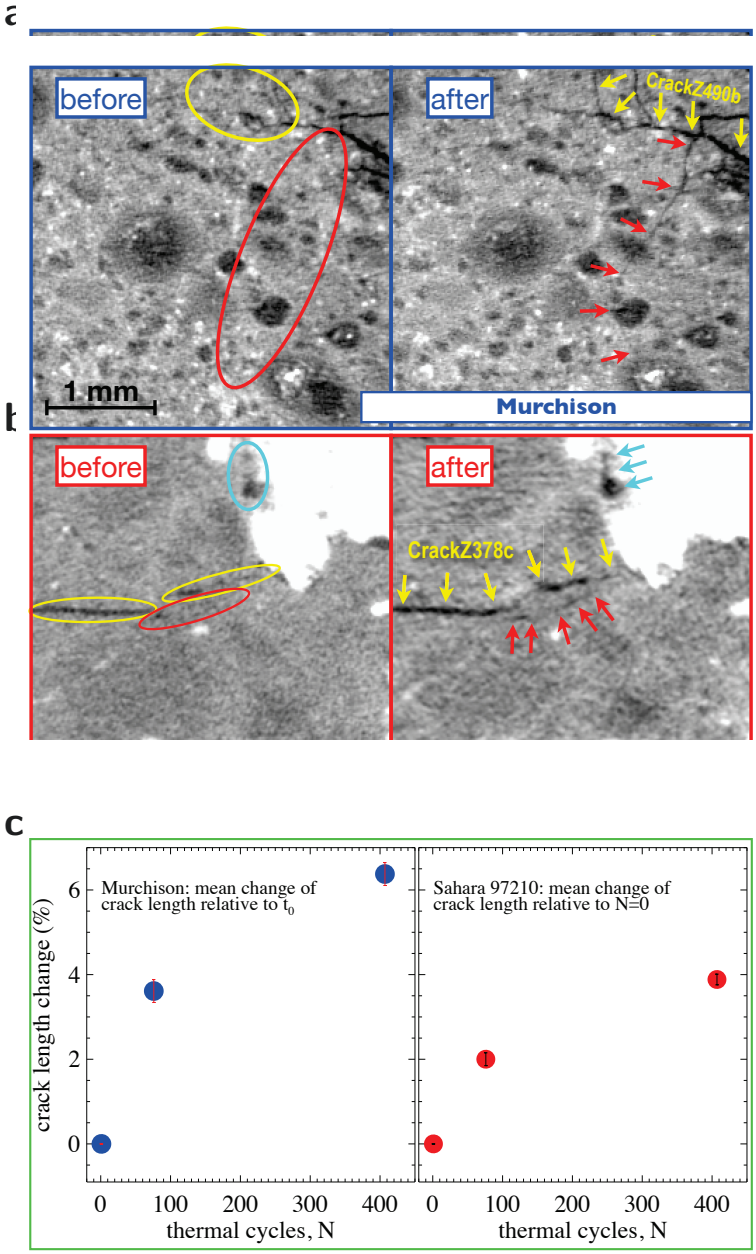

Fig. 7.4: Experimental observations of thermal fatigue crack growth in cm-sized samples of two meteorites: (a) Murchison (CM2) and (b) Sahara 97210 (LL3.2). (c) Measurements of thermal fatigue crack growth (in terms of relative crack length extension) after 76 and 331 thermal cycles.

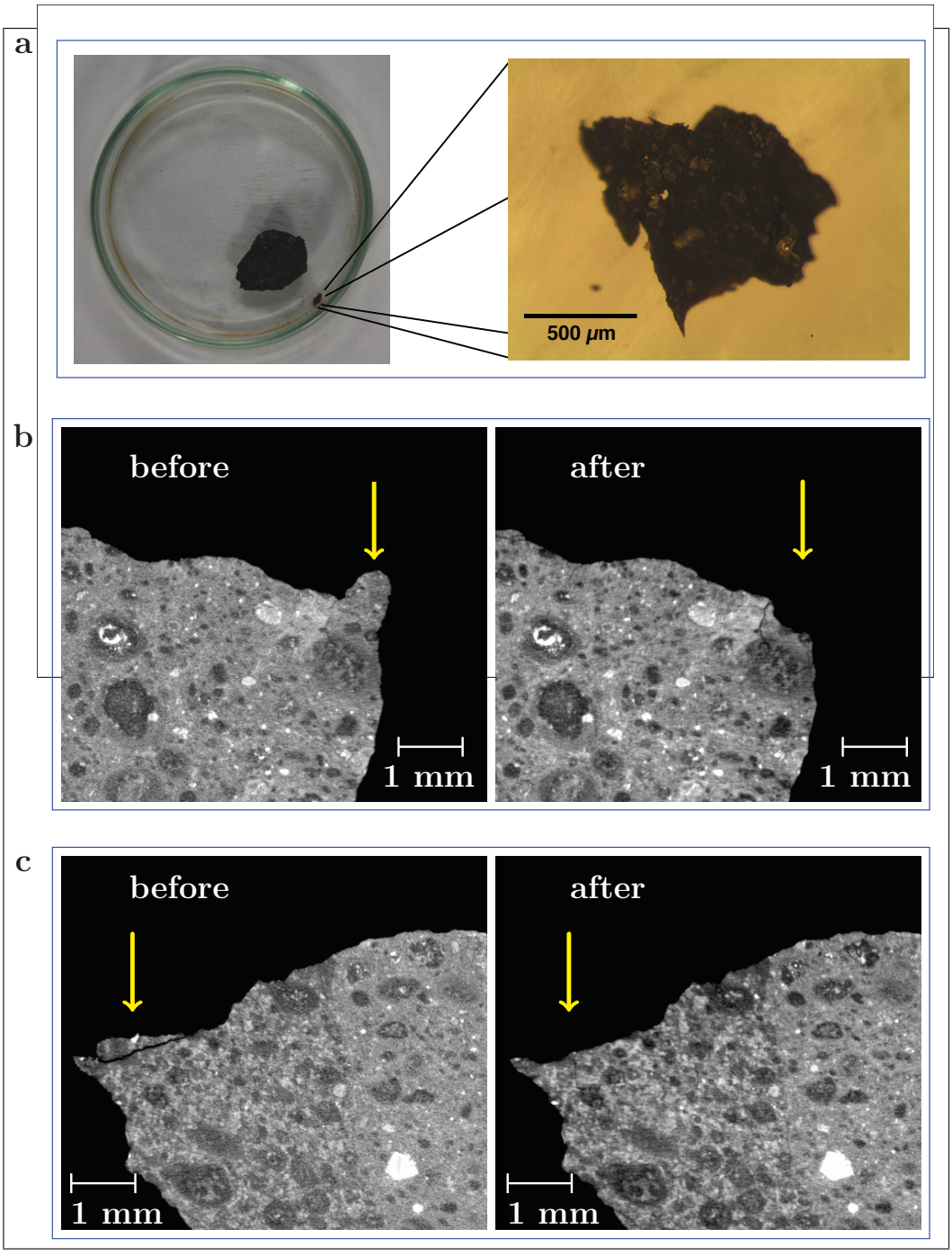

Fig. 7.5: Regolith formation from Murchison in the laboratory. (a) The sample of Murchison and (enlarged) one of its small fragments, containing several visible chondrules, found in the sample holder after temperature cycling. (b) and (c) Tomographic slices of regions of the same sample of Murchison before and after temperature cycling. The arrows indicate fragments that broke off from Murchison.

This is because the X-ray intensity is not constant between different CT scans, causing variability of the meteorite voxel counts, the background counts, and the noise level among CT scans of the same meteorite. The crack width is measured at all points along the crack length and crack height, within a volume of interest of the meteorite that includes the crack or a portion thereof. The same volume of interest is used for the a single crack at t_0, t_1, and t_2 on the aligned CT scans. The volume of interest, variable for each unique crack, is obtained through the following procedure:

1. chose a plane (e.g. the x-y plane) along which the crack mainly extends
2. extract several slices from the CT volume parallel to the considered plane (typically, ten slices are considered)
3. for each slice, one must physically draw a segmented line that follows the crack as close as possible
4. compute the volume of the crack portion using Eq. (7.1), i.e.

$$V = \sum_{i=n}^{N} \sum_{j=1}^{M_i} \sum_{k=1}^{L_{i,j}} W_{i,j,k} \times g_{i,j,k} \times (\Delta\lambda)^3, \tag{7.1}$$

where $W_{i,j,k}$ is the crack width at the k-th position along the j-th segment of length $L_{i,j}$ on the i-th slice of the volume of interest. The initial and final slices are n and N, respectively, and M is the number of segments. The value of $g_{i,j,k}$ is equal to 1 or 0 depending on whether the width determination was accepted or deemed invalid using the procedure described in the next paragraph. As for the width of the crack, we use the Full Width at Half Maximum of the Gaussian function that best

fits the intensity profile of the meteorite perpendicular to the segment. We prefer to give the volume of the crack instead of its average width. This is because cracks typically have large width variations throughout their volume. The accuracy of the crack width determination is estimated in each point by means of a Monte Carlo method that attempts to fit a Guassian function up to 9000 times to the meteorite intensity profile in order to have at least 30 valid fits. Gaussian random noise (with a standard deviation given by noise in the CT data) is added to the voxel counts at each iteration. If at t_0, or t_1, or t_2 the dispersions of the widths, centers, or amplitudes of the Guassian fits are larger than some threshold values that, once tuned, are kept constant for both meteorites at all times, the point is deemed as not containing a crack and is excluded from the sums of Eq. (7.1) at t_0 and t_1 and t_2 (by setting the corresponding value of g to zero).

The crack length measurement method is similar to the one used for the crack volume determination, but with two main differences. First, we select a volume of interest that includes one or more crack tips, typically by constructing the segments such that they partially extend beyond the crack tip(s). This is because any potential increase in the length of the crack due to temperature cycling must happen at the crack tip. Next, for each slice, we count the number of voxels where g=1, i.e. where a valid width of the crack is found. Note that, contrary to the method used for the measurement of the crack volume, we do not set g=0 at t_0 and t_1 and t_2 if g=0 at t_0 or t_1 or t_2. We observe that our method fails to fit a Gaussian function to the

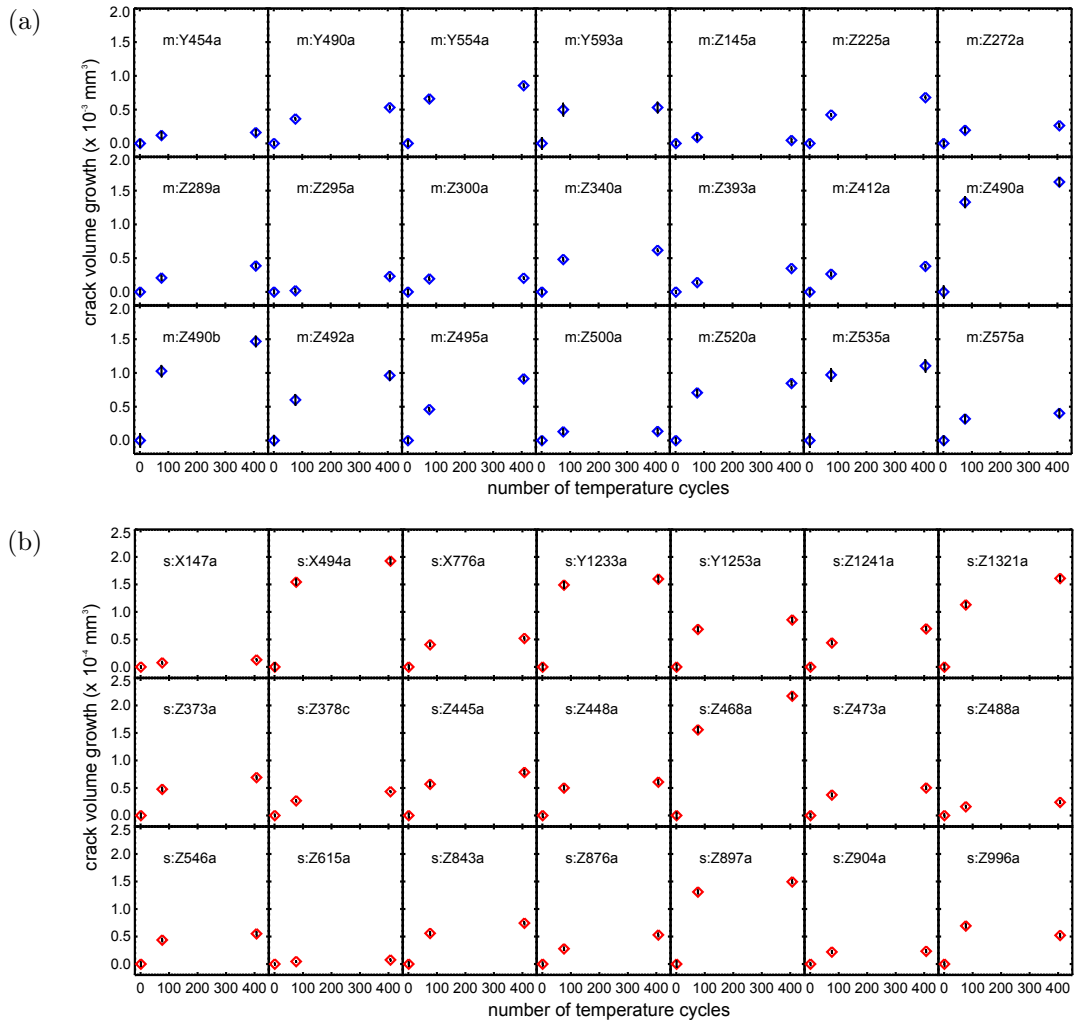

Fig. 7.6: Volume growth of individual cracks as a function of the number of temperature cycles.

meteorite intensity profile beyond the crack tip or that the dispersions of the Gaussian parameters becomes very large, indicating the absence of a crack. The length of the crack averaged over the slices of interest is given by Eq. (7.2)

$$L = \frac{1}{N-n} \sum_{i=n}^{N} \sum_{j=1}^{M_i} \sum_{k=1}^{L_{i,j}} g_{i,j,k} \times (\Delta \ell) \tag{7.2}$$

(see Eq. (7.1) for the meaning of symbols). We take the standard error of the mean

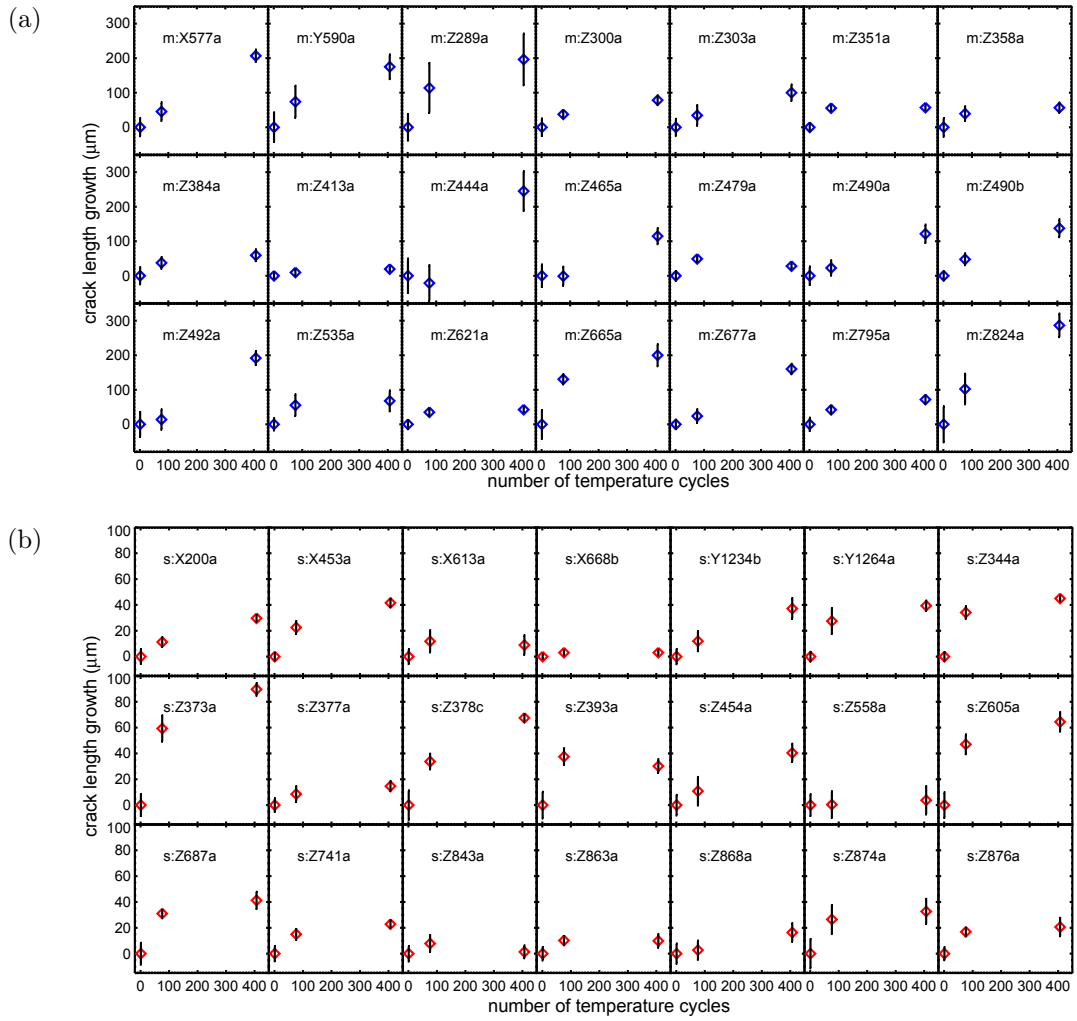

Fig. 7.7: Length growth of individual cracks as a function of the number of temperature cycles.

as the error on the length of the crack. This same process is applied to the CT scans of the meteorites at t_0, t_1 and t_2 in order to measure the evolution of crack length as a function of the number of the cycles.

We were concerned that processes other than thermal fatigue could affect crack growth in our experiments. For example the water freeze-thaw effect plays an important role in the opening of cracks in terrestrial rocks. Atmospheric moisture in the

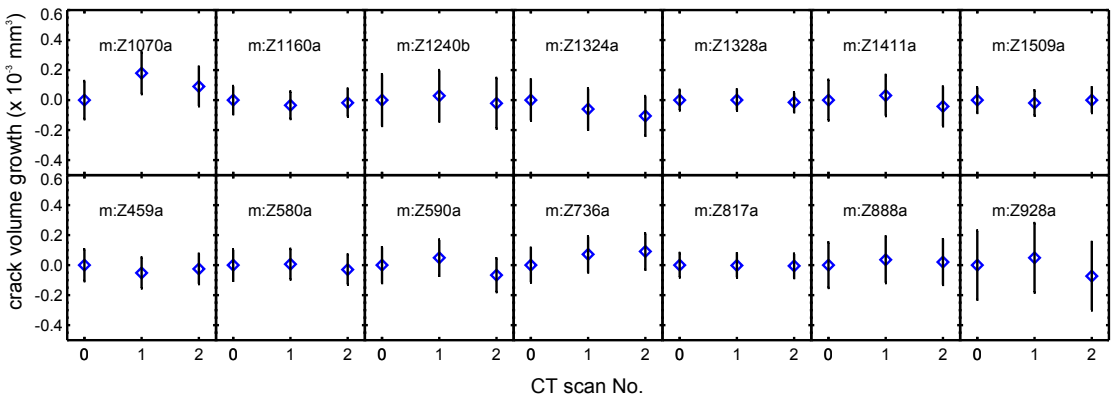

Fig. 7.8: No crack growth is observed without the application of thermal excursions.

cracks of our specimens could, in principle, have been present and may have facilitated the opening and the lengthening of cracks. However, we rule out this mechanism in our experiments by a couple of counter measures. First, temperature cycling of our samples is carried out under an anhydrous atmosphere at a pressure of 1 bar. Next, before the temperature cycling begin, the meteorite specimens are exposed to a $\sim 10^{-2}$ bar-vacuum and later immersed in a Argon and Nitrogen gas for several hours in order to eliminate potential traces of humidity.

We were also concerned that the transport of the meteorites from the climatic chamber to the CT scanner may have stressed the samples and affected the crack growth. We rule out this effect by obtaining CT scans of a sample of the meteorite Murchison that was transported from the climatic chamber to the CT scanner, but not subjected to temperature cycles. We repeat this procedure twice. Visual inspection of the CT images show no obvious change in the position, width and length of the cracks, and no formation of new cracks. Also, no fragments flaking off from the surface

of the Murchison specimen were found (analysis of the CT scans shows no obvious change in the surface of the specimen). Volume measurements of several cracks in the specimen of the Murchison meteorite that was transported but not subjected to temperature cycles show no variation within the error bars (Fig. 7.8).

7.3 A multiscale modeling approach

Having demonstrated that the temperature variations on near-Earth asteroids are large enough to initiate some degree of crack growth on surface rocks, the next natural question is how much time is required for these cracks to propagate far enough to break the rocks and contribute to the generation of finer regolith. Our measurements show that, under laboratory conditions, pre-existing cracks are extending in length at a rate of about 0.5 mm/year (average of Murchison and Sahara 97210). A constant crack propagation rate would suggest that a 1 cm rock on the surface of an NEA could fragment into smaller pieces in less than 20 years, several orders of magnitude faster than comminution by micrometeoroid impacts, which requires about 2 My on NEAs and about 20 My on MBAs. However, crack propagation rates are typically a non-linear function of crack size, demanding a detailed analysis of the fracture mechanics to investigate whether such a rapid growth rate would be maintained to the point of fragmentation and whether thermal fragmentation can also occur for different cycle periods, larger rocks, and at lower temperatures, e.g. MBAs.

7.3.1 Summary of multiscale modeling approach

To provide a deeper understanding of the thermal fatigue crack growth kinetics we develop a microstructurally informed thermal fatigue model that couples nonequilibrium thermal transport [177, 178], micromechanics and linear elastic fracture mechanics [179], as well as the well-established Paris fatigue crack growth law [184]. This coupled thermomechanical model enables us to analyze the progressive crack growth from the early stages to final fragmentation, a process that likely evolves over very long timescales not amenable to laboratory experiments.

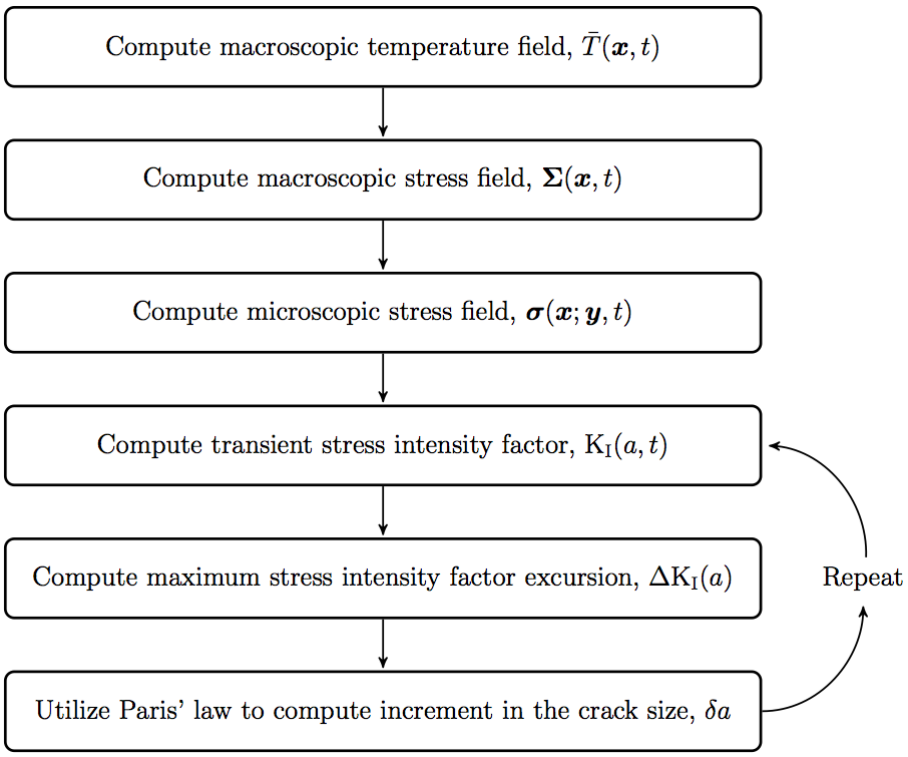

Fig. 7.9: Flow chart showing the key steps in the our procedure to compute the thermal fatigue crack growth kinetics accounting for the role of both macroscopic thermal gradients and microstructure.

Figure 7.9 provides a flow chart that outlines this procedure, which begins with solving the associated transient thermal transport problem to obtain the macroscopic temperature field as a function of time. Next, we compute the time-dependent stress field associated with the transient thermal gradients. We then compute the local stress variations in the microstructure and combine the two stress fields using the superposition principle. Next, the transient stress intensity factor for the current crack size is computed, accounting for the combined effect of thermal gradient stresses and local stresses in the microstructure. Finally, the maximum stress intensity excursion experience over a thermal cycles is utilized in Paris' law to compute the current crack growth rate.The Paris fatigue crack growth law relates the rate at which the crack length, a, extends as a function of the number of loading cycles, N, to the maximum stress intensity factor [184] excursion, $\Delta \mathrm{K_I}$, i.e.

$$\frac{da}{dN} = C \left\{ \Delta \mathrm{K_I}(a) \right\}^n , \tag{7.3}$$

where C and n are material properties fit to experimental fatigue data [185]. The primary challenge in the fatigue crack growth analysis is computing the stress intensity factor, $\mathrm{K_I}$, which depends on the details of the stress field in the vicinity of the crack tip.

7.3.2 Transient multiscale thermoelastic stress field

The purpose of this section is to approximate the two-scale transient stress field, $\boldsymbol{\Sigma}(\boldsymbol{x},t)$ and $\boldsymbol{\sigma}(\boldsymbol{x};\boldsymbol{y},t)$, that would develop in a heterogeneous linear thermoelastic material subject to a transient temperature field $\bar{T}(\boldsymbol{x},t)$. Consider the two-scale body shown in Fig. 7.10 with two macroscale observable quantities, namely macroscopic stress, $\boldsymbol{\Sigma}(\boldsymbol{x},t)$, and macroscopic temperature, $\bar{T}(\boldsymbol{x},t)$, which are functions of the macroscale material coordinate $\boldsymbol{x}$. Likewise, the microscale quantities $\boldsymbol{\sigma}(\boldsymbol{x};\boldsymbol{y},t)$ and $T(\boldsymbol{x};\boldsymbol{y},t)$ are functions of microscale material coordinate $\boldsymbol{y}$. The macroscale quan-

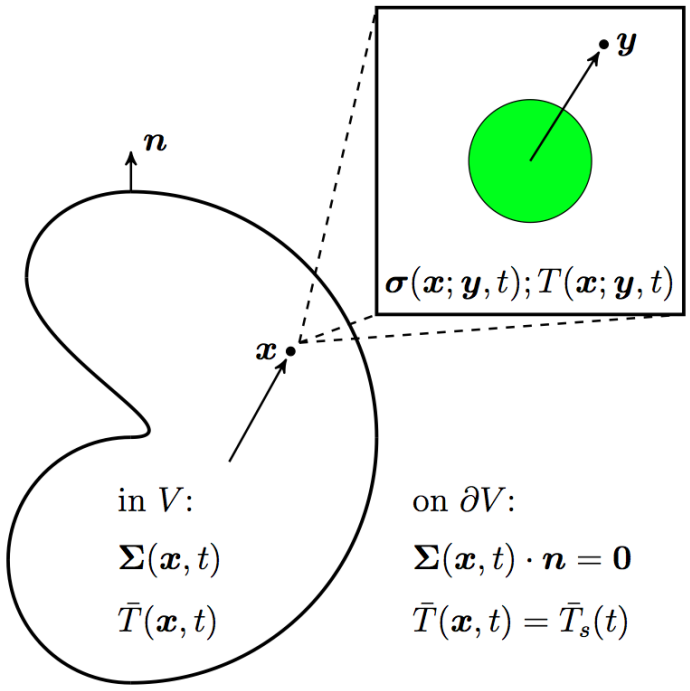

Fig. 7.10: Schematic of the two scale representation (macroscale and microscale) of a general body with microstructure. ∂V is the surface of the body of volume V. A macroscopic transient temperature and stress field, i.e. $\bar{T}(\boldsymbol{x},t)$ and $\boldsymbol{\Sigma}(\boldsymbol{x},t)$, develop as a result of the boundary conditions $\bar{T}(\boldsymbol{x},t) = \bar{T}_s(t)$ and $\boldsymbol{\Sigma}(\boldsymbol{x},t)\cdot\boldsymbol{n}$. In addition, the microscopic transient temperature and stress field, i.e. $T(\boldsymbol{x};\boldsymbol{y},t)$ and $\boldsymbol{\sigma}(\boldsymbol{x};\boldsymbol{y},t)$, must be considered.

tities are related to the microscale quantities through a suitable volumetric average, i.e. $\boldsymbol{\Sigma}(\boldsymbol{x},t) = v^{-1}\int_v \boldsymbol{\sigma}(\boldsymbol{x};\boldsymbol{y},t)dv$ and $\bar{T}(\boldsymbol{x},t) = v^{-1}\int_v T(\boldsymbol{x};\boldsymbol{y},t)dv$.

The microscale is heterogeneous, approximated by spherical inclusions embedded in a matrix. The linear thermoelastic properties of the inclusions are as follows: bulk modulus K_i, shear modulus μ_i, and thermal expansion coefficient α_i. Likewise, the linear thermoelastic properties of the matrix are K_m, μ_m, and α_m. The macroscale is homogenized with effective linear thermoelastic properties of $\bar{K}$, $\bar{\mu}$, and $\bar{\alpha}$ (see Table 7.1).

7.3.2.1 Macroscale transient temperature field

We begin with the calculation of the macroscopic transient temperature field $\bar{T}(\boldsymbol{x},t)$. Consider the idealized case in which the macroscopic body, e.g. a spherical boulder on the surface of an asteroid as shown in Fig. 7.1, is a sphere of outer radius R_o, subjected to a particular macroscopic spherically-symmetric transient temperature boundary condition $\bar{T}_s(t)$. This spherically-symmetric temperature boundary condition is fairly representative of the temperature field generated in our laboratory experiments, but may only be thought of as a loose approximation for the case of boulders on the surface of rotating asteroids. The spherically symmetric macroscopic temperature field $\bar{T}(R,t)$ is governed by the general thermal diffusion equation, i.e.

$$\bar{\kappa}\nabla^2\bar{T}(\boldsymbol{x},t) = \frac{\partial}{\partial t}\bar{T}(\boldsymbol{x},t). \tag{7.4}$$

Applying the surface boundary condition and requiring finite temperature at the origin, $R = 0$, the solution of Eq. (7.4) is

$$\bar{T}(R,t) = \bar{T}_s(t) + \sum_{j=1}^{\infty} \frac{R_o}{R} \sin\left(\lambda_j R\right) f_j(t), \tag{7.5}$$

where $\lambda_j = \frac{j\pi}{R_o}$ and

$$f_j(t) = \int_0^t \frac{2(-1)^j}{j\pi} \frac{\partial \bar{T}_s(\tau)}{\partial \tau} \exp\left\{\bar{\kappa}\lambda_j^2(\tau - t)\right\} d\tau. \tag{7.6}$$

We choose a simple periodic equation for the boundary condition $\bar{T}_s(t)$ that is representative of the conditions experienced by the meteorites in our laboratory experiments, i.e.

$$\bar{T}_s(t) = \bar{T}_0 + \frac{1}{2}\Delta\bar{T}_s \sin\left(\omega t\right), \tag{7.7}$$

where $\bar{T}_0$ is the initial and mean temperature, $\Delta\bar{T}_s$ is the full temperature excursion, and $\omega = \frac{2\pi}{P}$ with P being the period. For our laboratory experiments the period is $P = 2.2$ hours and the surface temperature exersion of $\Delta\bar{T}_s = 190$ K. Eq. (7.6) may be integrated exactly and takes the simplified form of

$$f_j(t) = \frac{(-1)^j \Delta\bar{T}_s}{j\pi\left(\frac{\bar{\kappa}^2\lambda_j^4}{\omega^2} + 1\right)} \left(\sin(\omega t) + \frac{\bar{\kappa}\lambda_j^2}{\omega}\left\{\cos(\omega t) - \exp(-\bar{\kappa}\lambda_j^2 t)\right\}\right). \tag{7.8}$$

The inverse exponential term in Eq. (7.8), which carries the initial condition information, quickly approaches zero on a time scale of $t \approx R_o^2/2\bar{\kappa}$. This timescale is on the order of $0.01 - 100$ thermal cycles for our present interests. Therefore, one may take the limit of Eq. (7.8) as a sufficiently accurate approximation, i.e.

$$f_j^{\infty}(t) = f_j(t \to \infty) = \frac{(-1)^j \Delta\bar{T}_s}{j\pi\left(\frac{\bar{\kappa}^2\lambda_j^4}{\omega^2} + 1\right)} \left(\sin(\omega t) + \frac{\bar{\kappa}\lambda_j^2}{\omega}\cos(\omega t)\right). \tag{7.9}$$

7.3.2.2 Macroscale thermoelastic stress field

The macroscopic stresses $\boldsymbol{\Sigma}(\boldsymbol{x},t)$ develop as a result of spatial gradients in the macroscopic transient temperature field $\bar{T}(\boldsymbol{x},t)$. Consider the case in which the macroscopic body may be approximated as a sphere of outer radius R_o, subjected to a spherically-symmetric macroscopic transient temperature field $\bar{T}(R,t)$, where R is the macroscopical radial coordinate. Again, this assumption is most applicable to our laboratory experiments. Assuming inertial forces to be negligible, the spherical body must satisfy macroscopic equilibrium, i.e.

$$\boldsymbol{\nabla}\cdot\boldsymbol{\Sigma}(\boldsymbol{x},t)=\mathbf{0} \tag{7.10}$$

subject to the a traction-free boundary condition on the surface $R=R_o$ and finite stress at the center $R=0$, i.e.

$$\boldsymbol{\Sigma}(R=R_o,t)\cdot\boldsymbol{e}_R=\mathbf{0} \qquad \text{and} \qquad ||\boldsymbol{\Sigma}(R=0,t)||<\infty, \tag{7.11}$$

where $\boldsymbol{e}_R$ is the radial unit vector. The macroscopic linear thermoelastic constitutive equation takes the form

$$\boldsymbol{\Sigma}(R,t)=\left(\bar{K}-\frac{2}{3}\bar{\mu}\right)\Big(\boldsymbol{I}:\boldsymbol{E}(R,t)\Big)\,\mathbf{I}+2\bar{\mu}\boldsymbol{E}(R,t)-3\bar{K}\bar{\alpha}\Delta\bar{T}(R,t)\mathbf{I}, \tag{7.12}$$

where $\Delta\bar{T}(R,t)=\bar{T}(R,t)-\bar{T}_0$ with $\bar{T}_0$ being the reference temperature. The macroscopic linear strain tensor is defined as

$$\boldsymbol{E}(R,t)=\frac{1}{2}\left\{\boldsymbol{\nabla}\boldsymbol{u}(R,t)+(\boldsymbol{\nabla}\boldsymbol{u}(R,t))^T\right\}, \tag{7.13}$$

with $\boldsymbol{u}(R,t)$ being the displacement vector. Combining Eq. (7.10), Eq. (7.12), and Eq. (7.13) into a single ordinary differential equation we obtain

$$\frac{\partial}{\partial R}\left\{\frac{1}{R^2}\frac{\partial}{\partial R}\left[R^2\boldsymbol{e}_R\cdot\boldsymbol{u}(R,t)\right]\right\}=\bar{\alpha}\frac{1+\bar{\nu}}{1-\bar{\nu}}\frac{\partial\bar{T}(R,t)}{\partial R}, \tag{7.14}$$

with $\bar{\nu}=\frac{3\bar{K}-2\bar{\mu}}{6\bar{K}+2\bar{\mu}}$ being the macroscopic Poisson ratio. Eq. (7.14) has a general solution of

$$\boldsymbol{e}_R\cdot\boldsymbol{u}(R,t)=\bar{\alpha}\frac{1+\bar{\nu}}{1-\bar{\nu}}\frac{\int_0^R\bar{T}(R,t)R^2dR}{R^2}+C_1(t)R+\frac{C_2(t)}{R^2}, \tag{7.15}$$

and is the only nonzero component of the displacement vector $\boldsymbol{u}(R,t)$. Applying the boundary conditions Eq. (7.11) to Eq. (7.15) the constants are obtained as

$$C_1(t)=\bar{\alpha}\frac{4\bar{\mu}^*}{3\bar{K}}\frac{\int_0^{R_o}\bar{T}(R,t)R^2dR}{R_o^3}\qquad\text{and}\qquad C_2(t)=0, \tag{7.16}$$

where $\bar{\mu}^*=\frac{1+\bar{\nu}}{1-\bar{\nu}}\mu$. The nonzero components of the stress tensor are the radial stress

$$\Sigma_{RR}(R,t)=4\bar{\alpha}\bar{\mu}^*\left\{\frac{\int_0^{R_o}\bar{T}(R,t)R^2dR}{R_o^3}-\frac{\int_0^R\bar{T}(R,t)R^2dR}{R^3}\right\}, \tag{7.17}$$

and the two hoop stresses

$$\Sigma_{\Theta\Theta}(R,t)=2\bar{\alpha}\bar{\mu}^*\left\{\frac{\int_0^{R_o}2\bar{T}(R,t)R^2dR}{R_o^3}+\frac{\int_0^R\bar{T}(R,t)R^2dR}{R^3}-\bar{T}(R,t)\right\}, \tag{7.18}$$

with $\Sigma_{\Phi\Phi}(R,t)=\Sigma_{\Theta\Theta}(R,t)$. Substituting the transient temperature field Eq. (7.5), derived in subsubsection 7.3.2.1, into Eq. (7.17) and Eq. (7.18) to obtain the particular radial stress field, i.e.

$$\Sigma_{RR}(R,t)=4\bar{\alpha}\bar{\mu}^*\sum_{j=1}^{\infty}g_j^R(R)f_j(t), \tag{7.19}$$

where $g_j^R(R)$ is defined as

$$g_j^R(R) = \frac{(-1)^{j+1}}{j\pi} + \frac{\cos\left(\frac{j\pi R}{R_o}\right)}{j\pi R^2/R_o^2} - \frac{\sin\left(\frac{j\pi R}{R_o}\right)}{j^2\pi^2 R^3/R_o^3}. \tag{7.20}$$

The particular hoop stress field is expressed as

$$\Sigma_{\Theta\Theta}(R,t) = 2\bar{\alpha}\bar{\mu}^* \sum_{j=1}^{\infty} g_j^{\Theta}(R) f_j(t), \tag{7.21}$$

where $g_j^{\Theta}(R)$ is defined as

$$g_j^{\Theta}(R) = 2\frac{(-1)^{j+1}}{j\pi} - \frac{\sin\left(\frac{j\pi R}{R_o}\right)}{R/R_o} - \frac{\cos\left(\frac{j\pi R}{R_o}\right)}{j\pi R^2/R_o^2} + \frac{\sin\left(\frac{j\pi R}{R_o}\right)}{j^2\pi^2 R^3/R_o^3}. \tag{7.22}$$

7.3.2.3 Microscale thermoelastic stress field

In general, additional microscale stresses in excess of the macroscale stresses are generated by both the heterogeneous microstructure, i.e., $\alpha_i \neq \alpha_m$, as well as microscale gradients in the microscale temperature field, i.e., $\boldsymbol{\nabla}_{\boldsymbol{y}} T(\boldsymbol{x};\boldsymbol{y},t)$. For simplicity, we assume that the microscale temperature field is equal to the macroscopic temperature field at a particular macroscale location, i.e. $T(\boldsymbol{x};\boldsymbol{y},t) = \bar{T}(\boldsymbol{x},t)$, thus neglecting any microscopic gradients in the microscopic temperature field.

Let the spherical inclusions of radii r_c be located on a cubic lattice with lattice parameter 2ℓ (see Fig. 7.11). The microscopic stress tensor associated with the thermal mismatch, $\boldsymbol{\sigma}^{TM}$, is defined such that $\boldsymbol{\sigma}(\boldsymbol{x};\boldsymbol{y},t) = \boldsymbol{\Sigma}(\boldsymbol{x},t) + \boldsymbol{\sigma}^{TM}(\boldsymbol{x};\boldsymbol{y},t)$ and is calculated through a self-consistent, two-phase composite spheres approach. The method approximates the periodic array of spherical inclusions as a two-phase spherical assemblage with appropriate boundary conditions [179]. This approach approximates

the stress field interactions between inclusions [179]. The thermoelastic constitutive relations for both the inner solid sphere and outer spherical shell are expressed as:

$$\boldsymbol{\sigma}^{TM} = \begin{cases} \left(K_i - \frac{2}{3}\mu_i\right)\left(\boldsymbol{I} : \boldsymbol{\varepsilon}^{TM}\right)\mathbf{I} + 2\mu_i\boldsymbol{\varepsilon}^{TM} - 3K_i\alpha_i\Delta\bar{T}\,\mathbf{I} & 0 \leq ||\boldsymbol{y}|| \leq r_c \\ \left(K_m - \frac{2}{3}\mu_m\right)\left(\boldsymbol{I} : \boldsymbol{\varepsilon}^{TM}\right)\mathbf{I} + 2\mu_m\boldsymbol{\varepsilon}^{TM} - 3K_m\alpha_m\Delta\bar{T}\,\mathbf{I} & r_c < ||\boldsymbol{y}|| \leq \ell, \end{cases} \tag{7.23}$$

using tensorial notation and where $\boldsymbol{\varepsilon}^{TM}$ is the total microscopic linear strain associated with the thermal mismatch.

The microscopic equilibrium equation yields the following solution for the microscopic hoop stresses associated with thermal mismatch:

$$\sigma_{\theta\theta}^{TM}(\boldsymbol{x};\boldsymbol{y},t) = K^*\Delta\alpha\Delta\bar{T}(\boldsymbol{x},t)\begin{cases} r_c^3\ell^{-3} - 1 & 0 \leq ||\boldsymbol{y}|| \leq r_c \\ \frac{1}{2}r_c^3||\boldsymbol{y}||^{-3} + r_c^3\ell^{-3} & r_c < ||\boldsymbol{y}|| \leq \ell, \end{cases} \tag{7.24}$$

where $\Delta\alpha = \alpha_i - \alpha_m$, $\Delta\bar{T}(\boldsymbol{x},t) = \bar{T}(\boldsymbol{x},t) - \bar{T}_0$, and K^* is defined as:

$$K^* = \frac{12\mu_m K_i K_m}{3K_iK_m + 4\mu_m K_m + 4\mu_m(K_i - K_m)r_c^3\ell^{-3}}. \tag{7.25}$$

7.3.3 Thermal fatigue crack growth kinetics

Returning to the body shown in Fig. 7.10, consider now the introduction of a planar crack originating from the surface of this body Fig. 7.11. On the macroscale the crack cuts through the diameter of the rock, and on the microscale the crack is assumed to cut through the array of chondrules.

7.3.3.1 Transient stress intensity factor

In order to perform the fatigue crack propagation analysis it is necessary to obtain an expression for the stress intensity factor $\mathrm{K_I}$ which is dependent on both the loading and the geometry [184]. The stress intensity factor most closely associated with our geometry and loading conditions was obtained by ref. [186] as

$$\mathrm{K_I}(a,t) = \int_0^a d\xi \frac{2\boldsymbol{e}_n^c \cdot \boldsymbol{\sigma}(\xi,t)\boldsymbol{e}_n^c}{\sqrt{2\pi(a-\xi)}} \sum_{i=0}^{3} M_i \left(1-\frac{\xi}{a}\right)^{i/2}, \tag{7.26}$$

where $\boldsymbol{\sigma} = \boldsymbol{\Sigma} + \boldsymbol{\sigma}^{TM}$ is the total microscopic tensorial stress field that would develop along the crack plane if the crack were not present, $\boldsymbol{e}_n^c$ is the unit normal to the crack plane, and M_i are highly nonlinear functions of the ratio of crack length to body diameter that may be found in [186]. The geometric parameters M_i were obtained for a planar crack originating at the surface of an infinitely long cylindrical body. The

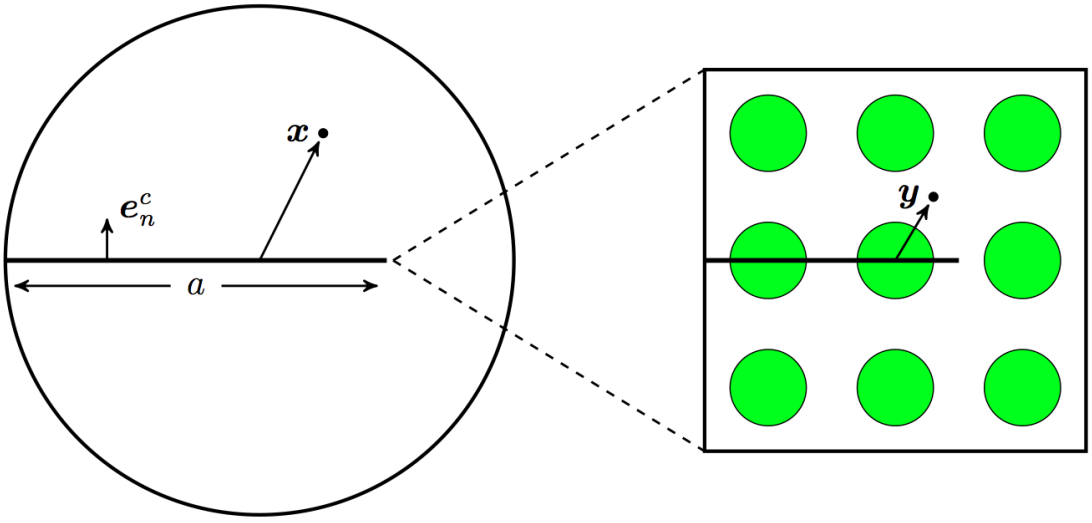

Fig. 7.11: Schematic of the two scale representation (macroscale and microscale) of a general body possessing a planar crack of length a that interacts with the microstructure. The inclusions are positioned on a cubic lattice with spacing of ℓ.

author is unaware of a closed-form expression for the K_I associated with our spherical geometry; however, due to their similarity we assume the geometric parameters M_i for the spherical body should be similar to those of the cylindrical body.

For the spherically symmetric temperature and stress fields, the total microscopic hoop stress $\sigma_{\theta\theta} = \Sigma_{\Theta\Theta} + \sigma_{\theta\theta}^{TM}$ is utilized in Eq. (7.26) to obtain the expression for the transient stress intensity factor that arises from both thermal mismatch, i.e. $\Delta\alpha \neq 0$ and macroscopic temperature gradients, i.e.

$$K_I(a,t) = \int_0^a d\xi \frac{2\sigma_{\theta\theta}(y(|R_o - \xi|), t)}{\sqrt{2\pi(a-\xi)}} \sum_{i=0}^{3} M_i \left(1 - \frac{\xi}{a}\right)^{i/2}, \tag{7.27}$$

where $|R_o - \xi| = R$. Since K_I is linear with respect to the stress it may be decomposed as $K_I = \bar{K}_I + K_I^{TM}$, where $\bar{K}_I$ is the part of the stress intensity factor associated with $\Sigma_{\Theta\Theta}$ and K_I^{TM} is the part associated with $\sigma_{\theta\theta}^{TM}$. Making use of Eq. (7.21), the part of the stress intensity factor associated with $\Sigma_{\Theta\Theta}$ may be expressed as

$$\bar{K}_I(a,t) = 2\bar{\alpha}\bar{\mu}^* \sum_{i=0}^{3}\sum_{j=1}^{\infty} M_i f_j(t) \int_0^a d\xi \frac{g_j^{\Theta}(|R_o - \xi|)}{\sqrt{2\pi(a-\xi)}} \left(1 - \frac{\xi}{a}\right)^{i/2}. \tag{7.28}$$

Making use of Eq. (7.24), the part of the stress intensity factor associated with $\sigma_{\theta\theta}^{TM}$ may be expressed as

$$K_I^{TM}(a,t) = K^* \Delta\alpha \sum_{i=0}^{3}\sum_{k=1}^{\widetilde{k}} M_i \, \Delta\bar{T}(|R_o - \xi_k|, t) \int_{\xi_k - \ell}^{\min(\xi_k+\ell, a)} d\xi \frac{h(|\xi - \xi_k|)}{\sqrt{2\pi(a-\xi)}} \left(1 - \frac{\xi}{a}\right)^{i/2}, \tag{7.29}$$

where $\xi_k = (2k-1)\ell$ are the discrete locations of the centers of the chondrules along the crack plane, $\widetilde{k}$ is defined such that $\xi_{\widetilde{k}} - \ell < a \leq \xi_{\widetilde{k}} + \ell$ and is related to the number

of chondrules along the crack plane, and $h(|\xi - \xi_k|)$ is defined as

$$h(|\xi - \xi_k|) = \begin{cases} \frac{r_c^3}{\ell^3} - 1 & 0 \leq |\xi - \xi_k| \leq r_c \\ \frac{1}{2}\frac{r_c^3}{|\xi - \xi_k|^3} + \frac{r_c^3}{\ell^3} & r_c < |\xi - \xi_k| \leq \ell. \end{cases} \tag{7.30}$$

7.3.4 Numerical methods

The purpose of this section is to discuss the numerical methods utilized to obtain approximate solutions of Eq. (7.3). Unfortunately, there is no analytic solution for the integral in Eq. (7.28), i.e.

$$\bar{\zeta}_{ij}(a) \triangleq \int_0^a d\xi \frac{g_j^\Theta(|R_o - \xi|)}{\sqrt{2\pi(a-\xi)}} \left(1 - \frac{\xi}{a}\right)^{i/2}. \tag{7.31}$$

However, a purely numerical approximation of Eq. (7.31) is problematic because the denominator of the integrand approaches zero, i.e. $\sqrt{2\pi(a-\xi)} \to 0$, as ξ approaches the upper limit of the integral, i.e. $\xi \to a$. This numerical issue may be avoided through a semi-analytic approach. Consider the discretization of $g_j^\Theta(|R_o - \xi|)$ into $\widetilde{m}$ continuous, linear segments

$$g_j^\Theta(|R_o - \xi|) \approx \left(\frac{\Delta g_j^\Theta}{\xi_{m+1} - \xi_m} (\xi - \xi_m) + {}^m g_j^\Theta \right) w(\xi, \xi_m, \xi_{m+1}), \tag{7.32}$$

where $w(\xi, \xi_m, \xi_{m+1}) \triangleq H(\xi - \xi_m) - H(\xi - \xi_{m+1})$ is essentially a top hat function, ${}^m g_j^\Theta = g_j^\Theta(|R_o - \xi_m|)$ are the values of the function at discrete locations ξ_m, and by definition $\Delta g_j^\Theta = {}^{m+1} g_j^\Theta - {}^m g_j^\Theta$, $\xi_{m+1} = \xi_m + a/\widetilde{m}$, and $\xi_0 = 0$. Utilization of Eq. (7.32) in Eq. (7.31) permits a well-behaved semi-analytic approximation expressed as

$$\bar{\zeta}_{ij}(a) \approx \sqrt{\frac{2a}{\pi}} \sum_{m=0}^{\widetilde{m}} \left(\frac{{}^m g_j^\Theta - \widetilde{m}\xi_m \Delta g_j^\Theta / a}{(i+1)} + \frac{2\widetilde{m}\Delta g_j^\Theta}{(i+1)(i+3)} \right). \tag{7.33}$$

The integral in Eq. (7.29) does permit an analytic solution, which is defined as

$$\zeta_{ik}^{\Delta\alpha}(a) = \int_{\xi_k-\ell}^{\min(\xi_k+\ell,a)} d\xi \frac{h(|\xi-\xi_k|)}{\sqrt{2\pi(a-\xi)}} \left(1-\frac{\xi}{a}\right)^{i/2}. \tag{7.34}$$

Due to the excessive length of $\zeta_{ik}^{\Delta\alpha}(a)$, we do not present its closed form; however, the solution is readily obtainable.

In order to make use of the transient stress intensity factor Eq. (7.27) in the solution of Eq. (7.3) it is necessary to obtain the maximum stress intensity factor excursion $\Delta K_I(a)$ experienced over a particular cycle. Since we are dealing with thermal cyclic stress the crack tip experience both tensile and compressive stresses over a full cycle; therefore, ignoring crack closure [187], the lowest stress intensity factor that the crack tip experiences is simply zero. Thus, the maximum stress intensity factor excursion experienced is simply the maximum transient stress intensity factor experienced over a full cycle, i.e.

$$\begin{aligned}\Delta K_I(a) = K_I(a,t_{max}) = 2\bar{\alpha}\bar{\mu}^* \sum_{i=0}^{3}\sum_{j=1}^{\infty} M_i f_j(t_{max})\bar{\zeta}_{ij}(a) + \\ K^*\Delta\alpha \sum_{i=0}^{3}\sum_{k=1}^{\widetilde{k}} M_i\ \Delta\bar{T}(|R_o-\xi_k|, t_{max})\zeta_{ik}^{\Delta\alpha}(a)\end{aligned} \tag{7.35}$$

where t_{max} is defined as the particular time within a cycle at which the maximum stress intensity factor is experienced. t_{max} is obtained by differentiating Eq. (7.27) with respect to time and setting the resultant equal to zero, i.e.

$$\left.\frac{\partial}{\partial t}K_I(a,t)\right|_{t_{max}} = \left.\frac{\partial}{\partial t}\bar{K}_I(a,t)\right|_{t_{max}} + \left.\frac{\partial}{\partial t}K_I^{TM}(a,t)\right|_{t_{max}} = 0. \tag{7.36}$$

Eq. (7.36) may be solved to obtain t_{max} as

$$t_{max}(a) = \eta\frac{P}{2} + \frac{P}{2\pi}\tan^{-1}\left(\frac{\beta_1^{\Delta\alpha}(a) + \bar{\beta}_2(a) + \beta_2^{\Delta\alpha}(a)}{\bar{\beta}_3(a) + \beta_3^{\Delta\alpha}(a)}\right) \qquad \eta = 0, 1, 2, 3, ... \quad (7.37)$$

where $\beta_1^{\Delta\alpha}(a), \bar{\beta}_2(a), \beta_2^{\Delta\alpha}(a), \bar{\beta}_3(a)$, and $\beta_3^{\Delta\alpha}(a)$ are expressed as

$$\begin{aligned}
\beta_1^{\Delta\alpha}(a) &= K^*\Delta\alpha\sum_{i=0}^{3}\sum_{k=1}^{\widetilde{k}}\ \tfrac{1}{2}M_i\zeta_{ik}^{\Delta\alpha}(a)\\
\bar{\beta}_2(a) &= 2\bar{\alpha}\bar{\mu}^*\sum_{i=0}^{3}\sum_{j=1}^{\infty}\frac{(-1)^j M_i}{j\pi}\left(\frac{\bar{\kappa}^2\lambda_j^4}{\omega^2}+1\right)^{-1}\bar{\zeta}_{ij}(a)\\
\beta_2^{\Delta\alpha}(a) &= K^*\Delta\alpha\sum_{i=0}^{3}\sum_{j=1}^{\infty}\sum_{k=1}^{\widetilde{k}}\frac{(-1)^j M_i}{j\pi}\left(\frac{\bar{\kappa}^2\lambda_j^4}{\omega^2}+1\right)^{-1}\frac{R_o}{|R_o-\xi_k|}\sin\left(\lambda_j|R_o-\xi_k|\right)\zeta_{ik}^{\Delta\alpha}(a) \quad (7.38)\\
\bar{\beta}_3(a) &= 2\bar{\alpha}\bar{\mu}^*\sum_{i=0}^{3}\sum_{j=1}^{\infty}\frac{(-1)^j M_i}{j\pi}\left(\frac{\bar{\kappa}\lambda_j^2}{\omega}+\frac{\omega}{\bar{\kappa}\lambda_j^2}\right)^{-1}\bar{\zeta}_{ij}(a)\\
\beta_3^{\Delta\alpha}(a) &= K^*\Delta\alpha\sum_{i=0}^{3}\sum_{j=1}^{\infty}\sum_{k=1}^{\widetilde{k}}\frac{(-1)^j M_i}{j\pi}\left(\frac{\bar{\kappa}\lambda_j^2}{\omega}+\frac{\omega}{\bar{\kappa}\lambda_j^2}\right)^{-1}\frac{R_o}{|R_o-\xi_k|}\sin\left(\lambda_j|R_o-\xi_k|\right)\zeta_{ik}^{\Delta\alpha}(a).
\end{aligned}$$

With t_{max} obtained, the maximum stress intensity factor excursion $\Delta K_I(a)$ experienced over a particular cycle may now be utilized in Eq. (7.3) to obtain the rate of the thermal fatigue crack propagation. The resulting non-linear ordinary differential equation, Eq. (7.3) after substituting in Eq. (7.35), is solved numerically through an adaptive 4th order Runge–Kutta method providing the crack size as a function of the number of thermal cycles.

7.3.5 Modification to account for more general thermal boundary conditions

The microstructurally informed thermal fatigue crack growth model derived throughout this section captures the conditions and physics relevant to our laboratory ex-

periments. However, a more representative transient temperature field associated with boulders on the surface of rotating asteroids may be obtained by relaxing the spherical boundary conditions. We utilized a finite difference method to numerically obtain an approximation of the transient macroscopic temperature field as a function of distance from the asteroid surface. For this effort we utilized the same boundary conditions and finite-difference implementation of [177], but we adopted a higher spatial resolution of 0.025 times the heat penetration depth (see [177]), and the maximum depth is set at 1024 resolution elements. We model a surface area at the equator of a rotating asteroid. We set the initial temperature to 0 K, and allow the temperature field to evolve until the mid-day temperature achieves a steady state (varying by $<$ 0.1 K at mid-day each day on the asteroid). The parameters that control the values of $\bar{T}(\boldsymbol{x}, t)$ are the thermal inertia, Γ, the bolometric albedo, A, and the asteroid rotation period, P. We model two cases whose thermal parameters are taken from [183], i.e. $\Gamma = 640$ J m^{-2} s$^{-0.5}$ K^{-1} and A $= 0.02$ for carbonaceous chondrites with $\Gamma = 1800$ J m^{-2} s$^{-0.5}$ K^{-1} and A $= 0.1$ for ordinary chondrites (see Table 7.1). We set $P = 6$ hours, which is appropriate for small asteroids. The thermal model does not account for the rock boundaries, which increase the porosity of the medium resulting in lower thermal inertia and likely increasing the thermal gradients.

We then utilize a computational procedure to transfer the numerical solution for the temperature field obtained from the finite difference calculations to a commercial finite element code. The maximum tensile stresses (and maximum stress intensity fac-

tor) experienced at an arbitrary location in the body does not necessarily correspond to the times at which the surface temperature achieves a maximum (or minimum). Therefore, the computational procedure requires the transfer of the entire temperature field as a function of time for a full thermal cycle. Once the temperature field is incorporated in the finite element code obtaining the stress field is trivial. However, we are then faced with a substantial computational challenge when it comes to computing the transient stress intensity factor K_I as a function of crack size a.

As this procedure is clearly rather tedious, it is advantageous to obtain an approximate analytic solution of macroscopic stress field that results from the temperature field numerically computed with the finite difference code. With an analytic approximation of the stress field, the stress intensity factor is then readily obtainable through Eq. (7.26). We performed a series of finite element calculations on spherical bodies of radius R_o to obtain such an approximation, which may be expressed as

$$\Sigma_n(\xi,t) \triangleq \boldsymbol{e}_n^c \cdot \boldsymbol{\Sigma}(\xi,t) \cdot \boldsymbol{e}_n^c = \frac{\bar{\alpha}\bar{E}}{1-\bar{\nu}} \int_{-R_o}^{R_o} \left(\frac{\bar{T}(\hat{\xi},t) - \bar{T}(\xi,t)}{6R_o} + \frac{\xi\hat{\xi}}{2R_o^3}\bar{T}(\hat{\xi},t) \right) d\hat{\xi}, \quad (7.39)$$

where $\bar{E} = 9\bar{K}\bar{G}/(3\bar{K}+\bar{G})$ is the effective macroscopic Young's modulus. Eq. (7.39) results in nil stress for constant and linear temperature fields. Fig. 7.12 provides a comparison of Eq. (7.39) with the stress fields obtained from finite element calculations with three different imposed nonlinear temperature fields. The large scale, i.e. $\mathcal{O}(R_o)$, variations in the finite element stress field are in very good agreement with Eq. (7.39). The finite element simulations have additional fine scale, i.e. $<< \mathcal{O}(R_o)$, stress variations. This happens to be an artifact of the finite element simulations

that required the discretization of the temperature field into 26 discrete portions of constant temperature. Considering this point, Eq. (7.39) is deemed a suitable approximation. It is worth noting that Eq. (7.39) is very similar to the analytic solution for the stress field associated with a thin plate subject to a through-thickness temperature distribution, differing only by a factor of 3.

The transient stress intensity factor resulting from these macroscopic thermal gradient stresses may now be expressed analytically as

$$K_I(a,t) = \frac{2\bar{\alpha}\bar{E}}{1-\bar{\nu}} \int_0^a \int_{-R_o}^{R_o} d\hat{\xi} d\xi \frac{\sum_{i=0}^{3} M_i \left(1-\xi/a\right)^{i/2}}{\sqrt{2\pi(a-\xi)}} \left(\frac{\bar{T}(\hat{\xi},t) - \bar{T}(\xi,t)}{6R_o} + \frac{\xi\hat{\xi}}{2R_o^3}\bar{T}(\hat{\xi},t) \right). \tag{7.40}$$

The numerical procedure outlined in subsection 7.3.4 may then be utilized to numerically compute the stress intensity factor (and its maximum value) in a computationally efficient and well-behaved manner. A representative set of maximum stress

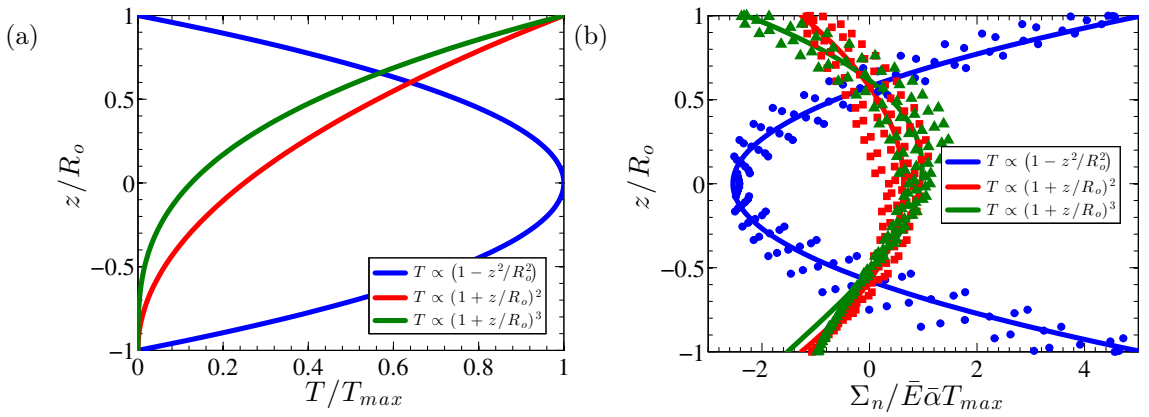

Fig. 7.12: Comparison of finite element simulations with analytic model expressed in Eq. (7.39). (a) Three nonlinear temperature profiles considered resulting in (b) an associated nonlinear macroscopic stress field. Here T_{max} is the maximum temperature in the temperature field.

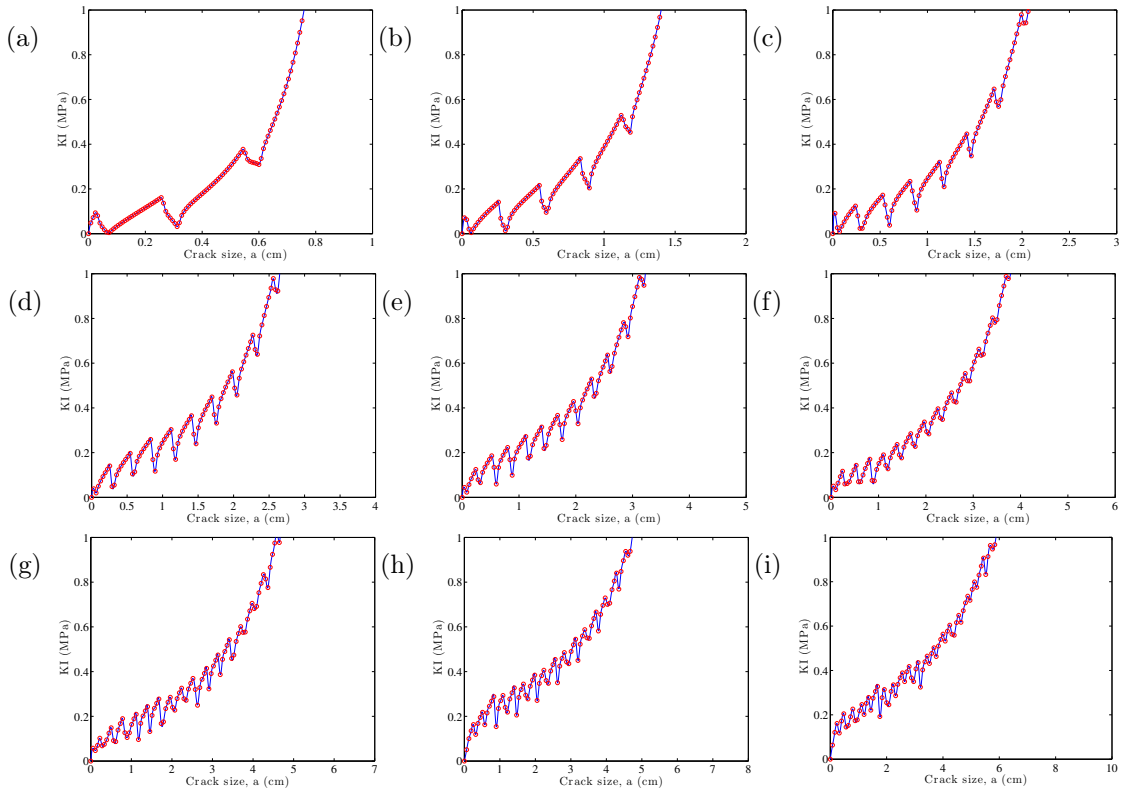

Fig. 7.13: A representative set of maximum stress intensity factors as a function of crack size considering microstructure and thermal gradients.

intensity factors obtained from this numerical procedure are shown in Fig. 7.13, which may then be utilized to compute the fatigue crack growth kinetics via Eq. (7.3).

7.4 Model predictions and implications

First, we compare the crack growth measured in our laboratory experiments with model prediction. We use thermal boundary conditions simulating those of the laboratory experiments: i.e. that the entire surface of a rock of 1 cm in diameter is forced to follow sinusoidal temperature oscillations with ΔT=190 K and a period of

2.2 hours. Considering the idealized nature of the model, the agreement with the experimental measurements is satisfactory (see Fig. 7.14 inset) and indicates that we have captured the essential aspects of thermal fatigue crack growth. Fig. 7.14 also provides a prediction of the number of thermal cycles that would have been required to completely fragment the laboratory rocks. Clearly, these types of extremely long timescales are not amenable to laboratory experiments.

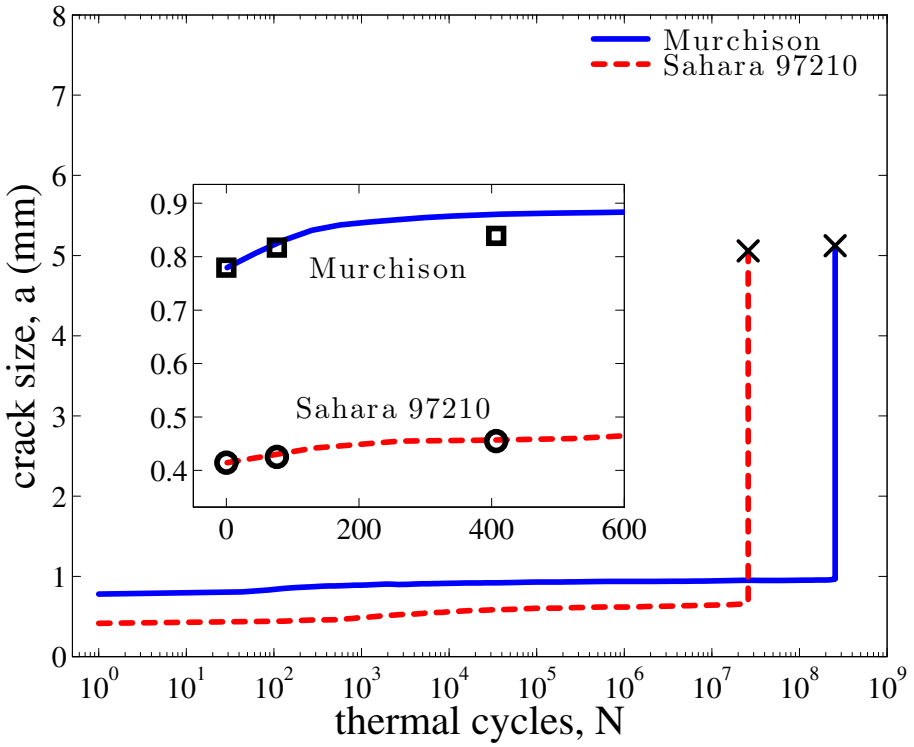

Fig. 7.14: Crack size as a function of the number of temperature cycles predicted by our model and comparison with experimental data for two particular cracks. Main plot: pre-existing cracks of 0.76 mm for Murchison and of 0.41 mm for Sahara 97210 originating at the surface of the samples progressively propagate through the meteorites' diameter. The "X" indicates that the crack has reached a length equal to the meteorite diameter and, therefore, full fragmentation occurs. The figure inset shows the comparison of the model with the length growth measured in our experiments for the same two cracks.

Next, we use the model to provide predictions for the time (number of day/night temperature cycles) required to achieve thermal fragmentation for surface rocks with sizes between 1 and 10 cm (see Fig. 7.1) on C and S-type asteroids at 1 and 2.5 AU from the Sun. Here, the cycle period is taken to be 6 hours, which is more appropriate than 2.2 hours for most small asteroids. Again, the day/night temper-

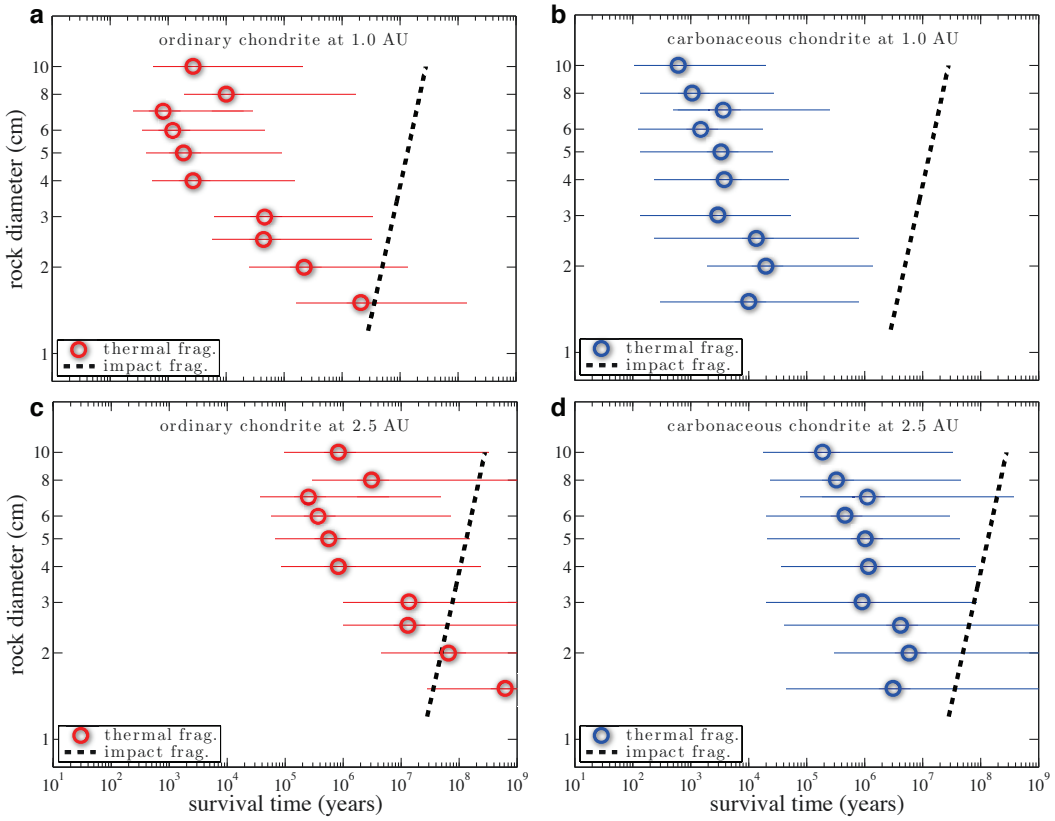

Fig. 7.15: Time required to break rocks on asteroids. Symbols show the time required to thermally fragment 90% of rocks for the nominal values of model parameters. The thick dashed lines show the time at which 90% of these same rocks are broken by micrometeoroid impacts. (a) ordinary chondrite-like asteroid at 1 AU from the Sun; (b) carbonaceous chondrite-like at 1 AU; (c) ordinary chondrite-like at 2.5 AU; and (d) carbonaceous chondrite-like at 2.5 AU. Error bars show the change in the thermal fragmentation time when model parameters are varied within their uncertainties (see subsection 7.4.1).

ature variations, temperature gradients and mechanical stresses are calculated using boundary conditions appropriate for asteroid surfaces radiatively heated by the Sun. We use a conservative definition of rock fragmentation in our model, namely, that an initial 30 μm-long crack grows to a length equal to diameter of the rock. Shorter cracks can still fragment irregular rocks or by merging with other growing cracks.

Our results (see Fig. 7.15) clearly demonstrate that, at 1 AU from the Sun, cm-sized rocks fragment on asteroids at least an order of magnitude faster by thermal fragmentation than by comminution by micrometeoroid impacts, the previously assumed dominant mechanism. We also find (Fig. 7.15) that while larger rocks require more time to fragment by micrometeoroid impact, the trend is reversed for thermal fragmentation. Therefore, thermal fragmentation of a 10 cm rock is predicted to occur orders of magnitude faster than by micrometeoroid impact. Although the speed of thermal fatigue is reduced at larger heliocentric distance (see Fig. 7.3), we still find (Fig. 7.15) that thermal fatigue fragmentation, in general, dominates over the rock breakup by micrometeoroid impacts even in the inner Main Belt and even whether the values of the model parameters are varied within their errors (see Fig. 7.16). As regolith formation by thermal fragmentation does not depend on asteroid size (at least to first order), this process occurs also on larger asteroids (e.g. from several tens to several hundreds of km in size).

Table 7.1: Assumed thermophysical properties.

	Units	CC meteorite	OC meteorite	Ref.
Paris exponent, n		3.84	3.84	[185]
Paris pre-factor, C	$\mathrm{m}\,[\mathrm{MPa}\,\sqrt{\mathrm{m}}]^{-n}$	3×10^{-4}	3×10^{-4}	[185]
Bulk modulus, $\bar{K}$	GPa	29	56	[188, 189]
Chondrule modulus K_i	GPa	113	113	[190]
Shear modulus, $\bar{\mu}$	GPa	18	29	[188, 189]
Bulk CTE, $\bar{\alpha}$	K^{-1}	8.5×10^{-6}	8.5×10^{-6}	[190]
Chondrule CTE, α_i	K^{-1}	10.4×10^{-6}	10.4×10^{-6}	[192]
Thermal conductivity, κ	$\mathrm{W\ m^{-1}\ K^{-1}}$	0.5	1.88	[183]
Heat capacity, C	$\mathrm{J\ kg^{-1}\ K^{-1}}$	500	550	[183]
Bulk density, ρ	$\mathrm{kg\ m^{-3}}$	1662	3150	[183]
Average chondrule radius	mm	0.78	1.16	this work
Average chondrule spacing	mm	1.6	1.4	this work
Thermal inertia, Γ	$\mathrm{J\ m^{-2}\ s^{-0.5}\ K^{-1}}$	640	1800	[183]
Bolometric albedo, A		0.02	0.1	-
Asteroid rotation period, P	hours	6	6	-
Lab cycle period, P	hours	2.2	2.2	-

7.4.1 Uncertainty quantification

Lastly, we outline a procedure for providing some degree of model validation and uncertainty quantification. The chondrule size r_c and spacing ℓ are known with a high degree of accuracy as these are measured from our CT scans. On the other hand, we expect a ∼30% relative uncertainty on the values of the thermophysical parameters since their values were obtained through direct measurement on meteorites [178, 188–192]. We thus calculate our model for several sets of values of the thermophysical parameters that we choose to within 30% of the nominal parameter values and find an order of magnitude change in the predicted number of thermal cycles to achieve rock fragmentation. This implies an order of magnitude change in the survival time of rocks in Fig. 7.15 and, therefore, that thermal fragmentation remains dominant over meteoroid impacts as a regolith generation mechanism.

To the best of the authors' knowledge, no systematic fatigue crack growth experiments have been conducted on asteroid or meteorite materials. Therefore, we took the Paris' law parameters of Carrara's marble [185], which satisfactorily predicts the fatigue crack growth observed in our experiments (inset of Fig. 7.14). Paris' law parameters dramatically different from those of Carrara's marble will result in greater model-experiment discrepancy (Fig. 7.16), which is defined as:

$$\text{Model} - \text{experiment discrepancy} = \left| \frac{a_{model}(N) - a_{exp}(N)}{a_{exp}(N) - a_{exp}(N=0)} \right| \tag{7.41}$$

where a_{model} and a_{exp} are the crack lengths predicted by the model and those mea-

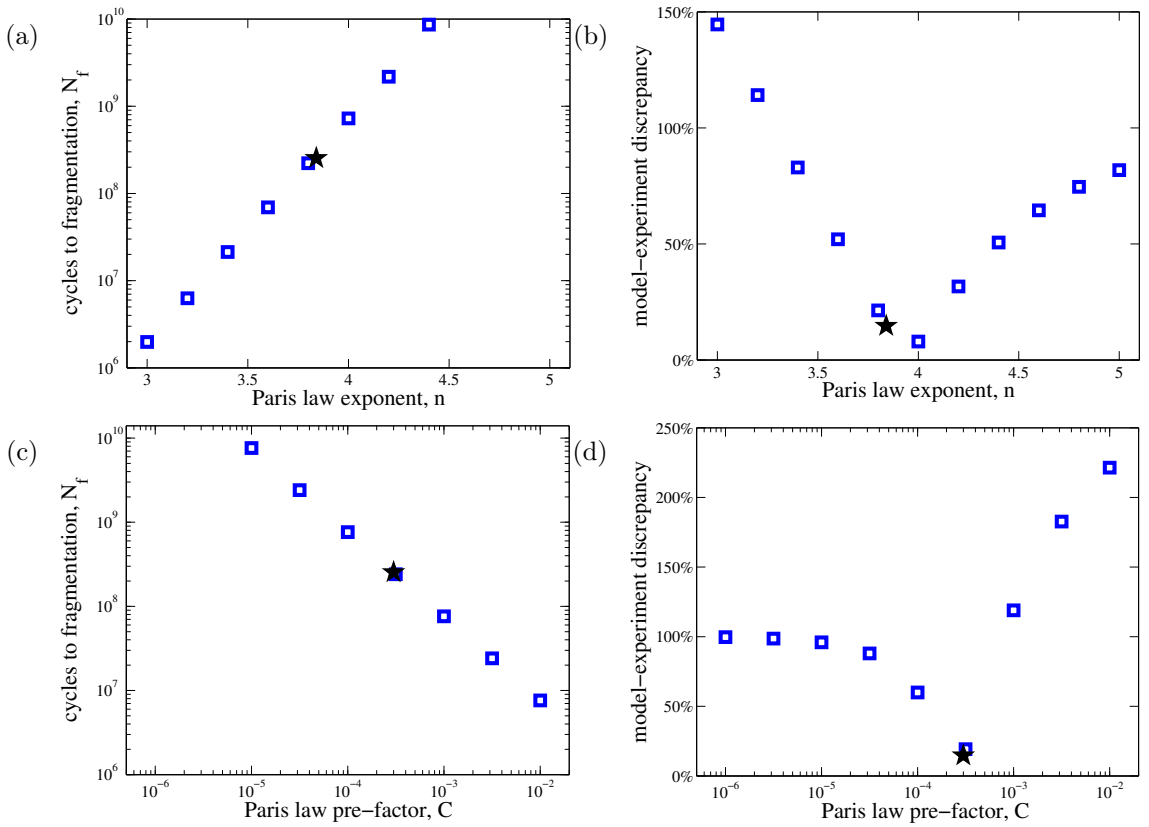

Fig. 7.16: Sensitivity of the model results to Paris' law parameter variations. The stars indicate model results for the nominal value of the parameters given in Table 7.1. (a) Number of temperature cycles until fragmentation for a rock of 1 cm in diameter as a function of the Paris' law exponent n. (b) Discrepancy between the model and the experimental crack growth, defined by Eq. (7.41), as a function of the Paris' law exponent value. (c) Number of cycles until rock fragmentation as a function of the Paris' law factor C. (d) Discrepancy between the model and the experimental crack growth as a function of the Paris' law factor C.

sured from our laboratory experiments, respectively. Even if the Paris' law exponent was 30% larger than the assumed value (Fig. 7.16), then the model would still predict that thermal fragmentation is the dominant regolith generation mechanism over comminution by micrometeroid impact.

7.5 Summary of key findings

We argue that asteroid rock thermal fragmentation has observable implications: by breaking down rocks into smaller pieces and thus exposing new surface area, thermal fragmentation can provide a mechanism to make fresh regolith. Since the process of thermal fragmentation is strongly dependent on the value of ΔT, the rate of thermal fragmentation increases with decreasing perihelion distance (Fig. 7.3). Observations show that the fraction of S-complex NEAs with fresh surfaces (the so-called Q-types) is increasing with decreasing perihelion distance with a dependence [180] that mimics the curves of the NEAs ΔT. From this result, a concrete testable prediction is that more regolith should be found on NEAs that, during their chaotic dynamical evolution, are likely to have spent more time with smaller perihelion distances [181].

We also predict that small NEAs (e.g. 100 m in radius) with low perihelion distances ($q < 0.3$ AU) could be eroded by thermal fragmentation and radiation pressure sweeping [182] in time scales shorter than their dynamical lifetime. For instance, at 0.3 AU the solar radiation pressure can sweep grains of some mm in radius [182]; these grains can be produced by thermal fragmentation of cm-sized rocks in less that $\sim$200 yr. Therefore, low-perihelion NEAs loose roughly 5×10^{-5} m/yr of regolith, implying that the entire object is eroded in about 2 Myr. Since thermal fragmentation is faster for C-type NEAs than for S-type NEAs (see Fig. 7.15), we predict that erosion would be faster for carbonaceous NEAs, providing an explanation for the shortage of low-albedo, carbonaceous Aten type NEAs [170].

Chapter 8

Concluding remarks and future directions

8.1 Concluding remarks

This thesis has covered a range of topics related to the time-dependent failure of materials subject to extreme dynamic environments. Two particular extreme environments were considered, with the vast majority of the work focused on the failure response of metals subject to very high rate deformation ($10^4 - 10^{10}$ s^{-1}). Secondarily, we study the failure response of planetary materials subject to the types of extreme environments experienced in our Solar System. The focus of the thesis has been on the development of multi-scale mechanism-based failure models that are predictive while also shedding light on the most important governing mechanisms in these extreme

environments. Broadly speaking, we find that the most important consideration for the failure response of materials in extreme environments is *the role of a dynamically evolving hierarchy of interacting defects.*

Our first examination of this consideration was with regards to the kinetics of twins in chapter 2. There we made use of molecular dynamics simulations and theory to study the fundamental relationship between twin boundaries and a lower-length scale defect, twinning dislocations, and to some extent a larger-length scale defect, grains. The physical picture painted in Fig. 2.1 illustrates that the mechanism of twin growth occurs through the propagation of twinning dislocations along the twin boundary. These twinning dislocations nucleate at favorable nucleation sites, assumed here to be grain boundaries. The velocity at which the twin boundaries propagate is therefore controlled by a combination of the rate of twinning dislocation emission from the grain boundary and the rate at which these twinning dislocations propagate along the twin boundary.

In chapter 3, we explored this theme further by examining the fundamental relationship between dynamic void growth, discrete dislocation kinetics, and the dynamic evolution of dislocation densities in the vicinity of the void surface. We find that for larger voids ($\gtrsim$ 200 nm) dynamic void growth is limited by the inertial resistance of the accelerating solid material around the growing void. However, for smaller voids ($\lesssim$ 200 nm) the dynamics of the voids are governed entirely by the combination of discrete dislocation kinetics and the dynamic evolution of dislocation densities in the

vicinity of the void surface. The importance of the evolving dislocation density is made clear in Fig. 3.9, which demonstrates the shutdown of void growth at large growth factors ($a/A \sim 10 - 100$) as a result of an exhaustion of the mobile dislocation density. These considerations help to shed light on a few key experimental observations related to the failure of metals at very high rates of deformation.

Chapter 4 provides a discussion of one particular mechanism for replenishing the supply of mobile dislocation density in the vicinity of a dynamically growth void: dislocation emission. This emission-driven replenishment allows voids to continue growing past the shutdown point ($a/A \sim 10-100$). In order to incorporate dislocation emission in our general mechanism-based framework discussed in chapter 6 it was first necessary to extend the state-of-the-art critical criterion for dislocation emission (Lubarda [11]). The three most important extensions include

- ✦ a general three-dimensional macroscopic stress state
- ✦ temperature dependence
- ✦ finite porosity.

These extensions permit the incorporation of the dislocation emission mechanism in the analysis of ductile failure of materials and structures subject to arbitrary loading paths. Towards this aim, it was also necessary to establish a methodology for independently calibrating the model parameters and providing a more proper model validation against molecular dynamics simulations. Having calibrated and validated

the dislocation emission criterion, we utilized the model to explore some anomalous behaviors associated with high surface energies and nonlinear elasticity, including

- ✦ tension-compression asymmetry
- ✦ *smaller is weaker* behavior
- ✦ spontaneous dislocation emission.

Chapter 5 effectively incorporates the key findings of chapter 3 and chapter 4 into a simple multi-scale mechanism-based framework for predicting the spall strength of ductile metals. With this framework in hand, we are able to effectively demonstrate the role of a dynamically evolving hierarchy of defects on dynamic ductile failure. Under the most extreme loading conditions ($\gtrsim 10^7$ s^{-1}) generated in laser shock experiments and related applications, the dynamic failure response is governed by a hierarchy of shock-induced defects on cascading length scales, a complex mechanism that may be summarized as follows

1. A shock wave generates a preponderance of defects and a temperature rise
2. Numerous dislocation intersections generate a large number of jogs
3. Dragging of these jogs produces a superconcentration of vacancies
4. Mobility of vacancies is enhanced by temperature and tensile strains
5. Mobility is further enhanced by *pipe diffusion* through the dislocation network

6. Vacancies cluster together to form *void embryos* of a few nanometers in size

7. Dislocation emission assists the growth of these voids to failure.

Without the consideration of all of these interacting defects, one would likely assume that vacancies are irrelevant in dynamic ductile failure due to the extremely short time scales. Nevertheless, chapter 5 demonstrates the implied importance of vacancy clustering and subsequent dislocation emission on the spall strength of high-purity single crystals as well as polycrystalline FCC metals at extreme tensile loading rates.

Under somewhat less extreme loading conditions ($\lesssim 10^6$ s^{-1}), the dynamic failure response is governed not by the shock-induced microstructure, but rather by the pre-existing material microstructure, e.g. second-phase particles, grain boundaries, triple junctions, etc. Making use of the mechanism-based failure model proposed in chapter 5 we are able to shed some light on a number of traditionally perplexing observations in the literature and provide some predictions that may have technological significance, e.g.

- ✦ an anomalous Hall-Petch (grain size) effect for spall strength
- ✦ a limit to spall strength enhancement through purity level refinement
- ✦ a complex dependence on the shock-induced microstructure
- ✦ a prediction of the *ideal* spall strength of metals

Chapter 5 makes a number of assumptions that lead to a simplified analysis that is very instructional and helps in the development of a general intuition about these

problems. Although these assumptions seem reasonable for the prediction of one-dimensional spall failure, they may not necessarily be valid under more general loading conditions. In chapter 6, we provide an extension of the mechanism-based framework to account for arbitrary three-dimensional loading paths, anisotropic materials or crystals that experience significant hardening, and a more rigorous treatment of the nonequilibrium thermodynamics and inelastic dissipations.

In chapter 7, we turned our attention to a second extreme environment: our Solar System. In particular, we examined the competition between impact processes and thermal processes on the surface evolution of near-Earth asteroids and similar celestial bodies. The problem served as an excellent example of the power of our simple multi-scale mechanism-based approach. We developed a simple and computationally-efficient framework capable of resolving the short timescales associated with nonequilibrium thermal transport, $\mathcal{O}(\text{seconds})$, as well as the extremely long timescales associated with breakup and fragmentation of surface rocks by gradual fatigue crack growth, $\mathcal{O}(10^4 - 10^9 \text{ years})$. In addition to the challenges brought on by the timescales, the problem also involves a number of relevant length scales, including the size and rotation period of the asteroid, the size and geometry of a surface rock, as well as the size and spacing of material heterogeneities. Making use of this simple mechanism-based model, calibrated against laboratory experiments, we were to demonstrate that impact mechanisms are not necessarily the most dominant mechanism of surface evolution on asteroids, as was widely believed in the planetary

science community. Instead, thermal fragmentation seems to play the dominant role on small near-Earth asteroids.

8.2 Future directions

Although the thesis has provided a fairly significant contribution to our understanding of materials in extreme environments through the use of these simple mechanism-based models, the approach does have its limitations. Our simple mechanism-based approach may find its greatest utility in helping to strategically define targeted areas where a higher-fidelity computational or experimental analysis will pay the greatest dividends. A few such areas of interests are briefly outlined below:

Coupled DD-DTEM analysis of dynamic void growth:

The kinetics of defects is one area that stands to greatly benefit from the recent development of the dynamic transmission electron microscope (DTEM), illustrated in Fig. 8.1. As discussed in chapter 3, voids in metals may grow in size by as much as a few orders of magnitude. Such growth demands huge plastic deformation around the growing void, and the dynamics of the void growth are highly sensitive to the dislocation substructure evolution. A focused ion beam (FIB) may be utilized to manufacture sub-micron voids of various sizes in TEM thin films. Subsequently, the thin films may be subjected to a short, pulsed mechanical loading causing the void to

dynamically grow. The DTEM has the time resolution, $\mathcal{O}(\mu s)$, necessary to be able to capture the time-resolved growth of the void as well as the time-resolved evolution and mobility of the dislocation substructure around the growing void.

The beauty of the DTEM is that it probes material response at very small length scales ($\sim 10^1 - 10^3$ nm) with remarkable time resolution, $\mathcal{O}(\mu s)$. These scales directly overlap with the current computational capabilities of discrete defect dynamics simulations. As such, the entire DTEM experiment could be modeled with discrete dislocation dynamics simulations. Together, the experiments and simulations would allow us to construct better dislocation substructure evolution laws than the current state-of-the-art models utilized in chapter 3.

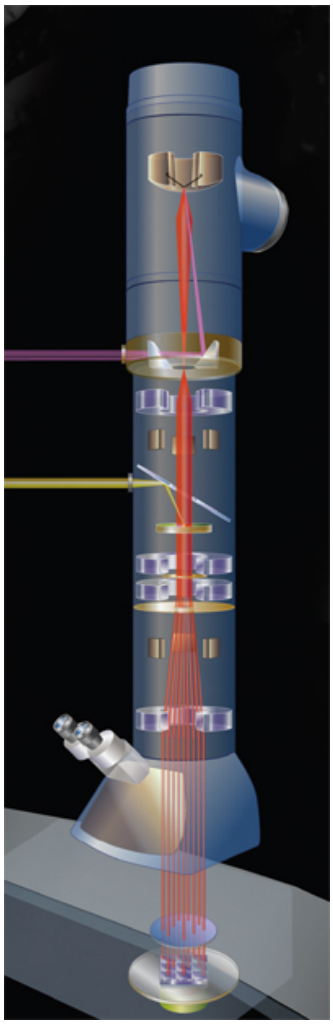

Figure 8.1: Schematic of dynamic transmission electron microscope (DTEM) (image courtesy of Lawrence Livermore National Laboratory).

Utilizing the same set-up it may be possible to provide *in-situ* visualization of dislocation emission from the void surface and its associated kinetics. The primary chal-

lenge here would be fabricating TEM films thin enough such that all pre-existing dislocations may be annealed out of the sample. The result is that the material must nucleate dislocations to mechanically deform, with dislocation emission being favorable over homogeneous nucleation. Characterizing the kinetics of the process would be particularly exciting as some of our preliminary dislocation analysis seems to indicate that the emission kinetics may not necessarily obey the Arrhenius relation as assumed in chapter 5, but rather the rate-limiting step may be related to the time required for dislocations to glide a sufficient distance from the void surface. At a far enough distance from the void surface the previously emitted dislocation no longer strongly interacts with the next dislocation attempting to escape the void surface.

Coupled DD-LKMC simulations of vacancy clustering in shocked metals:

In chapter 4 and chapter 5 we have assumed that vacancy clustering operates on timescales short enough to be relevant to dynamic ductile failure. However, we made little attempt to rigorously investigate the kinetics of this process. The kinetics were, however, probed by Reina et al. [69], who made use of the Lattice Kinetic Monte Carlo (LKMC) method to study the kinetics of vacancy clustering in an otherwise perfect crystal, see for example Fig. 8.2(a). Their predicted kinetics were too slow to be operative in dynamic ductile failure (other than at temperatures very near melt). Nevertheless, the mechanism may still be feasible when one considers *pipe diffusion* which allows vacancies to zip along dislocation cores orders of magnitude faster than

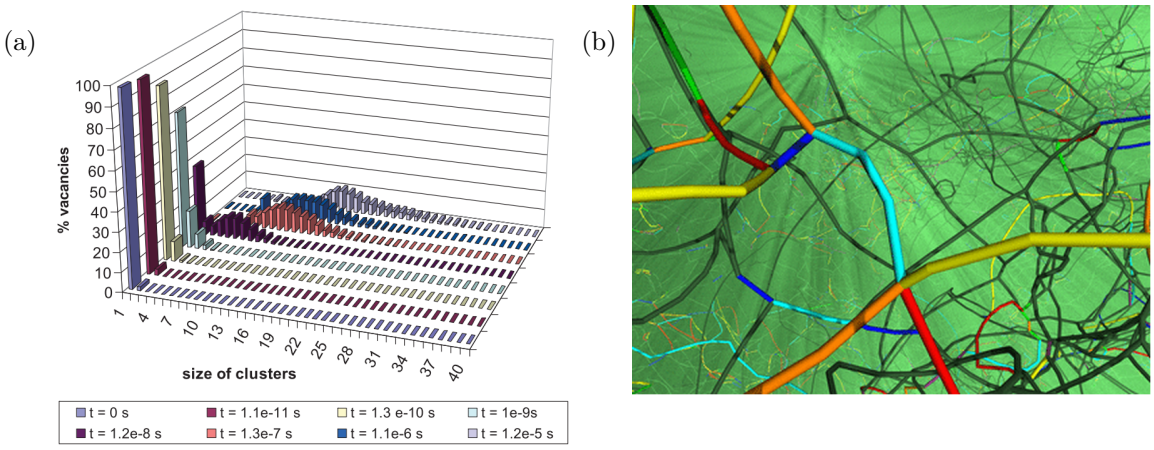

Figure 8.2: Example computations of (a) vacancy clustering kinetics in an otherwise perfect crystal predicted by Lattice Kinetic Monte Carlo (LKMC) simulations Reina et al. [69] and (b) dislocation substructure formation predicted by ParaDiS (courtesy of Lawrence Livermore National Laboratory).

through the perfect lattice. Since shocked metals possess many dislocations, one would assume that *pipe diffusion* would significantly accelerate the process of vacancy clustering. Fortunately, incorporating the effects of *pipe diffusion* in the analysis of vacancy clustering is fairly straightforward. One strategy involves first utilizing a dislocation dynamics (DD) code, e.g. ParaDiS, to generate a three-dimensional dislocation network representative of that found in shock materials, see for example Fig. 8.2(b). Next, the dislocation line segments may be extracted from the DD code and be incorporated in the LKMC simulations as a *network of enhanced mobility*. Vacancies will be allowed to move orders of magnitude faster along this network. With this tool in hand we would then be able to more realistically capture the kinetics of vacancy clustering, allowing us to better understand the role of this mechanism in ductile failure. Additionally, the coupled DD-LKMC simulations may be utilized in

providing a better understanding of the fundamental processes associated with creep failure and radiation damage in metals.

Mesoscale implementation of mechanism-based framework:

In chapters 5, 6, and 7 we emphasized the importance of microstructure in the failure of materials in extreme environments. However, our simple analyses misses some of the fine-scale details, particularly with respect to the complex stress fields that develop around material heterogeneities. The relevance of these stress concentrations may be better understood through a computational mesoscale implementation of our mechanism-based framework. Such an implementation would be able to resolve these fine scale details that are often critical to the failure process, see for example Fig. 8.3(a), and is particularly powerful when coupled with Digital Image Correlation

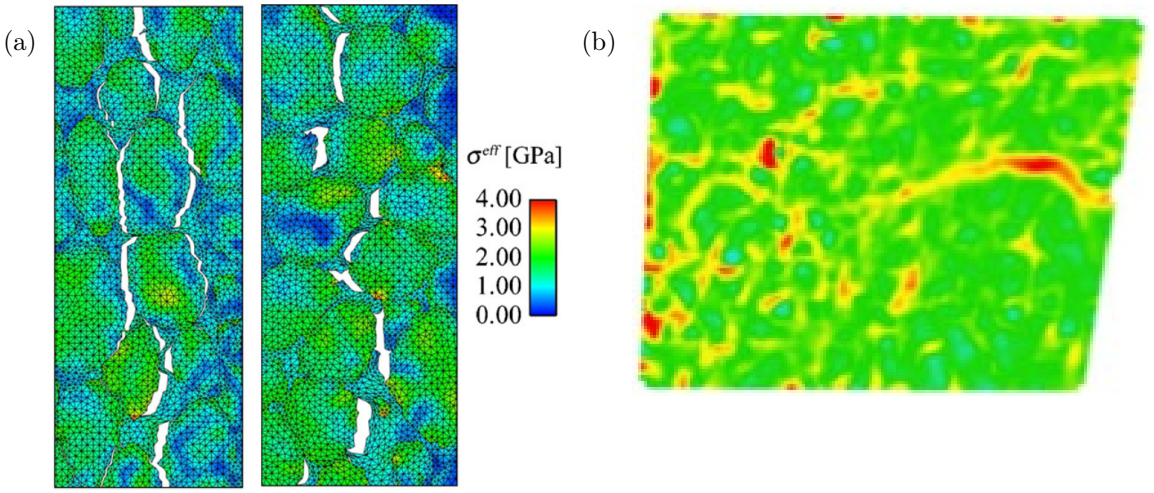

Figure 8.3: (a) Example of a mesoscale calculation demonstrating the microstructural dependence of a spall crack in a tungsten alloy [193] and (b) Digital Image Correlation (DIC) strain map of thermal crack propagation (from right to left) through a heterogeneous meteorite sample (collaborative work with Kavan Hazeli).

(DIC) experiments as shown in Fig. 8.3(b).

Chapter 6 has provided a thermodynamically-consistent framework for dynamic ductile failure of FCC crystals that is very amenable to a crystal plasticity implementation. Such an implementation would allow us to examine some aspects of grain boundary engineering for improved spall strength and dynamic ductility of polycrystalline metals. The framework would also be particularly valuable to the analysis of materials and structures that experience stresses high enough to activate dislocation emission. Consider, for example, the analysis of a ductile crack propagating through a single crystal nanostructure, e.g. a nanopiller. If the nanostructure is small enough than it may be possible to anneal out all the dislocations. In this case, the ductile crack growth may be governed by vacancy clustering and dislocation emission in the process zone ahead of the crack tip.

Bibliography

[1] National Academy of Engineering. Grand challenges for engineering, 2008. URL http://www.engineeringchallenges.org.

[2] J. Wadsworth, G.W. Crabtree, and eds. Hemley, R.J. Basic research needs for materials under extreme environments: Report of the basic energy sciences workshop on materials under extreme environments. Technical report, US Department of Energy, Office of Basic Energy Sciences, June 11-13, 2007 2008.

[3] Bevan M French. Traces of catastrophe: A handbook of shock-metamorphic effects in terrestrial meteorite impact structures. *Technical Report, LPI-Contrib-954*, 1, 1998.

[4] Wai Chan and Keith Taylor. Ultrahigh-speed imaging: Taking the hype out of hypervelocity, 2010. URL http://www.laserfocusworld.com/articles/2010/06/ultrahigh-speed-imaging.html.

[5] Marc A Meyers. *Dynamic behavior of materials*. John Wiley & Sons, 1994.

[6] European Space Agency (ESA). Hypervelocity impacts and protecting spacecraft, 2013. URL http://www.esa.int/Our_Activities/Operations/Space_Debris/Hypervelocity_impacts_and_protecting_spacecraft.

[7] John D Morrow and Ronald E Musante. Active spall suppression armor, June 19 1990. US Patent 4,934,245.

[8] William Walters. Introduction to shaped charges. Technical report, DTIC Document, 2007.

[9] Franz Roters, Philip Eisenlohr, Thomas R Bieler, and Dierk Raabe. *Crystal Plasticity Finite Element Methods: In Materials Science and Engineering*. John Wiley & Sons, 2010.

[10] Ryan A Austin and David L McDowell. A dislocation-based constitutive model for viscoplastic deformation of fcc metals at very high strain rates. *International Journal of Plasticity*, 27(1):1–24, 2011.

[11] Vlado A Lubarda. Emission of dislocations from nanovoids under combined loading. *International Journal of Plasticity*, 27(2):181–200, 2011.

[12] NP Daphalapurkar, JW Wilkerson, TW Wright, and KT Ramesh. Kinetics of a fast moving twin boundary in nickel. *Acta Materialia*, 68:82–92, 2014.

[13] John P Hirth and Jens Lothe. *Theory of dislocations*. John Wiley and Sons, 1982.

[14] M. Chen, E. Ma, K.J. Hemker, H. Sheng, Y. Wang, and X. Cheng. Deformation twinning in nanocrystalline aluminum. *Science*, 300:1275–1277, 2003.

[15] YT Zhu, XZ Liao, and XL Wu. Deformation twinning in nanocrystalline materials. *Prog. Mater. Sci.*, 57(1):1–62, 2012.

[16] Y.M. Wang, A.M. Hodge, J. Biener, A.V. Hamza, D.E. Barnes, K. Liu, and T.G. Nieh. Deformation twinning during nanoindentation of nanocrystalline Ta. *Appl. Phys. Lett.*, 86(10):101915, 2005. doi: 10.1063/1.1883335.

[17] J.W. Christian and S. Mahajan. Deformation twinning. *Prog. Mater. Sci.*, 39 (1-2):1–157, 1995.

[18] D.R. Chichili, K.T. Ramesh, and K.J. Hemker. The high-strain-rate response of alpha-titanium: Experiments, deformation mechanisms and modeling. *Acta Mater.*, 46(3):1025–1043, 1998. doi: 10.1016/S1359-6454(97)00287-5.

[19] L.E. Murr, M.A. Meyers, C.-S. Niou, Y.J. Chen, S. Pappu, and C. Kennedy. Shock-induced deformation twinning in tantalum. *Acta Mater.*, 45(1):157–175, 1997.

[20] T Zhu and H Gao. Plastic deformation mechanism in nanotwinned metals: An insight from molecular dynamics and mechanistic modeling. *Scripta Mater.*, 66: 843–848, 2012.

[21] E Faran and D Shilo. Implications of twinning kinetics on the frequency response in NiMnGa actuators. *Appl. Phys. Lett.*, 100(151901):1–4, 2012.

[22] J.D Clayton. *Mechanical Twinning in Crystal Plasticity, In Nonlinear Mechanics of Crystals.* Springer Netherlands, 2011.

[23] E.V. Esquivel, L.E. Murr, M. Trillo, and M. Baquera. Comparison of microstructures for plane shock-loaded and impact crater-related nickel: the microtwin-microband transition. *J Mater. Sci.*, 38:2223–2231, 2003.

[24] YB Wang, ML Sui, and E Ma. In situ observation of twin boundary migration in copper with nanoscale twins during tensile deformation. *Phil. Mag. Lett.*, 87 (12):935–942, 2007.

[25] D.L. Olmstead, L.G.Jr. Hector, W.A. Curtin, and R.J. Clifton. Atomistic simulations of dislocation mobility in Al, Ni and Al/Mg alloys. *Mod. Simul. Mater. Sci. Engng.*, 13:371–388, 2005.

[26] H. Tsuzuki, P.S. Branicio, and J.P. Rino. Molecular dynamics simulation of fast dislocations in copper. *Acta Mater.*, 57:1843–1855, 2009.

[27] Q. Hu, L. Li, and N.M. Ghoniem. Stick-slip dynamics of coherent twin boundaries in copper. *Acta Mater.*, 57(16):4866–4873, 2009.

[28] R. Abeyaratne and S. Vedantam. A lattice-based model of the kinetics of twin boundary motion. *J. Mech. Phys. Sol.*, 51:1675–1700, 2003.

[29] E Faran and D Shilo. The kinetic relation for twin wall motion in NiMnGa. *J Mech. Phys. Sol.*, 59(5):975–987, 2011.

[30] F. Hildebrand and R. Abeyaratne. An atomistic investigation of the kinetics of detwinning. *J. Mech. Phys. Sol.*, 56:1296–1319, 2008.

[31] S. Plimpton. Fast parallel algorithms for short-range molecular dynamics. *J. Comput. Phys.*, 117:1–19, 1995.

[32] Y. Mishin, D. Farkas, M.J. Mehl, and D.A. Papaconstantopoulos. Interatomic potentials for monoatomic metals from experimental data and ab initio calculations. *Phys. Rev. B*, 59(5):3393–3407, 1999.

[33] C.A. Becker, F. Tavazza, and L.E. Levine. Implications of the choice of interatomic potential on calculated planar faults and surface properties in nickel. *Phil. Mag.*, 91(27):3578–3597, 1999.

[34] A. Serra and D.J. Bacon. Modeling the motion of {11-22} twinning dislocation in the hcp metals. *Mat. Sc. Engng. A*, 400-401:496–498, 2005.

[35] J.D. Honeycutt and H.C. Andersen. Molecular dynamics study of melting and freezing of small lennard-jones clusters. *J. Phys. Chem*, 91(19):4950–4963, 1987.

[36] R.J.E. Clausius. On a mechanical theorem applicable to heat. *Phil. Mag.*, 40: 122–127, 1870.

[37] J.C. Maxwell. Van der waals on the continuity of the gaseous and liquid states. *Nature*, 10:477–480, 1974.

[38] N.P. Daphalapurkar and K.T. Ramesh. Orientation dependence of the nucleation and growth of partial dislocations and possible twinning mechanisms in aluminum. *J Mech. Phys. Sol.*, 60:277–294, 2012.

[39] A. Vainchtein. The role of spinodal region in the kinetics of lattice phase transitions. *J. Mech. Phys. Sol.*, 58:227–240, 2010.

[40] J. Mielnicki. Elastic waves in (100),(110), and (111) planes of cubic crystals. *IEEE Trans. Sonics and Ultrasonics*, 19(1):15–18, 1972.

[41] C. Liu, Y. Huang, and A.J. Rosakis. Shear dominated transonic interfacial crack growth in a bimaterial–ii. asymptotic fields and favorable velocity regimes. *J Mech Phys Solids*, 43(2):189–206, 1995.

[42] J. Weertman. Uniformly moving transonic and supersonic dislocations. *J Appl. Phys.*, 38:5293–5301, 1967.

[43] J. Weertman. Subsonic type earthquake dislocation moving at approximately $\sqrt{2}\times$shear wave velocity on interface between half spaces of slightly different elastic constants. *Geophys. Res. Lett.*, 29(10):1–4, 2002.

[44] V.I. Alshits. *The phonon-dislocation interaction and its role in dislocation drag-*

ging and thermal resistivity, In Elastic Strain Fields and Dislocation Mobility, ed. V.L. Indenbom and J. Lothe. Elsevier Science, Amsterdam, 1992.

[45] G. Leibfried. Uber den einfluss thermisch angeregter schallwellen auf die plastische deformation. *Zeitschrift fur Physik*, 127(4):344–356, 1950.

[46] E. Bitzek and P. Gumbsch. Dynamic aspects of dislocation motion:atomistic simulations. *Materials Science and Engineering A*, 400-401:40–44, 2005.

[47] R.J. Clifton. On the analysis of elastic/visco-plastic waves of finite uniaxial strain. *In Shock Waves and the Mechanical Properties of Solids. Ed. Burke, J.J., Weiss, V., Syracuse University Press, Syracuse, NY*, pages 73–116, 1970.

[48] J.D. Clayton. A continuum description of nonlinear elasticity, slip and twinning, with application to sapphire. *Proc R Soc A*, 465(2101):307–334, 2009.

[49] Ryan A Austin and David L McDowell. Parameterization of a rate-dependent model of shock-induced plasticity for copper, nickel, and aluminum. *International Journal of Plasticity*, 32:134–154, 2012.

[50] JW Wilkerson and KT Ramesh. A dynamic void growth model governed by dislocation kinetics. *Journal of the Mechanics and Physics of Solids*, 2014.

[51] NR Barton, JV Bernier, R Becker, A Arsenlis, R Cavallo, J Marian, M Rhee, H-S Park, BA Remington, and RT Olson. A multiscale strength model for

extreme loading conditions. *Journal of applied physics*, 109(7):073501–073501, 2011.

[52] Frank A McClintock. A criterion for ductile fracture by the growth of holes. *Journal of Applied Mechanics*, 35:363, 1968.

[53] J R Rice and Dennis Michael Tracey. On the ductile enlargement of voids in triaxial stress fields*. *Journal of the Mechanics and Physics of Solids*, 17(3): 201–217, 1969.

[54] DR Curran, L Seaman, and DA Shockey. Dynamic failure of solids. *Physics reports*, 147(5):253–388, 1987.

[55] Ben Freund. *Dynamic Fracture*. Cambridge University Press, New York, 1990.

[56] Viggo Tvergaard. Material failure by void growth to coalescence. *Advances in applied Mechanics*, 27(1):83–151, 1990.

[57] RF Bishop, Rodney Hill, and NF Mott. The theory of indentation and hardness tests. *Proceedings of the Physical Society*, 57(3):147, 1945.

[58] Rodney Hill. *The mathematical theory of plasticity*, volume 11. Oxford university press, 1950.

[59] John M Ball. Discontinuous equilibrium solutions and cavitation in nonlinear elasticity. *Philosophical Transactions of the Royal Society of London. Series A, Mathematical and Physical Sciences*, pages 557–611, 1982.

[60] Y Huang, JW Hutchinson, and V Tvergaard. Cavitation instabilities in elastic-plastic solids. *Journal of the Mechanics and Physics of Solids*, 39(2):223–241, 1991.

[61] X.Y. Wu. *The dynamic growth of voids in viscoplastic materials*. PhD thesis, The Johns Hopkins University, Baltimore, MD, 2002.

[62] J Belak. On the nucleation and growth of voids at high strain-rates. *Journal of computer-aided materials design*, 5(2-3):193–206, 1998.

[63] Robert E Rudd and James F Belak. Void nucleation and associated plasticity in dynamic fracture of polycrystalline copper: an atomistic simulation. *Computational materials science*, 24(1):148–153, 2002.

[64] Eduardo M Bringa, Sirirat Traiviratana, and Marc A Meyers. Void initiation in fcc metals: Effect of loading orientation and nanocrystalline effects. *Acta Materialia*, 58(13):4458–4477, 2010.

[65] VA Lubarda, MS Schneider, DH Kalantar, BA Remington, and MA Meyers. Void growth by dislocation emission. *Acta Materialia*, 52(6):1397–1408, 2004.

[66] ET Seppälä, J Belak, and RE Rudd. Effect of stress triaxiality on void growth in dynamic fracture of metals: A molecular dynamics study. *Physical Review B*, 69(13):134101, 2004.

[67] Sirirat Traiviratana, Eduardo M Bringa, David J Benson, and Marc A Meyers.

Void growth in metals: atomistic calculations. *Acta Materialia*, 56(15):3874–3886, 2008.

[68] Marc A Meyers, Sirirat Traiviratana, VA Lubarda, David J Benson, and Eduardo M Bringa. The role of dislocations in the growth of nanosized voids in ductile failure of metals. *Jom*, 61(2):35–41, 2009.

[69] C Reina, J Marian, and M Ortiz. Nanovoid nucleation by vacancy aggregation and vacancy-cluster coarsening in high-purity metallic single crystals. *Physical Review B*, 84(10):104117, 2011.

[70] MP Ariza, I Romero, M Ponga, and M Ortiz. Hotqc simulation of nanovoid growth under tension in copper. *International journal of fracture*, 174(1):75–85, 2012.

[71] G Le Roy, JD Embury, G Edwards, and MF Ashby. A model of ductile fracture based on the nucleation and growth of voids. *Acta Metallurgica*, 29(8):1509–1522, 1981.

[72] A Needleman. A continuum model for void nucleation by inclusion debonding. *Journal of applied mechanics*, 54(3):525–531, 1987.

[73] TC Lindley, G Oates, and CE Richards. A critical of carbide cracking mechanisms in ferride/carbide aggregates. *Acta Metallurgica*, 18(11):1127–1136, 1970.

[74] AS Argon, J Im, and R Safoglu. Cavity formation from inclusions in ductile fracture. *Metallurgical Transactions A*, 6(4):825–837, 1975.

[75] FM Beremin. Cavity formation from inclusions in ductile fracture of a508 steel. *Metallurgical Transactions A*, 12(5):723–731, 1981.

[76] AA Benzerga, Jacques Besson, and André Pineau. Anisotropic ductile fracture: Part i: experiments. *Acta Materialia*, 52(15):4623–4638, 2004.

[77] Arthur L Gurson. Continuum theory of ductile rupture by void nucleation and growth. part i. yield criteria and flow rules for porous ductile media. Technical report, Brown Univ., Providence, RI (USA). Div. of Engineering, 1975.

[78] Viggo Tvergaard and Alan Needleman. Analysis of the cup-cone fracture in a round tensile bar. *Acta Metallurgica*, 32(1):157–169, 1984.

[79] B Budiansky, JW Hutchinson, and S Slutsky. Void growth and collapse in viscous solids. *Mechanics of solids*, pages 13–45, 1982.

[80] Siavouche Nemat-Nasser and Muneo Hori. Void collapse and void growth in crystalline solids. *Journal of applied physics*, 62(7):2746–2757, 1987.

[81] M Haghi and L Anand. Analysis of strain-hardening viscoplastic thick-walled sphere and cylinder under external pressure. *International Journal of Plasticity*, 7(3):123–140, 1991.

[82] JK Knowles and MT Jakub. Finite dynamic deformations of an incompressible elastic medium containing a spherical cavity. *Archive for Rational Mechanics and Analysis*, 18(5):367–378, 1965.

[83] MM Carroll and AC Holt. Static and dynamic pore-collapse relations for ductile porous materials. *Journal of Applied Physics*, 43(4):1626–1636, 1972.

[84] Jo N Johnson. Dynamic fracture and spallation in ductile solids. *Journal of Applied Physics*, 52(4):2812–2825, 1981.

[85] Raul Cortés. Dynamic growth of microvoids under combined hydrostatic and deviatoric stresses. *International journal of solids and structures*, 29(13):1637–1645, 1992.

[86] Raul Cortés. The growth of microvoids under intense dynamic loading. *International journal of solids and structures*, 29(11):1339–1350, 1992.

[87] Ze-Ping Wang. Growth of voids in porous ductile materials at high strain rate. *Journal of applied physics*, 76(3):1535–1542, 1994.

[88] J Zheng, YL Bai, and ZP Wang. Influence of inertial and thermal effects on the dynamic growth of voids in porous ductile materials. *Le Journal de Physique IV*, 4(C8):C8–765, 1994.

[89] X Y Wu, K T Ramesh, and T W Wright. The coupled effects of plastic strain

gradient and thermal softening on the dynamic growth of voids. *International journal of solids and structures*, 40(24):6633–6651, 2003.

[90] X Y Wu, K T Ramesh, and T W Wright. The dynamic growth of a single void in a viscoplastic material under transient hydrostatic loading. *Journal of the Mechanics and Physics of Solids*, 51(1):1–26, 2003.

[91] X Y Wu, K T Ramesh, and T W Wright. The effects of thermal softening and heat conduction on the dynamic growth of voids. *International journal of solids and structures*, 40(17):4461–4478, 2003.

[92] M Ortiz and A Molinari. Effect of strain hardening and rate sensitivity on the dynamic growth of a void in plastic material. *Journal of applied mechanics*, 59 (1):48–53, 1992.

[93] W Tong and G Ravichandran. Dynamic pore collapse in viscoplastic materials. *Journal of applied physics*, 74(4):2425–2435, 1993.

[94] W Tong and G Ravichandran. Inertial effects on void growth in porous viscoplastic materials. *Journal of applied mechanics*, 62(3):633–639, 1995.

[95] RW Klopp, RJ Clifton, and TG Shawki. Pressure-shear impact and the dynamic viscoplastic response of metals. *Mechanics of Materials*, 4(3):375–385, 1985.

[96] GI Kanel, SV Razorenov, A Bogatch, AV Utkin, VE Fortov, and DE Grady.

Spall fracture properties of aluminum and magnesium at high temperatures. *Journal of applied physics*, 79(11):8310–8317, 1996.

[97] VE Fortov, VV Kostin, and S Eliezer. Spallation of metals under laser irradiation. *Journal of applied physics*, 70(8):4524–4531, 1991.

[98] JP Cuq-Lelandais, M Boustie, L Berthe, T De Rességuier, P Combis, JP Colombier, M Nivard, and A Claverie. Spallation generated by femtosecond laser driven shocks in thin metallic targets. *Journal of Physics D: Applied Physics*, 42(6):065402, 2009.

[99] E Moshe, S Eliezer, Z Henis, M Werdiger, E Dekel, Y Horovitz, S Maman, IB Goldberg, and D Eliezer. Experimental measurements of the strength of metals approaching the theoretical limit predicted by the equation of state. *Applied Physics Letters*, 76(12):1555–1557, 2000.

[100] GI Kanel, SV Razorenov, K Baumung, and J Singer. Dynamic yield and tensile strength of aluminum single crystals at temperatures up to the melting point. *Journal of Applied Physics*, 90(1):136–143, 2001.

[101] T W Wright and K T Ramesh. Dynamic void nucleation and growth in solids: A self-consistent statistical theory. *Journal of the Mechanics and Physics of Solids*, 56(2):336–359, 2008.

[102] T W Wright and K T Ramesh. Statistically informed dynamics of void growth

in rate dependent materials. *International Journal of Impact Engineering*, 36 (10):1242–1249, 2009.

[103] JA Gorman, DS Wood, and T Vreeland. Mobility of dislocations in aluminum. *Journal of Applied Physics*, 40(2):833–841, 1969.

[104] Günther Leibfried. Über den einfluß thermisch angeregter schallwellen auf die plastische deformation. *Zeitschrift für Physik*, 127(4):344–356, 1950.

[105] A Molinari and TW Wright. A physical model for nucleation and early growth of voids in ductile materials under dynamic loading. *Journal of the Mechanics and Physics of Solids*, 53(7):1476–1504, 2005.

[106] Ahmed Amine Benzerga and Jacques Besson. Plastic potentials for anisotropic porous solids. *European Journal of Mechanics-A/Solids*, 20(3):397–434, 2001.

[107] JD Eshelby. Uniformly moving dislocations. *Proceedings of the Physical Society. Section A*, 62(5):307, 1949.

[108] JE Dorn, J Mitchell, and F Hauser. Dislocation dynamics. *Experimental mechanics*, 5(11):353–362, 1965.

[109] DC Ahn, P Sofronis, M Kumar, J Belak, and R Minich. Void growth by dislocation-loop emission. *Journal of applied physics*, 101(6):063514–063514, 2007.

[110] Christophe Czarnota, Nicolas Jacques, Sebastien Mercier, and Alain Molinari. Modelling of dynamic ductile fracture and application to the simulation of plate impact tests on tantalum. *Journal of the Mechanics and Physics of Solids*, 56 (4):1624–1650, 2008.

[111] Nicolas Jacques, Sebastien Mercier, and Alain Molinari. Effects of microscale inertia on dynamic ductile crack growth. *Journal of the Mechanics and Physics of Solids*, 60(4):665–690, 2012.

[112] Lynn Seaman, Donald R Curran, and Donald A Shockey. Computational models for ductile and brittle fracture. *Journal of Applied Physics*, 47(11):4814–4826, 1976.

[113] E Moshe, S Eliezer, E Dekel, A Ludmirsky, Z Henis, M Werdiger, IB Goldberg, N Eliaz, and D Eliezer. An increase of the spall strength in aluminum, copper, and metglas at strain rates larger than 10 7 s-1. *Journal of applied physics*, 83 (8):4004–4011, 1998.

[114] Nicholas A Pedrazas, Daniel L Worthington, D Allen Dalton, Paul A Sherek, Sean P Steuck, Hernan J Quevedo, Aaron C Bernstein, Eric M Taleff, and Todd Ditmire. Effects of microstructure and composition on spall fracture in aluminum. *Materials Science and Engineering: A*, 536:117–123, 2012.

[115] Yizhe Tang, Eduardo M Bringa, Bruce A Remington, and Marc A Meyers.

Growth and collapse of nanovoids in tantalum monocrystals. *Acta Materialia*, 59(4):1354–1372, 2011.

[116] James R Rice and Robb Thomson. Ductile versus brittle behaviour of crystals. *Philosophical magazine*, 29(1):73–97, 1974.

[117] Frederick Seitz. On the generation of vacancies by moving dislocations. *Advances in Physics*, 1(1):43–90, 1952.

[118] NF Mott. Cxvii. a theory of work-hardening of metal crystals. *Philosophical Magazine*, 43(346):1151–1178, 1952.

[119] NF Mott. Lxxviii. a theory of work-hardening of metals ii: Flow without slip-lines, recovery and creep. *Philosophical magazine*, 44(354):742–765, 1953.

[120] NP Mott. Xx. note on the electronic structure of the transition metals. *Philosophical Magazine*, 44(349):187–190, 1953.

[121] Vikram Gavini. Role of the defect core in energetics of vacancies. *Proceedings of the Royal Society A: Mathematical, Physical and Engineering Science*, 465 (2110):3239–3266, 2009.

[122] AM Cuitino and M Ortiz. Ductile fracture by vacancy condensation in fcc single crystals. *Acta materialia*, 44(2):427–436, 1996.

[123] Celia Reina, Bo Li, Kerstin Weinberg, and Michael Ortiz. A micromechanical model of distributed damage due to void growth in general materials and under

general deformation histories. *International Journal for Numerical Methods in Engineering*, 93(6):575–611, 2013.

[124] T Mori and K Tanaka. Average stress in matrix and average elastic energy of materials with misfitting inclusions. *Acta metallurgica*, 21(5):571–574, 1973.

[125] J Dundurs and T Mura. Interaction between an edge dislocation and a circular inclusion. *Journal of the Mechanics and Physics of Solids*, 12(3):177–189, 1964.

[126] Vlado A Lubarda. Image force on a straight dislocation emitted from a cylindrical void. *International Journal of Solids and Structures*, 48(5):648–660, 2011.

[127] Jianxiang Peng, Fuqian Jing, Dahong Li, and Lili Wang. Pressure and temperature dependence of shear modulus and yield strength for aluminum, copper, and tungsten under shock compression. *Journal of applied physics*, 98(1): 013508, 2005.

[128] DJ Oh and RA Johnson. Simple embedded atom method model for fec and hcp metals. *Journal of Materials Research*, 3(03):471–478, 1988.

[129] Vaclav Vitek and David J Srolovitz. *Atomistic simulation of materials: beyond pair potentials*. Plenum Publishing Corporation, 1989.

[130] Mike P Allen, Dominic J Tildesley, et al. *Computer simulation of liquids*. Clarendon press Oxford, 1987.

[131] Albert M Iskandarov, Sergey V Dmitriev, and Yoshitaka Umeno. Temperature effect on ideal shear strength of al and cu. *Physical Review B*, 84(22):224118, 2011.

[132] Kejie Zhao, Liangliang Fan, and Changqing Chen. Multiaxial behavior of nanoporous single crystal copper: a molecular dynamics study. *Acta Mechanica Solida Sinica*, 22(6):650–656, 2009.

[133] WR Tyson and WA Miller. Surface free energies of solid metals: Estimation from liquid surface tension measurements. *Surface Science*, 62(1):267–276, 1977.

[134] KJ Zhao, CQ Chen, YP Shen, and TJ Lu. Molecular dynamics study on the nano-void growth in face-centered cubic single crystal copper. *Computational Materials Science*, 46(3):749–754, 2009.

[135] Ping Yi and Michael Falk. Atomistic modeling of defect structure and mobility in mg: Void-assisted dislocation nucleation. In *Materials in Extreme Dynamic Environments Fall Meeting Poster Session*, Towson, MD, October 2014.

[136] Levente Vitos, AV Ruban, Hans Lomholt Skriver, and J Kollar. The surface energy of metals. *Surface Science*, 411(1):186–202, 1998.

[137] Andrew David Brown, Leda Wayne, Quan Pham, Kapil Krishnan, Pedro Peralta, Sheng-Nian Luo, Brian M Patterson, Scott Greenfield, Darrin Byler, Kenneth J McClellan, et al. Microstructural effects on damage nucleation in shock-

loaded polycrystalline copper. *Metallurgical and Materials Transactions A*, pages 1–9, 2014.

[138] Jianmin Qu and Mohammed Cherkaoui. *Fundamentals of Micromechanics of Solids*. Wiley Online Library, 2006.

[139] Roger W Minich, James U Cazamias, Mukui Kumar, and Adam J Schwartz. Effect of microstructural length scales on spall behavior of copper. *Metallurgical and Materials Transactions A*, 35(9):2663–2673, 2004.

[140] Tarabay Antoun. *Spall fracture*. Springer, 2003.

[141] X Chen, JR Asay, SK Dwivedi, and DP Field. Spall behavior of aluminum with varying microstructures. *Journal of applied physics*, 99(2):023528, 2006.

[142] CL Williams, KT Ramesh, and DP Dandekar. Spall response of 1100-o aluminum. *Journal of Applied Physics*, 111(12):123528, 2012.

[143] John D Eshelby. The determination of the elastic field of an ellipsoidal inclusion, and related problems. *Proceedings of the Royal Society of London. Series A. Mathematical and Physical Sciences*, 241(1226):376–396, 1957.

[144] NJ Petch. The ductile-brittle transition in the fracture of α-iron: I. *Philosophical Magazine*, 3(34):1089–1097, 1958.

[145] GI Kanel and SV Razorenov. Anomalies in the temperature dependences of

the bulk and shear strength of aluminum single crystals in the submicrosecond range. *Physics of the Solid State*, 43(5):871–877, 2001.

[146] Darby J Luscher, Curt A Bronkhorst, Coleman N Alleman, and Francis L Addessio. A model for finite-deformation nonlinear thermomechanical response of single crystal copper under shock conditions. *Journal of the Mechanics and Physics of Solids*, 61(9):1877–1894, 2013.

[147] Hans Ziegler. *An introduction to thermomechanics*. Elsevier, 1983.

[148] P Rosakis, AJ Rosakis, G Ravichandran, and J Hodowany. A thermodynamic internal variable model for the partition of plastic work into heat and stored energy in metals. *Journal of the Mechanics and Physics of Solids*, 48(3):581–607, 2000.

[149] J Hodowany, G Ravichandran, AJ Rosakis, and P Rosakis. Partition of plastic work into heat and stored energy in metals. *Experimental Mechanics*, 40(2): 113–123, 2000.

[150] WS Farren and GI Taylor. The heat developed during plastic extension of metals. *Proceedings of the Royal Society of London. Series A*, 107(743):422–451, 1925.

[151] Geoffrey Ingram Taylor and H Quinney. The latent energy remaining in a metal

after cold working. *Proceedings of the Royal Society of London. Series A*, 143 (849):307–326, 1934.

[152] John D Clayton. Modeling effects of crystalline microstructure, energy storage mechanisms, and residual volume changes on penetration resistance of precipitate-hardened aluminum alloys. *Composites Part B: Engineering*, 40 (6):443–450, 2009.

[153] Derek Hull and David J Bacon. *Introduction to dislocations*, volume 257. Pergamon Press Oxford, 1984.

[154] RM Christensen. *Mechanics of composite materials*. John Wiley & Sons. Inc., 1979.

[155] N Ramakrishnan and K Sivakumar. An equation of state for porous materials under shock loading. *Bulletin of Materials Science*, 11(1):75–85, 1988.

[156] JW Hutchinson. Bounds and self-consistent estimates for creep of polycrystalline materials. *Proceedings of the Royal Society of London. A. Mathematical and Physical Sciences*, 348(1652):101–127, 1976.

[157] D Peirce, RJ Asaro, and A Needleman. An analysis of nonuniform and localized deformation in ductile single crystals. *Acta metallurgica*, 30(6):1087–1119, 1982.

[158] Robert J Asaro. Crystal plasticity. *Journal of applied mechanics*, 50(4b):921–934, 1983.

[159] Robert J Asaro and A Needleman. Overview no. 42 texture development and strain hardening in rate dependent polycrystals. *Acta metallurgica*, 33(6):923–953, 1985.

[160] Marco Delbo, Guy Libourel, Justin Wilkerson, Naomi Murdoch, Patrick Michel, KT Ramesh, Clément Ganino, Chrystele Verati, and Simone Marchi. Thermal fatigue as the origin of regolith on small asteroids. *Nature*, 508(7495):233–236, 2014.

[161] Veverka, J. *et al.* The landing of the near-shoemaker spacecraft on asteroid 433 eros. *Nature* **413**, 390–393 (2001).

[162] Yano, H. *et al.* Touchdown of the hayabusa spacecraft at the muses sea on itokawa. *Science* **312**, 1350–1353 (2006).

[163] Gundlach, B. & Blum, J. A new method to determine the grain size of planetary regolith. *Icarus* **223**, 479–492 (2013).

[164] Housen, K. R., Wilkening, L. L., Chapman, C. R. & Greenberg, R. Asteroidal regoliths. *Icarus* **39**, 317–351 (1979).

[165] Hoerz, F. & Cintala, M. Impact experiments related to the evolution of planetary regoliths. *Meteoritics & Planetary Science* **32**, 179–209 (1997).

[166] Housen, K. R. & Holsapple, K. A. Ejecta from impact craters. *Icarus* **211**, 856–875 (2011).

[167] McFadden, L., Eppes, M., Gillespie, A. & Hallet, B. Physical weathering in arid landscapes due to diurnal variation in the direction of solar heating. *Geological Society of America Bulletin* **117**, 161–173 (2005).

[168] Luque, A., Ruiz-Agudo, E., Cultrone, G., Sebastián, E. & Siegesmund, S. Direct observation of microcrack development in marble caused by thermal weathering. *Environ Earth Sci* **62**, 1375–1386 (2011).

[169] Viles, H. *et al.* Simulating weathering of basalt on mars and earth by thermal cycling. *Geophys. Res. Lett.* **37**, L18201 (2010).

[170] Mainzer, A. *et al.* Characterizing subpopulations within the near-earth objects with neowise: Preliminary results. *The Astrophysical Journal* **752**, 110–126 (2012).

[171] Michel, P. & Richardson, D. C. Collision and gravitational reaccumulation: Possible formation mechanism of the asteroid itokawa. *Astronomy & Astrophysics* **554**, L1 (2013).

[172] Hoerz, F., Schneider, E., Gault, D. E., Hartung, J. B. & Brownlee, D. E. Catastrophic rupture of lunar rocks - a monte carlo simulation. *Lunar Science Institute* **13**, 235–258 (1975).

[173] Nesvorný, D. *et al.* Cometary origin of the zodiacal cloud and carbonaceous

micrometeorites. implications for hot debris disks. *The Astrophysical Journal* **713**, 816–836 (2010).

[174] Briani, G., Morbidelli, A., Gounelle, M. & Nesvorný, D. Evidence for an asteroid-comet continuum from simulations of carbonaceous microxenolith dynamical evolution. *Meteoritics & Planetary Science* **46**, 1863–1877 (2011).

[175] Andrew J Dombard, Olivier S Barnouin, Louise M Prockter, and Peter C Thomas. Boulders and ponds on the asteroid 433 eros. *Icarus*, 210(2):713–721, 2010.

[176] Jamie Molaro and Shane Byrne. Rates of temperature change of airless landscapes and implications for thermal stress weathering. *Journal of Geophysical Research: Planets (1991–2012)*, 117(E10), 2012.

[177] Spencer, J. R., Lebofsky, L. A. & Sykes, M. V. Systematic biases in radiometric diameter determinations. *Icarus* **78**, 337–354 (1989).

[178] Čapek, D. & Vokrouhlický, D. Thermal stresses in small meteoroids. *A&A* **519**, A75 (2010).

[179] Christensen, R. M. Mechanics of composite materials. *Krieger Publishing Company, Malabar, FL* 1–679 (1979).

[180] Marchi, S., Magrin, S., Nesvorný, D., Paolicchi, P. & Lazzarin, M. A spectral slope versus perihelion distance correlation for planet-crossing asteroids.

Monthly Notices of the Royal Astronomical Society: Letters **368**, L39–L42 (2006).

[181] Marchi, S., Delbo', M., Morbidelli, A., Paolicchi, P. & Lazzarin, M. Heating of near-earth objects and meteoroids due to close approaches to the sun. *Monthly Notices of the Royal Astronomical Society* 147–153 (2009).

[182] Jewitt, D. The active asteroids. *The Astronomical Journal* **143**, 66–80 (2012).

[183] Opeil, C. P., Consolmagno, G. J. & Britt, D. T. The thermal conductivity of meteorites: New measurements and analysis. *Icarus* **208**, 449–454 (2010).

[184] Janssen, M., Zuidema, J. & Wanhill, R. Fracture mechanics (second edition). *Spon Press* 1–365 (2004).

[185] Migliazza, M., Ferrero, A. & Spagnoli, A. Experimental investigation on crack propagation in carrara marble subjected to cyclic loads. *International Journal of Rock Mechanics and Mining Sciences* **48**, 1038–1044 (2011).

[186] Glinka, G. & Shen, G. Universal features of weight functions for cracks in mode i. *Engng. Fract. Mech.* **40**, 1135–1146 (1991).

[187] Suresh, S. Fatigue of materials (edition 2, illustrated, reprint, revised). *Cambridge University Press* 1–679 (1998).

[188] Medvedev, R. V., Gorbatsevich, F. I. & Zotkin, I. T. Determination of the

physical properties of stony meteorites with application to the study of processes of their destruction. *Meteoritika* **44**, 105–110 (1985).

[189] Flynn, G. J. Physical properties of meteorites and interplanetary dust particles: Clues to the properties of the meteors and their parent bodies. *Earth Moon and Planets* **95**, 361–374 (2004).

[190] Hazen, R. M. Temperature, pressure and composition: structurally analogous variables. *Physics and Chemistry of Minerals* **1.1**, 83–94 (1977).

[191] Anderson, O., Isaak, D. & Oda, H. Thermoelastic parameters for six minerals at high temperature. *Journal of Geophysical Research* **96**, 18037–18046 (1991).

[192] Smyth, J. R. High temperature crystal chemistry of fayalite. *Am Mineral* **60**, 1092–1097 (1975).

[193] TJ Vogler and JD Clayton. Heterogeneous deformation and spall of an extruded tungsten alloy: plate impact experiments and crystal plasticity modeling. *Journal of the Mechanics and Physics of Solids*, 56(2):297–335, 2008.

Vita

Justin Wilkerson was born in Dallas, Texas, on April 11, 1987 to Paula and Robert Wilkerson. In 2009 he graduated with highest honors from Texas A&M University with a Bachelor of Science in Aerospace Engineering. In 2010 he entered the Mechanical Engineering Ph.D. program at Johns Hopkins University, where he obtained a Master of Science in Engineering in 2013 and completed the requirements for the degree of Doctor of Philosophy in 2014.

At Texas A&M, Justin worked with Drs. Daniel Davis and Dimitris Lagoudas on the development of multifunctional nanocomposites. At Johns Hopkins, he worked with Dr. K.T. Ramesh on the mechanics of materials in extreme environments. Starting in January 2015, Justin will continue to pursue his research and teaching interests as an assistant professor in the mechanical engineering department at the University of Texas at San Antonio (UTSA).

Justin's academic achievements have been recognized and supported by a number of honors and awards, including the National Defense Science and Engineering Graduate (NDSEG) Fellowship, the National Science Foundation (NSF) Graduate Research Fellowship, and the Ammon S. Andes Award presented annually to recognize the nation's top aerospace engineering graduate.